Springer Tracts in Modern Physics 257

Maurizio Dapor

Transport of Energetic Electrons in Solids

Computer Simulation with Applications to Materials Analysis and Characterization

Second Edition

Springer

Springer Tracts in Modern Physics

Volume 257

Springer Tracts in Modern Physics provides comprehensive and critical reviews of topics of current interest in physics. The following fields are emphasized:

- Elementary Particle Physics
- Condensed Matter Physics
- Light Matter Interaction
- Atomic and Molecular Physics
- Complex Systems
- Fundamental Astrophysics

Suitable reviews of other fields can also be accepted. The Editors encourage prospective authors to correspond with them in advance of submitting a manuscript. For reviews of topics belonging to the above mentioned fields, they should address the responsible Editor as listed in "Contact the Editors".

More information about this series at http://www.springer.com/series/426

Maurizio Dapor

Transport of Energetic Electrons in Solids

Computer Simulation with Applications to Materials Analysis and Characterization

Second Edition

Springer

Maurizio Dapor
European Centre for Theoretical Studies
in Nuclear Physics and Related Areas
Trento
Italy

ISSN 0081-3869 ISSN 1615-0430 (electronic)
Springer Tracts in Modern Physics
ISBN 978-3-319-47490-8 ISBN 978-3-319-47492-2 (eBook)
DOI 10.1007/978-3-319-47492-2

Library of Congress Control Number: 2016954513

Printed on acid-free paper

This Springer imprint is published by Springer Nature
The registered company is Springer International Publishing AG
The registered company address is: Gewerbestrasse 11, 6330 Cham, Switzerland

To my dearest father, always alive in my mind and in my heart

Preface to the Second Edition

This book describes all the scattering mechanisms (elastic and inelastic) of electrons with the atoms of the target in a way in the simplest possible way. The use of quantum mechanics mechanims is described in detail for the investigation of interaction processes of electrons with matter. This book presents the strategies of the Monte Carlo method and compares numerous results of the simulations and the experimental data available in the literature. The new content of this extended and updated second edition includes the derivation of the Rutherford formula, details about the calculation of the phase shifts that are used in the relativistic partial wave expansion method, and the description of the Mermin theory. The role of secondary electrons in the proton cancer therapy is discussed as well in the chapter devoted to applications: Monte Carlo results on the radial distribution of the energy deposited in solids by secondary electrons generated by energetic proton beams are presented in this context.

Povo — Maurizio Dapor
August 2016

Preface to the First Edition

In modern physics we are interested in systems with many degrees of freedom. Let us consider, for example, the number of atoms in a solid, the number of electrons in an atom, or the number of electrons of a beam interacting with many atoms and electrons of a solid.

In many situations, these systems can be described by the calculations of definite integrals of very high dimension. An example is the evaluation of the classical partition function for a gas of many atoms at a temperature T. The Monte Carlo method provides us with a very accurate way to calculate high-dimensional definite integrals: It evaluates the integrand at a random sampling of abscissa.

The Monte Carlo method is also used for evaluating the many physical quantities necessary for the study of the interactions of particle beams with solid targets. The simulation of the involved physical processes, by random sampling, allows us for the solution of many particle transport problems. Letting the particles carry out an artificial, random walk—taking into account the effect of the single collisions—it is possible to accurately evaluate the diffusion process.

This book is devoted to electron-beam interactions with solid targets. As a researcher in this field, I am persuaded that a book on kV electron transport in solids can be very useful. It is difficult, for the newcomer, to find this topic exhaustively treated, and the beginner can be overwhelmed by the great number of published papers.

The Monte Carlo simulation is the most powerful theoretical method for evaluating the physical quantities related to the interaction of electrons with a solid target. A Monte Carlo simulation can be considered as an idealized experiment. The simulation does not investigate the fundamental principles of the interaction. It is necessary to know them—in particular the energy loss and angular deflection phenomena—to produce a good simulation.

This book is complementary to many other texts dedicated to similar subjects (including my book entitled Electron-Beam Interactions with Solids, published by Springer-Verlag in 2003) for the following two aspects.

1. I have, on the one hand, systematically minimized the mathematical contents of the most difficult theoretical parts. Since the essential concept to be grasped is the meaning of the various cross sections, the mathematical details, for the sake of clarity, have been deliberately avoided. I have reduced the theoretical part to the presentation of the energy loss and the angular deflections, providing simple recipes to calculate the stopping power, the differential inverse inelastic mean free path, and the differential elastic scattering cross section. This allowed me to avoid an in-depth description of the quantum theory. Mathematical contents and details can be found in the Appendices, in my previous book, and in many other books dedicated to modern physics and quantum mechanics.
2. In the derivation and use of the simpler theoretical transport models, I have, on the other hand, included many details. I think, indeed, that there is a need of a basic physical picture in order to provide the beginner with a solid background about electron transport in solids. This can be only achieved by a step-by-step derivation of the analytical formulas.

Comparing available experimental data with simulation results is a fundamental step in evaluating the quality of the Monte Carlo codes. Selected applications of the Monte Carlo method to kV electron transport in solids are presented in the second part of this book. This book compares computational simulations and experimental data in order to offer a more global vision.

Povo Maurizio Dapor
October 2013

Acknowledgments

I would like to gratefully thank my beloved children and my dearest parents for their immense patience and their generous willingness to help.

I wish to express my warm gratitude to my cherished Roberta for her encouragement and continuous support.

It is also a pleasure to mention many people, friends, and colleagues who, with their enthusiasm, invaluable suggestions, ideas, and competence, considerably contributed to achieve the results presented in this book: I am, in particular, very grateful to Diego Bisero, Lucia Calliari, Giovanni Garberoglio, and Simone Taioli for their help and sincere friendship.

I am also indebted to all the researchers who made possible, with their help, the completion of the project: Isabel Abril, Martina Azzolini, Nicola Bazzanella, Mauro Borghesi, Eric Bosch, Mauro Ciappa, Michele Crivellari, Pablo de Vera, Sergey Fanchenko, Wolfgang Fichtner, Massimiliano Filippi, Rafael Garcia-Molina, Stefano Gialanella, Stephan Holzer, Emre Ilgüsatiroglu, Beverley J. Inkson, Mark A.E. Jepson, Alexander Koschik, Robert C. Masters, Antonio Miotello, Tommaso Morresi, Francesco Pederiva, Cornelia Rodenburg, John M. Rodenburg, Manoranjan Sarkar, Paolo Scardi, Giorgina Scarduelli, Siegfried Schmauder, Emanuele Scifoni, Stefano Simonucci, Laura Toniutti, Chia-Kuang (Frank) Tsung, Jochen Wambach, Quan Wan, and Wolfram Weise.

I would like to thank all my colleagues at Interdisciplinary Laboratory for Computational Science (LISC) in Trento for the fruitful discussions. The stimulating atmosphere of LISC provided the ideal environment to work on this project.

I am grateful to Maria Del Huerto Flammia for assisting me with the grammar proofreading of this book.

I acknowledge the support of the Leverhulme Trust through the visiting professorship VP1-2014-011 (Department of Engineering Materials of the University of Sheffield).

I also wish to thank the European Centre for Theoretical Studies in Nuclear Physics and Related Areas (ECT*), the Trento Institute for Fundamental Physics and Applications (TIFPA), the Department of Engineering Materials of the

University of Sheffield, the Integrated Systems Laboratory of the Swiss Federal Institute of Technology (ETH) of Zurich, and the Departament de Física Aplicada of the Universitat d'Alacant.

Contents

Chapter 1
Electron Transport in Solids

The Monte Carlo (MC) method is used for evaluating the many physical quantities necessary to the study of the interactions of particle-beams with solid targets. Studies of backscattered and secondary electrons are of great interest for many analytical techniques. A better comprehension of the processes which occur before the emission of backscattered and secondary electrons would allow a more comprehensive understanding of surface physics.

1.1 Motivation: Why Are Electrons Important

Electrons continuously interact with the matter around us. Plasma processing of materials, electron lithography, electron microscopy and spectroscopies, plasma-wall in fusion reactors, interaction of charged particles with the surfaces of space-crafts, and hadron therapy represent only a few technological examples where electrons are involved and play a role.

In fact, we use electron beams for our purposes, either on the front of production of materials or on that of their characterization. Let us think of the many applications such as processing of materials with plasma and of the local melting of materials for joining large components. We use electron beams also in electron lithography, an important technique utilized for the production of microelectronics devices. Let us consider the importance of the beams of electrons in material characterization, performed using techniques such as electron microscopy and all electron spectroscopies. Electrons interact with the surfaces of space-crafts. Plasma-wall interaction in fusion reactors also involves electron-matter interaction. Electrons play a role also in cancer proton therapy, where cascades of secondary electrons are produced. These very low energy electrons are toxic for human body cells, since they produce damage to the biomolecules due to ionizations/excitations and the resulting break of chemical bonds. Also secondary electrons which have ultra-low energy – and which, for a long

M. Dapor, *Transport of Energetic Electrons in Solids*,
Springer Tracts in Modern Physics 257, DOI 10.1007/978-3-319-47492-2_1

time, were thought to be relatively harmless – are dangerous for biomolecules due to the so-called *dissociative electron attachment*. And, of course, we want to minimize the effects of irradiation on the healthy tissues near to the diseased cells.

In all the cases above, modeling the interaction of electrons with matter is very important, as it can be used to provide a solid theoretical interpretation of experimental evidence.

These are the reasons for which an accurate and detailed study of the interaction mechanisms of electrons with matter is of paramount importance.

1.2 The Monte Carlo Method

The world is ruled by quantum mechanics. The investigation of the processes of electron-matter interaction requires the use of quantum mechanics-based techniques. And since, typically, the number of particles involved in these processes is huge, it is crucial to use statistical approaches, such as those represented by the Monte Carlo method. This method provides a very accurate description of many of the phenomena that we can observe in nature when electrons interact with materials.

The Monte Carlo method is a numerical procedure which uses random numbers, theory of probability, and statistics to evaluate multiple integrals.

Suppose we need to calculate the area of a closed surface. In order to do so, we can surround the curve with a square of known side. Then we generate a large number of random points inside the square. Whenever a random point falls within the surface, we update a counter. When the number of points is very large, the ratio of those fallen within the surface and the total number of generated points will approach the ratio between the (unknown) area of the surface and the (known) area of the square.

It is very important to emphasize that, when the number of dimensions is high (as it is when dealing with all statistical problems) the Monte Carlo method is the best numerical procedure for the calculation of multiple integrals. Complicated problems of physics involving very large numbers of particles can be addressed with the Monte Carlo method: it can realize real numerical simulations of physical processes such as the interaction of an electron beam with a solid.

The Monte Carlo method is used, in particular, for evaluating the many physical quantities necessary to the study of the interactions of particle-beams with solid targets. By letting the particles carry out an artificial, random walk – taking into account the effect of the single collisions – it is possible to accurately evaluate the diffusion process [1–4].

1.3 The Monte Carlo Ingredients

To work properly, the Monte Carlo method needs a set of input data describing the interaction of the particle beam with the target. Such data specify the kind of materials and, of course, the kind of incident particles. The interactions of the particles

impinging on the specimen with the target atoms can be described by the cross-sections that describe different physical phenomena. In fact various kinds of interaction occur during the passage of the electrons through the material.

In particular we will investigate the elastic electron-atom processes, described by the so-called elastic scattering cross-section. The elastic scattering cross-section can be described by an equation known as the *screened Rutherford cross-section* formula. This is an analytical expression valid when the energy of the incident electrons is relatively high and the atomic numbers of the target atoms are relatively low, as it was deduced within the so-called *first Born approximation*. But, since the case of low energy electrons and high atomic numbers is not well described by such a simple formula, in order to simulate the elastic scattering cross-section with a more general formulation – valid for all energies and atomic numbers – a more complex approach is necessary, which is known as the *relativistic partial wave expansion method* (Mott cross-section [5]).

Concerning the inelastic scattering cross-section, we will use semi-empirical analytical formulas, when possible, and the so-called dielectric Ritchie's theory [6] for dealing with the more general cases.

When electron energy becomes relatively small (let us say, smaller than 20–30 eV, depending on the investigated material) another very important mechanism of energy loss (and energy gain) is related to the creation (and annihilation, respectively) of phonons. For describing such a phenomenon, we will introduce the electron-phonon cross-section utilizing the Fröhlich's theory [7].

In the end, in many cases also trapping phenomena are important and need to be considered in the simulations. They can be due to the polarization of materials (insulators) induced by the passage of very slow electrons through them [8] and/or also to defects in the materials. When dealing with insulating materials, trapping phenomena are mainly due to the so called polaronic effect, i.e., to the creation of quasi-particles constituted by slow electrons with the polarization field around them [8]. In the case of metals and semiconductors, traps are mainly due to defects in the materials (i.e., impurities, structural defects, grain boundaries etc.).

1.4 Electron-Beam Interactions with Solids

During their travel in the solid, the incident electrons lose energy and change direction at each collision with the atoms bound in the solid. Because of the large difference between the masses of the electron and the atomic nucleus, nuclear collisions deflect electrons with very small kinetic energy transfers. This process is described by the differential elastic scattering cross-section (which can be calculated by the so-called relativistic partial wave expansion method, corresponding to the Mott cross-section [5]). The Mott cross-section can be approximated with the screened Rutherford formula: this is possible when the conditions corresponding to the first Born approximation are satisified, i.e., for high energy and for low atomic number of the target atom. Additionally, excitation and ejection of atomic electrons, and excitation of

plasmons, affect the energy dissipation. These processes only slightly affect the direction of the incident electron in the solid, so that they can be described as inelastic events. Plasmon excitations are ruled by the equations for the differential inverse inelastic mean free path, calculated by the use of Ritchie's dielectric theory [6]. The Fröhlich theory [7] can be used for describing the quasi-elastic electron-phonon interactions in insulating materials. Electron-phonon interactions are considered quasi-elastic for the corresponding energy losses and gains are very small when compared to the plasmon energy losses. When, in insulating materials, electron kinetic energies considerably decreases, trapping phenomena due to the polaronic effect have to be taken into account as well [8].

While for electron kinetic energies higher than 10 keV, MC simulations provide excellent results by just using the Rutherford differential elastic scattering cross-section (elastic scattering) and the Bethe-Bloch stopping power formula or semi-empirical stopping power[1] formulas (inelastic scattering), when the electron energies become much smaller than 5 keV – and this is the case of secondary electron emission – this approach fails [10]. There are many reasons, and the most important ones are related to the three following facts:

(i) As the Rutherford formula is a result of the first Born approximation, it is a high energy approximation.

(ii) Also the Bethe-Bloch formula is valid only for quite high energies; in particular, the Bethe-Bloch stopping power does not provide the correct predictions when the electron energy E becomes smaller than the mean ionization energy I. It reaches a maximum and then approaches zero as E approaches I / 1.166. Below I / 1.166, the predicted stopping power becomes negative. The use of semi-empiric approaches can sometimes mitigate the problem. Actually, numerical approaches based on the calculation of the dielectric function - as a function of the energy loss and of the momentum transfer - are necessary to calculate low energy inelastic processes.

(iii) The inclusion of the stopping power in the MC code corresponds to the use of the so-called *continuous-slowing-down approximation* (CSDA). Such a way of describing energy losses completely neglects that actually electrons lose their energy in several inelastic collisions. Sometimes an electron can even lose all its energy in a single collision. In other words, any realistic model of the electron trajectories should avoid the approximation of continuity in describing the electron energy losses. CSDA can be used (and will be used, when possible, in the present work as well) but only in cases where the details of the energy loss mechanisms are not crucial for the accurate description of the process under investigation. CSDA can be used, for example, for the calculation of the backscattering coefficient. We will see that, in some specific cases, even the calculation of the secondary electron yield can be performed using CSDA. On

[1] In this book we will use the expression *stopping power* instead of *stopping force* to indicate the energy loss per unit distance of the electron in the solid. Even if consistent with the units, and hence more accurate, the use in the literature of the expression *stopping force*, as observed by Peter Sigmund [9], is only slowly appearing, after a hundred years of use of the term *stopping power*.

the contrary, the description of the energy distributions of the emitted electrons (both backscattered and secondary) have to be performed avoiding the approximation of continuity in the energy loss processes and including *energy straggling* (ES) – i.e., the statistical fluctuations of the energy loss due to the different energy losses suffered by each electron travelling in the solid – in the calculations.

A detailed approach able to accurately describe low energy elastic and inelastic scattering and to appropriately take into account the energy straggling is required for the description of secondary electron cascade. The whole cascade of secondary electrons must be followed: indeed any truncation, or cut off, underestimates the secondary electron emission yield. Also, as already discussed, for insulating materials the main mechanisms of energy loss cannot be limited to the electron-electron interaction for, when the electron energy becomes very small (lower than 10–20 eV, say), inelastic interactions with other particles or quasi-particles are responsible for electron energy losses. In particular, at very low electron energy, trapping phenomena due to electron-polaron interactions (polaronic effects) and electron-phonon interactions are the main mechanisms of electron energy loss. For electron-phonon interaction, even phonon annihilations and the corresponding energy gains should be taken into account. Actually the energy gains are often neglected, for their probability of occurence is very small: much smaller, in any case, than the probability of phonon creation.

Summarizing, incident electrons are scattered and lose energy, due to the interactions with the atoms of the specimen, so that the incident electrons direction and kinetic energy are changed. It is usual to describe the collision events assuming that they belong to three distinct kinds: elastic (scattering with atomic nuclei), quasi-elastic (scattering with phonons) and inelastic (scattering with the atomic electrons and trapping due to the polaronic effect).

1.5 Electron Energy-Loss Peaks

Electron energy-loss spectroscopy treats the primary process in which the incident electron loses amounts of energy which characterize the target material (see, for example, Refs. [6, 11–30]). An electron spectrum represents the number of electrons as a function of the energy they have after interaction with a target. The spectrum can be represented as a function of either the electron energy or of the electron energy-loss. In this second case, the first peak on the left of the spectrum, centered at zero energy-loss, is known as the *zero-loss peak*. Also known as the *elastic peak*, it collects all the electrons which were transmitted – in transmission electron energy loss spectroscopy (TEELS) – or backscattered – in reflection electron energy loss spectroscopy (REELS) – without any measurable energy loss: it includes both the electrons which did not suffer any energy loss and those which were transmitted (TEELS) or backscattered (REELS) after one or more quasi-elastic collisions with

phonons (for which the energy transferred is so small that, with conventional spectrometers, it cannot be experimentally resolved). In TEELS, elastic peak includes also all the electrons which were not scattered at all, namely which were not deflected during their travel inside the target and did not lose energy.

Actually, the energy of electrons of the elastic peak is slightly reduced. This is due to the recoil energy transferred to the atoms of the specimen. Elastic peak electron spectroscopy (EPES) is the technique devoted to the analysis of the line-shape of the elastic peak [31, 32]. Since lighter elements show larger energy shifts, EPES can be used to detect hydrogen in polymers and hydrogenated carbon-based materials [33–40] measuring the energy difference between the position of the carbon elastic peak and that of the hydrogen elastic peak: this difference between the energy positions of the elastic peaks – for incident electron energy in the range 1000–2000 eV – is in the neighborhood of 2–4 eV.

In the first 30–40 eV from the elastic peak a generally quite broad peak collects all the electrons which suffered inelastic interaction with the outer-shell atomic electrons. Typically it includes electrons which suffered energy loss due to inelastic interaction with plasmons (*plasmon-losses*) and corresponding to inter-band and intra-band transitions. If the sample is sufficiently thick (in TEELS) and in the case of bulk targets (in REELS), the probability that an electron, before emerging from the specimen, has suffered more than one inelastic collision with plasmons is not negligible: such multiple electron-plasmon inelastic collisions are represented in the spectrum by the presence of a set of equidistant peaks (the distance from each other being given by the plasma energy). The relative intensities of these multiple inelastic scattering peaks decrease as the energy loss increases, demonstrating that the probability of suffering one inelastic collision is greater than the probability of suffering two inelastic collisions, which is in turn higher than the probability of suffering three inelastic collisions, and so on. Of course, in transmission EELS, the number of measurable plural scattering peaks is also a function of the thickness of the sample. Plural scattering peaks at multiples of the plasma energy are clearly observable – in the energy-loss region between the elastic peak and approximately 100–200 eV (i.e., in the energy spectrum, between 100–200 eV and the elastic peak) – when the film thickness is greater than the electron inelastic mean free path. On the other hand, when the film thickness is much smaller that the electron inelastic mean free path, a strong elastic peak and only the first plasmon-loss peak can be observed in the energy-loss region below 100–200 eV (i.e., above 100–200 eV from the elastic peak, in the energy spectrum).

For higher energy-losses, edges (of relatively low intensity with respect to the plasmon-losses), corresponding to inner-shell atomic electron excitations, can be observed in the spectrum. These edges are followed by slow falls, as the energy-loss increases. The energy position of these steps or, better, sharp rises, corresponds to the ionization threshold. The energy-loss of each edge is an approximate measure of the binding energy of the inner-shell energy level involved in the inelastic scattering process.

With an energy resolution better than 2 eV, it is possible to observe, in the low-loss peaks and in the ionization threshold edges, detailed features related to the band structure of the target and its crystalline characteristics. For example, in carbon, plasmon peaks can be found at different energies in the spectrum, according to the carbon structure. This is due to the different valence-electron densities of the different allotropic forms of carbon, such as diamond, graphite, C60-fullerite, glassy carbon, and amorphous carbon [26, 41].

For an excellent review about electron energy-loss spectra, see the Egerton book [26].

1.6 Auger Electron peaks

Also Auger electron peaks can be observed in the spectrum: they are due to the presence of doubly ionized atoms. Auger [42] and Meitner [43] noted the presence of pairs of tracks – originating from the same point – in X-ray irradiated cloud chambers filled with an inert gas. One of them had a variable length which depended on the energy of the incident radiation. The other track had a fixed length. Auger suggested the presence of doubly ionized atoms in the gas. Two years later, Wentzel made the hypothesis of a two-step process. A primary ionization, in the Wentzel interpretation, was followed by a decay process [44]. The incident radiation ionizes the system in the inner shell S. The system can then decay according to two alternative mechanisms. One is radiative: one electron drops out of an outer shell R into the inner shell S and a photon is emitted. The other one is non-radiative: one electron drops out of an outer shell R into the inner shell S, and the excess of energy is used to eject out of the shell R' another electron (the Auger electron). The two processes are competitive. In the electron spectrum, Auger electron peaks – due to the non-radiative process – can be recognized.

1.7 Secondary Electron Peak

Secondary electrons – produced by a cascade process – are those electrons extracted from the atoms by inelastic electron-electron collisions. Actually not all the secondary electrons generated in the solid emerge form the target. In order to emerge from the surface, the secondary electrons generated in the solid must reach the surface and satisfy given angular and energetic conditions. Of course, only the secondary electrons which are able to emerge from the target are included in the spectrum. Their energy distribution presents a pronounced peak in the region of the spectrum below 50 eV. The secondary electron emission yield is conventionally measured by integrating the area of the spectrum from 0 to 50 eV (including, in such a way, also the tail of backscattered electron whose number, in this energy region is actually negligible – unless the primary energy be very low as well).

1.8 Characterization of Materials

Simulation of transport of electrons in materials has been demonstrated to be very important for many applications. The determination of electron emission from solids irradiated by a particle beam is of crucial importance, especially in connection with the analytical techniques that utilize electrons to investigate chemical and compositional properties of solids in the near surface layers.

Electron spectroscopies and microscopies, examining how electrons interact with matter, represent fundamental tools to investigate electronic and optical properties of matter. Electron spectroscopies and microscopies allow to study the chemical composition, the electronic properties, and the crystalline structure of materials. According to the energy of the incident electrons, a broad range of spectroscopic techniques can be utilized: for example, low energy electron diffraction (LEED) allows to investigate the crystalline structure of surfaces, Auger electron spectroscopy (AES) permits to analyze the chemical composition of the surfaces of solids, electron energy loss spectroscopy – both in transmission, when the spectrometer is combined with transmission electron microscope, and in reflection – can be used to characterize materials by comparing the shape of the plasmon-loss peaks and the fine-structure features due to interband and intraband transitions with those of suitable standards, elastic peak electron spectroscopy is an useful tool to detect the presence of hydrogen in carbon-based materials.

The study of the properties of a material using electron probes requires the knowledge of the physical processes corresponding to the interaction of the electrons with the particular material under investigation. A typical AES peak of an atomic spectrum, for example, has a width in the range from 0.1 to 1.0 eV. In a solid, many energy levels are involved which are very close in energy, so that broad peaks are typically observed in AES spectra of solids. Their features also depend on the instrumental resolution. Another important characteristic of the spectra is related to the shift in energy of the peaks due to chemical environment: indeed the core energy levels of an atom are shifted when it is a part of a solid. This property is used to characterize materials, as the shift can be determined theoretically or by comparison with suitable standards. Even the changes in spectral intensities and the appearence of secondary peaks can be used for analyzing unknown materials. Electron spectra are used for self-supported thin film local thickness measurements, multilayer surface thin film thickness evaluation, doping dose determination in semiconductors, radiation damage investigations, and so on.

The backscattering electron coefficient can be used for non-destructive evaluation of over-layer film thickness [45, 46], while the study of the energy distribution of the backscattered electrons may be utilized for materials characterization through the study of the shape of plasmon-loss peaks [47, 48].

Secondary electron investigation allows extraction of critical dimensions by modeling the physics of secondary electron image formation [49–51]. It permits to investigate doping contrast in *p-n* junctions and to evaluate accurate nanometrology for the most advanced CMOS processes [52, 53].

1.9 Summary

Transport Monte Carlo simulation is a very useful mathematical tool for describing many important processes relative to the interaction of electron beams with solid targets. In particular, the backscattered and secondary electron emission from solid materials can be investigated with the use of the Monte Carlo method.

Many applications of the Monte Carlo study of backscattered and secondary electrons concern materials analysis and characterization. Among the many applications of MC simulations to analysis and characterization, we can mention non-destructive evaluation of over-layer film thickness [45, 46], materials characterization through the study of the main features of the electron spectra and the shape of plasmon-loss peaks [47], extraction of critical dimensions by modeling the physics of secondary electron image formation [49–51], and doping contrast in *p-n* junctions for the evaluation of accurate nanometrology for the most advanced CMOS processes [52, 53].

References

1. R. Shimizu, D. Ze-Jun, Rep. Prog. Phys. **55**, 487 (1992)
2. D.C. Joy, *Monte Carlo Modeling for Electron Microscopy and Microanalysis* (Oxford University Press, New York, 1995)
3. M. Dapor, *Electron-Beam Interactions with Solids: application of the Monte Carlo Method to Electron Scattering Problems* (Springer, Berlin, 2003)
4. C.G.H. Walker, L. Frank, I. Müllerová, Scanning **9999**, 1 (2016)
5. N.F. Mott, Proc. R. Soc. London Ser. **124**, 425 (1929)
6. R.H. Ritchie, Phys. Rev. **106**, 874 (1957)
7. H. Fröhlich, Adv. Phys. **3**, 325 (1954)
8. J.P. Ganachaud, A. Mokrani, Surf. Sci. **334**, 329 (1995)
9. P. Sigmund, *Particle Penetration and Radiation Effects* (Springer, Berlin, 2006)
10. M. Dapor, Phys. Rev. B **46**, 618 (1992)
11. R.H. Ritchie, A. Howie, Philos. Mag. **36**, 463 (1977)
12. H. Ibach, *Electron Spectroscopy for Surface Analysis* (Springer, Berlin, 1977)
13. P.M. Echenique, R.H. Ritchie, N. Barberan, J. Inkson, Phys. Rev. B **23**, 6486 (1981)
14. H. Raether, *Excitation of Plasmons and Interband Transitions by Electrons* (Springer, Berlin, 1982)
15. D.L. Mills, Phys. Rev. B **34**, 6099 (1986)
16. D.R. Penn, Phys. Rev. B **35**, 482 (1987)
17. J.C. Ashley, J. Electron Spectrosc. Relat. Phenom. **46**, 199 (1988)
18. F. Yubero, S. Tougaard, Phys. Rev. B **46**, 2486 (1992)
19. Y.F. Chen, C.M. Kwei, Surf. Sci. **364**, 131 (1996)
20. Y.C. Li, Y.H. Tu, C.M. Kwei, C.J. Tung, Surf. Sci. **589**, 67 (2005)
21. A. Cohen-Simonsen, F. Yubero, S. Tougaard, Phys. Rev. B **56**, 1612 (1997)
22. Z.-J. Ding, J. Phys. Condens. Matter **10**, 1733 (1988)
23. Z.-J. Ding, R. Shimizu, Phys. Rev. B **61**, 14128 (2000)
24. Z.-J. Ding, H.M. Li, Q.R. Pu, Z.M. Zhang, R. Shimizu, Phys. Rev. B **66**, 085411 (2002)
25. W.S.M. Werner, W. Smekal, C. Tomastik, H. Störi, Surf. Sci. **486**, L461 (2001)
26. R.F. Egerton, *Electron Energy-Loss Spectroscopy in the Electron Microscope*, 3rd edn. (Springer, New York, 2011)
27. R.F. Egerton, Rep. Prog. Phys. **72**, 016502 (2009)

28. S. Taioli, S. Simonucci, L. Calliari, M. Filippi, M. Dapor, Phys. Rev. B **79**, 085432 (2009)
29. S. Taioli, S. Simonucci, M. Dapor, Comput. Sci. Discov. **2**, 015002 (2009)
30. S. Taioli, S. Simonucci, L. Calliari, M. Dapor, Phys. Rep. **493**, 237 (2010)
31. G. Gergely, Progr. Surf. Sci. **71**, 31 (2002)
32. A. Jablonski, Progr. Surf. Sci. **74**, 357 (2003)
33. D. Varga, K. Tökési, Z. Berènyi, J. Tóth, L. Kövér, G. Gergely, A. Sulyok, Surf. Interface Anal. **31**, 1019 (2001)
34. A. Sulyok, G. Gergely, M. Menyhard, J. Tóth, D. Varga, L. Kövér, Z. Berènyi, B. Lesiak, A. Jablonski, Vacuum **63**, 371 (2001)
35. G.T. Orosz, G. Gergely, M. Menyhard, J. Tóth, D. Varga, B. Lesiak, A. Jablonski, Surf. Sci. **566–568**, 544 (2004)
36. F. Yubero, V.J. Rico, J.P. Espinós, J. Cotrino, A.R. González-Elipe, Appl. Phys. Lett. **87**, 084101 (2005)
37. V.J. Rico, F. Yubero, J.P. Espinós, J. Cotrino, A.R. González-Elipe, D. Garg, S. Henry, Diam. Relat. Mater. **16**, 107 (2007)
38. D. Varga, K. Tökési, Z. Berènyi, J. Tóth, L. Kövér, Surf. Interface Anal. **38**, 544 (2006)
39. M. Filippi, L. Calliari, Surf. Interface Anal. **40**, 1469 (2008)
40. M. Filippi, L. Calliari, C. Verona, G. Verona-Rinati, Surf. Sci. **603**, 2082 (2009)
41. R. Garcia-Molina, I. Abril, C.D. Denton, S. Heredia-Avalos, Nucl. Instrum. Methods Phys. Res. B **249**, 6 (2006)
42. P. Auger, P. Ehrenfest, R. Maze, J. Daudin, R.A. Fréon, Rev. Modern Phys. **11**, 288 (1939)
43. L. Meitner, Z. Phys. **17**, 54 (1923)
44. G. Wentzel, Z. Phys. **43**, 524 (1927)
45. M. Dapor, N. Bazzanella, L. Toniutti, A. Miotello, S. Gialanella, Nucl. Instrum. Methods Phys. Res. B **269**, 1672 (2011)
46. M. Dapor, N. Bazzanella, L. Toniutti, A. Miotello, M. Crivellari, S. Gialanella, Surf. Interface Anal. **45**, 677 (2013)
47. M. Dapor, L. Calliari, G. Scarduelli, Nucl. Instrum. Methods Phys. Res. B **269**, 1675 (2011)
48. M. Dapor, L. Calliari, S. Fanchenko, Surf. Interface Anal. **44**, 1110 (2012)
49. M. Dapor, M. Ciappa, W. Fichtner, J. Micro/Nanolith. MEMS MOEMS **9**, 023001 (2010)
50. M. Ciappa, A. Koschik, M. Dapor, W. Fichtner, Microelectron. Reliab. **50**, 1407 (2010)
51. A. Koschik, M. Ciappa, S. Holzer, M. Dapor, W. Fichtner, Proc. SPIE **7729**, 77290X–1 (2010)
52. M. Dapor, M.A.E. Jepson, B.J. Inkson, C. Rodenburg, Microsc. Microanal. **15**, 237 (2009)
53. C. Rodenburg, M.A.E. Jepson, E.G.T. Bosch, M. Dapor, Ultramicroscopy **110**, 1185 (2010)

Chapter 2
Cross-Sections: Basic Aspects

In the electron microscopies and spectroscopies, electrons penetrate a material experiencing many different scattering processes. For a realistic description of the electron emission, it is necessary to know all the scattering mechanisms involved [1, 2].

This chapter is devoted to the introduction of the concepts of cross-section and stopping power. For an excellent review of the topics treated in this chapter, also see Ref. [1]. The chosen approach is deliberately elementary, since the focus is on the basic aspects of the penetration theory. Specific details will be provided in the next chapters and in the Appendices.

From the macroscopic point of view, the *cross-section* represents the area of a target that can be hit by a projectile, so that it depends on the geometrical properties of both the target and the projectile. Let us consider, for example, a point bullet impinging on a spherical target whose radius is r. The cross-section σ of the target is, in such a case, simply given by $\sigma = \pi r^2$.

In the microscopic world the concept has to be generalized in order to take into account that the cross-section does not only depend on the projectile and on the target, but also on their relative velocity and on the physical phenomena we are interested in: examples are represented by the *elastic scattering cross-section* and the *inelastic scattering cross-section* of electrons (projectiles) impinging on atoms (targets). The elastic scattering cross-section describes the interactions in which the kinetic energy of the incident particle (the electron) does not change and is as a consequence the same before and after the interaction. The inelastic scattering cross-section, on the other hand, describes the collisions corresponding to an energy transfer from the incident particle (the electron) to the target (the atom): as a consequence, the kinetic energy of the incident electron decreases due to the interaction so that the electron slows down. As the cross-section is a function of the kinetic energy of the incident electron, after every inelastic collision the cross-sections (both elastic and inelastic) of the subsequent collision, if any, will be changed accordingly.

In real experiments, the investigators cannot measure the cross-section for a single electron which hits a single atom. The typical experiment consists, instead, in the collision of a great number of electrons, called the *beam*, with a medium constituted

M. Dapor, *Transport of Energetic Electrons in Solids*,
Springer Tracts in Modern Physics 257, DOI 10.1007/978-3-319-47492-2_2

by a configuration of many atoms and/or molecules (a gas, for example, or an amorphous or crystalline solid). The electrons constituting the beam have, in principle, all the same initial energy (the primary energy) and do not interact with each other but only with the atoms of the medium. Actually, in practical cases, the energies of the electrons constituting the primary beam are distributed around the primary energy which has to be considered their mean energy. Furthermore, the electrons of the beam do not interact only with the target atoms (or molecules) but with each other as well. Neglecting these interactions corresponds to investigating the so-called *low current beam approximation* [1].

2.1 Cross-Section and Probability of Scattering

Let us indicate with σ the cross-section of the physical effect we are interested in describing, and with J the density current, i.e., the number of electrons per unit area and per unit time in the beam. Let us indicate, furthermore, with N the number of target atoms per unit volume in the target and with S the area of the target where the beam is spread. Let us assume that the beam spreading is homogeneous. If z is the depth where the collisions occur, then the volume where the electrons interact with the stopping medium is given by zS and, as a consequence, the number of collisions per unit time can be calculated by $NzSJ\,\sigma$. As the product of S by J is the number of electrons per unit time, the quantity

$$P = Nz\sigma \tag{2.1}$$

represents the mean number of collisions per electron. In the hypothesis that the target thickness z is very small (thin layers) or the density of the target atoms N is very small (gas targets), so that $P \ll 1$, P represents the probability that an electron suffers a collision while travelling in the medium.

In order to take into account that in the great majority of the experiments the projectile undergoes many collisions, let us associate to the trajectory of each particle a cylindrical volume $V = z\sigma$ and calculate the probability P_ν to hit ν target particles in this volume. If the positions of any two targets particle are not correlated like in the case, for example, of an ideal gas, such a probability is given by the Poisson distribution

$$P_\nu = \frac{(NV)^\nu}{\nu!}\exp(-NV) = \frac{(Nz\sigma)^\nu}{\nu!}\exp(-Nz\sigma)\,, \tag{2.2}$$

where $\nu = 0, 1, 2, 3, \ldots$

Let us firstly consider the single collision problem, $\nu = 1$. The probability of hitting precisely one particle in the volume $z\sigma$ is given by

$$P_1 = P_{(\nu=1)} = (Nz\sigma)\exp(-Nz\sigma)\,, \tag{2.3}$$

so that, in the limit $Nz\sigma \ll 1$,

$$P_1 \cong P = Nz\sigma\,, \tag{2.4}$$

which is the same result deduced above.

Also note that, in the same limit, the probability for no collision at all is given by $1 - P = 1 - Nz\sigma$. This is the first order in $Nz\sigma$ of the well known Lambert and Beer's absorption law:

$$P_0 = P_{(\nu=0)} = \exp(-Nz\sigma)\,. \tag{2.5}$$

Note that, to the first order in $Nz\sigma$, the probability for double events is equal to zero.

As it is well known, one of the characteristics of the Poisson distribution is that its expected value and variance are identical. In particular, the average value $\langle\nu\rangle$ and the variance $\langle(\nu - \langle\nu\rangle)^2\rangle$, are given by

$$\langle\nu\rangle = \langle(\nu - \langle\nu\rangle)^2\rangle = Nz\sigma\,, \tag{2.6}$$

so that the relative fluctuation goes to zero as the reciprocal of the square root of $\langle\nu\rangle = Nz\sigma$:

$$\sqrt{\frac{\langle(\nu - \langle\nu\rangle)^2\rangle}{\langle\nu\rangle^2}} = \frac{1}{\sqrt{\nu}}\,. \tag{2.7}$$

2.2 Stopping Power and Inelastic Mean Free Path

Let us now consider the collisions with the stopping medium resulting in a kinetic energy transfer from the projectile to the target atoms and/or molecules constituting the target. Let us assume that the energy transfer T_i ($i = 1, 2, ...$) is small with respect to the incident particle kinetic energy E. Let us also assume that ν_i is the number of events corresponding to the energy loss T_i, so that the total energy ΔE lost by an incident particle passing through a thin film of thickness Δz is given by $\sum_i \nu_i T_i$.

As the mean number of type i collisions, according to Eq. (2.6), is given by $\langle\nu_i\rangle = N\Delta z\sigma_i$, where σ_i is the energy-loss cross-section, the energy loss is given by

$$\langle\Delta E\rangle = N\Delta z\sum_i T_i\sigma_i\,. \tag{2.8}$$

The *stopping power* is defined as

$$\frac{\langle\Delta E\rangle}{\Delta z} = N\sum_i T_i\sigma_i\,, \tag{2.9}$$

and the *stopping cross-section* S is given by

$$S = \sum_i T_i \, \sigma_i \,, \tag{2.10}$$

so that

$$\frac{\langle \Delta E \rangle}{\Delta z} = NS \,. \tag{2.11}$$

If the spectrum of the energy loss is continuous, instead of discrete, the stopping cross-section assumes the form

$$S = \int T \, \frac{d\sigma_{\text{inel}}}{dT} \, dT \,, \tag{2.12}$$

the stopping power is given by

$$\frac{\langle \Delta E \rangle}{\Delta z} = N \int T \, \frac{d\sigma_{\text{inel}}}{dT} \, dT \,, \tag{2.13}$$

and the *total inelastic scattering cross-section* σ_{inel} can be calculated by

$$\sigma_{\text{inel}} = \int \frac{d\sigma_{\text{inel}}}{dT} \, dT \,, \tag{2.14}$$

where $d\sigma_{\text{inel}}/dT$ is the so-called *differential inelastic scattering cross-section*. Once the total inelastic scattering cross-section σ_{inel} is known, the *inelastic mean free path* λ_{inel} can be calculated by

$$\lambda_{\text{inel}} = \frac{1}{N \, \sigma_{\text{inel}}} \,. \tag{2.15}$$

2.3 Range

While the inelastic mean free path is the average distance between two inelastic collisions, the *maximum range* is the total path length of the projectile. It can be easily estimated – using the simple approach we are describing in this section – in all the cases in which the *energy straggling*, i.e., the statistical fluctuations in energy loss, can be neglected. Indeed, in this case, the energy of the incident particle is a decreasing function of the depth z calculated from the surface of the target, so that $E = E(z)$. As the stopping cross-section is a function of the incident particle energy, $S = S(E)$, the Eq. (2.11) assumes the form of the following differential equation

$$\frac{dE}{dz} = -NS(E) \,, \tag{2.16}$$

where the minus sign has been introduced in order to take into account that, as already stated, the projectile energy $E(z)$ is a decreasing function of the depth z. Indicating with E_0 the initial energy of the projectiles (the so-called *beam primary energy*) the maximum range R can be easily obtained by the integration [3, 4]:

$$R = \int_0^R dz = \int_{E_0}^0 dE \, \frac{dz}{dE} , \tag{2.17}$$

so that

$$R = \int_0^{E_0} \frac{dE}{N \, S(E)} . \tag{2.18}$$

2.4 Energy Straggling

Actually the range calculated in such a way can be different from the real one because of the statistical fluctuations of the energy loss. The consequences of such a phenomenon, known as energy straggling, can be evaluated following a procedure similar to the one used for introducing the stopping cross-section.

Let us firstly consider then, as before, the discrete case and calculate the variance Ω^2, or mean square fluctuation, in the energy loss ΔE, given by

$$\Omega^2 = \langle (\Delta E - \langle \Delta E \rangle)^2 \rangle . \tag{2.19}$$

Since

$$\Delta E - \langle \Delta E \rangle = \sum_i (\nu_i - \langle \nu_i \rangle) \, T_i , \tag{2.20}$$

we have, due to the statistical independence of the collisions and the properties of the Poisson distribution,

$$\Omega^2 = \sum_i \langle (\nu_i - \langle \nu_i \rangle)^2 \rangle \, T_i^2 = \sum_i \langle \nu_i \rangle \, T_i^2 . \tag{2.21}$$

As a consequence, taking into account that $\langle \nu_i \rangle = N \Delta z \sigma_i$, the energy straggling can be expressed as

$$\Omega^2 = N \, \Delta z \sum_i T_i^2 \, \sigma_i = N \, \Delta z \, W \tag{2.22}$$

where we have introduced the straggling parameter defined as

$$W = \sum_i T_i^2 \, \sigma_i . \tag{2.23}$$

If the spectrum of the energy loss is continuous, instead of discrete, the straggling parameter assumes the form

$$W = \int T^2 \frac{d\sigma_{\text{inel}}}{dT} dT \,. \tag{2.24}$$

2.5 Summary

In this chapter, the elementary theory of electron penetration in solid targets has been briefly described [1]. We have discussed the fundamental concepts of cross-section, stopping power, maximum range of penetration, and energy straggling. Details of specific applications and calculations of the scattering mechanisms along with the main theoretical approaches, which describe the cross-sections relative to the interaction of the incident electrons with atomic nuclei, atomic electrons, plasmons, phonons, and polarons, will be the subject of the next chapters.

References

1. P. Sigmund, *Particle Penetration and Radiation Effects* (Springer, Berlin, 2006)
2. M. Dapor, *Electron-Beam Interactions with Solids: Application of the Monte Carlo Method to Electron Scattering Problems* (Springer, Berlin, 2003)
3. M. Dapor, Phys. Rev. B **43**, 10118 (1991)
4. M. Dapor, Surf. Sci. **269/270**, 753 (1992)

Chapter 3
Scattering Mechanisms

This chapter is devoted to the main mechanisms of scattering (elastic, quasi-elastic, and inelastic) that are relevant to the description of the interaction of electron beams with solid targets.

Firstly the elastic scattering cross-section will be described, comparing the screened Rutherford formula to the more accurate Mott cross-section [1]. The Mott theory is based on the relativistic partial wave expansion method and the numerical solution of the Dirac equation in a central field. The Mott cross-section is in better agreement with the available experimental data when electron energy is smaller than ∼5–10 keV.

We will also briefly describe the Fröhlich theory [2], which describes the quasi-elastic events occurring when electron energy is very low and the probability of electron–phonon interaction becomes significant. We will discuss energy loss and energy gain due to electron phonon-interactions, and see that electron energy gains can be safely neglected, while electron energy losses are fractions of eV.

The Bethe–Bloch stopping power formula [3] and semi-empiric approaches [4, 5] will be presented, along with the limits of these models for the calculation of energy losses.

The Ritchie dielectric theory [6] will then be considered, which is used for the accurate calculation of electron energy losses due to electron–plasmon interaction.

Polaronic effect will be also mentioned, as it is an important mechanism for trapping very slow electrons in insulating materials [7].

A discussion about the inelastic mean free path will be provided that takes into account all the inelastic scattering mechanisms introduced in this chapter.

Lastly, surface phenomena will be described along with numerical calculations of surface and bulk plasmon loss spectra.

Many details about the most important theoretical models presented in this chapter can be found in the Appendices.

M. Dapor, *Transport of Energetic Electrons in Solids*,
Springer Tracts in Modern Physics 257, DOI 10.1007/978-3-319-47492-2_3

3.1 Elastic Scattering

Electron-atom elastic scattering is the main responsible for the angle deflection of electrons traveling in solid targets. For some reviews about the subject of elastic scattering see, for example, Refs. [8–13].

Elastic scattering is not only the cause of the electron deflection: it also accounts for electron energy-loss problems, for it contributes to change the angular distribution of the inelastically scattered electrons [9, 10].

Since a nucleus is much more massive that an electron, the energy transfer is very small and, typically, negligible in an electron–nucleus collision. The great majority of elastic collisions regard the interaction of the incident electrons with the electrostatic nuclear field in regions that are far from the center of mass of the nucleus where, due to both the inverse square law and the shielding of the nucleus by the atomic electrons, the potential is relatively weak. For this reason, many electrons are elastically scattered through small angles.

Conservation of energy and momentum requires small transfers of energy between the electrons and the nuclei that depend on the angle of scattering. Even if the electron energy transfers are a very small fraction of eV, in many circumstances they cannot be neglected. Furthermore it has to be noted that, despite this general rule, in a few cases significant energy transfers are possible. Indeed, even if electron energy-losses are typically very small and often irrelevant in electron–nucleus collisions, for the very rare cases of head-on collisions, where the scattering angle is equal to 180°, the energy transfer can be, for the case of light elements, higher than the displacement energy, namely the energy necessary to displace the atom from its lattice position. In these cases, displacement damage and/or atom removal (sputtering) can be observed [9, 10, 14].

The differential elastic scattering cross-section represents the probability per unit solid angle that an electron be elastically scattered by an atom, and is given by the square modulus of the complex scattering amplitude f, which is a function of the scattering angle ϑ, of the incident electron energy E_0, and of the (mean) atomic number Z of the target. The angular distribution, once taken into account that the Coulomb potential is screened by the atomic electrons, can be calculated either by the use of the first Born approximation (screened Rutherford cross-section) or, in order to obtain more accurate results – in particular for low-energy electrons –, by solving the Schrödinger equation in a central field (partial wave expansion method, PWEM).

Typically, for the case of the screened Rutherford formula obtained within the first Born approximation, the screening of atomic electrons is described by the Wentzel formula [15], which corresponds to a Yukawa exponential attenuation of the nuclear potential as a function of the distance from the center of mass of the nucleus. The more accurate partial wave expansion method requires a better description of the screening, so that Dirac–Hartree–Fock–Slater methods are generally used for calculating the screened nuclear potential in this case.

A further improved approach for obtaining a very accurate calculation of the differential elastic scattering cross-section, valid also for relativistic electrons, is the so-called relativistic partial wave expansion method (RPWEM), – which is based on the solution of the Dirac equation in a central field (Mott cross-section) – where the sum of the squares of the moduli of two complex scattering amplitudes f and g is required for the calculation of the elastic scattering probabilities [1]. Also in this case, Dirac–Hartree–Fock–Slater methods are utilized to calculate the shielded nuclear potential.

3.1.1 Mott Cross-Section Versus Screened Rutherford Cross-Section

The relativistic partial wave expansion method (Mott theory) [1] permits to calculate the differential elastic scattering cross-section as follows:

$$\frac{d\sigma_{\mathrm{el}}}{d\Omega} = \mid f \mid^2 + \mid g \mid^2 , \tag{3.1}$$

where $f(\vartheta)$ and $g(\vartheta)$ are the scattering amplitudes (direct and spin-flip, respectively). For details about the Mott theory and the calculation of the scattering amplitudes $f(\vartheta)$ and $g(\vartheta)$, see Chap. 11 and Refs. [11, 13]. Also see Refs. [12, 16–18] for several applications.

Once the differential elastic scattering cross-section has been calculated, the total elastic scattering cross-section σ_{el} and the first transport elastic scattering cross-section σ_{tr} can be computed using the following equations:

$$\sigma_{\mathrm{el}} = \int \frac{d\sigma_{\mathrm{el}}}{d\Omega}\, d\Omega , \tag{3.2}$$

$$\sigma_{\mathrm{tr}} = \int (1 - \cos\vartheta)\, \frac{d\sigma_{\mathrm{el}}}{d\Omega}\, d\Omega . \tag{3.3}$$

It can be interesting to investigate the high energy and low atomic number limits of the Mott theory (corresponding to the first Born approximation). Along with the assumption that the atomic potential can be written according to the Wentzel formula [15]:

$$V(r) = -\frac{Z\, e^2}{r} \exp\left(-\frac{r}{a}\right) , \tag{3.4}$$

where r is the distance between the incident electron and the nucleus, Z the target atomic number, e the electron charge, and a approximately represents the screening of the nucleus by the orbital electrons, given by

$$a = \frac{a_0}{Z^{1/3}}, \tag{3.5}$$

where a_0 is the Bohr radius, the first Born approximation permits to write the differential elastic scattering cross-section in an analytic closed form. It is the so-called screened Rutherford cross-section:

$$\frac{d\sigma_{\mathrm{el}}}{d\Omega} = \frac{Z^2 e^4}{4E^2} \frac{1}{(1 - \cos\theta + \alpha)^2}, \tag{3.6}$$

$$\alpha = \frac{me^4\pi^2}{h^2} \frac{Z^{2/3}}{E} \tag{3.7}$$

In these equations, m is the electron mass and h is the Planck constant.

The screened Rutherford formula has been largely used even if it is unable to describe all the features corresponding to the elastic scattering as a function of the scattering angle that one can observe when incident electron kinetic energies are lower than ~5–10 keV and the target atomic number is relatively high. In Figs. 3.1, 3.2, 3.3 and 3.4 the differential elastic scattering cross-section $d\sigma_{\mathrm{el}}/d\Omega$ (DESCS) – calculated with both the Mott and the Rutherford theories – are compared. The presented data concern two different elements (Cu and Au) and two different energies (1000 and 3000 eV). From the comparison clearly emerges that the Rutherford theory approaches the Mott theory as the atomic number decreases and the primary energy increases. Indeed, the Rutherford formula can be deduced assuming the first Born approximation, which is valid when

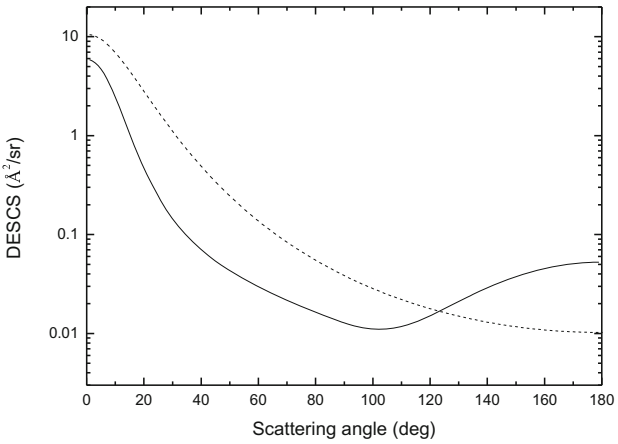

Fig. 3.1 Calculation of the differential elastic scattering cross-section of 1000 eV electrons scattered by Cu as a function of the scattering angle. *Solid line* Relativistic partial wave expansion method (Mott theory). *Dashed line* Screened Rutherford formula, Eq. (3.6)

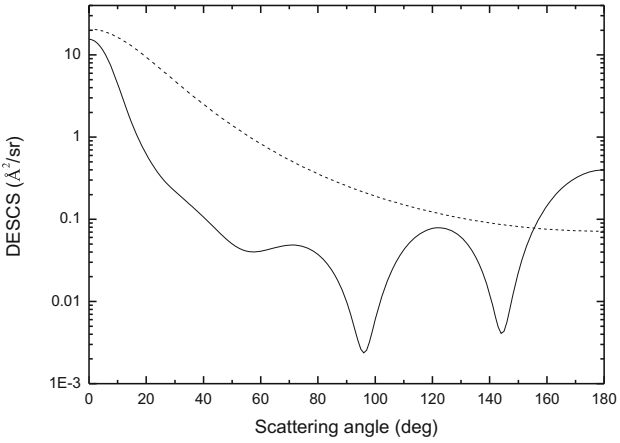

Fig. 3.2 Calculation of the differential elastic scattering cross-section of 1000 eV electrons scattered by Au as a function of the scattering angle. *Solid line* Relativistic partial wave expansion method (Mott theory). *Dashed line* Screened Rutherford formula, Eq. (3.6)

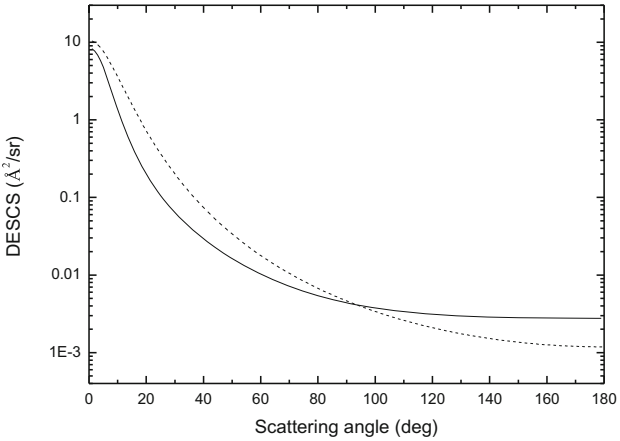

Fig. 3.3 Calculation of the differential elastic scattering cross-section of 3000 eV electrons scattered by Cu as a function of the scattering angle. *Solid line* Relativistic partial wave expansion method (Mott theory). *Dashed line* Screened Rutherford formula, Eq. (3.6)

$$E \gg \frac{e^2}{2a_0} Z^2 \,. \tag{3.8}$$

In other words, the higher the electron energy – in comparison with the atomic potential – the higher the accuracy of the Rutherford theory (see, in particular, Fig. 3.3). Anyway, the Rutherford formula represents a decreasing function of the scattering angle, so that it should not be surprising that it cannot describe the features that emerge as the electron energy is low and the atomic number is high (see, in particular, Fig. 3.2).

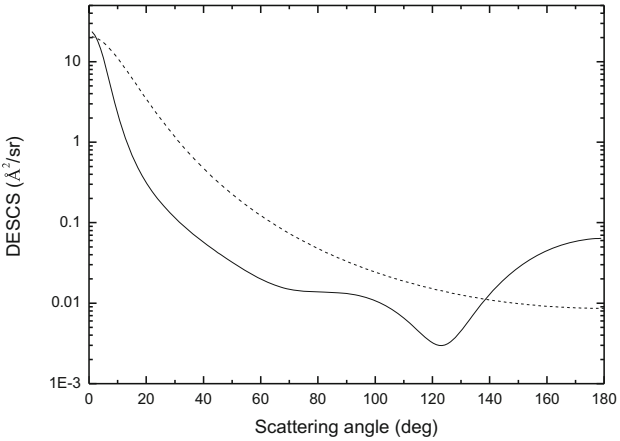

Fig. 3.4 Calculation of the differential elastic scattering cross-section of 3000 eV electrons scattered by Au as a function of the scattering angle. *Solid line* Relativistic partial wave expansion method (Mott theory). *Dashed line* Screened Rutherford formula, Eq. (3.6)

In Monte Carlo simulations, when the electron primary energy is higher than 10 keV, Rutherford cross-section is sometimes used – instead of the more accurate Mott cross-section – mainly because it provides a very simple analytic way to calculate both the cumulative probability of elastic scattering into an angular range from 0 to θ, $P_{\rm el}(\theta, E)$, and the elastic scattering mean free path, $\lambda_{\rm el}$. Even if not used by the simulations presented in this book, where numerical calculations of Mott cross-section will always be utilized (see Fig. 3.5, where Mott cross section is represented for 1000 eV electrons in Al), it might be useful to see how $P_{\rm el}(\theta, E)$ and $\lambda_{\rm el}$ can be calculated in a completely analytic way taking advantage of the particular form of the screened Rutherford formula. In the first Born approximation these quantities are in fact given, respectively, by

$$P_{\rm el}(\theta, E) = \frac{(1 + \alpha/2)\,(1 - \cos\theta)}{1 + \alpha - \cos\theta}\,, \tag{3.9}$$

$$\lambda_{\rm el} = \frac{\alpha\,(2 + \alpha)\,E^2}{N\,\pi\,e^4\,Z^2}\,, \tag{3.10}$$

where N is the number of atoms per unit volume in the target. The demonstration of these equations is quite easy. Indeed

$$P_{\rm el}(\theta, E) = \\ = \frac{e^4 Z^2}{4\sigma_{\rm el} E^2} \int_0^{\theta} \frac{2\pi \sin\vartheta\, d\vartheta}{(1 - \cos\vartheta + \alpha)^2} = \frac{\pi e^4 Z^2}{2\sigma_{\rm el} E^2} \int_{\alpha}^{1-\cos\theta+\alpha} \frac{du}{u^2}\,,$$

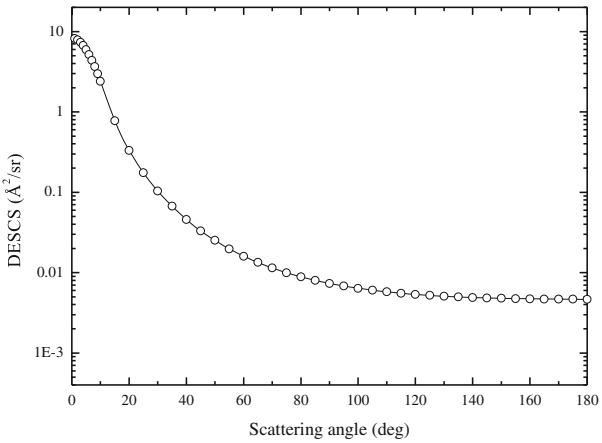

Fig. 3.5 Differential elastic scattering cross-section of 1000 eV electrons scattered by Al as a function of the scattering angle. *Solid line* Present calculations (Mott theory) [13]. *Circles* Salvat and Mayol calculations (Mott theory) [19]

where

$$\sigma_{\mathrm{el}} = \frac{e^4 Z^2}{4E^2} \int_0^{\pi} \frac{2\pi \sin\vartheta \, d\vartheta}{(1 - \cos\vartheta + \alpha)^2} = \frac{\pi e^4 Z^2}{2E^2} \int_{\alpha}^{2+\alpha} \frac{du}{u^2} .$$

Since

$$\int_{\alpha}^{1-\cos\theta+\alpha} \frac{du}{u^2} = \frac{1 - \cos\theta}{\alpha(1 - \cos\theta + \alpha)}$$

and

$$\int_{\alpha}^{2+\alpha} \frac{du}{u^2} = \frac{1}{\alpha(1 + \alpha/2)} ,$$

Equations (3.9) and (3.10) immediately follow.

Note that from the cumulative probability expressed by Eq. (3.9) it follows that the scattering angle can be easily calculated from:

$$\cos\theta = 1 - \frac{2\alpha \, P_{\mathrm{el}}(\theta, E)}{2 + \alpha - 2P_{\mathrm{el}}(\theta, E)} . \tag{3.11}$$

Due to the excellent agreement between experimental data and Mott cross-section (see, for a comparison, Fig, 3.6), the most recent Monte Carlo codes (and also all

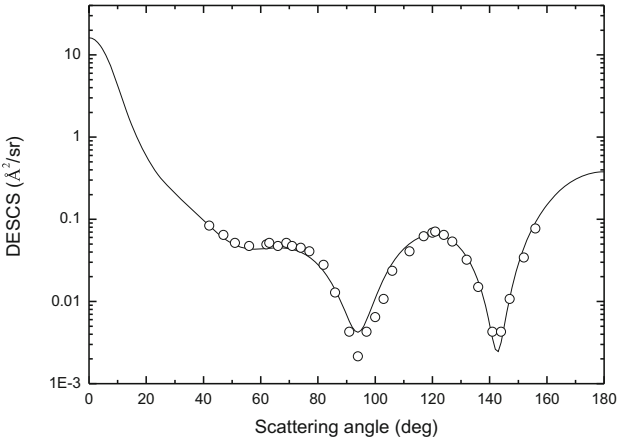

Fig. 3.6 Differential elastic scattering cross-section of 1100 eV electrons scattered by Au as a function of the scattering angle. *Solid line* Present calculations (Mott theory) [13]. *Circles* Reichert experimental data [20]

the calculations presented in this book) use the Mott cross-section to describe the differential elastic scattering cross-section – and the cumulative probability necessary for sampling the scattering angle. Nevertheless, it is worth stressing that excellent results can also be obtained using the simple screened Rutherford formula, Eq. (3.6), provided that the kinetic primary energy of the incident electrons is higher than 10 keV [21].

3.2 Quasi-elastic Scattering

Due to thermal excitations, atoms in crystalline structures vibrate around their equilibrium lattice sites. These vibrations are known as *phonons*. A mechanism of energy loss (and energy gain as well) is represented by the interaction of the electrons with the optical modes of the lattice vibrations. These transfers of small amounts of energy among electrons and lattice vibrations are due to quasi-elastic processes known as *phonon creation* (electron energy-loss) and *phonon annihilation* (electron energy-gain) [2, 22]. Phonon energies do not exceed $k_B T_D$, where k_B is the Boltzmann constant and T_D is the Debye temperature. As typically $k_B T_D$ is not greater than 0.1 eV, the energy losses and gains due to electron–phonon interaction are usually smaller than 0.1 eV, so that they are generally not resolved by conventional spectrometers [9]. These mechanisms of electron energy loss – and, with much smaller probability, energy gain – are particularly relevant when the electron energy is low (few eV) [7].

3.2.1 Electron–Phonon Interaction

According to Fröhlich [2] and Llacer and Garwin [22], the inverse mean free path for electron energy loss due to phonon creation can be written as

$$\lambda_{\text{phonon}}^{-1} = \frac{1}{a_0} \frac{\varepsilon_0 - \varepsilon_\infty}{\varepsilon_0\, \varepsilon_\infty} \frac{\hbar\omega}{E} \frac{n(T) + 1}{2} \ln\left[\frac{1 + \sqrt{1 - \hbar\omega/E}}{1 - \sqrt{1 - \hbar\omega/E}}\right], \tag{3.12}$$

where E is the energy of the incident electron, $W_{\text{ph}} = \hbar\omega$ the electron energy loss (in the order of 0.1 eV), ε_0 the static dielectric constant, ε_∞ the high frequency dielectric constant, a_0 the Bohr radius and

$$n(T) = \frac{1}{e^{\hbar\omega/k_{\text{B}}T} - 1} \tag{3.13}$$

the occupation number. Notice that a similar equation can be written to describe electron energy gain (corresponding to phonon annihilation). The occurrence probability of phonon annihilation is much lower than that of phonon creation. Electron energy gain can thus be safely neglected for many practical purposes.

For further details about electron–phonon interaction and Fröhlich theory [2, 22] see Chap. 12.

3.3 Inelastic Scattering

Let us consider now the inelastic scattering due to the interaction of the incident electrons with the atomic electrons located around the nucleus (both the core and the valence electrons). For an excellent review about this subject, see Ref. [9].

If the incident electron energy is high enough, it can excite an *inner-shell* electron that can make a transition from its ground state to one of the unoccupied electron states above the Fermi level. Due to energy conservation, the incident electron loses an amount of energy equal to the difference between the state above the Fermi level occupied by the excited atomic electron and its ground state; while the atom is left in an ionized state. The following de-excitation of the target atom generates an excess energy that can be released in one of two competitive ways: either generating an X-ray photon (Energy dispersive spectroscopy, EDS, is based on this process) or by the emission of another electron: this is the phenomenon on which Auger electron spectroscopy, AES, is based.

Outer-shell inelastic scattering can occur according to two alternative processes. In the first one, an outer-shell electron can suffer a single-electron excitation. A typical example is constituted by inter-band and intra-band transitions. If the atomic electron excited in such a way is able to reach the surface with an energy higher than the potential barrier between the vacuum level and the minimum of the conduction band,

it can emerge from the solid as a secondary electron, the energy needed for this transition being provided by the fast incident electron. De-excitation can occur through the emission of electromagnetic radiation in the visible region – corresponding to the phenomenon known as cathode-luminescence – or through radiation-less processes generating heat. Outer-shell electrons can also be excited in collective states corresponding to the oscillation of the valence electrons denoted as plasma resonance. It is generally described as the creation of quasi-particles known as *plasmons*, with energies – characteristic of the material – that range, typically, in the interval from 5 to 30 eV. Plasmon decay generates secondary electrons and/or produces heat.

3.3.1 Stopping: Bethe–Bloch Formula

In the continuous-slowing-down approximation, energy losses are calculated by utilizing the stopping power. Using a quantum mechanical treatment, Bethe [3] proposed the following formula for the stopping power:

$$-\frac{dE}{dz} = \frac{2\pi e^4 N Z}{E} \ln\left(\frac{1.166E}{I}\right), \tag{3.14}$$

where I represents the mean ionization energy which, according to Berger and Seltzer [23], can be approximated by the following simple formula:

$$I = (9.76 + 58.8\, Z^{-1.19})\, Z\,. \tag{3.15}$$

The Bethe–Bloch formula is valid for energies higher than $\sim I$. It approaches zero as E approaches $I/1.166$. When E becomes smaller than $I/1.166$, the stopping power predicted by the Bethe–Bloch formula becomes negative. Therefore, the low-energy stopping power requires a different approach (see the dielectric approach below).

3.3.2 Stopping: Semi-empiric Formulas

The stopping power can also be described using semi-empiric expressions, such as the following;

$$-\frac{dE}{dz} = \frac{K_e N Z^{8/9}}{E^{2/3}}, \tag{3.16}$$

proposed in 1972 by Kanaya and Okayama (with $K_e = 360\,\text{eV}^{5/3}\,\text{Å}^2$) [5]. The latter formula allows to analytically evaluate the maximum range of penetration R as a function of the primary energy E_0, where

$$R = \int_{E_0}^{0} \frac{dE}{dE/dz} = \frac{3E_0^{5/3}}{5K_e N Z^{8/9}} \propto E_0^{1.67}. \tag{3.17}$$

A similar empirical formula for the evaluation of the maximum range of penetration of electrons in solid targets was proposed, for the first time in 1954, by Lane and Zaffarano [4] who found that their range-energy experimental data (obtained by investigating electron transmission in the energy range 0–40 keV by thin plastic and metal films) fell within 15 % of the results obtained by the following simple equation:

$$E_0 = 22.2 R^{0.6}, \tag{3.18}$$

where E_0 was expressed in keV and R in mg/cm^2. As a consequence, the Kanaya and Okayama formula is consistent with the Lane and Zaffarano experimental observations, which are described as well by the relationship

$$R \propto E_0^{1.67}. \tag{3.19}$$

3.3.3 Dielectric Theory

In order to obtain a very accurate description of the electron energy loss processes, of the stopping power, and of the inelastic mean free path, valid even when electron energy is low, it is necessary to consider the response of the ensemble of conduction electrons to the electromagnetic field generated by the electrons passing through the solid: this response is described by a complex dielectric function. In Chap. 13 the Ritchie theory [6, 24] is described: it demonstrates, in particular, that the energy loss function, $f(k, \omega)$, necessary to calculate both the stopping power and the inelastic mean free path, is the reciprocal of the imaginary part of the dielectric function

$$f(k, \omega) = \mathrm{Im}\left[\frac{1}{\varepsilon(k, \omega)}\right]. \tag{3.20}$$

In Eq. (3.20), $\hbar\mathbf{k}$ represents the momentum transferred and $\hbar\omega$ the electron energy loss.

Once the energy loss function has been obtained, the differential inverse inelastic mean free path can be calculated as [25]

$$\frac{d\lambda_{\mathrm{inel}}^{-1}}{d\hbar\omega} = \frac{1}{\pi E a_0} \int_{k_-}^{k_+} \frac{dk}{k} f(k, \omega), \tag{3.21}$$

where

$$\hbar k_{\pm} = \sqrt{2mE} \pm \sqrt{2m(E - \hbar\omega)}, \tag{3.22}$$

E is the electron energy, m the electron mass, and a_0 the Bohr radius. The limits of integration, expressed by Eq. (3.22), come from conservation laws (see Sect. 5.2.3).

In order to calculate the dielectric function, and hence the energy loss-function, let us consider the electric displacement $\boldsymbol{\mathcal{D}}$ [17, 18]. If $\boldsymbol{\mathcal{P}}$ is the polarization density of the material, and $\boldsymbol{\mathcal{E}}$ the electric field, then

$$\boldsymbol{\mathcal{P}} = \chi_\varepsilon \boldsymbol{\mathcal{E}}\,, \tag{3.23}$$

where

$$\chi_\varepsilon = \frac{\varepsilon - 1}{4\pi} \tag{3.24}$$

and

$$\boldsymbol{\mathcal{D}} = \boldsymbol{\mathcal{E}} + 4\pi\boldsymbol{\mathcal{P}} = (1 + 4\pi\chi_\varepsilon)\boldsymbol{\mathcal{E}} = \varepsilon\boldsymbol{\mathcal{E}}\,. \tag{3.25}$$

If n is the density of the outer-shell electrons, i.e., the number of outer-shell electrons per unit volume in the solid, and ξ the electron displacement due to the electric field, then

$$\boldsymbol{\mathcal{P}} = e\,n\,\xi\,, \tag{3.26}$$

so that

$$|\boldsymbol{\mathcal{E}}| = \frac{4\pi e\,n\,\xi}{\varepsilon - 1}\,. \tag{3.27}$$

Let us consider the classical model of electrons elastically bound, with elastic constants $k_\mathrm{n} = m\omega_\mathrm{n}^2$ and subject to a frictional damping effect, due to collisions, described by a damping constant Γ. We have indicated here with m the electron mass and with ω_n the natural frequencies. The electron displacement satisfies the equation [26]

$$m\,\ddot{\xi} + \beta\dot{\xi} + k_\mathrm{n}\,\xi = e\,\boldsymbol{\mathcal{E}} \tag{3.28}$$

where $\beta = m\Gamma$. Assuming that $\xi = \xi_0 \exp(i\omega t)$, a straightforward calculation allows to conclude that

$$\varepsilon(0,\omega) = 1 - \frac{\omega_\mathrm{p}^2}{\omega^2 - \omega_\mathrm{n}^2 - i\,\Gamma\omega}\,, \tag{3.29}$$

where ω_p is the *plasma frequency*, given by

$$\omega_\mathrm{p}^2 = \frac{4\pi n\,e^2}{m}\,. \tag{3.30}$$

Let us now consider a superimposition of free and bound oscillators. In such a case the dielectric function can be written as:

$$\varepsilon(0,\omega) = 1 - \omega_{\mathrm{p}}^2 \sum_n \frac{f_{\mathrm{n}}}{\omega^2 - \omega_{\mathrm{n}}^2 - i\,\Gamma_{\mathrm{n}}\omega}\,, \tag{3.31}$$

where Γ_{n} are positive frictional damping coefficients and f_{n} are the fractions of the valence electrons bound with energies $\hbar\omega_{\mathrm{n}}$.

The extension of the dielectric function from the optical limit (corresponding to $k = 0$) to $k > 0$ is obtained including, in the previous formula, an energy $\hbar\omega_k$ related to the dispersion relation, so that

$$\varepsilon(k,\omega) = 1 - \omega_p^2 \sum_n \frac{f_n}{\omega^2 - \omega_n^2 - \omega_k^2 - i\,\Gamma_n\omega}\,. \tag{3.32}$$

In the determination of the dispersion relation, one has to take into account a constraint, known as the *Bethe ridge*. According to the Bethe ridge, as $k \to \infty$, $\hbar\omega_k$ should approach $\hbar^2k^2/2m$. Of course, an obvious way to obtain this result (the simplest one, actually) is to assume that [25, 27],

$$\hbar\omega_k = \frac{\hbar^2k^2}{2m}\,. \tag{3.33}$$

Another way of satisfying the constraint represented by the Bethe ridge is to use, according to Ritchie [6] and to Richie and Howie [24], the following equation :

$$\hbar^2\,\omega_k^2 = \frac{3\,\hbar^2\,v_F^2\,k^2}{5} + \frac{\hbar^4\,k^4}{4\,m^2}\,, \tag{3.34}$$

where v_F represents the velocity of Fermi.

Once the dielectric function is known, the loss function $\mathrm{Im}[1/\varepsilon(k,\omega)]$ is given by

$$\mathrm{Im}\left[\frac{1}{\varepsilon(k,\omega)}\right] = -\frac{\varepsilon_2}{\varepsilon_1^2 + \varepsilon_2^2}\,, \tag{3.35}$$

where

$$\varepsilon(k,\omega) = \varepsilon_1(k,\omega) + i\varepsilon_2(k,\omega)\,, \tag{3.36}$$

The calculation of the energy loss function can be also performed through the direct use of experimental optical data. In Figs. 3.7 and 3.8, the optical energy loss function of polymethyl methacrylate and silicon dioxide are represented, respectively.

A quadratic extension into the energy- and momentum-transfer plane of the energy loss function allows the extension of the dielectric function from the optical limit to $k > 0$ [32–34].

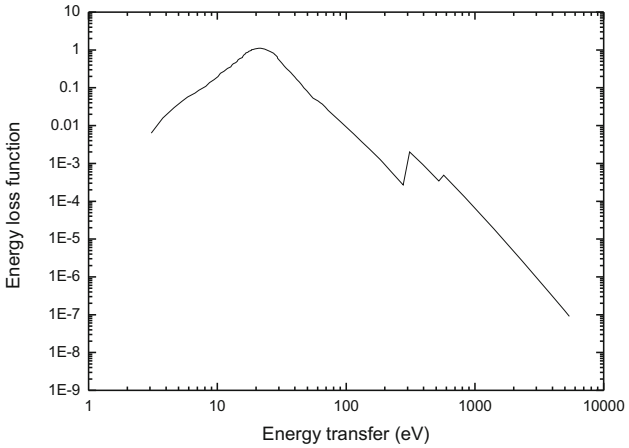

Fig. 3.7 Optical energy loss function for electrons in Polymethyl Methacrylate. For energies lower than 72 eV we used the optical data of Ritsko et al. [28]. For higher energies the calculation of the optical loss function was performed by using the Henke et al. atomic photo-absorption data [29, 30]

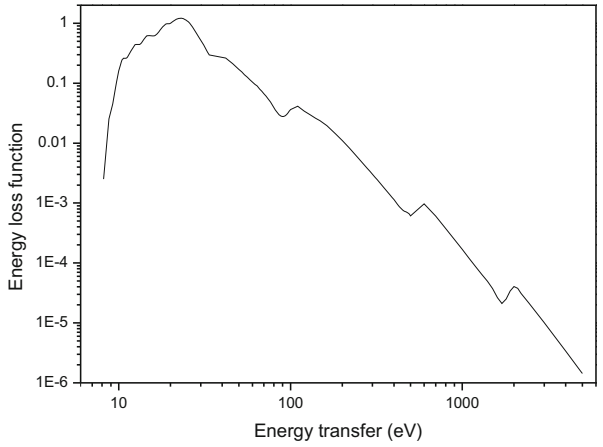

Fig. 3.8 Optical energy loss function for electrons in silicon dioxide (SiO_2). For energies lower than 33.6 eV we used the optical data of Buechner [31]. For higher energies the calculation of the optical loss function was performed by using the Henke et al. atomic photo-absorption data [29, 30]

Penn [32] and Ashley [33, 34] calculated the energy loss function by using optical data and by extending as discussed above the dielectric function from the optical limit to $k > 0$. According to Ashley [33, 34], the inverse inelastic mean free path $\lambda_{\text{inel}}^{-1}$ of electrons penetrating solid targets can be calculated by:

$$\lambda_{\text{inel}}^{-1}(E) = \frac{me^2}{2\pi\hbar^2 E} \int_0^{W_{max}} \text{Im}\left[\frac{1}{\varepsilon(0, w)}\right] L\left(\frac{w}{E}\right) dw\,, \tag{3.37}$$

where E is the incident electron energy and $W_{\max} = E/2$ (as usual, we have indicated with e the electron charge and with $\hbar$ the Planck constant h divided by 2π). According to Ashley, in the dielectric function $\varepsilon(\boldsymbol{k}, w)$, the momentum transfer $\hbar\boldsymbol{k}$ was set to 0 and the ε dependence on $\boldsymbol{k}$ was factorised through the function $L(w/E)$. Ashley [33] demonstrated that a good approximation of the function $L(x)$ is given by:

$$L(x) = (1-x)\ln\frac{4}{x} - \frac{7}{4}x + x^{3/2} - \frac{33}{32}x^2 . \tag{3.38}$$

The calculation of the stopping power, $-dE/dz$, can be performed by using the following equation [33]:

$$-\frac{dE}{dz} = \frac{me^2}{\pi\hbar^2 E}\int_0^{W_{\max}} \mathrm{Im}\left[\frac{1}{\varepsilon(0,w)}\right] S\left(\frac{w}{E}\right) w\, dw , \tag{3.39}$$

where

$$S(x) = \ln\frac{1.166}{x} - \frac{3}{4}x - \frac{x}{4}\ln\frac{4}{x} + \frac{1}{2}x^{3/2} - \frac{x^2}{16}\ln\frac{4}{x} - \frac{31}{48}x^2 . \tag{3.40}$$

The inelastic mean free path and the stopping power for positrons may be calculated in a similar way [34]:

$$(\lambda_{\mathrm{inel}}^{-1})_{\mathrm{p}} = \frac{me^2}{2\pi\hbar^2 E}\int_0^{W_{\max}} \mathrm{Im}\left[\frac{1}{\varepsilon(0,w)}\right] L_{\mathrm{p}}\left(\frac{w}{E}\right) dw , \tag{3.41}$$

$$\left(-\frac{dE}{dz}\right)_{\mathrm{p}} = \frac{me^2}{2\pi\hbar^2 E}\int_0^{W_{\max}} \mathrm{Im}\left[\frac{1}{\varepsilon(0,w)}\right] S_{\mathrm{p}}\left(\frac{w}{E}\right) w\, dw , \tag{3.42}$$

where

$$L_{\mathrm{p}}(x) = \ln\left(\frac{1 - x/2 + \sqrt{1-2x}}{1 - x/2 - \sqrt{1-2x}}\right) \tag{3.43}$$

and

$$S_{\mathrm{p}}(x) = \ln\left(\frac{1 - x + \sqrt{1-2x}}{1 - x - \sqrt{1-2x}}\right) . \tag{3.44}$$

In Figs. 3.9 and 3.10 the stopping powers of electrons in PMMA and in SiO_2 are, respectively, shown. In Figs. 3.11 and 3.12 the inelastic mean free paths of electrons in PMMA and in SiO_2 are also, respectively, represented. The present calculations, obtained using the Ashley theory that we just described. are compared with results of other authors.

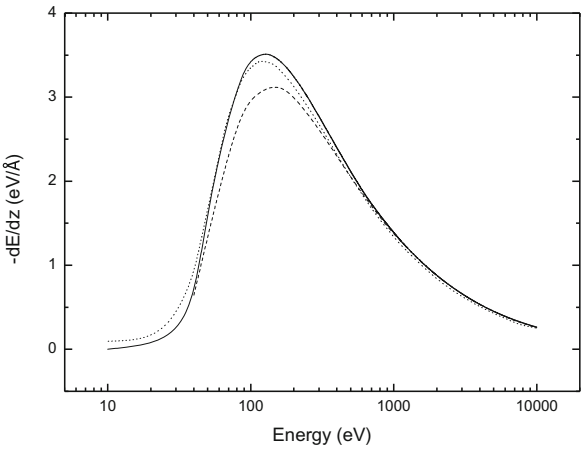

Fig. 3.9 Stopping power of electrons in PMMA. The *solid line* represents the present calculation, obtained according to the Ashley recipe [33]. The *dashed line* provides the Ashley original results [33]. *Dotted line* describes the Tan et al. computational results [35]. The different optical energy loss functions used in the three cases explain the differences in the calculations

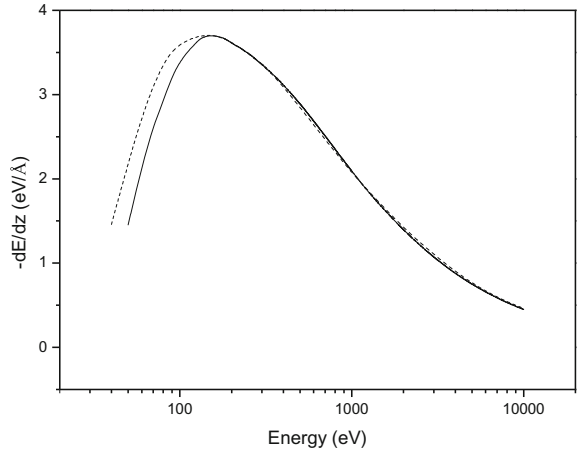

Fig. 3.10 Stopping power of electrons in SiO_2. The *solid line* represents the present calculation, obtained according to the Ashley recipe [33]. The *dashed line* provides the Ashley and Anderson data [36]. The different optical energy loss functions utilized in the two cases explain the differences in the calculations

Once $\varepsilon(0, w)$ is known, the electron differential inverse inelastic mean free path $d\lambda_{\text{inel}}^{-1}(w, E)/dw$ can be calculated by using the following equation:

$$\frac{d\lambda_{\text{inel}}^{-1}(w, E)}{dw} = \frac{me^2}{2\pi\hbar^2 E}\text{Im}\left[\frac{1}{\varepsilon(0, w)}\right] L\left(\frac{w}{E}\right) . \tag{3.45}$$

3.3.4 Sum of Drude Functions

Ritchie and Howie [24] have proposed to calculate the energy loss function as a linear superimposition of Drude functions, as follows:

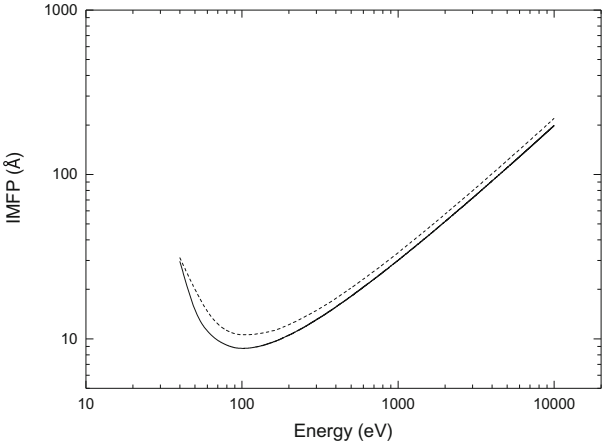

Fig. 3.11 Inelastic mean free path of electrons in PMMA due to electron–electron interaction. The *solid line* represents the present calculation, based on the Ashely model [33]. The *dashed line* describes the original Ashley results [33]. The differences in the two calculations are due to the different optical energy loss functions utilized

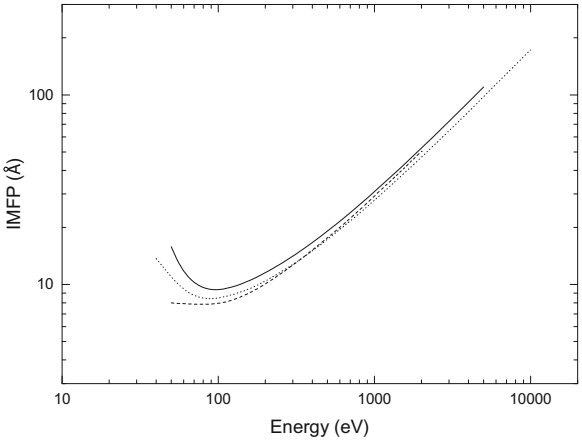

Fig. 3.12 Inelastic mean free path of electrons in SiO_2 due to electron–electron interaction. The *solid line* represents the present calculation, based on the Ashely model [33]. The *dashed line* describes the Ashley and Anderson data [36]. The *dotted line* provides the Tanuma, Powell and Penn computational results [37]. The differences in the calculations are due to the different optical energy loss functions utilized

$$\mathrm{Im}\left[\frac{1}{\varepsilon(k,\omega)}\right] = \sum_{\mathrm{n}} \frac{A_{\mathrm{n}}\,\Gamma_{\mathrm{n}}\,\hbar\omega}{[w_{\mathrm{n}}^2(k) - \hbar^2\omega^2]^2 + \hbar^2\omega^2\Gamma_{\mathrm{n}}^2}\,, \tag{3.46}$$

where, according to Eq. (3.34),

$$w_{\mathrm{n}}(k) = \sqrt{w_{\mathrm{n}}^2 + \frac{12E_{\mathrm{F}}}{5}\frac{\hbar^2k^2}{2m} + \left(\frac{\hbar^2k^2}{2m}\right)^2}\,, \tag{3.47}$$

Table 3.1 Parameters calculated by Garcia-Molina et al. [39] to fit the contribution to the optical energy loss function of the outer electrons for five selected carbon allotropes (amorphous carbon, glassy carbon, C60-fullerite, graphite, and diamond)

Target	n	w_n (eV)	Γ_n (eV)	A_n (eV^2)
Amorphous carbon	1	6.26	5.71	9.25
	2	25.71	13.33	468.65
Glassy carbon	1	2.31	4.22	0.96
	2	5.99	2.99	6.31
	3	19.86	6.45	77.70
	4	23.67	12.38	221.87
	5	38.09	54.42	110.99
C60-fullerite	1	6.45	2.45	6.37
	2	14.97	6.26	16.52
	3	24.49	13.06	175.13
	4	28.57	12.24	141.21
	5	40.82	27.21	141.47
Graphite	1	2.58	1.36	0.18
	2	6.99	1.77	7.38
	3	21.77	8.16	73.93
	4	28.03	6.80	466.69
	5	38.09	68.03	103.30
Diamond	1	22.86	2.72	22.21
	2	29.93	13.61	140.64
	3	34.77	11.43	843.85

In these equations, E_F is the Fermi energy, and w_n, Γ_n, A_n are the excitation energies, the damping constants, and the strengths, for $k = 0$ [38]. Garcia-Molina et al. [39] provided, for example, the values of these parameters, calculated from the fit of experimental optical data for five allotropic forms of carbon (amorphous carbon, glassy carbon, C60-fullerite, graphite, and diamond). In Table 3.1 the Garcia-Molina et al. parameters have been reported, for the reader's convenience. The optical energy loss functions so calculated for these five carbon allotrops are represented in Fig. 3.13.

In Fig. 3.14 the differential inverse inelastic mean free path for the considered allotrops of carbon, calculated by [see Eqs. (3.20) and (3.21)]

$$\frac{d\lambda_{\text{inel}}^{-1}}{d\hbar\omega} = \frac{1}{\pi a_0 E}\int_{k_-}^{k_+}\frac{dk}{k}\,\text{Im}\left[\frac{1}{\varepsilon(k,\omega)}\right], \tag{3.48}$$

where k_- and k_+ are given by Eq. (3.22), is represented as a function of the energy loss $w = \hbar\omega$ for incident electron energy $E = 250\,\text{eV}$. The comparison with the shapes of the curves representing the optical energy loss function of Fig. 3.13 clearly shows the effect of the dispersion law, Eq. (3.34): the peaks broaden and become more asymmetric (see the tail on their right side).

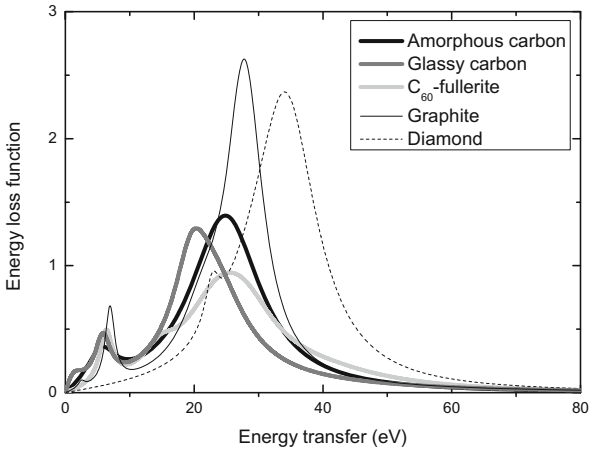

Fig. 3.13 Optical energy loss function of selected allotropic forms of carbon (amorphous carbon, glassy carbon, C60-fullerite, graphite, and diamond) as a function of the excitation energy, calculated by sum of Drude–Lorentz functions, according to Ritchie and Howie [24], using the Garcia-Molina et al. parameters [39]

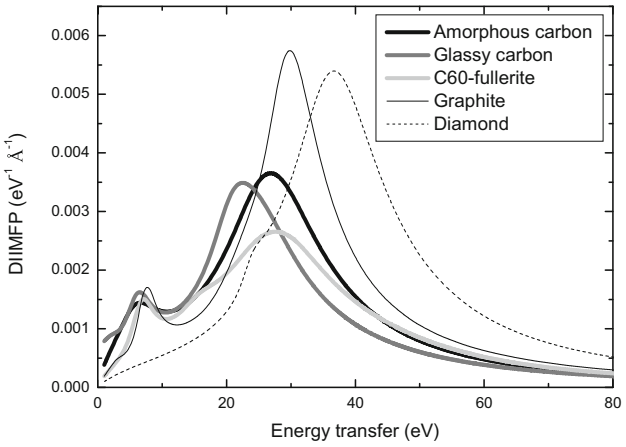

Fig. 3.14 Differential inverse inelastic mean free path for electrons impinging upon several allotropic forms of carbon (amorphous carbon, glassy carbon, C60-fullerite, graphite, and diamond) as a function of the electron energy loss, calculated using Drude–Lorentz functions. The incident electron energy is $E = 250\,\mathrm{eV}$

Figure 3.15 shows, for the five considered allotropic forms of carbon, the electron inelastic mean free path, i.e. the reciprocal of

$$\lambda_{\mathrm{inel}}^{-1} = \int_{W_{\mathrm{min}}}^{W_{\mathrm{max}}} \frac{d\lambda_{\mathrm{inel}}^{-1}}{dw} dw\,, \tag{3.49}$$

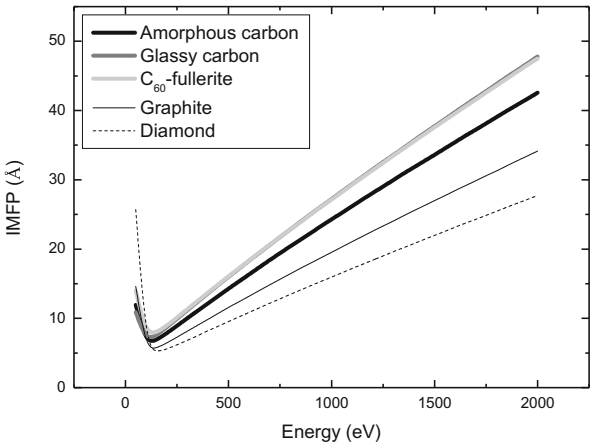

Fig. 3.15 Inelastic mean free path for electrons impinging upon several allotropic forms of carbon (amorphous carbon, glassy carbon, C60-fullerite, graphite, and diamond) as a function of the electron kinetic energy, calculated using Drude–Lorentz functions

where, according to Ref. [38], $W_{\min}$ is set to zero for conductors and to the energy of the band gap for semiconductors and insulating materials. $W_{\max}$ represents the minimum between $E - E_{\text{Pauli}}$ and $(E + W_{\min})/2$. Note that, for metals, $E_{\text{Pauli}} = E_{\text{F}}$. Garcia-Molina et al., recently proposed the value $E_{\text{Pauli}} = 4\,\text{eV}$ for several biomaterials [40]. In the same paper, Garcia-Molina et al. set $W_{\min}$ to the energy gap for the outer-shell electron excitations and to the inner-shell threshold energy for the inner-shell electron excitations [40]. According to Emfietzoglou et al. [38], the factor 1/2 in $W_{\max}$ is due to the fact that electrons cannot be distinguished (with the convention to consider the incident electron as the most energetic one after the collision).

3.3.5 The Mermin Theory

A more accurate approach to the calculation of the ELF is based on the use of the Mermin functions [41] instead of the Drude–Lorentz functions in the sum. This method is the Mermin energy loss function-generalized oscillator strength (MELF-GOS) method proposed by Abril et al. [42]. Details of the MELF-GOS method can be found in Chap. 15. According to Abril et al. [42], a linear combination of Mermin-type energy loss functions, one per oscillator, allows to calculate the electron ELF for any given material. The procedure is very similar to the previous one. Unlike that, Mermin functions are used instead of Drude–Lorenz functions. Please note that the Mermin theory includes the dispersion law, and it is not necessary, as is the case for the Drude–Lorentz approach, to introduce an approximate expression of it to extend the ELF beyond the optical domain. The Mermin differential inverse inelastic mean free path of electrons in PMMA is represented in Fig. 3.16, for kinetic energies of the incident electrons ranging from 50 to 1000 eV.

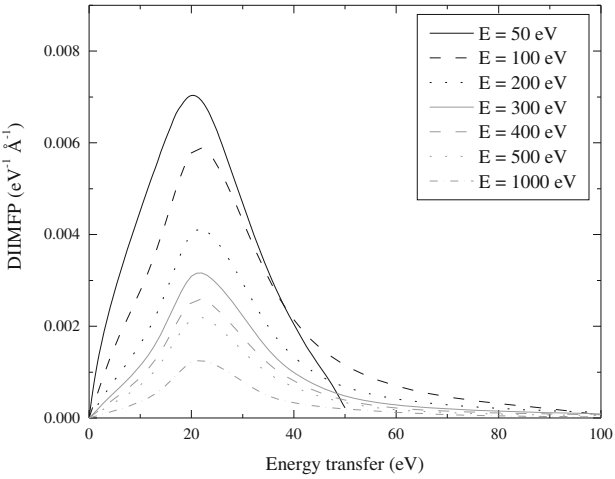

Fig. 3.16 Mermin differential inverse inelastic mean free path of electrons in PMMA as a function of the energy loss for selected values of the incident electron kinetic energy E in the range 50–1000 eV [46]. The calculations are based on the MELF-GOS method [42] (see Chap. 15 for details)

The inverse of the integral of every curve presented in Fig. 3.16 provides, for each kinetic energy E, the inelastic mean free path.

According to de la Cruz and Yubero [43], the values of the inelastic mean free path calculated using the Tanuma, Powell and Penn (TPP) empirical predictive formula [44] are systematically higher than the corresponding values calculated within the Mermin theory. For PMMA, according to our calculation, when $E = 100\,\text{eV}$ the Mermin IMFP is equal to 6.3 Å while when $E = 1000\,\text{eV}$ it is equal to 27.6 Å. According to TPP, the inelastic mean free path of PMMA is equal to 7.9 Å for $E = 100\,\text{eV}$ and to 33.7 Å for $E = 1000\,\text{eV}$ [44]. Approaches based on the Drude–Lorentz theory also provide values of the inelastic mean free path systematically higher than those obtained using the Mermin theory. The inelastic mean free path of PMMA calculated according to the Drude–Lorentz theory is equal to 10.1 Å for $E = 100\,\text{eV}$ and to 33.5 Å for $E = 1000\,\text{eV}$ [45].

3.3.6 *Exchange Effects*

Exchange effects in the electron–electron interaction are due to the fact that scattered electrons cannot be distinguished from ejected electrons. In order to take into account the exchange effects, the differential inverse inelastic mean free path have to be calculated as

$$\frac{d\lambda_{\text{inel}}^{-1}}{d\hbar\omega} = \frac{1}{\pi a_0 E}\int_{k_-}^{k_+}\frac{dk}{k}\left[1 + f_{\text{ex}}(k)\right]\text{Im}\left[\frac{1}{\varepsilon(k,\omega)}\right], \tag{3.50}$$

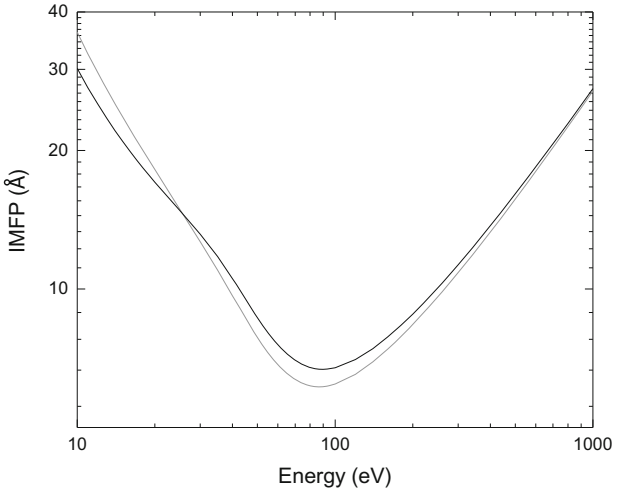

Fig. 3.17 Mermin inelastic mean free path of electrons in PMMA [48] calculated according to the MELF-GOS method [42] (see Chap. 15 for details). *Black line* with exchange. *Gray line* without exchange. *Courtesy* of P. de Vera, I. Abril, R. Garcia-Molina

where, according to the Born–Ochkur approximation [47],

$$f_{\mathrm{ex}}(k) = \left(\frac{\hbar k}{m\upsilon}\right)^4 - \left(\frac{\hbar k}{m\upsilon}\right)^2 . \tag{3.51}$$

In Eq. (3.51) m is the electron mass and υ is the electron velocity.

The Mermin inelastic mean free path of electrons in PMMA, calculated including the Born–Ochkur approximation in order to take into account the exchange effects (black line) is compared, in Fig. 3.17, with the Mermin inelastic mean free path of electrons in PMMA calculated without exchange effects (gray line) [48]. The calculations are based on the MELF-GOS method [42].

3.3.7 Polaronic Effect

A low-energy electron moving in an insulating material induces a polarization field that has a stabilizing effect on the moving electron. This phenomenon can be described as the generation of a quasi-particle called polaron. The polaron has a relevant effective mass and mainly consists of an electron (or a hole created in the valence band) with its polarization cloud around it. According to Ganachaud and Mokrani [7], the polaronic effect can be described assuming that the inverse inelastic mean free path governing the phenomenon – that is proportional to the probability for a low-energy electron to be trapped in the ionic lattice – is given by

$$\lambda_{\text{pol}}^{-1} = C\, e^{-\gamma E} \tag{3.52}$$

where C and γ are constants depending on the dielectric material. Thus the lower the electron energy, the higher the probability for an electron to lose its energy and to create a polaron. This approach implicitly assumes that, once has been generated a polaron, the residual kinetic energy of the electron is negligible. Furthermore, it is assumed that the electron stays trapped in the interaction site. This is quite a rough approximation, as trapped electrons – due to phonon induced processes – can actually hop from one trapping site to another. Anyway, it is often a sufficiently good approximation for Monte Carlo simulation purposes, so that it will be used in this book when we will deal with secondary electron emission from insulating materials.

3.4 Inelastic Mean Free Path

We have already discussed the fact that the main mechanism which determines the inelastic scattering cross-section and the relative energy losses, for energies higher than 50 eV, is the interaction of the incident electrons with the collective excitations of the electron sea, known as plasmons. Such energy loss mechanisms can be described by calculating the so-called energy loss function, i.e., the reciprocal of the imaginary part of the dielectric function. The Ritchie theory [6, 24] can be used – starting from the knowledge of the dependence of the dielectric function upon both the energy loss and the momentum transfer – to calculate the differential inverse electron inelastic mean free path and the electron inelastic mean free path. When the electron energy is higher than 50 eV, both the electron inelastic mean free path and the electron stopping power calculated within the dielectric formalism are in very good agreement with the experiment (and with theoretical data obtained by other investigators).

When, on the other hand, the electron energy becomes lower than 50 eV, the dielectric formalism alone is no longer able to accurately describe the energy loss phenomena. In fact, as the electron energy decreases, the electron inelastic mean free path calculated using only the electron–electron interaction increases indefinitely (see Figs. 3.11 and 3.12), while the stopping power goes quickly to zero (see Figs. 3.9 and 3.10). This means that if only electron–electron interactions were active for inelastic scattering, electrons with such a low energy would no longer interact inelastically (i.e., losing energy) with the solid. As a consequence they would travel without any change in their kinetic energy. For a semi-infinite target, this very long travel in the solid would either continue forever or until the electron reaches the surface of the material and is able to emerge.

As a matter of fact, we know that when the energy becomes lower than 20–30 eV further mechanisms of energy loss becomes very important (electron–phonon and electron–polaron interactions) so that the actual inelastic mean free path approaches zero as the electron energy goes to zero.

3.5 Surface Phenomena

Bulk and surface plasmon losses. The plasma frequency ω_p is given, in the Drude free electron theory, by Eq. (3.30) and represents the frequency of the volume collective excitations, which correspond to the propagation in the solid of *bulk plasmons* with energy

$$E_p = \hbar\omega_p \,. \tag{3.53}$$

In the electron energy loss spectra, it is thus expected to observe a bulk plasmon peak whose maximum is located at an energy E_p [given by Eq. (3.53)] from the elastic or zero-loss peak.

Also, features related to *surface plasmon* excitations appear in spectra acquired either in reflection mode from bulk targets or in transmission mode from very thin samples or small particles [49]. Indeed, in the proximity of the surface, due to the Maxwell's equation boundary conditions, surface excitations modes (surface plasmons) take place with a resonance frequency slightly lower than the bulk resonance frequency.

A rough evaluation of the energy of the surface plasmons can be performed – for a free electron metal – through the following very simple considerations [9]. In general, similarly to the volume plasmons propagating inside the solid, in the presence of an interface between two different materials – which we indicate here with a and b –, longitudinal waves travel as well along the interface. From continuity considerations it follows that [9]

$$\varepsilon_a + \varepsilon_b = 0 \,, \tag{3.54}$$

where we have indicated with ε_a the dielectric function on side a and with ε_b the dielectric function on side b of the interface. Let us now consider the particular case of a vacuum/metal interface and ignore, for the sake of simplicity, the damping, so that $\Gamma \approx 0$. Then, if a represents the vacuum, we have

$$\varepsilon_a = 1 \,, \tag{3.55}$$

and

$$\varepsilon_b \approx 1 - \frac{\omega_p^2}{\omega_s^2} \,, \tag{3.56}$$

where we have indicated with ω_s the frequency of the longitudinal waves of charge density traveling along the surface. Then we obtain, from Eq. (3.54)

$$2 - \frac{\omega_p^2}{\omega_s^2} = 0.$$

As a consequence, the surface plasmon energy $E_s = \hbar\omega_s$, i.e. the surface plasmon peak position in the energy loss spectrum, is expected to be found at an energy

$$E_s = \frac{E_p}{\sqrt{2}} \tag{3.57}$$

from the position of the elastic peak.

Chen and Kwei theory. Chen and Kwei [50] used the dielectric theory to show that the differential inverse inelastic mean free path for electrons emerging from a solid surface can be split up into two terms. The first one is the differential inverse inelastic mean free path in an infinite medium. The second one is the so-called surface term which is related to a surface layer extending on both sides of the vacuum-solid interface. As a consequence, electrons can interact inelastically with the solid even if outside, if they are close enough to the surface. Spectra of electrons originating near to the surface are therefore influenced by these surface effects.

The original version of the Chen and Kwei theory concerned only outgoing projectiles [50]. It was generalized by Li et al. [51] for incoming projectiles. See Chap. 14 for details.

So the theory predicts different trends for the inverse inelastic mean free path (IIMFP) for incoming and outgoing electrons when electrons are close to the surface: in particular, the inverse inelastic mean free path of the incoming electrons is found to slightly oscillate around the mean value, i.e., the bulk inverse inelastic mean free path. This phenomenon is attributed to the behavior of the electrons passing through the surface.

Using the Chen and Kwei theory, one can calculate the dependence on z of the inverse inelastic mean free path, for any given electron kinetic energy. In Figs. 3.18

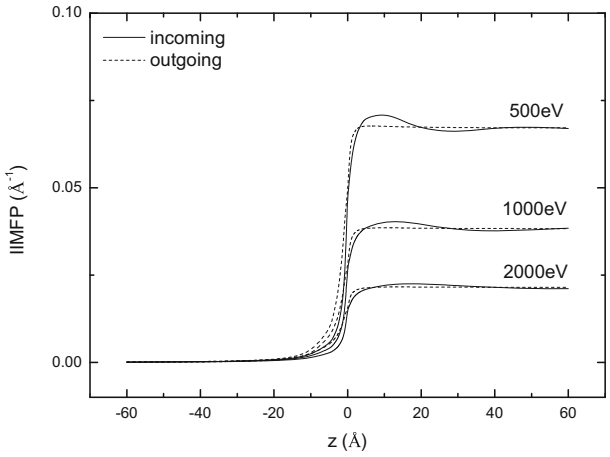

Fig. 3.18 Inverse inelastic mean free path (IIMFP) electrons in Al as a function of the distance from the surface (in the solid and in the vacuum) for several kinetic energies of both incoming and outgoing electrons

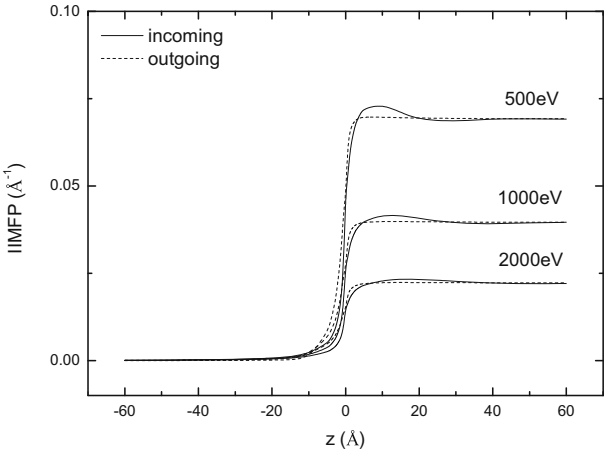

Fig. 3.19 Inverse inelastic mean free path (IIMFP) electrons in Si as a function of the distance from the surface (in the solid and in the vacuum) for several kinetic energies of both incoming and outgoing electrons

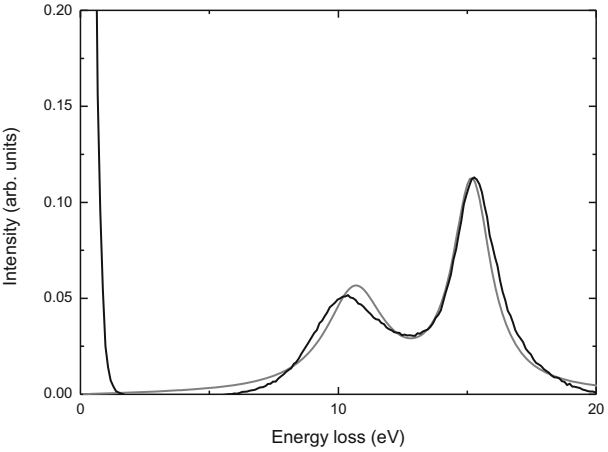

Fig. 3.20 Comparison between the experimental (*black line*) and theoretical (*gray line*) electron energy loss spectra for 1000 eV electrons impinging upon Al [52]. Calculated and experimental spectra were normalized to a common height of the bulk plasmon peak after linear background subtraction. Experimental data: *courtesy* of Lucia Calliari and Massimiliano Filippi

and 3.19 the inverse inelastic mean free path of Al and Si, respectively, are presented as a function of the electron's energy and depth (both outside and inside the solid).

The Chen and Kwei theory [50] and its generalization by Li et al. [51] have been recently used for simulating the surface and bulk plasmon loss peaks in Al and Si [52].

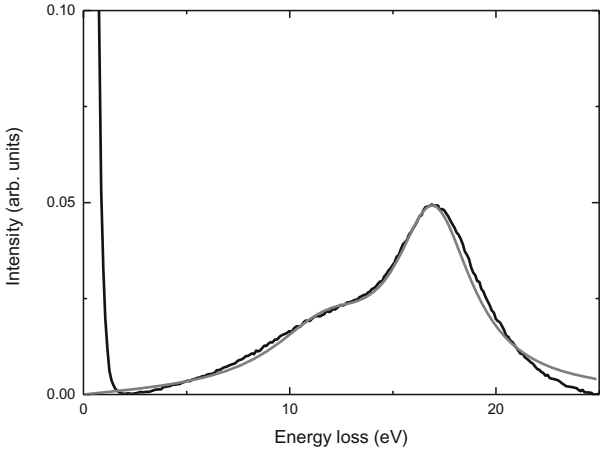

Fig. 3.21 Comparison between the experimental (*black line*) and theoretical (*gray line*) electron energy loss spectra for 1000 eV electrons impinging upon Si [52]. Calculated and experimental spectra were normalized to a common height of the bulk plasmon peak after linear background subtraction. Experimental data: *courtesy* of Lucia Calliari and Massimiliano Filippi

The energy loss spectrum can be calculated under the assumption that experimental spectra arise from electrons undergoing a single large angle elastic scattering event (so-called V-type trajectories [53]). In Figs. 3.20 and 3.21, the present calculation based on the combination of the Chen and Kwei and Li et al. theory [50, 51] with a single V-type trajectory modeling for Al and Si, are compared to experimental data [52]. Calculated and experimental spectra are normalized to a common height of the bulk plasmon peak.

3.6 Summary

In this chapter, elastic and inelastic scattering cross-sections were described. They are the main ingredients of the Monte Carlo simulation.

In particular, the elastic scattering collisions can be calculated by the Mott cross-section, the electron–plasmon inelastic scattering events by the Ritchie dielectric theory, and electron–phonon energy losses by the Fröhlich theory. Polaronic effects can be computed according to Ganachaud and Mokrani.

Chen and Kwei theory and its generalization due to Li et al. were also described. These theories allow to deal with the surface phenomena, particularly important for the investigation of reflection electron energy loss spectroscopy when the incident electron energy is smaller than 2–3 keV.

References

1. N.F. Mott, Proc. R. Soc. Lond. Ser. **124**, 425 (1929)
2. H. Fröhlich, Adv. Phys. **3**, 325 (1954)
3. H.A. Bethe, Ann. Phys. Leipz. **5**, 325 (1930)
4. R.O. Lane, D.J. Zaffarano, Phys. Rev. **94**, 960 (1954)
5. K. Kanaya, S. Okayama, J. Phys. D. Appl. Phys. **5**, 43 (1972)
6. R.H. Ritchie, Phys. Rev. **106**, 874 (1957)
7. J.P. Ganachaud, A. Mokrani, Surf. Sci. **334**, 329 (1995)
8. P. Sigmund, *Particle Penetration and Radiation Effects* (Springer, Berlin, 2006)
9. R.F. Egerton, *Electron Energy-Loss Spectroscopy in the Electron Microscope*, 3rd edn. (Springer, New York, 2011)
10. R.F. Egerton, Rep. Prog. Phys. **72**, 016502 (2009)
11. A. Jablonski, F. Salvat, C.J. Powell, J. Phys. Chem. Data **33**, 409 (2004)
12. M. Dapor, J. Appl. Phys. **79**, 8406 (1996)
13. M. Dapor, *Electron-Beam Interactions with Solids: Application of the Monte Carlo Method to Electron Scattering Problems* (Springer, Berlin, 2003)
14. M.L. Jenkin, M.A. Kirk, *Characterization of Radiation Damage by Electron Microscopy*, IOP Series Microscopy in Materials Science (Institute of Physics, Bristol, 2001)
15. G. Wentzel, Z. Phys. **40**, 590 (1927)
16. S. Taioli, S. Simonucci, L. Calliari, M. Filippi, M. Dapor, Phys. Rev. B **79**, 085432 (2009)
17. S. Taioli, S. Simonucci, M. Dapor, Comput. Sci. Discov. **2**, 015002 (2009)
18. S. Taioli, S. Simonucci, L. Calliari, M. Dapor, Phys. Rep. **493**, 237 (2010)
19. F. Salvat, R. Mayol, Comput. Phys. Commun. **74**, 358 (1993)
20. E. Reichert, Z. Phys. **173**, 392 (1963)
21. M. Dapor, Phys. Rev. B **46**, 618 (1992)
22. J. Llacer, E.L. Garwin, J. Appl. Phys. **40**, 2766 (1969)
23. M.J. Berger, S.M. Seltzer, National Research Council Publication, Whasington D.C. vol. 1133 (1964), p. 205
24. R.H. Ritchie, A. Howie, Philos. Mag. **36**, 463 (1977)
25. F. Yubero, S. Tougaard, Phys. Rev. B **46**, 2486 (1992)
26. H. Raether, *Excitation of Plasmons and Interband Transitions by Electrons* (Springer, Berlin, 1982)
27. A. Cohen-Simonsen, F. Yubero, S. Tougaard, Phys. Rev. B **56**, 1612 (1997)
28. J.J. Ritsko, L.J. Brillson, R.W. Bigelow, T.J. Fabish, J. Chem. Phys. **69**, 3931 (1978)
29. B.L. Henke, P. Lee, T.J. Tanaka, R.L. Shimabukuro, B.K. Fujikawa, At. Data Nucl. Data Tables **27**, 1 (1982)
30. B.L. Henke, P. Lee, T.J. Tanaka, R.L. Shimabukuro, B.K. Fujikawa, At. Data Nucl. Data Tables **54**, 181 (1993)
31. U. Buechner, J. Phys. C: Solid State Phys. **8**, 2781 (1975)
32. D.R. Penn, Phys. Rev. B **35**, 482 (1987)
33. J.C. Ashley, J. Electron Spectrosc. Relat. Phenom. **46**, 199 (1988)
34. J.C. Ashley, J. Electron Spectrosc. Relat. Phenom. **50**, 323 (1990)
35. Z. Tan, Y.Y. Xia, X. Liu, M. Zhao, Microelectron. Eng. **77**, 285 (2005)
36. J.C. Ashley, V.E. Anderson, IEEE Trans. Nucl. Sci. **NS28**, 4132 (1981)
37. S. Tanuma, C.J. Powell, D.R. Penn, Surf. Interface Anal. **17**, 911 (1991)
38. D. Emfietzoglou, I. Kyriakou, R. Garcia-Molina, I. Abril, J. Appl. Phys. **114**, 144907 (2013)
39. R. Garcia-Molina, I. Abril, C.D. Denton, S. Heredia-Avalos, Nucl. Instrum. Methods Phys. Res. B **249**, 6 (2006)
40. R. Garcia-Molina, I. Abril, I. Kyriakou, D. Emfietzoglou, Surf. Interface Anal. (2016). doi:10.1002/sia.5947
41. N.D. Mermin, Phys. Rev. B **1**, 2362 (1970)
42. I. Abril, R. Garcia-Molina, C.D. Denton, F.J. Pérez-Pérez, N.R. Arista, Phys. Rev. A **58**, 357 (1998)

43. W. de la Cruz, F. Yubero, Surf. Interface Anal. **39**, 460 (2007)
44. S. Tanuma, C.J. Powell, D.R. Penn, Surf. Interface Anal. **21**, 165 (1994)
45. M. Dapor, Nucl. Instrum. Methods Phys. Res. B **352**, 190 (2015)
46. M. Dapor, Front. Mater. **2**, 27 (2015)
47. V.I. Ochkur, Sov. Phys. J.E.T.P. **47**, 1766 (1964)
48. P. de Vera, I. Abril, R. Garcia-Molina, J. Appl. Phys. **109**, 094901 (2011)
49. C.J. Powell, J.B. Swann, Phys. Rev. **115**, 869 (1959)
50. Y.F. Chen, C.M. Kwei, Surf. Sci. **364**, 131 (1996)
51. Y.C. Li, Y.H. Tu, C.M. Kwei, C.J. Tung, Surf. Sci. **589**, 67 (2005)
52. M. Dapor, L. Calliari, S. Fanchenko, Surf. Interface Anal. **44**, 1110 (2012)
53. A. Jablonski, C.J. Powell, Surf. Sci. **551**, 106 (2004)

Chapter 4
Random Numbers

As Monte Carlo is a statistical method, the accuracy of its results depends on the number of simulated electron trajectories and on the pseudo-random number generator used to perform the simulations. We shall briefly summarize how pseudo-random numbers can be generated. We shall describe, as well, how to calculate selected random number distributions that are particularly relevant for the Monte Carlo method purposes [1].

We are firstly interested in a generator of pseudo-random numbers uniformly distributed in the range [0, 1]. Once it is given, we shall describe the way to generate pseudo-random numbers uniformly distributed in a given interval; pseudo-random numbers distributed according to the Poisson density of probability; and pseudo-random numbers distributed according to the Gauss density of probability [2].

4.1 Generating Pseudo-random Numbers

The algorithm most frequently used for the generation of pseudo-random numbers uniformly distributed in a given interval provides the entire sequence from a "seed" number: starting with an initial number, known as the seed, the subsequent random numbers are calculated using an equation that permits to obtain each random number from the previous one. Every number of the sequence is computable knowing the value of the last calculated random number [2, 3].

Let us suppose that μ_n is the $n^{\underline{th}}$ pseudo-random number. Then the next random number μ_{n+1} is given by

$$\mu_{n+1} = (a\mu_n + b) \bmod m \tag{4.1}$$

where a, b and m are three integer numbers. Choosing the values of the three "magic" numbers a, b, and m in a proper way, sequences of random numbers corresponding to the maximum period (which is equal to m) are obtained. In such a way, for every initial seed μ_0, all the integer numbers from 0 to $m - 1$ will be in the sequence.

M. Dapor, *Transport of Energetic Electrons in Solids*,
Springer Tracts in Modern Physics 257, DOI 10.1007/978-3-319-47492-2_4

Several proposals were provided for the three "magic" numbers a, b, and m. Statistical tests have been used to establish the values of the three numbers a, b, and m in order to appropriately approximate a sequence of integer random numbers uniformly distributed in the interval from 0 to $m - 1$ [2]. A simple proposal is the so-called "minimal standard" which corresponds to $a = 16807, b = 0, m = 2147483647$.

In order to obtain a sequence of real numbers uniformly distributed in the range [0, 1], it is sufficient to divide by m all the numbers obtained by Eq. (4.1).

Pseudo-random number generators used today in the programming languages such as C or C++ are more accurate than the minimal standard. They are based on an approach similar to that expressed by Eq. (4.1) [2].

4.2 Testing Pseudo-random Number Generators

A classical test to check the quality and the uniformity of a pseudo-random number generator consists in simulating $\pi = 3.14\ldots$ Let us generate a statistically significant number of pairs of random numbers in the range $[-1,\ 1]$. If the distribution of the generated pseudo-random numbers approached a perfectly uniform distribution of random numbers, then the fraction of generated points that lie within the unit circle (i.e., the number of pairs in the circle divided by the total number of generated pairs) should approach $\pi/4$. Using the random number generator "rand()" provided by the C++ compiler "Dev-C++ 4.9.9.0", we obtained for π the values 3.1411 ± 0.0005 with 10^7 pairs, 3.1415 ± 0.0001 with 10^8 pairs, and 3.1417 ± 0.0001 with 10^9 pairs.

4.3 Pseudo-random Numbers Distributed According to a Given Probability Density

Let us indicate with ξ a random variable defined in the range $[a, b]$ distributed according to a given probability density $p(s)$. If μ represents a random variable uniformly distributed in the range [0, 1], then the values of ξ can be obtained by the use of the equation:

$$\int_a^{\xi} p(s)\, ds = \mu\,. \tag{4.2}$$

4.4 Pseudo-random Numbers Uniformly Distributed in the Interval $[a, b]$

Starting from a distribution μ uniformly distributed in the range [0, 1], we can use Eq. (4.2) to obtain a uniform distribution η in the interval $[a, b]$. The distribution η corresponds to the probability density:

$$p_\eta(s) = \frac{1}{b-a}\,. \tag{4.3}$$

η satisfies the equation:

$$\mu = \int_a^\eta p_\eta(s)\,ds = \int_a^\eta \frac{ds}{b-a}\,. \tag{4.4}$$

As a consequence,

$$\eta = a + \mu(b-a)\,. \tag{4.5}$$

The expected value of the distribution is given by:

$$\langle\eta\rangle = (a+b)/2\,. \tag{4.6}$$

4.5 Pseudo-random Numbers Distributed According to the Poisson Density of Probability

Starting from a distribution μ uniformly distributed in the range [0, 1], we can use Eq. (4.2) to obtain the Poisson distribution as well. It is a very important distribution for the Monte Carlo simulations, as the stochastic process for multiple scattering follows a Poisson-type law. The Poisson distribution is defined by the following probability density:

$$p_\chi(s) = \frac{1}{\lambda}\exp\left(-\frac{s}{\lambda}\right)\,, \tag{4.7}$$

where λ is a constant.

A random variable χ distributed according to the Poisson law, and defined in the interval $[0, \infty)$, is given by the solution of the equation:

$$\mu = \int_0^\chi \frac{1}{\lambda}\exp\left(-\frac{s}{\lambda}\right)\,ds\,, \tag{4.8}$$

where μ is, as usual, a random variable uniformly distributed in the range [0, 1]. Then

$$\chi = -\lambda\ln(1-\mu)\,. \tag{4.9}$$

Since the distribution of $1-\mu$ is equal to that of μ, we also have:

$$\chi = -\lambda\ln(\mu)\,. \tag{4.10}$$

The constant λ is the expected value of χ:

$$\langle\chi\rangle = \lambda\,. \tag{4.11}$$

4.6 Pseudo-random Numbers Distributed According to the Gauss Density of Probability

In order to describe the elastic peak, we have to calculate random variables with Gaussian distribution. The sequences of random numbers distributed with Gaussian density are calculated in this work by using the Box-Muller method [2].

Let us indicate with μ_1 and μ_2 two sequences of random numbers uniformly distributed in the interval [0, 1]. Let us consider the transformation:

$$\gamma_1 = \sqrt{-2\ln\mu_1}\cos 2\pi\mu_2\,, \tag{4.12}$$

$$\gamma_2 = \sqrt{-2\ln\mu_1}\sin 2\pi\mu_2\,. \tag{4.13}$$

Algebraic manipulations permit to calculate μ_1 and μ_2,

$$\mu_1 = \exp\left[-\frac{1}{2}(\gamma_1^2+\gamma_2^2)\right], \tag{4.14}$$

$$\mu_2 = \frac{1}{2\pi}\arctan\frac{\gamma_2}{\gamma_1}\,. \tag{4.15}$$

Let us now consider the Jacobian determinant J of the random variables μ_1 and μ_2 with respect to the random variables γ_1 and γ_2. Since

$$\frac{\partial\mu_1}{\partial\gamma_1} = -\gamma_1\,\exp\left[-\frac{1}{2}(\gamma_1^2+\gamma_2^2)\right], \tag{4.16}$$

$$\frac{\partial\mu_1}{\partial\gamma_2} = -\gamma_2\,\exp\left[-\frac{1}{2}(\gamma_1^2+\gamma_2^2)\right], \tag{4.17}$$

$$\frac{\partial\mu_2}{\partial\gamma_1} = -\frac{1}{2\pi}\,\frac{\gamma_2}{\gamma_1^2+\gamma_2^2}\,, \tag{4.18}$$

and

$$\frac{\partial\mu_2}{\partial\gamma_2} = \frac{1}{2\pi}\,\frac{\gamma_1}{\gamma_1^2+\gamma_2^2}\,, \tag{4.19}$$

the Jacobian determinant J is given by

$$J = \frac{\partial\mu_1}{\partial\gamma_1}\frac{\partial\mu_2}{\partial\gamma_2} - \frac{\partial\mu_2}{\partial\gamma_1}\frac{\partial\mu_1}{\partial\gamma_2} = -g(\gamma_1)g(\gamma_2)\,, \tag{4.20}$$

where

$$g(\gamma) = \frac{\exp(-\gamma^2/2)}{\sqrt{2\pi}}\,. \tag{4.21}$$

Thus the two random variables γ_1 and γ_2 are distributed according to the Gaussian density.

4.7 Summary

We have described the algorithm most frequently used for the generation of pseudo-random numbers uniformly distributed in a given interval. It provides the whole sequence from a seed number. Starting with a given initial number, the algorithm computes the subsequent pseudo-random numbers according to a simple rule. Knowing the value of the last calculated pseudo-random number, any other number in the sequence can be easily computed. Once provided a generator of pseudo-random numbers uniformly distributed on the range [0, 1], sequences of pseudo-random numbers distributed according to given densities of probability can be obtained by the use of specific algorithms. Several examples, useful for the purposes of transport Monte Carlo, were provided in this chapter.

References

1. M. Dapor, Surf. Sci. **600**, 4728 (2006)
2. W.H. Press, S.A. Teukolsky, W.T. Vetterling, B.P. Flannery, *Numerical Recipes in C*, 2nd edn., The Art of Scientific Computing (Cambridge University Press, Cambridge, 1992)
3. S.E. Koonin, D.C. Meredith, *Computational Physics* (Addison-Wesley, Redwood City, 1990)

Chapter 5
Monte Carlo Strategies

Monte Carlo is one of the most powerful theoretical methods for evaluating the physical quantities related to the interaction of electrons with a solid target. A Monte Carlo simulation can be considered as an idealized experiment. The simulation does not investigate the fundamental principles of the interaction. It is necessary to have a good knowledge of them – in particular of the energy loss and angular deflection phenomena – to produce a good simulation. All the cross-sections and mean free paths have to be previously accurately calculated: they are then used in the Monte Carlo code in order to obtain the macroscopic characteristics of the interaction processes by simulating a large number of single particle trajectories and then averaging them. Due to the recent evolution in computer calculation capability, we are now able to obtain statistically significant results in very short calculation times.

Two main strategies can be utilized in order to simulate electron transport in solid targets. The first one, the so-called *continuous-slowing-down approximation*, is very simple and assumes that electrons continuously lose energy as they travel inside the solid, changing direction when elastic collisions occur. It is frequently used – for it is a very fast procedure – when the description of the statistical fluctuations of the energy loss due to the different energy losses suffered by each electron of the penetrating beam and of the shower of secondary electron are not crucial for simulating the desired quantities. This is the case, for example, for the calculation of the backscattering coefficient or the depth distribution of the absorbed electrons. If, instead, accurate descriptions of all the inelastic events which occur along the electron path – i.e., of the statistical fluctuations of the energy loss – are needed to study the investigated phenomena, a second strategy is required: a strategy where *energy straggling* is properly taken into account simulating all the single energy losses occurring along the electron trajectory (together with the description of the elastic events in order to take into account the changes of direction). This is the case, for example, for the calculation of the energy distribution of the electrons emitted by the surface of the solid target.

In this chapter both these strategies will be briefly described, while the discussion of specific features and details will be found in the chapters devoted to the applications.

M. Dapor, *Transport of Energetic Electrons in Solids*,
Springer Tracts in Modern Physics 257, DOI 10.1007/978-3-319-47492-2_5

For both the descriptions we will adopt spherical coordinates (r, θ, ϕ) and assume that a stream of monoenergetic electrons irradiates a solid target in the z direction. In some of the applications presented in the next chapters, we will consider also angles of incidence, with respect to the normal to the target surface, different from zero.

5.1 The Continuous-Slowing-Down Approximation

Let us firstly describe the Monte Carlo method based on the continuous-slowing-down approximation. It requires the use of the stopping power – for calculating the energy losses along the electron trajectories – while the electron angular deflections are ruled by the Mott cross-section.

5.1.1 The Step-Length

The stochastic process for multiple scattering is assumed to follow a Poisson-type law. The step-length Δs is then given by

$$\Delta s = -\lambda_{\mathrm{el}} \ln(\mu_1) \,, \tag{5.1}$$

where μ_1 is a random number uniformly distributed in the range [0, 1] and λ_{el} is the elastic mean free path:

$$\lambda_{\mathrm{el}} = \frac{1}{N \sigma_{\mathrm{el}}} \,. \tag{5.2}$$

Here we have indicated with N the number of atoms per unit volume in the solid and with σ_{el} the total elastic scattering cross-section, given by

$$\sigma_{\mathrm{el}}(E) = \int \frac{d\sigma_{\mathrm{el}}}{d\Omega} \, d\Omega = \int_0^{\pi} \frac{d\sigma_{\mathrm{el}}}{d\Omega} \, 2\,\pi \, \sin\vartheta \, d\vartheta \,. \tag{5.3}$$

5.1.2 Interface Between Over-Layer and Substrate

For surface films, the interface between the over-layer and the substrate must be properly taken into account. The change in the scattering probabilities per unit length in passing from the film to the substrate and vice versa, have to be considered, so that Eq. (5.1) has to be accordingly modified. Let us denote with p_1 and p_2 the scattering probabilities per unit length for the two materials, where p_1 refers to the material in which the last elastic collision occurred and p_2 to the other material and

let us indicate with d the distance along the scattering direction between the initial scattering and the interface. According to Horiguchi et al. [1] and Messina et al. [2], if μ_1 is a random number uniformly distributed in the range [0, 1], the step-length Δs is given by,

$$\Delta s = \begin{cases} \left(\frac{1}{p_1}\right)[-\ln(1-\mu_1)], & 0 \le \mu_1 < 1 - \exp(-p_1 d); \\ d + \left(\frac{1}{p_2}\right)[-\ln(1-\mu_1) - p_1 d], & 1 - \exp(-p_1 d) \le \mu_1 \le 1. \end{cases} \tag{5.4}$$

5.1.3 The Polar Scattering Angle

The polar scattering angle θ resulting from an elastic collision is calculated assuming that the probability of elastic scattering into an angular range from 0 to θ,

$$P_{\mathrm{el}}(\theta, E) = \frac{2\pi}{\sigma_{el}} \int_0^{\theta} \frac{d\sigma_{\mathrm{el}}}{d\Omega} \sin\vartheta \, d\vartheta \,, \tag{5.5}$$

is a random number μ_2 uniformly distributed in the range [0, 1]:

$$\mu_2 = P_{\mathrm{el}}(\theta, E) \,. \tag{5.6}$$

In other words, the sampling of the elastic scattering is performed looking for the angle of scattering corresponding to a random number uniformly distributed in the range [0, 1] (see Fig. 5.1). The angle of scattering, for any given electron energy, is calculated looking for the upper limit of integration in Eq. (5.5), once determined that μ_2 be equal to $P_{\mathrm{el}}(\theta, E)$ (Eq. (5.6)).

5.1.4 Direction of the Electron After the Last Deflection

The azimuth angle ϕ can assume any value selected by a random number μ_3 uniformly distributed in the range $[0, \ 2\pi]$.

Both the θ and ϕ angles refer to the last direction before the impact. The direction $\theta_z^{'}$ in which the electron is moving after the last deflection, relative to the z direction, is given by [3–5]

$$\cos\theta_z^{'} = \cos\theta_z \cos\theta - \sin\theta_z \sin\theta \cos\phi \,. \tag{5.7}$$

In the last equation, θ_z is the angle relative to the z direction before the impact. The step of trajectory along the z direction, Δz, is then obtained by

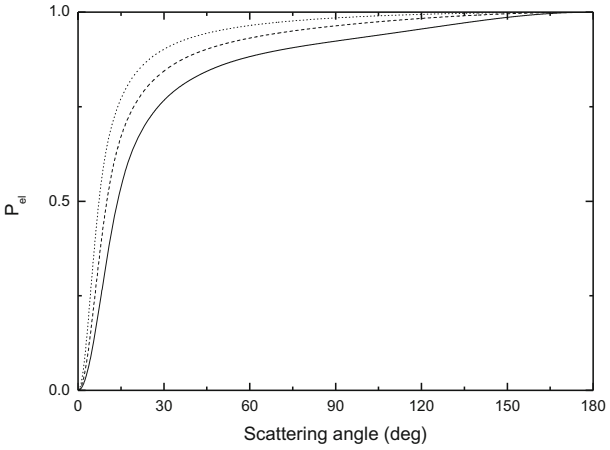

Fig. 5.1 Sampling of the elastic scattering angle for electrons in silicon. P_{el} is the cumulative probability for elastic scattering into an angular range from 0 to θ calculated numerically by solving the Dirac equation in a central field, according to the relativistic partial wave expansion method (Mott cross-section). *Solid line*: E = 500 eV; *dashed line*: E = 1000 eV; *dotted line*: E = 2000 eV

$$\Delta z = \Delta s \cos \theta_z^{'} . \tag{5.8}$$

The new angle $\theta_z^{'}$ is the incident angle θ_z corresponding to the next path length.

5.1.5 Electron Position in Three Dimensional Cartesian Coordinates

In order to describe, at each scattering point, the electron position in three dimensional Cartesian coordinates (x, y, z), let us indicate with Δs_n the length of n^{th} step. Thus

$$\begin{cases} x_{n+1} = x_n + \Delta s_n \sin\theta_n \cos\phi_n \\ y_{n+1} = y_n + \Delta s_n \sin\theta_n \sin\phi_n \\ z_{n+1} = z_n + \Delta s_n \cos\theta_n \end{cases} \tag{5.9}$$

where the following transformations

$$\begin{cases} \cos\theta_n = \cos\theta_{n-1}\cos\theta - \sin\theta_{n-1}\sin\theta\cos\phi \\ \sin(\phi_n - \phi_{n-1}) = \sin\theta\sin\phi/\sin\theta_n \\ \cos(\phi_n - \phi_{n-1}) = (\cos\theta - \cos\theta_{n-1}\cos\theta_n)/(\sin\theta_{n-1}\sin\theta_n) \end{cases} \tag{5.10}$$

relate the angles in the coordinate system of the target with the angles in the coordinate systems moving with the electron [5].

5.1.6 The Energy Loss

The basic idea of the continuous-slowing-down approximation, is that electrons lose energy with continuity while traveling in the solid: in order to calculate the energy loss along the various segments of the electron trajectory we use the stopping power.

Monte Carlo codes typically approximate the energy loss ΔE along the segment of trajectory Δz by the following equation

$$\Delta E = (dE/dz)\Delta z\,, \tag{5.11}$$

where $-dE/dz$ is the electron stopping power. With this approach, statistical fluctuations of the energy losses are completely neglected. As a consequence this kind of Monte Carlo strategy should be avoided when detailed information about energy loss mechanisms is required (for example when we need to calculate the energy distribution of the emitted electrons).

5.1.7 End of the Trajectory and Number of Trajectories

Each electron is followed until its energy becomes lower than a given value or until it emerges from the target surface. The selection of the cut off value of the energy depends on the particular problem one is investigating. For the calculation of the backscattering coefficient, for example, the electrons are followed until their energy becomes smaller than 50 eV.

It should be noted that even the number of trajectories is a crucial quantity to obtain statistically significant results and to improve the signal to noise ratio. In this work the typical number of trajectories, used for the presented simulations based on the continuous-slowing-down approximation strategy, ranges from 10^5 to 10^6, depending on the particular problem investigated.

5.2 The Energy-Straggling Strategy

Let us now describe the Monte Carlo method based on the energy-straggling strategy. It requires a detailed knowledge of all the energy loss mechanisms and probabilities (electron-electron, electron-phonon, electron-polaron cross-sections) while the electron angular deflections are ruled, as for the case of the continuous-slowing-down approximation, by the use of the Mott cross-section.

5.2.1 The Step-Length

The Monte Carlo method based on the energy-straggling strategy requires an approach different from that based on the continuous-slowing-down approximation. Also in this case the stochastic process for multiple scattering is assumed to follow a Poisson-type law. The step-length Δs is thus given by

$$\Delta s = -\lambda \ln(\mu_1)\,, \tag{5.12}$$

where μ_1 is, as for the previous case, a random number uniformly distributed in the range [0, 1]. Now λ is no longer the elastic mean free path. It is instead given by

$$\lambda = \frac{1}{N\,(\sigma_{\text{in}} + \sigma_{\text{el}})}\,, \tag{5.13}$$

where σ_{in} is the total inelastic scattering cross-sections (the sum of all the inelastic and quasi-elastic scattering cross-sections), i.e.,

$$\sigma_{\text{in}} = \sigma_{\text{inel}} + \sigma_{\text{phonon}} + \sigma_{\text{pol}} \tag{5.14}$$

and σ_{el} is the total elastic scattering cross-section (Mott cross-section). Therefore,

$$\lambda = \frac{1}{N\,(\sigma_{\text{inel}} + \sigma_{\text{phonon}} + \sigma_{\text{pol}} + \sigma_{\text{el}})}\,, \tag{5.15}$$

or, since $N\sigma_{\text{inel}} = 1/\lambda_{\text{inel}}$, $N\sigma_{\text{phonon}} = 1/\lambda_{\text{phonon}}$, $N\sigma_{\text{pol}} = 1/\lambda_{\text{pol}}$, and $N\sigma_{\text{el}} = 1/\lambda_{\text{el}}$,

$$\frac{1}{\lambda} = \frac{1}{\lambda_{\text{inel}}} + \frac{1}{\lambda_{\text{phonon}}} + \frac{1}{\lambda_{\text{pol}}} + \frac{1}{\lambda_{\text{el}}}\,. \tag{5.16}$$

5.2.2 Elastic and Inelastic Scattering

Before each collision, a random number μ_2 uniformly distributed in the range [0, 1] is generated and compared with the probability of inelastic scattering, p_{in}, given by

$$p_{\text{in}} = \frac{\sigma_{\text{in}}}{\sigma_{\text{in}} + \sigma_{\text{el}}} = \frac{\lambda}{\lambda_{\text{in}}}, \tag{5.17}$$

while that of elastic scattering is

$$p_{\text{el}} = 1 - p_{\text{in}}. \tag{5.18}$$

If the random number μ_2 is less than or equal to p_{in}, then the collision will be inelastic; otherwise, it will be elastic.

If the collision is inelastic, a similar procedure is followed to establish which kind of inelastic process will occur among the following ones: an electron-electron (Ritchie [6]), a quasi-elastic electron-phonon (Fröhlich [7]), or an electron-polaron (Ganachaud and Mokrani [8]) interaction.

If the collision is elastic, the polar scattering angle θ is calculated by generating a random number μ_3, uniformly distributed in the range [0, 1], representing the probability of elastic scattering into an angular range from 0 to θ:

$$\mu_3 = P_{\text{el}}(\theta, E) = \frac{1}{\sigma_{el}} \int_0^{\theta} \frac{d\sigma_{el}}{d\Omega} 2\pi \sin\vartheta \, d\vartheta \,. \tag{5.19}$$

In each electron-electron inelastic collision the function $P_{\text{inel}}(W, E)$ that provides the fraction of electrons losing energies less than or equal to W [9] (see Fig. 5.2 where the function $P_{\text{inel}}(W, E)$ is represented for 1000 eV electrons impinging on Si) is calculated: the energy loss W is obtained by generating a random number μ_4 uniformly distributed in the range [0, 1], and imposing that μ_4 is equal to $P_{\text{inel}}(W, E)$:

$$\mu_4 = P_{\text{inel}}(W, E) = \frac{1}{\sigma_{\text{inel}}} \int_0^{W} \frac{d\sigma_{\text{inel}}}{dw} dw \,. \tag{5.20}$$

Also a secondary electron is generated whose energy is equal to the energy lost by the incident electron, W.

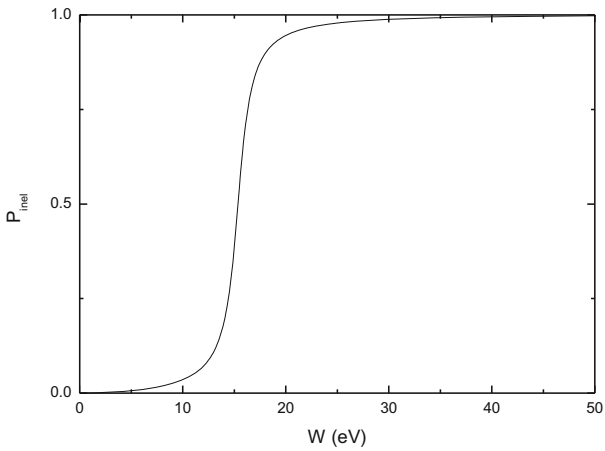

Fig. 5.2 Sampling of the energy loss for electrons in silicon. P_{inel} is the cumulative probability for inelastic collisions of electrons in Si (calculated according to the dielectric Ritchie theory) causing energy losses less than or equal to W. The cumulative probability is here represented, as a function of the energy loss W, for E = 1000 eV

If an electron-lattice interaction occurs, with the creation of a phonon, the energy lost by the electron is equal to the energy of the created phonon, W_{ph}.

Lastly, if a polaron is generated, the following approximation was adopted in this book: the electron ends its travel in the solid, as it is trapped where the interaction has taken place.

5.2.3 Electron-Electron Collisions: Scattering Angle

Let us consider the collision between two electrons. Let us assume that one of them is initially at rest. Let us indicate with $\boldsymbol{p}$ and E the initial momentum and energy, respectively, of the incident electron, with $\boldsymbol{p}'$ and E' the momentum and energy, respectively, of the incident electron after the collision, and with $\boldsymbol{q} = \boldsymbol{p} - \boldsymbol{p}'$ and $W = E - E'$ the momentum and energy, respectively, of the electron which was initially at rest (the so-called secondary electron) after the collision. Let us indicate with θ and θ_s, respectively, the polar scattering angles of the incident and of the secondary electrons. Useful relationships between these quantities can be provided using the so-called classical binary-collision model, which is sufficiently accurate for many practical purposes. Due to conservation of momentum and energy,

$$\sin\theta_s = \cos\theta\,, \tag{5.21}$$

where the polar scattering angle θ depends on the energy loss $W = E - E' = \Delta E$ according to the equation

$$\frac{W}{E} = \frac{\Delta E}{E} = \sin^2\theta\,. \tag{5.22}$$

Let us firstly demonstrate Eq. (5.21). To do that, we have to prove that the momentum of each of the two electrons in the final state is perpendicular to that of the other one. Let us then introduce the angle β between $\boldsymbol{p}'$ and $\boldsymbol{q}$. From momentum conservation,

$$\boldsymbol{p} = \boldsymbol{p}' + \boldsymbol{q}\,, \tag{5.23}$$

we obtain

$$p^2 = p'^2 + q^2 + 2p'q\cos\beta\,. \tag{5.24}$$

From conservation of energy,

$$E = E' + \Delta E\,, \tag{5.25}$$

it follows that

$$p^2 = p'^2 + q^2 . \tag{5.26}$$

The comparison between Eqs. (5.24) and (5.26) allows us to conclude, as anticipated, that

$$\beta = \frac{\pi}{2} , \tag{5.27}$$

which is equivalent to Eq. (5.21).

Let us now examine the consequences of the conservation laws on the dependence of the scattering angle θ – the angle between the initial momentum $\boldsymbol{p}$ and the final momentum $\boldsymbol{p'}$ of the incident electron – on the electron energy loss. As

$$\boldsymbol{p} - \boldsymbol{p'} = \boldsymbol{q} , \tag{5.28}$$

we obtain

$$q^2 = p^2 + p'^2 - 2pp' \cos\theta . \tag{5.29}$$

Equation (5.29) has two important consequences. The first one is that, in the final state, the absolute value of momentum $\boldsymbol{q}$ of the electron initially at rest, q, can assume only values belonging to the finite interval $[q_-, q_+]$ where

$$q_\pm = \sqrt{2mE} \pm \sqrt{2m(E - \Delta E)} , \tag{5.30}$$

as one can immediately see assuming that, in Eq. (5.29), $\theta = 0$ (corresponding to q_-) and $\theta = \pi$ (corresponding to q_+).

The second consequence of Eq. (5.29) is that it offers the possibility, when conservation of energy is considered as well, to obtain the relationship between the scattering angle and the energy loss of the incident electron represented by Eq. (5.22). Indeed, according to Eq. (5.26), $q^2 = p^2 - p'^2$, so that, comparing this result with that expressed by Eq. (5.29), we obtain

$$\cos^2\theta = \frac{p'^2}{p^2} = \frac{E'}{E} , \tag{5.31}$$

which is equivalent to Eq. (5.22).

5.2.4 Electron-Phonon Collisions: Scattering Angle

In the case of electron-phonon collision, the corresponding polar scattering angle can be calculated according to Llacer and Garwin [10]. Details can also be found in Chap. 12.

Indicating with μ_5 a new random number uniformly distributed in the range [0, 1], the polar scattering angle corresponding to an electron-phonon collision can be calculated as

$$\cos\theta = \frac{E + E'}{2\sqrt{E\,E'}}(1 - B^{\mu_5}) + B^{\mu_5}, \tag{5.32}$$

where

$$B = \frac{E + E' + 2\sqrt{E\,E'}}{E + E' - 2\sqrt{E\,E'}}. \tag{5.33}$$

5.2.5 Direction of the Electron After the Last Deflection

Once the polar scattering angle has been calculated, the azimuth angle is obtained by generating a random number μ_6 uniformly distributed in the range $[0,\ 2\pi]$. The direction $\theta_z^{'}$ in which the electron is moving after the last deflection, relative to the z direction, is calculated by Eq. (5.7). The Eqs. (5.9) and (5.10) have to be used, on the other hand, in order to describe, at each scattering point, the particle position in three dimensional Cartesian coordinates.

5.2.6 The First Step

According to Ref. [5], electrons make the first step without any scattering at the interface between the vacuum and the sample or, in other words, the energy losses and angular deflections occur at the last point of each step-length.

5.2.7 Transmission Coefficient

When dealing with very slow electrons, another important question to be considered is related to their capability to emerge from the surface of the solid [11].

In fact, the condition for an electron to emerge from the surface of a solid is not always satisfied. The interface with the vacuum represents a potential barrier, and not all the electrons that reach the surface can go beyond it. When the electrons reaching the surface cannot emerge, they are specularly reflected back in the material. This problem is particularly important when investigating secondary electron emission, as secondary electrons typically have very low energy (lower than 50 eV), so that they often cannot satisfy the condition to emerge.

When a very slow electron of energy E reaches the target surface, it can emerge from the surface only if this condition is satisfied

$$E \cos^2 \theta = \chi , \tag{5.34}$$

where θ is the angle of emergence with respect to the normal to the surface, measured inside the specimen, and χ is the so-called *electron affinity*, i.e. the potential barrier represented by the difference between the vacuum level and the bottom of the conduction band. Its value depends on the investigated material. For example, the electron affinity of un-doped silicon is 4.05 eV [12].

In order to study the transmission coefficient of slow electrons through the potential barrier χ, let us consider two regions along the z direction, inside and outside the solid, respectively. Let us further assume that the potential barrier χ is located at $z = 0$.

The first region, inside the solid, corresponds to the following solution of the Schrödinger equation:

$$\psi_1 = A_1 \exp(i\, k_1\, z) + B_1 \exp(-i\, k_1\, z) , \tag{5.35}$$

while the solution in the vacuum is given by:

$$\psi_2 = A_2 \exp(i\, k_2\, z) . \tag{5.36}$$

In these equations, A_1, B_1, and A_2 are three constants while k_1 and k_2 are, respectively, the electron wavenumbers in the solid and in the vacuum. They are given by

$$k_1 = \sqrt{\frac{2\, m\, E}{\hbar^2}} \cos \theta , \tag{5.37}$$

$$k_2 = \sqrt{\frac{2\, m\, (E - \chi)}{\hbar^2}} \cos \vartheta . \tag{5.38}$$

Here θ and ϑ represent the angles of emergence of the secondary electrons – with respect to the normal to the surface – measured, respectively, inside and outside the material.

As the following conditions of continuity have to be satisfied

$$\psi_1(0) = \psi_2(0) , \tag{5.39}$$

$$\psi_1'(0) = \psi_2'(0) , \tag{5.40}$$

we have

$$A_1 + B_1 = A_2 \,, \tag{5.41}$$

and

$$(A_1 - B_1)\, k_1 = A_2\, k_2 \,, \tag{5.42}$$

so that the transmission coefficient T can be easily calculated to be

$$T = 1 - \left| \frac{B_1}{A_1} \right|^2 = \frac{4\, k_1\, k_2}{(k_1 + k_2)^2} \,. \tag{5.43}$$

Taking into account the definition of electron wavenumbers given above, we obtain

$$T = \frac{4\sqrt{(1 - \chi/E)\cos^2\vartheta/\cos^2\theta}}{\left[1 + \sqrt{(1 - \chi/E)\cos^2\vartheta/\cos^2\theta}\right]^2} \tag{5.44}$$

Due to the conservation of the momentum parallel to the surface

$$E \sin^2\theta = (E - \chi) \sin^2\vartheta \,. \tag{5.45}$$

As a consequence

$$\cos^2\theta = \frac{(E - \chi)\cos^2\vartheta + \chi}{E} \,, \tag{5.46}$$

$$\cos^2\vartheta = \frac{E\cos^2\theta - \chi}{E - \chi} \,. \tag{5.47}$$

In conclusion, the transmission coefficient T is given, as a function of ϑ, by

$$T = \frac{4\sqrt{1 - \chi/[(E - \chi)\cos^2\vartheta + \chi]}}{\left\{1 + \sqrt{1 - \chi/[(E - \chi)\cos^2\vartheta + \chi]}\right\}^2} \,, \tag{5.48}$$

and, as a function of θ,

$$T = \frac{4\sqrt{1 - \chi/(E\cos^2\theta)}}{\left[1 + \sqrt{1 - \chi/(E\cos^2\theta)}\right]^2} \,. \tag{5.49}$$

Transmission Coefficient and Monte Carlo method. The transmission coefficient is an important quantity for the Monte Carlo description of low energy electrons emerging from the surface of a solid: the code generates a random number, μ_7,

uniformly distributed in the range [0, 1] and permits the electron to be emitted into the vacuum if the condition

$$\mu_7 < T \tag{5.50}$$

is satisfied. Those electrons which, once reached the surface, cannot satisfy the condition to emerge, are specularly reflected back into the bulk of the specimen without energy loss and can contribute to the generation of further secondary electrons.

5.2.8 *Inelastic Scattering Linkage to the Distance from the Surface*

In order to describe the surface plasmon loss peaks that can be observed in reflection electron energy loss spectroscopy when primary electron energy is smaller than ∼1000 eV, it is necessary to take into account that the inelastic scattering depends on the distance from the surface (in the solid and in vacuum) and on the angle of surface crossing (see Figs. 3.18 and 3.19). The consequence is that, in the Monte Carlo simulation, the sampling of the energy loss previously discussed (see Fig. 5.2) is no longer sufficient. If we wish to describe the surface phenomena, cumulative probabilities for inelastic collisions of electrons have to be calculated not only as a function of the energy loss W but also as a function of the distance from the surface. Furthermore, since in the Chen and Kwei and Li et al. [13, 14] theory also the vacuum (close to the surface) contributes to inelastic scattering, cumulative probabilities have to be calculated in the vacuum as well [15, 16]. In Fig. 5.3 the cumulative probability for inelastic collisions of electrons in Si is represented as a function of the energy loss for few selected distances from the surface – in the case of incoming electrons inside the solid. Note that, as z approaches ∞, the curves shown in Fig. 5.3 approach the "bulk" curve in Fig. 5.2.

In order to include in the Monte Carlo code the information that the electron inelastic mean free path explicitly depends on z, also the sampling procedure for the electron length between the successive scattering events has to be accordingly modified. Let us assume that the distribution function, $p_\chi(s)$, has the form [17]:

$$p_\chi(s) = \frac{1}{\lambda(s)} \exp\left[-\int_0^s \frac{ds'}{\lambda(s')}\right], \tag{5.51}$$

For a comparison, see Eq. (4.7), valid when λ does not depend on the depth.

Since this equation is difficult to solve, according to Ding and Shimizu [17] the following procedure can be followed to calculate z. The first step is to put $z = z_\mathrm{i}$, where z_i is the z component of the electron current position. If λ_min represents the minimum value of the mean free path (the inelastic one when the particle is in vacuum and, when it is in the material, calculated taking also into account the elastic mean free path), the second step involves the generation of two independent random numbers,

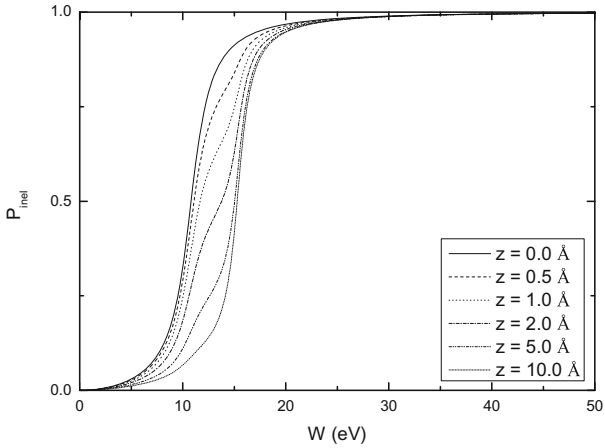

Fig. 5.3 Sampling of the energy loss for electrons in silicon. P_{inel} is the cumulative probability for inelastic collisions of electrons in Si (calculated according to the Chen and Kwei theory [13, 14]) causing energy losses less than or equal to W. The cumulative probability is represented as a function of the energy loss for few selected distances from the surface in the case of incoming electrons inside the solid. Similar curves can be calculated for incoming electrons outside the solid, outgoing electrons inside the solid, and outgoing electrons outside the solid. $E_0 = 1000\,\text{eV}$

μ_8 and μ_9, uniformly distributed in the range [0, 1]. A new value of z is calculated by the equation:

$$z = z_i - \cos\theta\,\lambda_{\min}\,\ln\mu_8\,. \tag{5.52}$$

If $\mu_9 \leq \lambda_{\min}/\lambda$, then the new value of z is accepted; otherwise we put $z = z_i$ (i.e., z is now considered as the new z component of the initial position), two new random numbers μ_8 and μ_9 are generated, and a new value of z is calculated according to Eq. (5.52).

Recent theoretical calculations and Monte Carlo results concerning surface and bulk plasmon loss peaks show a very good agreement with the available experimental data [17–27]. The agreement, in particular, between Monte Carlo simulated and experimental data is very good even on an absolute scale [17, 25, 26].

5.2.9 End of the Trajectory and Number of Trajectories

As for the case of the continuous-slowing-down approximation, described in the previous section, each electron is followed until its energy becomes lower than a given agreed threshold or until it emerges from the target surface. If, for example, we are studying the plasmon losses, the electrons can be followed until their energy becomes smaller than $E_0 - 150$ eV, as typically all the plasmon losses can be found

in the energy ranges from $E_0 - 150$ eV to E_0 (where we have indicated with E_0 the primary energy expressed in eV). If, instead, we are facing the problem of simulating the secondary electron energy distribution, the electrons must be followed until they reach a very small minimum energy (virtually equal to 0, even if a few eV can in some cases be considered acceptable.)

The number of trajectories is also a very important parameter. In this work, the typical number of trajectories, using the energy-straggling strategy for simulating spectra of energy distributions, ranges from 10^7 to 10^9.

5.3 Summary

In this chapter, the Monte Carlo method for the study of the transport of electrons in solid targets has been briefly described. Its main features and characteristics have been summarized, considering in particular two different strategies: one based on the so-called continuous-slowing-down approximation, the other one on a scheme that takes into account the energy straggling, i.e., the statistical fluctuations of the energy losses. Electron-atom, electron-electron, electron-phonon, and electron-polaron interactions have been considered with all the relating effects, both in term of energy losses and scattering angles.

References

1. T. Kobayashi, H. Yoshino, S. Horiguchi, M. Suzuki, Y. Sakakibara, Appl. Phys. Lett. **39**, 512 (1981)
2. G. Messina, A. Paoletti, S. Santangelo, A. Tucciarone, La Rivista del Nuovo Cimento **15**, 1 (1992)
3. J.F. Perkins, Phys. Rev. **126**, 1781 (1962)
4. M. Dapor, Phys. Rev. B **46**, 618 (1992)
5. R. Shimizu, D. Ze-Jun, Rep. Prog. Phys. **55**, 487 (1992)
6. R.H. Ritchie, Phys. Rev. **106**, 874 (1957)
7. H. Fröhlich, Adv. Phys. **3**, 325 (1954)
8. J.P. Ganachaud, A. Mokrani, Surf. Sci. **334**, 329 (1995)
9. H. Bichsel, Nucl. Instrum. Methods Phys. Res. B **52**, 136 (1990)
10. J. Llacer, E.L. Garwin, J. Appl. Phys. **40**, 2766 (1969)
11. M. Dapor, Nucl. Instrum. Methods Phys. Res. B **267**, 3055 (2009)
12. P. Kazemian, Progress towards Quantitive Dopant Profiling with the Scanning Electron Microscope (Doctorate Dissertation, University of Cambridge, 2006)
13. Y.F. Chen, C.M. Kwei, Surf. Sci. **364**, 131 (1996)
14. Y.C. Li, Y.H. Tu, C.M. Kwei, C.J. Tung, Surf. Sci. **589**, 67 (2005)
15. A. Jablonski, C.J. Powell, Surf. Sci. **551**, 106 (2004)
16. M. Dapor, L. Calliari, S. Fanchenko, Surf. Interface Anal. **44**, 1110 (2012)
17. Z.-J. Ding, R. Shimizu, Phys. Rev. B **61**, 14128 (2000)
18. M. Novák, Surf. Sci. **602**, 1458 (2008)
19. M. Novák, J. Phys. D Appl. Phys. **42**, 225306 (2009)
20. H. Jin, H. Yoshikawa, H. Iwai, S. Tanuma, S. Tougaard, e-J. Surf. Sci. Nanotech. **7**, 199 (2009)

21. H. Jin, H. Shinotsuka, H. Yoshikawa, H. Iwai, S. Tanuma, S. Tougaard, J. Appl. Phys. **107**, 083709 (2010)
22. I. Kyriakou, D. Emfietzoglou, R. Garcia-Molina, I. Abril, K. Kostarelos, J. Appl. Phys. **110**, 054304 (2011)
23. B. Da, S.F. Mao, Y. Sun, Z.J. Ding, e-J. Surf. Sci. Nanotechnol. **10**, 441 (2012)
24. B. Da, Y. Sun, S.F. Mao, Z.M. Zhang, H. Jin, H. Yoshikawa, S. Tanuma, Z.J. Ding, J. Appl. Phys. **113**, 214303 (2013)
25. F. Salvat-Pujol, Secondary-electron emission from solids: Coincidence experiments and dielectric formalism (Doctorate Dissertation, Technischen Universität Wien, 2012)
26. F. Salvat-Pujol, W.S.M. Werner, Surf. Interface Anal. **45**, 873 (2013)
27. T. Tang, Z.M. Zhang, B. Da, J.B. Gong, K. Goto, Z.J. Ding, Physica B **423**, 64 (2013)

Chapter 6
Backscattering Coefficient

The backscattered electron (BSE) emission coefficient is defined as the fraction of electrons of the primary beam emerging from the surface of an electron-irradiated target. Secondary electrons, generated in the solid by a cascade process of extraction of the atomic electrons, are not included in the definition of the backscattering coefficient. The energy cut-off is typically 50 eV. In other words, in a typical SEM experiment aimed at measuring the fraction of backscattered electrons, investigators consider as backscattered all the electrons emerging from the surface of the target with energies higher than the cut-off energy (50 eV), while all the electrons emerging with energies lower than this conventional cut-off are considered as secondary. Of course, secondary electrons with energy higher than any predefined cut-off energy and backscattered electrons with energy lower than such a cut-off also exist. If the primary energy of the incident electron beam is not too low (higher than $\approx$200–300 eV), the introduction of the 50 eV energy cut-off is generally considered as a good approximation, and it will be therefore adopted in this chapter. This choice is particularly useful, as we are interested in comparing the Monte Carlo results to experimental data that can be found in the literature, where the 50 eV energy cut-off approximation has been widely (always, actually) used.

6.1 Electrons Backscattered from Bulk Targets

When an electron beam impinges upon a solid target, some electrons of the primary beam are backscattered and re-emerge from the surface. We already know that the backscattering coefficient is defined as the fraction of the electrons of the incident beam which emerge from the surface with energy higher than 50 eV. This definition is very convenient and useful from the experimental point of view; it is also quite accurate, as the fraction of secondary electrons (i.e., the electrons extracted from the atoms of the target and able to reach the surface and emerge) with energy higher than 50 eV is negligible for any practical purpose, as is the fraction of backscattered electrons emerging with energy lower than 50 eV.

M. Dapor, *Transport of Energetic Electrons in Solids*,
Springer Tracts in Modern Physics 257, DOI 10.1007/978-3-319-47492-2_6

The backscattering coefficient of electrons in bulk targets has been studied both experimentally and theoretically. Many data, both experimental and theoretical, are available for energies higher than 5–10 keV [1, 2]. The case of energies lower than 5 keV has been investigated too, but not many experimental data are available. Furthermore, not all the authors agree about the behavior of the low energy backscattering coefficient; in particular there are very few data concerning the case in which the electron energy approaches 0. Some investigators have suggested, on the basis of experimental evidences, that the absorption coefficient should approach 0 and the backscattering coefficient should approach 1, as the energy approaches 0 [3, 4].

6.1.1 *The Backscattering Coefficient of C and Al Calculated by Using the Dielectric Theory (Ashley Stopping Power)*

If we cannot confirm that the backscattering coefficient reaches 1 as the energy approaches 0, the simulated data concerning C and Al show a general trend of the backscattering coefficient as a function of the primary energy that is consistent with this hypothesis. We have actually observed that, as the energy decreases from 10 keV to 250 eV, the simulations show that the backscattering coefficient of both C and Al increases.

In Fig. 6.1 we show the trend of the backscattering coefficient as a function of the electron beam primary energy for electrons impinging upon bulk targets of C and

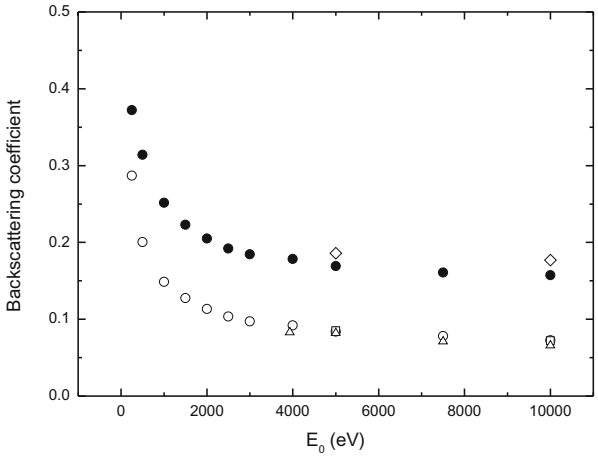

Fig. 6.1 Monte Carlo simulation of the trend of the backscattering coefficient η as a function of the electron beam primary energy E_0 for electrons impinging upon bulk targets of C (*empty circles*) and Al (*filled circles*). The stopping power was taken from Ashley [5] (dielectric theory). *Boxes* Bishop experimental data for C [6]. *Diamonds* Bishop experimental data for Al [6]. *Triangles* Hunger and Kükler experimental data for C [7]

Al as calculated by our Monte Carlo code. For the simulations presented here, the continuous-slowing-down approximation was adopted, and we calculated the stopping power by using the Ashley's recipe [5] (within the Ritchie dielectric theoretical scheme [8]). As everywhere in this book, the elastic scattering cross-section was calculated using the relativistic partial wave expansion method (Mott theory) [9]. The experimental data of Bishop [6] and Hunger and Kükler [7] are also presented in Fig. 6.1 for evaluating the accuracy of the Monte Carlo simulation.

In the case of both the examined elements, the backscattering coefficient increases as the energy decreases towards 250 eV.

6.1.2 *The Backscattering Coefficient of Si, Cu, and Au Calculated by Using the Dielectric Theory (Tanuma et al. Stopping Power)*

In Tables 6.1, 6.2, and 6.3 our Monte Carlo simulated data (for the backscattering coefficient of Si, Cu, and Au, respectively) are compared with the available experimental data (taken from Joy's database [10]). The Monte Carlo results were obtained using the stopping power taken from Tanuma et al. [11] (whithin the Ritchie dielectric theory [8]) for describing the inelastic processes, and the Mott theory [9] for describing the elastic scattering.

From these tables, one can observe that the backscattering coefficient is a decreasing function of the primary energy with the exception of gold, which presents an increasing trend as the energy increases in the range 1000–2000 eV. It is worth noting that the issue of the behavior of the backscattering coefficient at low primary energy is quite controversial. The reasons for the discrepancies between Monte Carlo and experimental data concerning the backscattering coefficient of low primary energy electrons, are not completely clear and deserve further investigations [16, 17]. Also,

Table 6.1 Backscattering coefficient of Si as a function of the electron primary kinetic energy. The elastic scattering cross-section was calculated using the Mott theory [9]. Continuous-slowing-down approximation was used; the stopping power was taken from Tanuma et al. [11] (dielectric theory). Comparison between the present Monte Carlo simulated results and the available experimental data (taken from Joy's database [10])

Energy (eV)	Monte Carlo	Bronstein and Fraiman [12]	Reimer and Tolkamp [13]
1000	0.224	0.228	0.235
2000	0.185	0.204	–
3000	0.171	0.192	0.212
4000	0.169	0.189	–
5000	0.162	–	0.206

Table 6.2 Backscattering coefficient of Cu as a function of the electron primary kinetic energy. The elastic scattering cross-section was calculated using the Mott theory [9]. Continuous-slowing-down approximation was used; the stopping power was taken from Tanuma et al. [11] (dielectric theory). Comparison between the present Monte Carlo simulated results and the available experimental data (taken from Joy's database [10])

Energy (eV)	Monte Carlo	Bronstein and Fraiman [12]	Koshikawa and Shimizu [14]	Reimer and Tolkamp [13]
1000	0.401	0.381	0.430	–
2000	0.346	0.379	0.406	–
3000	0.329	0.361	0.406	0.311
4000	0.317	0.340	–	–
5000	0.314	–	0.398	0.311

Table 6.3 Backscattering coefficient of Au as a function of the electron primary kinetic energy. The elastic scattering cross-section was calculated using the Mott theory [9]. Continuous-slowing-down approximation was used; the stopping power was taken from Tanuma et al. [11] (dielectric theory). Comparison between the present Monte Carlo simulated results and the available experimental data (taken from Joy's database [10])

Energy(eV)	Monte Carlo	Bronstein and Fraiman [12]	Reimer and Tolkamp [13]	Böngeler et al. [15]
1000	0.441	0.419	–	–
2000	0.456	0.450	–	0.373
3000	0.452	0.464	0.415	0.414
4000	0.449	0.461	–	0.443
5000	0.446	–	0.448	0.459

not all the experiments agree about the behavior of the low-energy backscattering coefficient in the range 1–3 keV [10].

6.2 Electrons Backscattered from One Layer Deposited on Semi-infinite Substrates

It is well known that over-layer films affect the electron backscattering coefficient of bulk targets. The experimental data available in the literature for backscattering coefficient are rather sparse and, sometimes, difficulties arise in their interpretation due to the lack of knowledge of the thickness, uniformity, and nature of the surface layers. In particular, a quantitative treatment of the effect of surface films deposited on bulk targets and a systematic comparison with experimental data are not available at the time being. The main ingredient of the present approach is the evaluation of the backscattered electron emission coefficient — that results from the interplay

between average atomic number and interaction volume — as compared to the actual thickness of the over-layer [18–21].

6.2.1 Carbon Overlayers (Ashley Stopping Power)

Let's start with the study of the low energy backscattering coefficient for the special case of layers of carbon deposited on aluminum [18].

Carbon films are deposited on various substrates (polymers, polyester fabrics, polyester yarns, metal alloys) both for experimental and technological motivations. There are a lot of technological uses of carbon films, as carbon characteristics are very useful in many fields. Carbon films deposited on polymeric substrates can be used to replace the metallic coatings on plastic materials used for food packaging. Carbon films are also widely employed in medical devices. Biomedical investigators have demonstrated that permanent thin films of pure carbon show an excellent haemo/biocompatibility: they are used, in particular, as coating for the stainless steel stents to be implanted in coronary arteries.

When investigating the behavior of the backscattering coefficient as a function of the primary energy for various film thicknesses, the appearance, for carbon film thicknesses exceeding ~100 Å on aluminum, of relative minima can be observed. These features are presented in Fig. 6.2 for a carbon film 400 Å -thick and in Fig. 6.3 for a carbon film 800 Å -thick. The backscattering coefficient reaches a relative minimum and then increases up to the aluminum backscattering coefficient. It then follows the decreasing trend typical of the backscattering coefficient of aluminum. An interesting characteristic of the relative minima is that their position shifts towards higher energies as the film thickness increases. This is quite reasonable because one expects that, in some way, the backscattering coefficient of the system should approach the behavior of the backscattering coefficient of aluminum for very thin carbon films and should approach the energy dependence of the backscattering coefficient of carbon for thick carbon films. So, as the film thickness increases, the positions of the relative minima shift towards higher energies while the peaks broaden.

The linear best fit of the behaviour of the Monte Carlo simulated position of the relative minimum $E_{\min}$ (in eV) of the backscattering curve as a function of the film thickness t (in Å)—for C thin films deposited on an Al substrates in the range 100–1000 Å–is given by $E_{\min} = m\,t + q$, where $m = (2.9 \pm 0.1)$ eV/Å and $q = (900 \pm 90)$ eV [22].

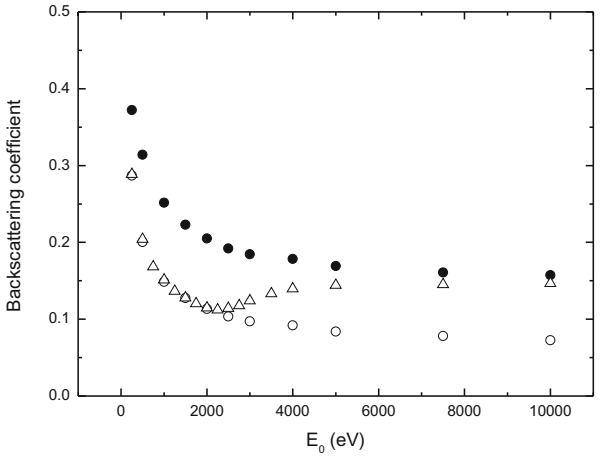

Fig. 6.2 *Triangles*: Monte Carlo simulation of the electron backscattering coefficient η for a carbon film 400 Å thick as a function of the beam primary energy E_0. *Empty circles* Monte Carlo backscattering coefficient of pure C. *Filled circles* Monte Carlo backscattering coefficient of pure Al. The stopping power was taken from Ashley [5] (dielectric theory)

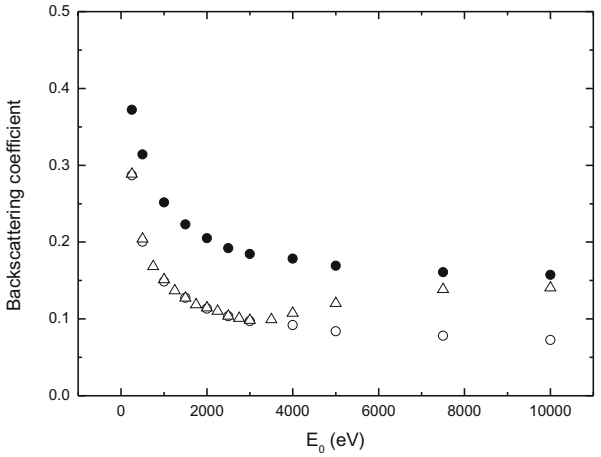

Fig. 6.3 *Triangles*: Monte Carlo simulation of the electron backscattering coefficient η for a carbon film 800 Å thick as a function of the beam primary energy E_0. *Empty circles* Monte Carlo backscattering coefficient of pure C. *Filled circles* Monte Carlo backscattering coefficient of pure Al. The stopping power was taken from Ashley [5] (dielectric theory)

6.2.2 *Gold Overlayers (Kanaya and Okayama Stopping Power)*

The behavior described above has been observed both numerically [18–22] and experimentally [20, 21] also for other materials. In all the cases, the backscattering coefficient of the system ranges from the value of the backscattering coefficient of the overlayer (for very low primary energy) to the value of the backscattering coefficient of the substrate (for very high primary energy). In the case of gold deposited on silicon, the backscattering coefficient reaches a relative maximum and then decreases to the silicon backscattering coefficient. In general, the backscattering coefficient of any system should resemble the behavior of the backscattering coefficient of the substrate for very thin films and approach the behavior of the backscattering coefficient of the material constituting the overlayer for thick films. So, as the film thickness increases, the position of the relative maximum (or minimum, depending on the constituting materials of overlayer and substrate) shifts towards higher energies while the peaks broaden [18, 19, 21, 22].

Figures 6.4 and 6.5 display the data points for the experimental backscattering coefficient and the relevant Monte Carlo results for two samples of gold layers deposited on silicon [21]. The nominal thickness of the gold films were, respectively, 250 and 500 Å. Data were normalized by dividing the curves by their respective maxima. The experimental and the Monte Carlo approaches provide similar results.

Similarly to the case of carbon on aluminum, Monte Carlo simulations predict that the energy position of the maximum, E_{max}, linearly depends on the gold overlayer thickness. The linear best fit of E_{max} as a function of the Au film thickness for

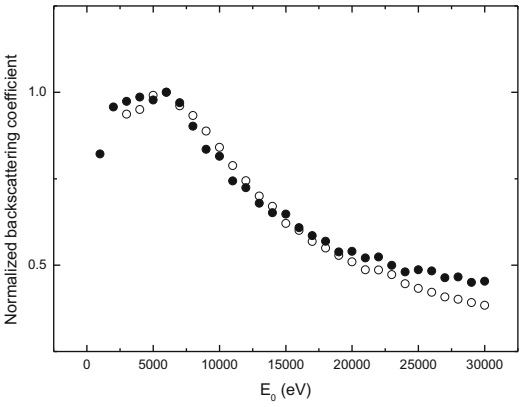

Fig. 6.4 Comparison between normalized experimental and present Monte Carlo backscattering coefficient as a function of the primary electron energy of an Au thin film deposited on a Si substrate [21]. *Empty symbols* experiment. *Filled symbols* Monte Carlo. The Au overlayer nominal thickness is 250 Å. Stopping power was calculated by using the Kanaya and Okayama semi-empiric formula [23]. Layer deposition: *courtesy* of Michele Crivellari. Experimental data: *courtesy* of Nicola Bazzanella and Antonio Miotello

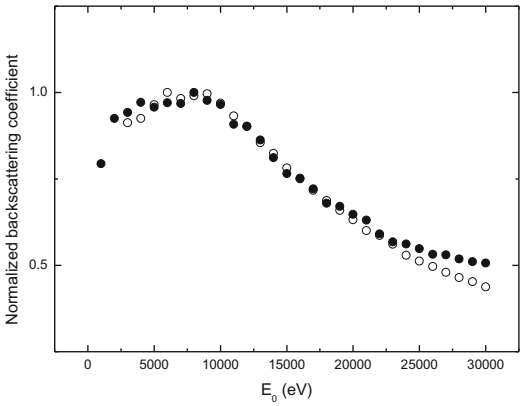

Fig. 6.5 Comparison between normalized experimental and present Monte Carlo backscattering coefficient as a function of the primary electron energy of an Au thin film deposited on a Si substrate [21]. *Empty symbols* experiment. *Filled symbols* Monte Carlo. The Au overlayer nominal thickness is 500 Å. Stopping power was calculated by using the Kanaya and Okayama semi-empiric formula [23]. Layer deposition: *courtesy* of Michele Crivellari. Experimental data: *courtesy* of Nicola Bazzanella and Antonio Miotello

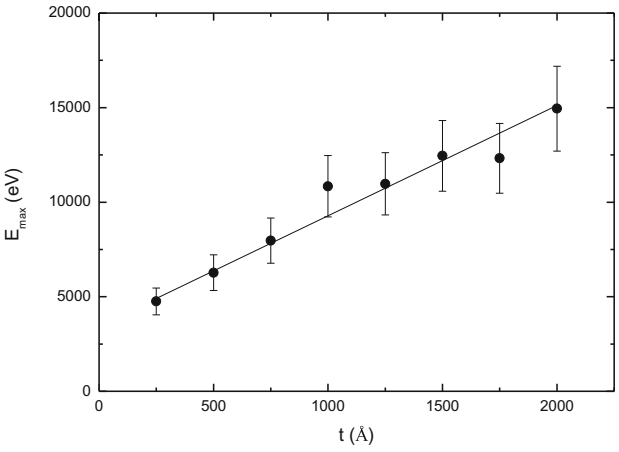

Fig. 6.6 Linear best fit of Monte Carlo simulated $E_{\max}$ (in eV) as a function of the film thickness t (in Å) for Au thin films deposited on a Si substrates in the range 250 Å-2000 Å [21]. $E_{\max} = m\,t + q$, where $m = 5.8$ eV/Å (standard error = 0.4 eV/Å) and $q = 3456$ eV (standard error = 373 eV) [21]

Au/Si systems is presented in Fig. 6.6 demonstrating that the Monte Carlo method makes it possible to evaluate the overlayer film thickness with nearly 20% uncertainty (estimated from the statistical fluctuations in the energy maximum) [21].

In view of the non-destructiveness, the proposed approach is definitely adding new potentiality to SEM-based experimental methods.

6.3 Electrons Backscattered from Two Layers Deposited on Semi-infinite Substrates

We are now interested in the calculation of the backscattering coefficient from two layers of different materials and thicknesses deposited on semi-infinite substrates. In particular, we will examine the backscattering from Cu/Au/Si and C/Au/Si systems.

In Fig. 6.7, Monte Carlo electron backscattering coefficient of Cu/Au/Si samples is represented. The Monte Carlo simulation code considers the Si substrate as a semi-infinite bulk, while the thickness of the intermediate Au layer is set at 500 Å. The behavior of η as a function of the primary energy, in the 1000–25000 eV range, is represented for different values of the Cu first layer thickness, in the 250–1000 Å range. Stopping power is calculated using the dielectric response theory.

Figure 6.8 shows the same quantities, obtained with the same conditions and calculated with the Monte Carlo code based on the Kanaya and Okayama semi-empiric formula.

The general trends obtained with the two codes are in good qualitative agreement: both codes predict that the general structure of the curves presents a minimum and a maximum. Furthermore both the minimum and the maximum shift towards higher primary energies as the Cu first layer thickness increases. Thus, this behavior is typical of the particular combination of the selected materials and of their thicknesses.

In order to further investigate and better understand the effects of layer thickness, in Figs. 6.9 and 6.10 the Monte Carlo backscattering coefficients, obtained with the dielectric response and the semi-empiric approach, respectively, have been repre-

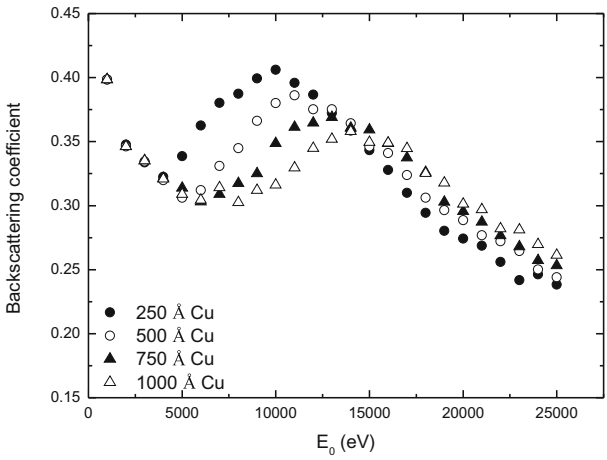

Fig. 6.7 Present Monte Carlo simulation of electron backscattering coefficient η of Cu/Au/Si samples. The Si substrate is semi-infinite, while the thickness of the intermediate Au layer is 500 Å. The behavior of η as a function of the primary energy is represented for different values of the Cu first layer thickness. Stopping power is calculated using the dielectric response theory

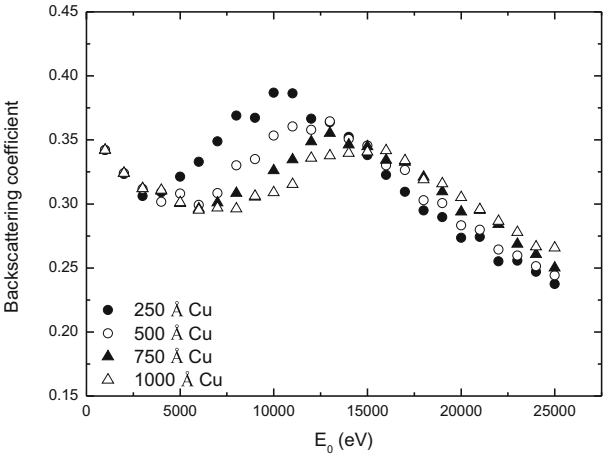

Fig. 6.8 Present Monte Carlo simulation of electron backscattering coefficient η of Cu/Au/Si samples. The Si substrate is semi-infinite, while the thickness of the intermediate Au layer is 500 Å. The behavior of η as a function of the primary energy is represented for different values of the Cu first layer thickness. Stopping power is calculated using the Kanaya and Okayama semi-empiric formula

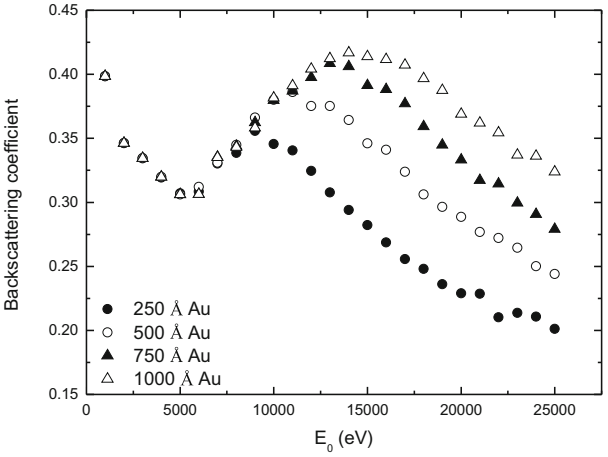

Fig. 6.9 Present Monte Carlo simulation of electron backscattering coefficient η of Cu/Au/Si samples. The Si substrate is semi-infinite, while the thickness of the first Cu layer is 500 Å. The behavior of η as a function of the primary energy is represented for different values of the Au intermediate layer thickness. Stopping power is calculated using the dielectric response theory

sented for the case in which the thickness of the first Cu layer is fixed (500 Å) while the intermediate Au film thickness ranges in the 250–1000 Å interval. Also in this case, the general behaviors obtained with the two approaches are in good qualitative agreement. The characteristic features present a trend different with respect to

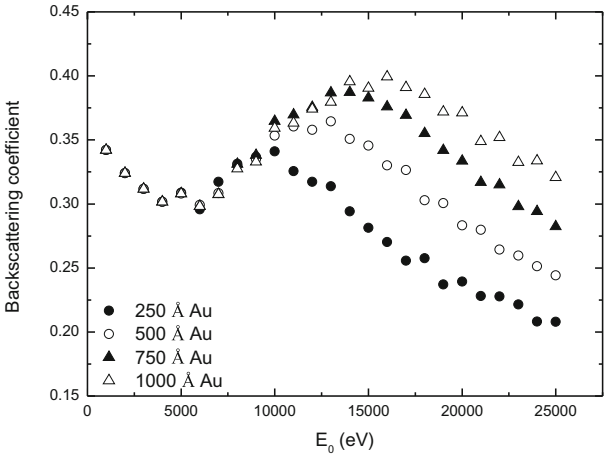

Fig. 6.10 Present Monte Carlo simulation of electron backscattering coefficient η of Cu/Au/Si samples. The Si substrate is semi-infinite, while the thickness of the first Cu layer is 500 Å. The behavior of η as a function of the primary energy is represented for different values of the Au intermediate layer thickness. Stopping power is calculated using the Kanaya and Okayama semi-empiric formula

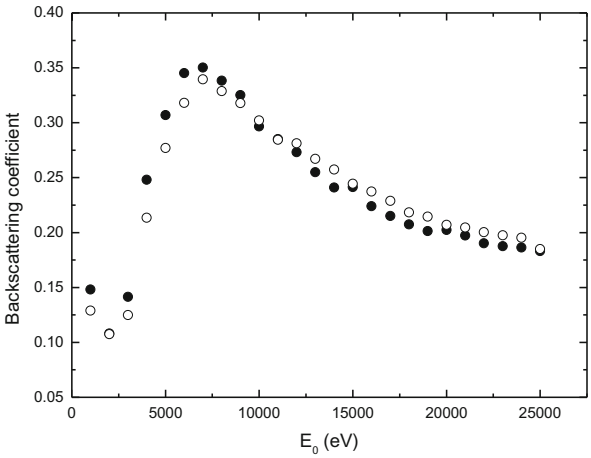

Fig. 6.11 Present Monte Carlo simulation of electron backscattering coefficient η of C/Au/Si samples. The Si substrate is semi-infinite, the thickness of the first C layer is 500 Å, and that of the intermediate Au layer is 250 Å. Backscattering coefficients η obtained using the dielectric response theory (*filled symbols*) and the semi-empiric Kanaya and Okayama approach (*empty symbols*), respectively, for calculating the stopping power, are compared

the previous one: while the position of the maximum shifts toward higher primary energies as the intermediate film thickness increases, the position of the minimum remains practically unchanged.

In order to study the agreement between the two codes, Figs. 6.11, 6.12 and 6.13 compare the calculation of the backscattering coefficients for various combinations of materials and thicknesses, obtained using the two Monte Carlo programs. The codes give practically indistinguishable results for the cases corresponding to the C/Au/Si

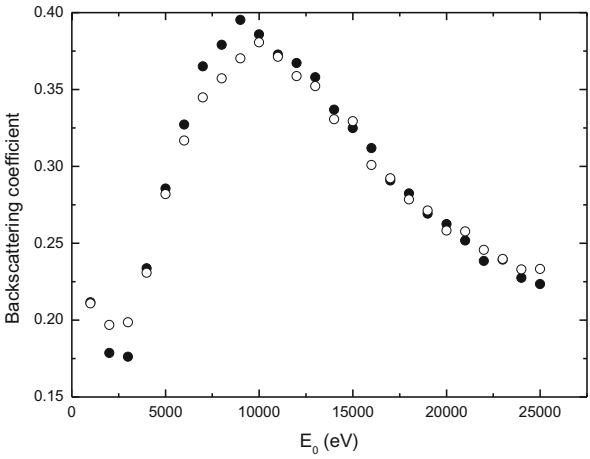

Fig. 6.12 Present Monte Carlo simulation of electron backscattering coefficient η of Al/Au/Si samples. The Si substrate is semi-infinite, the thickness of the first Al layer is 500 Å, and that of the intermediate Au layer is 500 Å. Backscattering coefficients η obtained using the dielectric response theory (*filled symbols*) and the semi-empiric Kanaya and Okayama approach (*empty symbols*), respectively, for calculating the stopping power, are compared

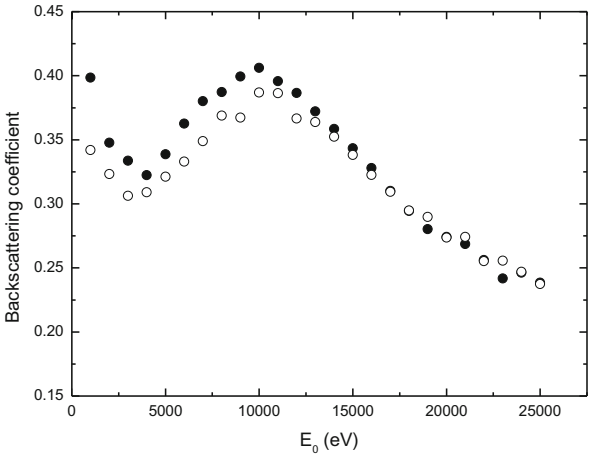

Fig. 6.13 Present Monte Carlo simulation of electron backscattering coefficient η of Cu/Au/Si samples. The Si substrate is semi-infinite, the thickness of the first Cu layer is 250 Å, and that of the intermediate Au layer is 500 Å. Backscattering coefficients η obtained using the dielectric response theory (*filled symbols*) and the semi-empiric Kanaya and Okayama approach (*empty symbols*), respectively, for calculating the stopping power, are compared

combination, while some difference can be observed, for the lowest energies, in the case of the Cu/Au/Si combinations.

6.4 A Comparative Study of Electron and Positron Backscattering Coefficients and Depth Distributions

To conclude this chapter, we will compare the Monte Carlo simulations of the backscattering coefficients and the depth distributions of electrons and positrons. Just to provide an example, we will consider the case of penetration of electrons and positrons in silicon dioxide. The presented results were obtained using the Ashley

theory for calculating the stopping power and the Mott cross-section for the computation of the differential elastic scattering cross-section [24].

The differences in the inelastic and elastic scattering cross-sections of low energy electrons and positrons, discussed in Chap. 3 and in Chap. 11, explain the results presented in Fig. 6.14. The depth profiles of electrons and positrons are different even for the highest energy examined (10 keV), for each particle reduces its energy during its travel in the solid, reaching the low values corresponding to significant differences in the cross-sections and stopping powers of electrons and positrons.

Indicating with $R(E_0)$ the maximum penetration range, for any given energy E_0, R can be easily determined by the curves in Fig. 6.14. From the presented depth profiles it is clear that the maximum penetration range in silicon dioxide is approximately the same for electrons and positrons, in the examined primary energy range.

For each primary energy E_0, the integration of the function $P(z)$ from $z = 0$ to $z = R$ gives the absorption coefficient $1 - \eta(E_0)$, where we indicated with $\eta(E_0)$ the backscattering coefficient. As the primary energy increases, the differences in the depth distributions of electrons and positrons grow smaller. While the maximum ranges of electrons and positrons are similar, the backscattering coefficients present very different trends (see Fig. 6.15). The positron backscattering coefficient does not depend on the primary energy and is always smaller than the electron backscattering coefficient. Instead, the electron backscattering coefficient is a decreasing function of the primary energy.

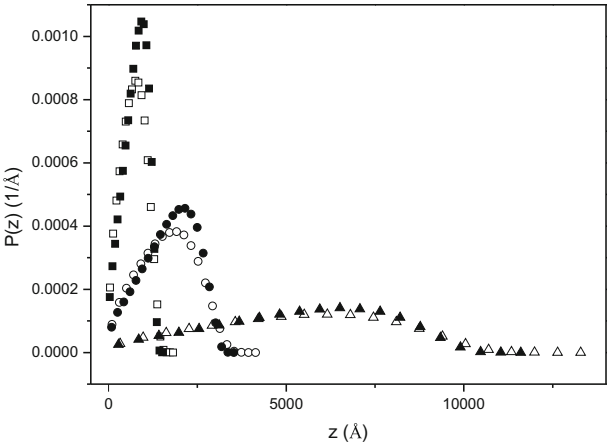

Fig. 6.14 Monte Carlo simulation of the depth profiles $P(z)$ of electrons (*empty symbols*) and positrons (*filled symbols*) in SiO_2 as a function of the depth inside the solid measured from the surface, z. E_0 is the primary energies of the particles. 3 keV (*squares*), 5 keV (*circles*) and 10 keV (*triangles*)

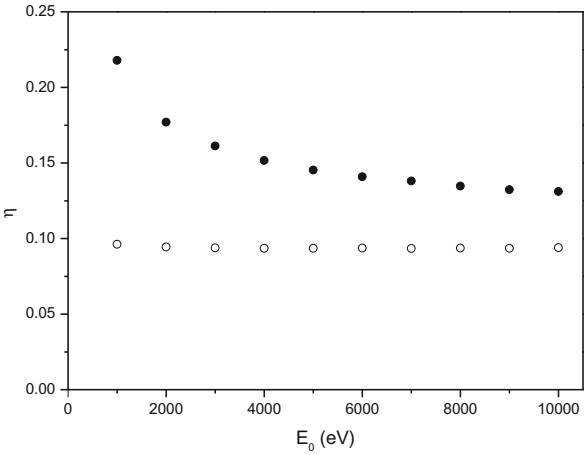

Fig. 6.15 Monte Carlo simulation of the backscattering coefficient η of electrons (*filled symbols*) and positrons (*empty symbols*) in SiO_2 as a function of the primary energy E_0

6.5 Summary

In this chapter, the Monte Carlo method was used for evaluating the backscattering coefficient of electrons (and positrons) impinging upon bulks and overlayers. In particular, for the case of surface films, it was calculated as a function of the thicknesses of the layers, their nature, and the electron primary energy. The code used in this chapter, utilizes the Mott cross-section for elastic scattering calculation and the continuous-slowing-down approximation for energy loss simulation. For the calculation of the stopping power, the Ritchie dielectric response theory [8] and the analytic semi-empirical formula proposed by Kanaya and Okayama [23] were used. Electron backscattering coefficients from several different combinations of layers and substrates were simulated. The main features of the backscattering coefficient as a function of the electron primary energy, which are represented by minima and maxima whose positions in energy depend on the particular combination of materials and thicknesses, are reproduced in similar ways using the two different stopping powers. The last section of this chapter presented a comparative study of electron and positron depth distributions and backscattering coefficients.

References

1. M. Dapor, Phys. Rev. B **46**, 618 (1992)
2. M. Dapor, *Electron-Beam Interactions with Solids: Application of the Monte Carlo Method to Electron Scattering Problems* (Springer, Berlin, 2003)
3. R. Cimino, I.R. Collins, M.A. Furman, M. Pivi, F. Ruggiero, G. Rumolo, F. Zimmermann, Phys. Rev. Lett. **93**, 014801 (2004)
4. M.A. Furman, V.H. Chaplin, Phys. Rev. Spec. Top. Accel. Beams **9**, 034403 (2006)
5. J.C. Ashley, J. Electron Spectrosc. Relat. Phenom. **46**, 199 (1988)

6. H.E. Bishop, Proc. 4ème Congrès International d'Optique des Rayons X et de Microanalyse pp. 153–158 (1967)
7. H.J. Hunger, L.G. Küchler, Phys. Status Solidi A **56**, K45 (1979)
8. R.H. Ritchie, Phys. Rev. **106**, 874 (1957)
9. N.F. Mott, Proc. R. Soc. Lond. Ser. **124**, 425 (1929)
10. D.C. Joy, (2008). http://web.utk.edu/srcutk/htm/interact.htm
11. S. Tanuma, C.J. Powell, D.R. Penn, Surf. Interface Anal. **37**, 978 (2005)
12. I.M. Bronstein, B.S. Fraiman, *Vtorichnaya Elektronnaya Emissiya* (Nauka, Moskva, 1969)
13. L. Reimer, C. Tolkamp, Scanning **3**, 35 (1980)
14. T. Koshikawa, R. Shimizu, J. Phys. D. Appl. Phys. **6**, 1369 (1973)
15. R. Böngeler, U. Golla, M. Kussens, R. Reimer, B. Schendler, R. Senkel, M. Spranck, Scanning **15**, 1 (1993)
16. J. Ch, Kuhr, H.J. Fitting, Phys. Status Solidi A **172**, 433 (1999)
17. M.M. El Gomati, C.G. Walker, A.M.D. Assa'd, M. Zadražil, Scanning **30**, 2 (2008)
18. M. Dapor, J. Appl. Phys. **95**, 718 (2004)
19. M. Dapor, Surf. Interface Anal. **40**, 714 (2008)
20. M. Dapor, N. Bazzanella, L. Toniutti, A. Miotello, S. Gialanella, Nucl. Instrum. Methods Phys. Res. B **269**, 1672 (2011)
21. M. Dapor, N. Bazzanella, L. Toniutti, A. Miotello, M. Crivellari, S. Gialanella, Surf. Interface Anal. **45**, 677 (2013)
22. M. Dapor, Surf. Interface Anal. **38**, 1198 (2006)
23. K. Kanaya, S. Okayama, J. Phys. D. Appl. Phys. **5**, 43 (1972)
24. M. Dapor, J. Electron Spectrosc. Relat. Phenom. **151**, 182 (2006)

Chapter 7
Secondary Electron Yield

Electron beams impinging upon solid targets induce the emission of secondary electrons (SE). These are the electrons extracted from the atoms in the solid due to the inelastic electron-atom interaction with electrons of the incident beam or with the other secondary electrons travelling in the solid. Some secondary electrons, after a number of elastic and inelastic interactions with the atoms in the solid, reach the solid surface satisfying the conditions to emerge from it. As we already know, the spectrum of the secondary electrons is contaminated by a contribution of the backscattered primary electrons. As this contamination can be safely neglected in the great majority of the practical situations that investigators encounter in the laboratory experiments, this effect is usually ignored, at least as a first approximation.

In this chapter the attention will be focused on the purely secondary electrons. The process of secondary-electron emission can be divided into two phenomena. The first one concerns the generation of secondary electrons as a consequence of the interaction between the incident electron beam and electrons bound in the solid. The second one is represented by the *cascade*, where the secondary electrons diffusing in the solid extract new secondary electrons generating a shower of electrons. As each secondary electron loses energy while traveling in the solid, the whole process proceeds until the energy of the secondary electron is no more sufficient to extract further secondary electrons or until it reaches the surface with enough energy to emerge. The number of the emitted secondary electrons divided by the number of the incident electrons is called *secondary electron emission yield*. The secondary electron emission yield is measured as the integral of the secondary electron energy distribution over the energy range from 0 to 50 eV. Secondary electron emission plays a fundamental role in scanning electron microscope imaging.

M. Dapor, *Transport of Energetic Electrons in Solids*,
Springer Tracts in Modern Physics 257, DOI 10.1007/978-3-319-47492-2_7

7.1 Secondary Electron Emission

In this chapter, secondary electron emission from polymethyl methacrylate (PMMA) and aluminum oxide (Al_2O_3) will be modeled quantitatively using the Monte Carlo code. This chapter is aimed at comparing, with the available experimental data, the results of the computational approaches described in the chapter devoted to the main features of the transport Monte Carlo modeling, i.e., the scheme based on the energy-straggling (ES) strategy and the method based on the continuous-slowing-down approximation (CSDA). In this way, it will be possible to understand the validity limits of the methods and to face the question of the CPU time costs in evaluating which approach is more convenient in the different circumstances. We will learn, on the one hand, that the use of the simple continuous-slowing-down approximation for the calculation of the secondary electron yield allows getting an agreement with the experiment similar to the one we can obtain with the more accurate (but CPU time-consuming) energy-straggling strategy. If, on the other hand, energy distribution of the secondary electrons is required, energy-straggling strategy becomes the only choice.

Secondary-electron emission involves very complex phenomena and a numerical treatment requires the detailed knowledge of the main interactions of the electrons with the solid target.

The most important processes that occur in the target are related to the production of individual electron transitions from the valence to the conduction band, to plasmon generation and to the elastic collisions with the screened potentials of the ions in the solids. If its energy is high enough, the electron can be subject to inelastic collisions with inner-shell electrons so that ionization occurs. Secondary electrons of very low energy also interact losing (and gaining) energy with phonons. In insulating materials, they can be trapped in the solid (polaronic effect). Each secondary electron can produce further secondary electrons during its travel inside the solid and, in order to obtain quantitative results, following the whole cascade is the best choice [1–3].

7.2 Monte Carlo Approaches to the Study of Secondary Electron Emission

The Monte Carlo calculation of the secondary electron emission yield can be performed either by taking into account all the details of the many mechanisms of the electron energy loss [1, 3–5] or by assuming a continuous-slowing-down approximation [6–8]. The use of the first approach has stronger physical basis but, due to the detailed description of all the collisions in the secondary electron cascade, it is a very time consuming scheme. The continuous-slowing-down approximation represents instead an approach that saves a lot of CPU time although its physical foundation is more questionable.

We report about the MC simulations of the secondary electron emission from PMMA and Al_2O_3 obtained with the two approaches. These simulations demonstrate that, if we just calculate the yield as a function of the primary energy, the two Monte Carlo schemes give equivalent results for any practical purposes.

The secondary electron yields calculated by means of the two approaches are very close. What is more, the two MC schemes give results in satisfactory agreement with the experiment. This means that, for the calculation of the secondary electron yield, the continuous-slowing-down approximation should be preferred, being much faster (more than ten times) than the more detailed scheme. If, on the other hand, secondary electron energy distributions are required, the continuous-slowing-down approximation cannot be used – for it is not able describe in a realistic way all the energy loss processes – and the detailed scheme becomes mandatory, even if, as far as CPU is concerned, it is much more time consuming [9, 10].

7.3 Specific MC Methodologies for SE Studies

7.3.1 Continuous-Slowing-Down Approximation (CSDA Scheme)

In the case of CSDA, as we know, the step length is calculated according to the equation $\Delta s = -\lambda_{\mathrm{el}} \ln \mu$ – where μ is a random number uniformly distributed in the range [0, 1] – while the energy loss ΔE along the segment of trajectory Δs is approximated by the equation $\Delta E = (dE/ds)\, \Delta s$. Compared to the description we gave in the chapter devoted to the Monte Carlo method, the secondary electron yield calculation using CSDA requires a few more pieces of information.

The secondary electron yield is calculated, according to Dionne [11], Lin and Joy [6], Yasuda et al. [7], and Walker et al. [8] assuming that (i) the number dn of secondary electrons generated along each step length ds, corresponding to the energy loss dE, is given by

$$dn = \frac{1}{\epsilon_{\mathrm{s}}} \frac{dE}{ds}\, ds = \frac{dE}{\epsilon_{\mathrm{s}}} \tag{7.1}$$

where ϵ_{s} is the effective energy necessary to generate a single secondary electron and (ii) the probability $P(z)$ that a secondary electron generated at depth z will reach the surface and emerge from it follows the exponential decay law

$$P(z) = e^{-z/\lambda_{\mathrm{s}}}, \tag{7.2}$$

where λ_{s} is the *effective* escape depth. Thus the secondary electron emission yield is given by

$$\delta = \int P(z)\, dn = \frac{1}{\epsilon_{\mathrm{s}}} \int e^{-z/\lambda_{\mathrm{s}}}\, dE\,. \tag{7.3}$$

7.3.2 Energy-Straggling (ES Scheme)

We have described in a previous chapter the details of the energy straggling strategy, so that we shall just deal with here the features of the scheme specific for the study of secondary electron emission. For further information about the adopted simulation methods, also see Ganachaud and Mokrani [1], Dapor et al. [5], and Dapor [9, 10].

If μ is a random number uniformly distributed in the interval [0, 1], every step length Δs of each electron traveling in the solid is calculated by adopting the Poisson statistics, so that $\Delta s = -\lambda \ln \mu$. In this equation, λ is the electron mean free path including all the scattering mechanisms involved. Its reciprocal, i.e., the so-called inverse inelastic mean free path, can be expressed as the sum total of all the inverse mean free paths of the interactions of the electrons with the target: in particular it is necessary to take into account the inverse mean free path relative to the elastic interactions among the incident electrons and the screened atomic nuclei, λ_{el}^{-1}, the one relative to the inelastic interactions among the incident electrons and the atomic ones, $\lambda_{\text{inel}}^{-1}$, the one relative to the electron-phonon interactions, $\lambda_{\text{phonon}}^{-1}$, and the one relative to the electron-polaron interaction, $\lambda_{\text{pol}}^{-1}$, so that $\lambda^{-1} = \lambda_{\text{el}}^{-1} + \lambda_{\text{inel}}^{-1} + \lambda_{\text{phonon}}^{-1} + \lambda_{\text{pol}}^{-1}$. If the collision is inelastic, the energy loss is calculated according to the specific inelastic scattering cross-section (electron-electron, electron-phonon, or electron-polaron). If the collision is elastic, the scattering angle is calculated according to the Mott cross-section. It should be noted that electron deflection mainly depends on the elastic scattering cross-section but even electron-electron inelastic interactions and electron-phonon quasi-elastic interactions are responsible for electron change of direction. The present Monte Carlo scheme takes into account the entire cascade of secondary electrons [2, 4, 5, 9, 10, 12–14]. The initial position of a secondary electron due to Fermi sea excitation is assumed to be at the site of the inelastic collision. In the calculations presented in this chapter, the polar and azimuth angles of secondary electrons are calculated, according to Shimizu and Ding Ze-Jun [15], assuming a random direction of the secondary electrons. This hypothesis of random direction of the generated secondary electrons implies that slow secondary electrons should be generated with spherical symmetry [15]. As this assumption violates momentum conservation rules – within the classical binary-collision model – in the next chapter a study will be provided which compares with experimental data the results obtained adopting spherical symmetry with those obtained applying momentum conservation within the classical binary-collision model. This study demonstrates that the determination of the energy distribution of the secondary electrons emitted by solid targets as well as the secondary emission yield are in better agreement with the experiment assuming that slow secondary electrons are generated with spherical symmetry [4].

7.4 Secondary Electron Yield: PMMA and Al_2O_3

The MC schemes described above, i.e., the energy straggling and the continuous-slowing-down approximation methods, account for the main interactions occurring to the secondary electrons along their travel in insulating targets [1]. In the following paragraphs, results obtained with the two schemes will be presented and comparison with the available experimental data will be provided.

7.4.1 Secondary Electron Emission Yield as a Function of the Energy

Experimental evidences show that, as the primary energy increases, the secondary electron emission yield increases until a maximum is reached. Then the yield decreases as the primary energy increases. It is quite easy to provide a simple qualitative explanation for this behavior: at very low primary energy, few secondary electrons are generated and, as the primary energy increases, so does the number of secondary electrons emerging from the surface. The average depth at which the secondary electrons escaping from the surface are generated also increases as the primary energy increases. When the energy becomes higher than a threshold which varies based on the target, the average depth of secondary electron generation becomes so deep that just a small amount of the generated secondary electrons are able to reach the surface satisfying the condition necessary to emerge from the sample and to be detected. We will show that both the MC schemes (ES and CSDA) confirm this behavior providing consistent quantitative explanations for it.

7.4.2 Comparison Between ES Scheme and Experiment

Even if the physical meaning of the parameters used by the ES MC code and appearing in the laws describing the interactions is clear – so that they are, at least in principle, measurable – in practice they can be determined only through an analysis of their influence on the simulated results and a comparison to the available experimental data.

The values of the parameters for PMMA were determined through such an analysis and Figs. 7.1 and 7.2, show the comparison with the available experimental data of the simulated results obtained using the detailed Monte Carlo scheme based on the energy-straggling strategy (ES scheme). We found out, for PMMA, the best fit with the following parameters values: $\chi = 4.68\,\text{eV}$, $W_{\text{ph}} = 0.1\,\text{eV}$, $C = 0.01\ \text{Å}^{-1}$, and $\gamma = 0.15\,\text{eV}^{-1}$. It should be noted that, performing a similar analysis, Ganachaud and Mokrani found out, for amorphous Al_2O_3, the following values of the parameters: $\chi = 0.5\,\text{eV}$, $W_{\text{ph}} = 0.1\,\text{eV}$, $C = 0.1\ \text{Å}^{-1}$, and $\gamma = 0.25\,\text{eV}^{-1}$ [1]. It should be noted as

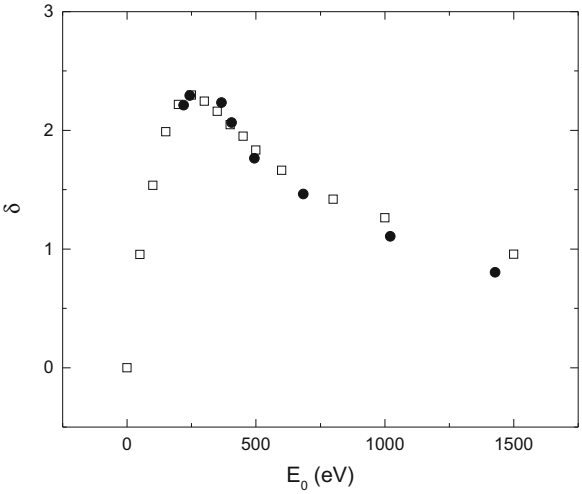

Fig. 7.1 Comparison between present Monte Carlo calculations and experimental data of Polymethyl Methacrylate (PMMA) secondary electron yield δ as a function of the primary electron energy. *Squares* represent Monte Carlo calculations based on the energy-straggling strategy and obtained with $\chi = 4.68\,\text{eV}$, $W_{\text{ph}} = 0.1\,\text{eV}$, $C = 0.01\ \text{Å}^{-1}$, and $\gamma = 0.15\,\text{eV}^{-1}$. The Monte Carlo data were obtained integrating the curves of energy distribution including all the electrons emerging with energy from 0 to the 50 eV. Experimental data: from Ref. [7, 16] (*circles*)

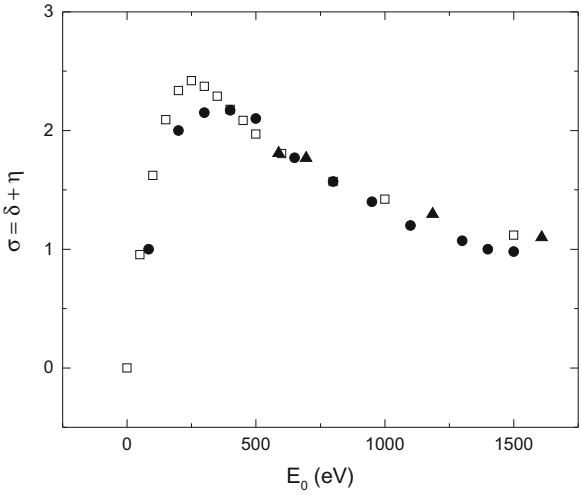

Fig. 7.2 Comparison between present Monte Carlo calculations and experimental data of Polymethyl Methacrylate (PMMA) total electron yield σ (secondary electron yield $\sigma+$ backscattering coefficient η) as a function of the primary electron energy. *Squares* represent Monte Carlo calculations based on the energy-straggling strategy and obtained with $\chi = 4.68\,\text{eV}$, $W_{\text{ph}} = 0.1\,\text{eV}$, $C = 0.01\ \text{Å}^{-1}$, and $\gamma = 0.15\,\text{eV}^{-1}$. The Monte Carlo data were obtained integrating the curves of energy distribution including all the electrons emerging with energy from 0 to the E_0. Experimental data: from Ref. [17] (*circles*) and from Refs. [18, 19] (*triangles*)

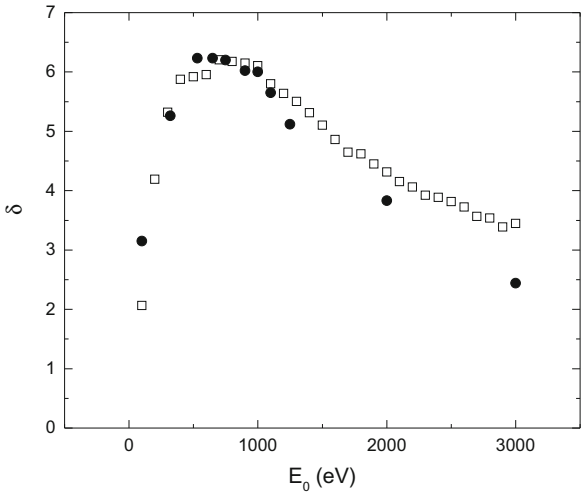

Fig. 7.3 Comparison between present Monte Carlo calculations and experimental data of Al_2O_3 secondary electron yield as a function of the primary electron energy. *Squares* represent Monte Carlo calculations based on the continuous-slowing-down approximation and obtained with $\lambda_s = 15.0$ Å and $\epsilon_s = 6.0$ eV. *Circles* are the Dawson experimental data [20]

well that the yield strongly depends on all these parameters. While both the electron affinity, χ, and the electron energy loss due to phonon creation, W_{ph}, are quantities that have been measured for many materials and whose values can be found in the scientific literature, less information is available concerning the two parameters C and γ (relative to the electron-polaron interaction).

7.4.3 Comparison Between CSDA Scheme and Experiment

The Monte Carlo code based on the CSDA scheme, also depends on two parameters: the effective escape depth, λ_s, and the effective energy necessary to generate a single secondary electron, ϵ_s.

The comparison of the results of the CSDA code with the available experimental data about Al_2O_3 [20] are shown in Fig. 7.3.

The values of the physical parameters used by the MC code based on the CSDA (i.e. the effective escape depth, λ_s, and the effective energy necessary to generate a single secondary electron, ϵ_s) for Al_2O_3 – in reasonable agreement with other physics reference data [1, 6] – are $\lambda_s = 15.0$Å and $\epsilon_s = 6.0$ eV.

The calculated value of the statistical distribution χ_s^2, considered to quantitatively evaluate the agreement between the CSDA Monte Carlo simulated data of Al_2O_3 (obtained using the parameters given above, i.e. $\lambda_s = 15.0$Å and $\epsilon_s = 6.0$ eV) and the examined experimental data is 0.905. The number ν of degrees of freedom is 11. The lower critical values of the χ_s^2 distribution for $\nu = 11$ is 3.053, and the probability p of exceeding this critical value is 0.99. As the calculated χ_s^2 is significantly smaller than the critical one, this means that, in the hypothesis that the Monte Carlo data approximate the experimental ones (the so-called null hypothesis), there is a

probability greater than 99 % that the observed discrepancies are due to statistical fluctuations. Similar results were also obtained when comparing the experimental results to the ES Monte Carlo simulated data.

7.4.4 CPU Time

The computation time needed for the ES code is much higher than the one for the CSDA code. For a typical simulation (1 keV electrons impinging upon PMMA), the CSDA scheme is more than ten times faster than the ES one. The reason for this great difference in CPU time is related to the secondary electron cascade. The ES MC strategy requires that the entire cascade be followed. The CSDA MC code, instead, is able to establish the number of secondary electrons produced at each step of every primary electron trajectory. Note that a further advantage of the CSDA MC strategy is the reduced number of parameters (only two against the four quantities required by the energy-straggling strategy).

Of course the ES MC code is based on a stronger physical background and allows one to calculate other important properties such as the secondary electron energy distribution and the lateral, angular, and depth distributions which are not accessible using the CSDA approximation (see next chapter).

In practical terms, the advantage in using the CSDA code with respect to just performing an empirical fit to the experimental data is related, of course, to other predictive capabilities of the Monte Carlo simulations. If it is true that, at the moment, the CSDA model requires a fit to existing data or to the results of the detailed simulation to calculate its free parameters, one should take into account that if the parameters were known for a large number of materials, they could be used for investigating many problems, different from the one we have used to find out the values of the parameters; such as, for example, the dependence of the secondary electron yield on the angle of incidence for any given primary energy, or the secondary electron emission from unsupported thin films (on both sides of the film), or the secondary electron emission yield from thin films deposited on different materials, and so on. Of course, all these possibilities are not accessible to a simple empirical fit to the experimental data.

In conclusion, the very fast CSDA MC code can be used for the calculation of the secondary electron yield. If secondary electron energy, lateral, and depth distributions, or detailed descriptions of the physics involved in the process are required, the ES MC strategy should be preferred, even if it requires much longer CPU time.

7.5 Summary

In this chapter the transport Monte Carlo method has been applied to the evaluation of the secondary electron emission from insulating materials (PMMA and Al_2O_3). The code has been validated by comparing the secondary electron yield obtained by

using Monte Carlo simulation with the available experimental data. In particular, an analysis of the results of two different approaches (energy-straggling scheme and continuous-slowing-down approximation scheme) for the determination of the yield of the secondary electrons emitted by insulating targets was presented. We have demonstrated that the two approaches give similar results concerning the secondary electron emission yield as a function of the electron primary energy. Furthermore the simulated results are in good agreement with the available experimental data. On the contrary, the evaluation of the secondary electron energy distribution requires the energy-straggling scheme in order to accurately take into account all the details of the energy loss mechanisms (see next chapter).

References

1. J.P. Ganachaud, A. Mokrani, Surf. Sci. **334**, 329 (1995)
2. M. Dapor, B.J. Inkson, C. Rodenburg, J.M. Rodenburg, Europhys. Lett. **82**, 30006 (2008)
3. J. Ch, Kuhr, H.J. Fitting, J. Electron. Spectrosc. Relat. Phenom. **105**, 257 (1999)
4. M. Dapor, Nucl. Instrum. Methods Phys. Res. B **267**, 3055 (2009)
5. M. Dapor, M. Ciappa, W. Fichtner, J. Micro/Nanolith, MEMS MOEMS **9**, 023001 (2010)
6. Y. Lin, D.C. Joy, Surf. Interface Anal. **37**, 895 (2005)
7. M. Yasuda, K. Morimoto, Y. Kainuma, H. Kawata, Y. Hirai, Jpn. J. Appl. Phys. **47**, 4890 (2008)
8. C.G. Walker, M.M. El-Gomati, A.M.D. Assa'd, M. Zadrazil, Scanning **30**, 365 (2008)
9. M. Dapor, Nucl. Instrum. Methods Phys. Res. B **269**, 1668 (2011)
10. M. Dapor, Prog. Nucl. Sci. Technol. **2**, 762 (2011)
11. G.F. Dionne, J. Appl. Phys. **44**, 5361 (1973)
12. C. Rodenburg, M.A.E. Jepson, E.G.T. Bosch, M. Dapor, Ultramicroscopy **110**, 1185 (2010)
13. M. Ciappa, A. Koschik, M. Dapor, W. Fichtner, Microelectron. Reliab. **50**, 1407 (2010)
14. A. Koschik, M. Ciappa, S. Holzer, M. Dapor, W. Fichtner, Proc. SPIE **7729**, 77290X-1 (2010)
15. R. Shimizu, D. Ze-Jun, Rep. Progr. Phys. **55**, 487 (1992)
16. L. Reimer, U. Golla, R. Bongeler, M. Kassens, B. Schindler, R. Senkel, Fiz. Tverd. Tela Adad. Nauk **1**, 277 (1959)
17. M. Boubaya, G. Blaise, Eur. Phys. J. Appl. Phys. **37**, 79 (2007)
18. L. Reimer, U. Golla, R. Bongeler, M. Kassens, B. Schindler, R. Senkel, Optik (Jena, Ger.) **92**, 14 (1992)
19. É.I. Rau, E.N. Evstaf'eva, M.V. Adrianov, Phys. Solid State **50**, 599 (2008)
20. P.H. Dawson, J. Appl. Phys. **37**, 3644 (1966)

Chapter 8
Electron Energy Distributions

As we know, the study of the electronic and optical properties of the matter is paramount for our comprehension of physical and chemical processes which occur in nanoclusters and solids [1]. Radiation damage, investigation of chemical composition, and electronic structure study, represent a few examples of the role played by the electron-matter interaction mechanisms. Electron spectroscopy and electron microscopy are fundamental tools to examine how electrons interact with the matter [2].

Electron spectroscopy includes a wide range of techniques. Low energy reflection electron energy loss spectroscopy and Auger electron spectroscopy, in particular, uses electron beams to analyze the surface of materials.

Both reflection electron energy loss spectroscopy and Auger electron spectroscopy are applications of the scattering theory [3]. They are based on scattering processes in which the initial state consists of electrons impinging upon solid-state targets, and final states are characterized by few non-interacting fragments. The analysis of the energy distribution of the fragments constitutes the main feature of these spectroscopies, as it provides insight about the properties of the examined system.

The spectrum, i.e., the plot of the intensity of the emitted electrons as a function of either the kinetic energy or the energy loss, represents a fingerprint of the investigated material [4–6].

8.1 Monte Carlo Simulation of the Spectrum

The numerical results we are going to present were obtained with a detailed modeling which takes into account all the described mechanisms of energy loss (electron-electron, electron-plasmon, electron-phonon, electron-polaron) and applies the Mott cross-section to deal with the elastic scattering events. Furthermore, the entire cascade of secondary electrons is followed. The whole Monte Carlo spectrum representing the energy distribution of electrons emerging from a PMMA sample due to a 200 eV electron beam irradiation is presented in Fig. 8.1 [6]. Similar spectra have

M. Dapor, *Transport of Energetic Electrons in Solids*,
Springer Tracts in Modern Physics 257, DOI 10.1007/978-3-319-47492-2_8

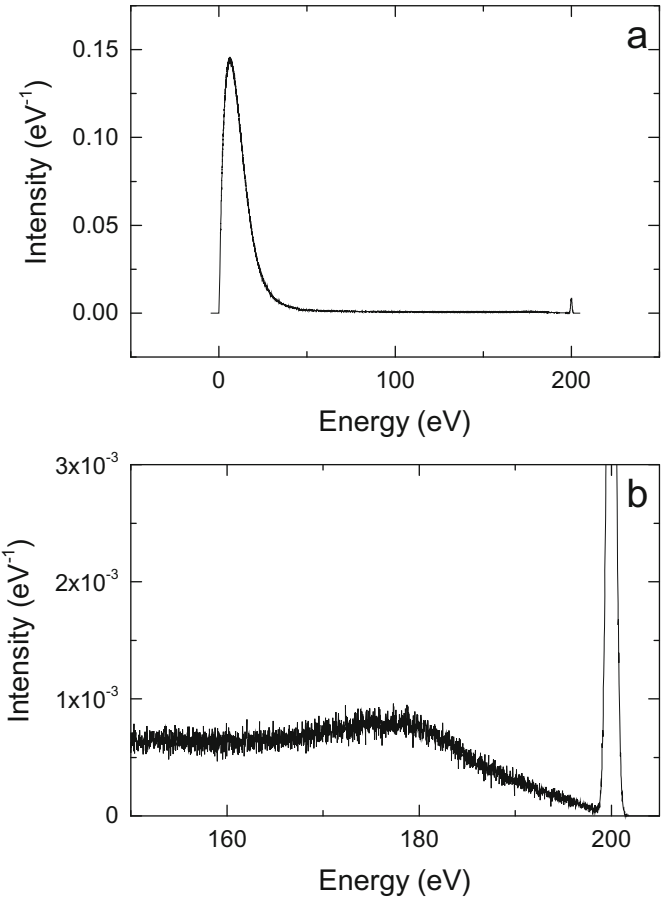

Fig. 8.1 MC calculation (ES scheme) of the spectrum representing the energy distribution of electrons emerging from a PMMA sample due to a 200 eV electron beam irradiation. **Panel a**: entire spectrum including the secondary electron peak (at low energy) and the elastic peak at 200 eV. **Panel b**: zoomed-in image of the spectrum including the plasmon peak and the elastic peak. The elastic peak, or zero loss peak, whose maximum can be found at the energy of the primary beam, represents the electrons which suffered only elastic scattering collisions. The plasmon peak represents the electrons of the primary electron beam that emerge from the surface after having suffered a single inelastic collision with a plasmon. Multiple collisions with plasmons are also present in the spectrum. The secondary electrons energy distribution presents a pronounced peak in the very low energy region of the spectrum, typically below 50 eV [6]

been observed for metals as well [4, 5]. For the purposes of present calculation, the target is considered as semi-infinite. It should be noted that the case of thin films requires special attention, in particular when the samples are thinner than the mean free path.

Many electrons of the primary electron beam can be backscattered, after having interacted with the atoms and electrons in the target. In a fraction of them the original kinetic energy remains unchanged, having suffered only elastic scattering collisions with the atoms of the target. We already know that these electrons constitute the so-called elastic peak, or zero-loss peak, whose maximum is located at the energy of the primary beam. In the simulation presented in Fig. 8.1 it is the narrow peak you can see at 200 eV.

The plasmon peak in Fig. 8.1, at ≈178 eV (≈ 22 eV from the elastic peak), represents the electrons of the primary electron beam that emerge from the surface after having suffered a single inelastic collision with a plasmon. Multiple collisions with plasmons are also present in the spectrum, although of very low intensity. A peak corresponding to a double inelastic scattering with plasmons at ≈156 eV (≈44 eV from the elastic peak) is scarcely visible in panel b of Fig. 8.1.

Electron-phonon energy losses are also present, but they are not visible in Fig. 8.1, for (i) their intensities are much lower than those of the elastic peak and (ii) they are very close to the much more intense elastic peak whose width is, on the other hand, rather wide (of the order of 1 eV): thus they are not resolved.

The spectrum includes also Auger electron peaks, due to the presence of doubly ionized atoms. They are not visible on this scale. An Auger peak (the oxygen K-LL Auger peak of the SiO_2 spectrum) with its background, obtained with an *ab-initio* method included in the present Monte Carlo code, will be shown below together with a comparison with experimental data.

Finally, as we already know, the secondary electrons produced by a cascade process are those electrons which have been extracted from the atoms by inelastic electron-electron collisions and manage to emerge from the target surface. Their Monte Carlo energy distribution presents a pronounced peak in the very low energy region of the spectrum, typically below 50 eV, and it is clearly visible in the simulated spectrum in Fig. 8.1. The secondary electron energy distributions of selected materials will be presented as well.

8.2 Plasmon Losses and Electron Energy Loss Spectroscopy

In order to briefly discuss the main features of plasmon losses, a numerical simulation concerning Graphite will be first presented. In this particular case, use has been made of experimental data taken from the literature to calculate the dielectric function and, hence, the energy loss function [7–11]. Note that similar semi-empiric approaches to the calculation of the plasmon losses can be used for other materials as well. In fact, experimental data concerning the energy loss function can be found in the literature for many materials. The case of SiO_2, for example, can be similarly treated using the experimental data in Refs. [7, 8, 12].

8.2.1 Plasmon Losses in Graphite

Let us consider the graphite electron energy-loss spectrum. It includes the zero-loss peak, the π and $\pi + \sigma$ plasmon loss peaks, due to inelastic scattering by outer shell electrons, and additional peaks at multiples of the $\pi + \sigma$ plasmon energy, due to multiple scattering. π plasmon peak is at around 7 eV while the first, the second, and the third $\pi + \sigma$ plasmon loss peaks are located around 27, 54, and 81 eV respectively.

Graphite is an anisotropic crystal. It is an uniaxial crystal with layered structure, so that the dielectric function is a tensor with only two different diagonal elements, one perpendicular and the other one parallel to the c-axis.

In Fig. 8.2 a comparison of the Monte Carlo results with experimental data for 500 eV electrons incident on graphite is presented [13].

The Monte Carlo results we present here were obtained using the graphite dielectric functions (parallel and perpendicular to the c-axis) taken from experimental data: for energies lower than 40 eV we used the data presented in Refs. [9–11] while, for energies higher than 40 eV, we used the optical data by Henke et al. [7, 8].

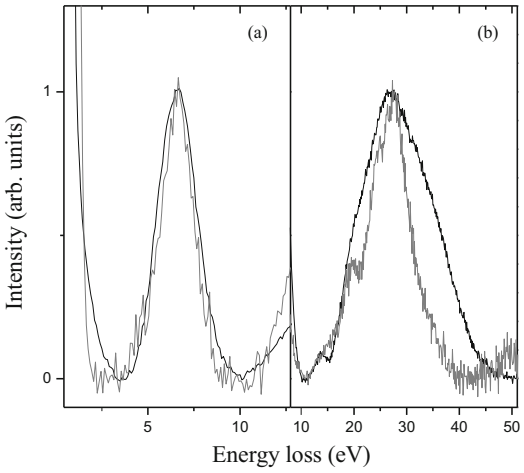

Fig. 8.2 Comparison between the experimental (*black line*) and Monte Carlo simulated (*gray line*) line-shape for the π (**panel a**) and the $\pi + \sigma$ (**panel b**) plasmon peaks [13]. The primary electron energy is 500 eV. The plasmon loss peaks are normalized to a common height after subtracting a linear background. The optical data were taken from Henke et al. [7, 8], while the data presented in Refs. [9–11] were utilized for energies lower than 40 eV. The Monte Carlo code was based on the ES scheme. Experimental data: *courtesy* of Lucia Calliari and Massimiliano Filippi

8.2.2 Plasmon Losses in Silicon Dioxide

Let us now consider the Monte Carlo simulation of the SiO_2 electron energy-loss spectrum (see Fig. 8.3) when incident electron energy is given by $E_0 = 2000$ eV. Dielectric function used in this simulation was taken by Buechner experimental data for energies lower than 33.6 eV [12] and obtained by the Henke et al. optical data for higher energies [7, 8].

The Monte Carlo simulated spectrum presents two plasmon loss peaks at ≈23 eV and at ≈46 eV corresponding to the single inelastic scattering and to the double inelastic scattering, respectively [14].

The main peak and its shoulders in the present calculations can be interpreted as interband transitions from the valence bands and the conduction band. The main plasmon loss at ≈23 eV and the shoulder located at ≈19 eV are attributed to excitations of the bonding bands, while the shoulders located at ≈15 eV and ≈13 eV are due to excitations of a nonbonding band [15].

In Fig. 8.3 an energy range is also shown, located between the main energy loss peak and the elastic peak, in which no backscattered electrons can be observed. Indeed, as the target is an insulator, electrons cannot transfer to the atomic electrons energies smaller than the value of the energy gap E_G between the valence and the conduction bands. As a consequence, no electrons of the primary beam with energy between $E_0 - E_G$ and E_0 (energy losses between 0 and E_G) can emerge from the target surface [14].

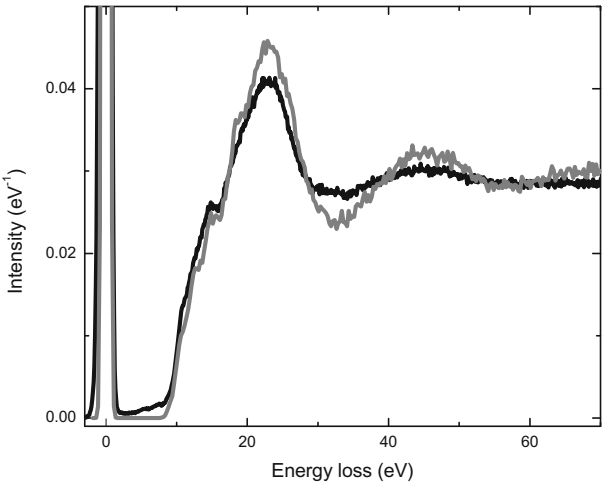

Fig. 8.3 Experimental (*black line*) and Monte Carlo simulated (*gray line*) energy-loss spectrum of 2000 eV electrons incident on SiO_2 [14]. The experimental and Monte Carlo spectra are normalized to a common area of the elastic peak. The optical data were taken from Henke et al. [7, 8], while the Buechner experimental energy loss function [12] was utilized for energies lower than 40 eV. The Monte Carlo code was based on the ES scheme. Experimental data: *courtesy* of Lucia Calliari and Massimiliano Filippi

8.3 Energy Losses of Auger Electrons

The present Monte Carlo code can be used to model the energy losses occurring in the Auger electrons during their travel in the solid – before emerging from the surface. In this context, the Monte Carlo code can be used to calculate the changes caused to the original electron energy distribution by energy losses suffered by the Auger electron on its way out of the solid. The original electron distribution was calculated using *ab initio* calculations of non-radiative decay spectra obtained by the program suite *SURface PhotoelectRon and Inner Shell Electron Spectroscopy* (SURPRISES). The physics of SURPRISES can be found in Refs. [16–18]. It is a program which performs *ab initio* calculations of photoionization and non-radiative decay spectra in nanoclusters and solid state systems.

The comparison between simulated and experimental Auger spectra requires to properly take into account the changes caused, to the Auger electron energy distribution, by the energy losses which the Auger electrons suffer along their travel in the solid toward the surface. Do to that, we use previously calculated *ab initio* Auger probability distribution as a source of electrons suffering inelastic processes. The theoretical Auger spectrum previously calculated using *ab initio* calculations was adopted to describe the initial energy distribution of the escaping electrons.

Auger electron generation is calculated assuming a constant depth distribution whose thickness, according to Ref. [19], was set to 40 Å. A plot of the calculation compared to the original experimental data – i.e., the experimental data presented without any deconvolution of energy losses – is given in Fig. 8.4. The original theoretical spectrum (*ab initio* calculation) is also provided.

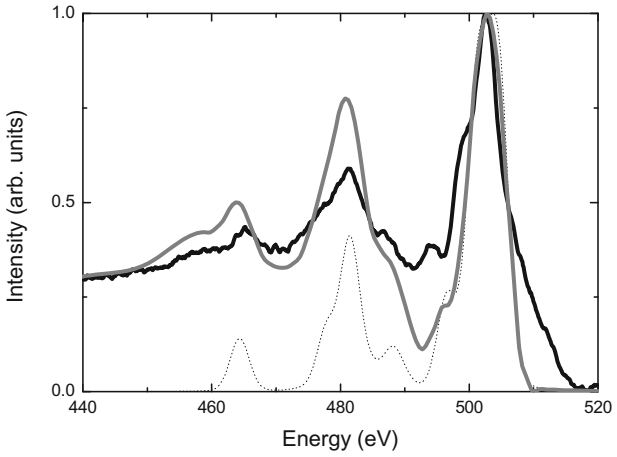

Fig. 8.4 OK-LL Auger spectrum in SiO_2. Comparison between the quantum mechanical theoretical data (*dotted line*), the Monte Carlo results (*gray continuous line*), and the original experimental data (*black continuous line*) [16]. Quantum mechanical theoretical data: courtesy of Stefano Simonucci and Simone Taioli. Experimental data: *courtesy* of Lucia Calliari and Massimiliano Filippi

One can see that the Monte Carlo energy loss calculation increases and broadens the Auger probability. The large broadening of the K-L_1L_{23} peak after the Monte Carlo treatment is due to the main plasmon of SiO_2 whose distance from the zero loss peak (≈23 eV: see Fig. 8.3) is the same as the distance between the K-$L_{23}L_{23}$ and K-L_1L_{23} features in the Auger spectrum.

A satisfactory agreement between the experiment and the combination of the *ab initio* calculation with the Monte Carlo simulation can be found: in particular a good accordance can be recognized in the energy position, in the relative intensities of the peaks, and in the background contribution over the entire investigated energy range.

8.4 Elastic Peak Electron Spectroscopy (EPES)

The analysis of the line-shape of the elastic peak is known as elastic peak electron spectroscopy (EPES) [20, 21]. The energy of electrons of the elastic peak is reduced by the energy transferred to the atoms of the target (the so-called recoil energy). Since the lightest elements present the largest energy shifts, EPES is, among electron spectroscopies, the only one able to detect hydrogen in polymers and hydrogenated carbon-based materials [22–29]. Hydrogen detection is obtained by measuring the energy difference between the position of the carbon (or the carbon + oxygen) elastic peak and that of the hydrogen elastic peak: this difference between the energy positions of the elastic peaks – for incident electron energy in the range 1000–2000 eV – is in the range from ≈2 to ≈4 eV, and increases as the kinetic energy of the incident electrons increases. The reason is that the mean recoil energy E_R for an atom of mass m_A is given by

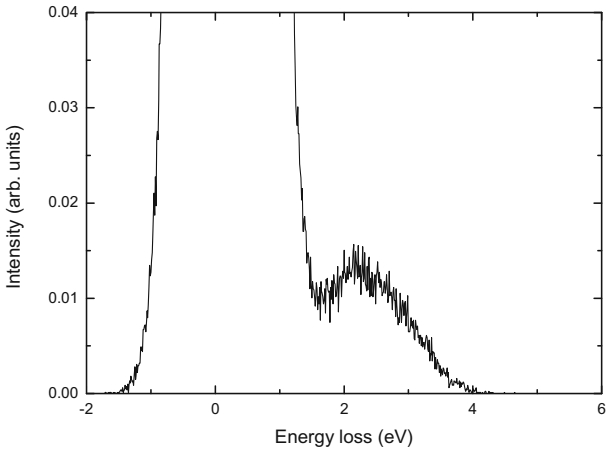

Fig. 8.5 Monte Carlo simulation of EPES for PMMA, showing the C+O (*left*) and the H (*right*) elastic peaks. $E_0 = 1500$ eV

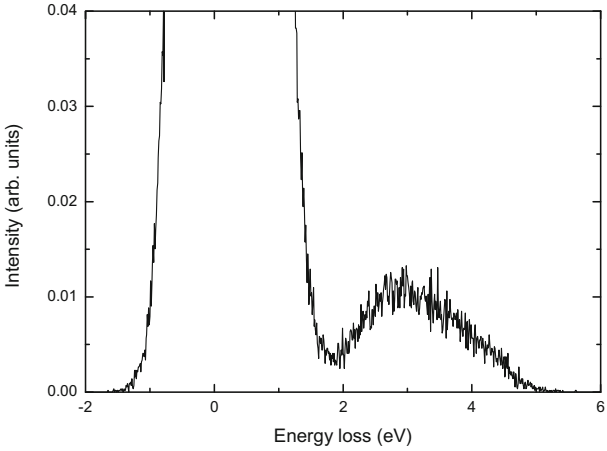

Fig. 8.6 Monte Carlo simulation of EPES for PMMA, showing the C+O (*left*) and the H (*right*) elastic peaks. $E_0 = 2000$ eV

$$E_R = \frac{4m}{m_A} E_0 \sin^2 \frac{\vartheta}{2} . \tag{8.1}$$

Monte Carlo simulated PMMA elastic peak electron spectra are presented in Figs. 8.5 ($E_0 = 1500$ eV) and 8.6 ($E_0 = 2000$ eV). The H elastic peak position is shifted in energy with respect to the C+O elastic peak, the difference in energy being an increasing function of the primary energy E_0.

8.5 Secondary Electron Spectrum

Another important feature of the electron energy spectrum is represented by the secondary-electron emission distribution, i.e., the energy distribution of those electrons that, once extracted from the atoms by inelastic collisions and having travelled in the solid, reach the surface with the energy sufficient to emerge. The energy distribution of the secondary electrons is confined in the low energy region of the spectrum, typically well below 50 eV. A very pronounced peak characterizes it, which is due to a cascade process in which every secondary electron generates, along its trajectory, further secondary electrons, so that a kind of shower of secondary electrons is created.

The first question is whether secondary electrons due to Fermi sea excitations are generated with spherical symmetry – violating in such a case momentum conservation – or if they are emitted conserving the momentum, as prescribed by the classical binary-collision theory (see Sect. 5.2.3). Since the energy distributions resulting from

these two processes are different, two versions of the Monte Carlo code were considered. One of the two versions adopts spherical symmetry for the angular distribution of the secondary electron emission at the site of generation, while the other one is based on momentum conservation. The results of the two Monte Carlo codes are compared to experimental data, in order to decide which one better describes the phenomena. We will show that the hypothesis of spherical symmetry provides results in better agreement with the experimental evidences than that of momentum conservation. This is in agreement with the suggestion given by Shimizu and Ding Ze Jun [30] to use spherical symmetry in the Monte Carlo simulation of secondary electron generation.

8.5.1 Initial Polar and Azimuth Angle of the SEs

The initial polar angle θ_s and the initial azimuth angle ϕ_s of each secondary electron can be calculated in two different ways. In the first one, based on the hypothesis that the secondary electrons emerge with spherical symmetry, their initial polar and azimuth angles are randomly determined as [30]

$$\theta_s = \pi \mu_1 , \tag{8.2}$$

$$\phi_s = 2 \pi \mu_2 \tag{8.3}$$

where μ_1 and μ_2 are random numbers uniformly distributed in the range [0, 1]. Even if such an approach violates momentum conservation and it is therefore questionable, Shimizu and Ding observed that, as slow secondary electrons are actually generated with spherical symmetry, it should be used and preferred when Fermi sea excitations are involved in the process of generation of secondary electrons [30]. Please note that we adopted spherical symmetry also in the Monte Carlo calculations devoted to the study of secondary electron yields (see previous chapter).

MCSS is the name attributed, in the present context, to the Monte Carlo code based on this method.

A second code is proposed in which momentum conservation is taken into account by using the classical binary-collision model so that, if θ and ϕ are, respectively, the polar and azimuth angle of the incident electron, then [30]

$$\sin \theta_s = \cos \theta , \tag{8.4}$$

$$\phi_s = \pi + \phi . \tag{8.5}$$

We will indicate, in the present context, with MCMC the Monte Carlo code corresponding to this second approach. The results of the MCSS and MCMC codes will be compared with theoretical and experimental data [31].

8.5.2 Comparison with Theoretical and Experimental Data

Secondary Electron Energy Distribution of Silicon and Copper. We present, in Fig. 8.7 and in Fig. 8.8, the energy distributions of the secondary electrons emitted by silicon and copper targets, respectively. The energy of the primary electron beam is E_0 = 1000 eV for silicon, while it is E_0 = 300 eV for copper. The Monte Carlo calculations obtained with the two different methods described above (MCSS and MCMC) are compared with the Amelio theoretical and experimental results [32].

Using the theory of Amelio for the comparison, the MCSS scheme gives results that show a much better agreement than the MCMC code. Indeed, in the range of primary energies examined and for both the materials considered, it is clear that, using the MCSS code, the position of the maxima and the general trend of the energy distributions are in excellent agreement with the Amelio data. On the other hand, the use of the MCMC code generates electron energy distributions that are in not such a good agreement with the Amelio data: the position of the maxima are shifted to

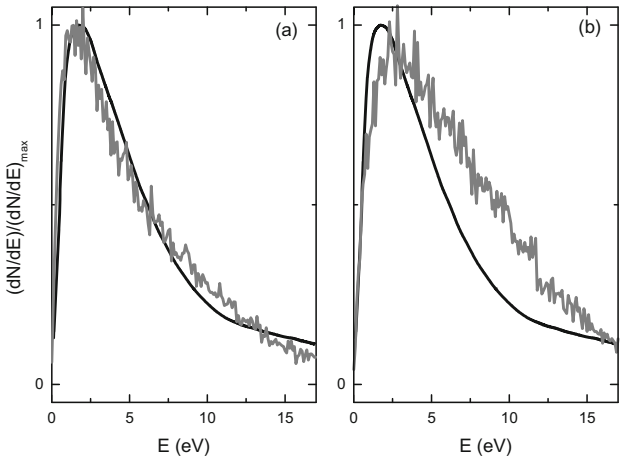

Fig. 8.7 Energy distribution of the secondary electrons emitted by a silicon target. The zero of the energy scale is located at the vacuum level. The present Monte Carlo calculations (*gray lines*) [31] are compared with the Amelio theoretical results (*black lines*) [32]. Data are normalized to a common maximum. The initial electron energy is 1000 eV. The zero of the energy scale is located at the vacuum level. The primary electron beam is normal to the surface. Electrons are accepted over an angular range from 0° to 90° integrated around the full 360° azimuth. **Panel a**: MCSS code. **Panel b**: MCMC code (see details in the text)

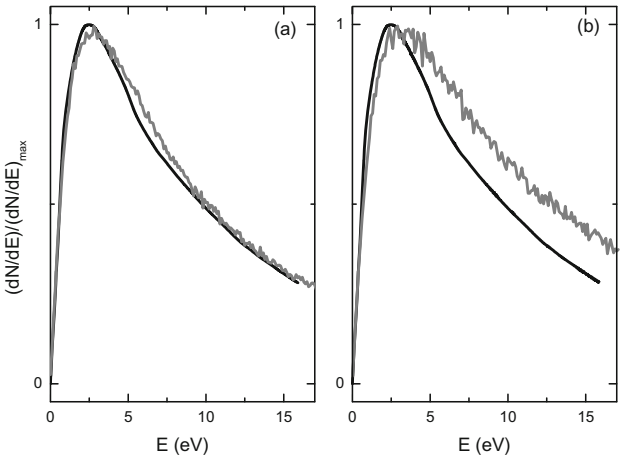

Fig. 8.8 Energy distribution of the secondary electrons emitted by a copper target. The present Monte Carlo calculations (*gray lines*) [31] are compared with the Amelio theoretical results (*black lines*) [32]. Data are normalized to a common maximum. The initial electron energy is 300 eV. The zero of the energy scale is located at the vacuum level. Electrons are accepted over an angular range from 0° to 90° integrated around the full 360° azimuth. The primary electron beam is normal to the surface. **Panel a**: MCSS code. **Panel b**: MCMC code (see details in the text)

higher energies and the shapes of the distributions are quite different from the Amelio energy distributions. It should be noted that experimental data concerning secondary electron energy distributions were reported by Amelio as well. In Table 8.1 and in Table 8.2 the main features regarding the energy distributions [i.e., the most probable energy (MPE) and the full width at half maximum (FWHM)] obtained with MCSS and MCMC are compared with the experimental data reported by Amelio.

The agreement of the MCSS results with the Amelio [32] data (and the disagreement between the MCMC and experimental results) can be attributed to the isotropy of the low-energy secondary electron emission due to: (i) post-collisional effects and consequent random energy and momentum transfer among secondary electrons; (ii) interactions with the conduction electrons, just after secondary electrons are emitted.

Table 8.1 Monte Carlo most probable energy (MPE) and full width at half maximum (FWHM) of secondary electron energy distributions obtained with two different schemes (MCSS and MCMC: see details in the text). The experimental data were reported by Amelio [32]. Calculations and measurements were carried out on bulks of Si irradiated by streams of electrons in the $+z$ direction. The primary energy of the incident electron beam was 1000 eV

Si (1000 eV)	MCSS	MCMC	Experiment
MPE (eV)	1.8	2.8	1.7
FWHM (eV)	5.3	8.5	5.0

Table 8.2 Monte Carlo most probable energy (MPE) and full width at half maximum (FWHM) of secondary electron energy distributions obtained with two different schemes (MCSS and MCMC: see details in the text). The experimental data were reported by Amelio [32]. Calculations and measurements were carried out on bulks of Cu irradiated by streams of electrons in the $+z$ direction. The primary energy of the incident electron beam was 300 eV

Cu (300 eV)	MCSS	MCMC	Experiment
MPE (eV)	2.8	3.5	2.8
FWHM (eV)	9.2	12	10

In conclusion, the results of the present investigation suggest that slow secondary electrons should be generated, in MC codes, with spherical symmetry in order to get agreement with experimental and theoretical data.

Secondary Electron Energy Distribution of Polymethyl Methacrylate. The Monte Carlo energy distribution of the electrons emerging from Polymethyl Methacrylate irradiated by an electron beam with primary energy E_0 = 1000 eV is presented in Fig. 8.9 [33]. The spectrum is simulated assuming that the primary electron beam is normal to the surface. The zero of the energy is located at the vacuum level. In the same figure, a comparison of the Monte Carlo simulated spectrum to the Joy et al. experimental electron energy distribution [34] is shown. The same conditions of the experiment are used for the simulation, i.e. acceptance angles in the range from 36° to

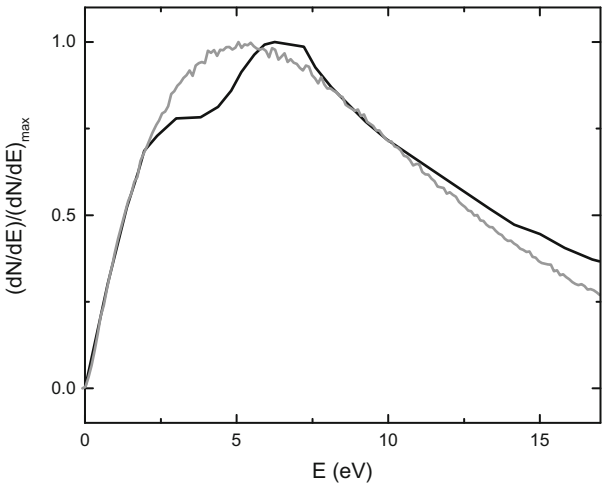

Fig. 8.9 Energy distribution of the secondary electrons emitted by a PMMA target. The present Monte Carlo calculations (*gray line*) [33] are compared with the Joy et al. experimental data (*black line*) [34]. Data are normalized to a common maximum. The initial electron energy is 1000 eV. The zero of the energy scale is located at the vacuum level. The primary electron beam is normal to the surface. Electrons are accepted, according to the Joy et al. experimental conditions, over an angular range from 36° to 48° integrated around the full 360° azimuth

48° integrated around the full 360° azimuth (Cylindrical Mirror Analyzer geometry). The Monte Carlo calculation describes very well the initial increase of the spectrum, the energy position of the maximum, and the full width at half maximum. The present Monte Carlo simulation is not able, on the other hand, to describe the fine structure of the peak, in particular the observed shoulder on the left of the maximum.

8.6 Summary

In this chapter, reflection electron energy loss spectra, Auger electron spectra, elastic peak electron spectra, and secondary electron energy spectra and were simulated by the Monte Carlo method. The results of the simulation of the spectra were compared with the available experimental data. The agreement between experiment and simulation was discussed.

References

1. R.M. Martin, *Electronic Structure*, Basic Theory and Practical Methods (Cambridge University Press, Cambridge, 2004)
2. M.D. Crescenzi, M.N. Piancastelli, *Electron Scattering and Related Spectroscopies* (World Scientific, Singapore, 1996)
3. R.G. Newton, *Scattering Theory of Wave and Particle* (Springer, New York, 1982)
4. R. Cimino, I.R. Collins, M.A. Furman, M. Pivi, F. Ruggiero, G. Rumolo, F. Zimmermann, Phys. Rev. Lett. **93**, 014801 (2004)
5. M.A. Furman, V.H. Chaplin, Special topics - accelerators and beams. Phys. Rev. **9**, 034403 (2006)
6. M. Dapor, Appl. Surf. Sci. (In press, 2016), http://dx.doi.org/10.1016/j.apsusc.2015.12.043
7. B.L. Henke, P. Lee, T.J. Tanaka, R.L. Shimabukuro, B.K. Fujikawa, At. Data Nucl. Data Tables **27**, 1 (1982)
8. B.L. Henke, P. Lee, T.J. Tanaka, R.L. Shimabukuro, B.K. Fujikawa, At. Data Nucl. Data Tables **54**, 181 (1993)
9. J. Daniels, C.V. Festenberg, H. Raether, K. Zeppenfeld, Springer Tracts in Mod. Phys. **54**, 78 (1970)
10. H. Venghauss, Phys. Status Solidi B **71**, 609 (1975)
11. A.G. Marinopoulos, L. Reining, A. Rubio, V. Olevano, Phys. Rev. B **69**, 245419 (2004)
12. U. Buechner, J. Phys. C: Solid State Phys. **8**, 2781 (1975)
13. M. Dapor, L. Calliari, M. Filippi, Nucl. Instrum. Methods Phys. Res. B **255**, 276 (2007)
14. M. Filippi, L. Calliari, M. Dapor, Phys. Rev. B **75**, 125406 (2007)
15. M.H. Reilly, J. Phys. Chem. Solids **31**, 1041 (1970)
16. S. Taioli, S. Simonucci, L. Calliari, M. Dapor, Phys. Rep. **493**, 237 (2010)
17. S. Taioli, S. Simonucci, L. Calliari, M. Filippi, M. Dapor, Phys. Rev. B **79**, 085432 (2009)
18. S. Taioli, S. Simonucci, M. Dapor, Comput. Sci. Discovery **2**, 015002 (2009)
19. G.A. van Riessen, S.M. Thurgate, D.E. Ramaker, J. Electron Spectrosc. Relat. Phenom. **161**, 150 (2007)
20. G. Gergely, Progr. Surf. Sci. **71**, 31 (2002)
21. A. Jablonski, Progr. Surf. Sci. **74**, 357 (2003)

22. D. Varga, K. Tökési, Z. Berènyi, J. Tóth, L. Kövér, G. Gergely, A. Sulyok, Surf. Interface Anal. **31**, 1019 (2001)
23. A. Sulyok, G. Gergely, M. Menyhard, J. Tóth, D. Varga, L. Kövér, Z. Berènyi, B. Lesiak, A. Jablonski, Vacuum **63**, 371 (2001)
24. G.T. Orosz, G. Gergely, M. Menyhard, J. Tóth, D. Varga, B. Lesiak, A. Jablonski, Surf. Sci. **566–568**, 544 (2004)
25. F. Yubero, V.J. Rico, J.P. Espinós, J. Cotrino, A.R. González-Elipe, Appl. Phys. Lett. **87**, 084101 (2005)
26. V.J. Rico, F. Yubero, J.P. Espinós, J. Cotrino, A.R. González-Elipe, D. Garg, S. Henry, Diam. Relat. Mater. **16**, 107 (2007)
27. D. Varga, K. Tökési, Z. Berènyi, J. Tóth, L. Kövér, Surf. Interface Anal. **38**, 544 (2006)
28. M. Filippi, L. Calliari, Surf. Interface Anal. **40**, 1469 (2008)
29. M. Filippi, L. Calliari, C. Verona, G. Verona-Rinati, Surf. Sci. **603**, 2082 (2009)
30. R. Shimizu, Ding Ze-Jun, Rep. Prog. Phys. **55**, 487 (1992)
31. M. Dapor, Nucl. Instrum. Methods Phys. Res. B **267**, 3055 (2009)
32. G.F. Amelio, J. Vac. Sci. Technol. **B7**, 593 (1970)
33. M. Dapor, Imaging & Microsc. **2**, 38 (2016)
34. D.C. Joy, M.S. Prasad, H.M. Meyer III, J. Microsc. **215**, 77 (2004)

Chapter 9
Applications

In this chapter we will discuss some important applications of the Monte Carlo method in nanometrology. We will describe, in particular, (1) the line-scan calculations of resist materials with given geometrical cross-sections deposited on silicon substrates; and (2) the energy selective SEM for image contrast in silicon *p-n* junctions.

9.1 Linewidth Measurement in Critical Dimension SEM

A very important application of the MC calculations of the secondary electron yield is related to nanometrology and linewidth measurement in critical dimension SEM [1–5]. In Refs. [1, 6] this problem has been recently investigated using an approach based on the energy-straggling strategy, described earlier in this work, and on the detailed description of all the main mechanisms of scattering (elastic electron-atom, quasi-elastic electron-phonon, and inelastic electron-plasmon and electron-polaron interactions) [7–9]. The corresponding energy straggling Monte Carlo module has been then included in the PENELOPE code [10–12].

9.1.1 Nanometrology and Linewidth Measurement in CD SEM

In order to provide metrics for the CMOS technologies, critical dimension measurements with sub-nanometer uncertainty have to be performed, in particular for the linewidth measurement of photoresist lines (PMMA lines, for example) used in electron beam lithography. The physics of image formation in scanning electron microscopy have to be understood and modeled. Monte Carlo simulation of the

M. Dapor, *Transport of Energetic Electrons in Solids*,
Springer Tracts in Modern Physics 257, DOI 10.1007/978-3-319-47492-2_9

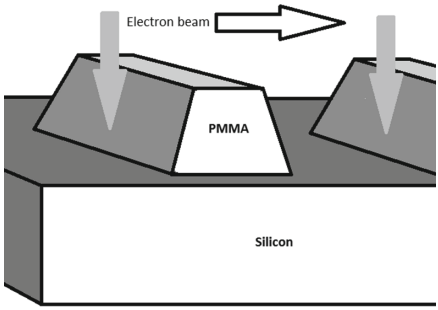

Fig. 9.1 Dielectric material (e.g. PMMA) with trapezoidal cross-section on silicon substrate. Linescans are acquired perpendicularly to the structures

generation and transport of secondary electrons – produced by low primary energy electrons – is today the most accurate method for obtaining information about image formation in scanning electron microscopy.

Typical structures of interest for CMOS technologies are dielectric lines (e.g. PMMA lines) on silicon substrates with trapezoidal cross-section (see Fig. 9.1). In SEM measurements with sub-nanometer uncertainty, the critical dimensions to be investigated are the bottom line width, the top line width, the slope of the rising edge, and the slope of the falling edge.

9.1.2 Lateral and Depth Distributions

The lateral and depth resolutions of secondary electron imaging are related to the diffusion of the secondary electrons in the solid. It seems therefore important, before proceeding, to investigate the extent of lateral and depth distributions of the emerging electrons. Figure 9.2 shows the lateral distribution of the secondary electrons

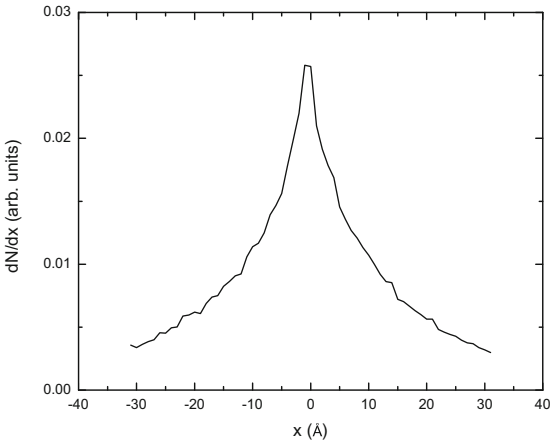

Fig. 9.2 Monte Carlo simulation of the lateral distribution dN/dx of the secondary electrons emerging from PMMA [6]. The electron primary energy E_0 is 1000 eV

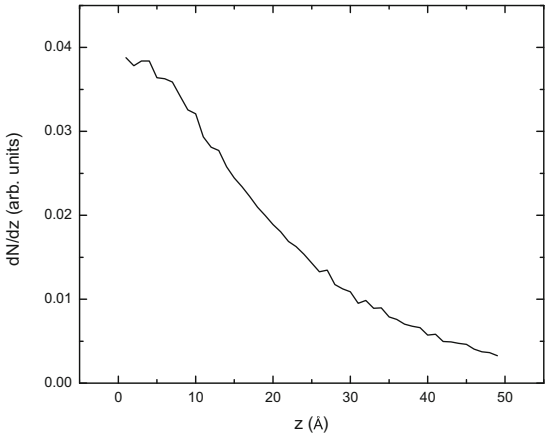

Fig. 9.3 Monte Carlo simulation of the depth distribution dN/dz of the sites where the secondary electrons that were able to emerge from the PMMA sample surface have been generated [6]. The electron primary energy E_0 is 1000 eV

emerging from PMMA, for a primary energy of 1000 eV, adopting a delta-shaped beam spot. Figure 9.3 presents, for the same energy, the depth distribution of the sites where the secondary electrons that were able to emerge from the sample surface have originated. Both Figs. 9.2 and 9.3 provide a general idea of the lateral and depth resolution of secondary electron emission. In agreement with the theoretical model, the lateral and depth distributions of emerging secondary electrons have an extent smaller than ~50 Å.

9.1.3 Linescan of a Silicon Step

Where the surface is flat, the secondary electron emission yield corresponds to that of normal incidence. Approaching the step on the negative x positions, a shadowing effect is observed that is due to the interception of the trajectories of the emerging secondary electrons by the step and, at the bottom edge of the step, the signal reaches its minimum value. The signal maximum is observed at top edge of the step. An intermediate level within the transition is observed in Fig. 9.4, according the behavior of the secondary electron yield as a function of angle of incidence.

9.1.4 Linescan of PMMA Lines on a Silicon Substrate

Figure 9.5 shows linescans obtained by simulating three adjacent PMMA lines on a silicon substrate. Additional geometry shadowing effects due to the neighbouring lines can be observed in the internal edge signals.

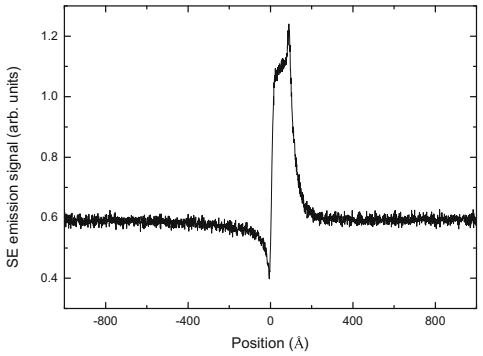

Fig. 9.4 Monte Carlo simulation of a linescan from a silicon step with side wall angle equal to 10° and incident electron energy equal to 700 eV. The shape of the signal is determined by the angle of incidence of the primary electrons, their energy, positions of incidence, and geometry. The simulation has been performed by means of a pencil beam. *Courtesy* of Mauro Ciappa and Emre Ilgüsatiroglu, ETH, Zurich

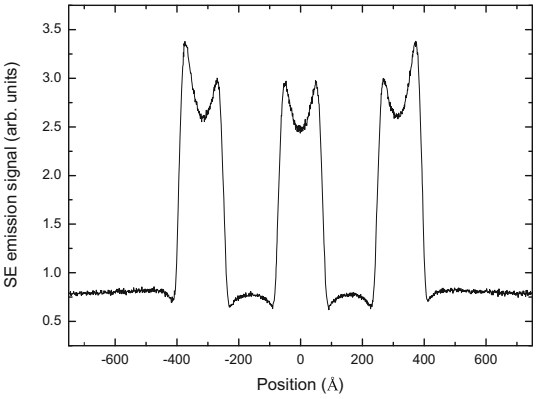

Fig. 9.5 Monte Carlo simulation of a linescan from PMMA *lines* (height: 200 Å, bottom width: 160 Å, top width: 125 Å, side wall angle: 5°) on a Si substrate scanned with a pencil-like electron beam at 500 eV. *Courtesy* of Mauro Ciappa and Emre Ilgüsatiroglu, ETH, Zurich

9.2 Application to Energy Selective Scanning Electron Microscopy

Monte Carlo simulations of secondary electron energy distribution and yield have important applications in the design and characterization of semiconductor devices, particularly in the investigation of the distribution of dopant atom concentrations at the nanometer scale. This application is known as *two-dimensional dopant mapping*. Two-dimensional dopant mapping based on the secondary electron emission is a technique which allows a fast investigation of dopant distributions in semiconductors. The dopant contrast can be explained by taking into account the electron affinity in Monte Carlo simulations to calculate the secondary electron emission from doped silicon [13].

9.2.1 Doping Contrast

A reliable method for mapping quantitatively the distribution of dopant atom concentrations at the nanometre scale is the use of secondary-electron contrast in the SEM [14–20]. Secondary-electron yield changes across a *p-n* junction [21]. The *p*-type region emits more secondary electrons than *n*-type region. As a consequence, the *p*-type is brighter in the SEM image.

The contrast C_{pn} can be calculated by

$$C_{\mathrm{pn}} = 200\frac{I_{\mathrm{p}} - I_{\mathrm{n}}}{I_{\mathrm{p}} + I_{\mathrm{n}}}, \tag{9.1}$$

where I_{p} and I_{n} represent the secondary electron emission yields of the *p*-type and *n*-type regions, respectively.

Increasing the electron affinity reduces the intensity of the lower end of the secondary electron emission spectrum, as electrons approaching the surface from the bulk meet an increased potential barrier. The integral of secondary electron emission spectrum provides the secondary-electron emission yield, so that the latter decreases as the electron affinity increases. Since the Fermi levels equilibrate at the *p-n* junction, the *p*-type region has lower electron affinity than the *n*-type region. Thus the *p*-type region emits more secondary electrons than the *n*-type region, as confirmed by the Monte Carlo simulation.

Actually, in a *p-n* junction, it is the difference in the electron affinities – the so-called *built-in* potential eV_{bi} – rather than the absolute values of the electron affinities, what determines the contrast. The bulk built-in potential can be easily calculated for a simple *p-n* junction. In the case of full ionisation, it is given by [22]:

$$eV_{\mathrm{bi}} = k_{\mathrm{B}}\,T\,\ln\frac{N_{\mathrm{a}}N_{\mathrm{d}}}{N_{\mathrm{i}}^2}, \tag{9.2}$$

where k_{B} is the Boltzmann constant, T is the absolute temperature, and N_{a}, N_{d}, and N_{i} are, respectively, the acceptor dopant carrier concentration, the donor dopant carrier concentration, and the intrinsic carrier concentration. Equation (9.2) allows to calculate the built-in potential if the doping levels of *n*- and *p*- regions in contact are known.

The value of the electron affinity of pure (un-doped) Si was reported to be 4.05 eV [23]. The Monte Carlo calculations were performed with $\chi = 3.75$ eV for the *p*-type sample and $\chi = 4.35$ eV for the *n*-type sample, and for an electron energy $E_0 = 1000$ eV. Using a specimen with doping levels of *p* and *n* consistent with these values of the electron affinities, and the same electron energy, a contrast of $C_{\mathrm{pn}} = (16 \pm 3)\,\%$ was reported by Elliott et al. [20]. The Monte Carlo simulated contrast is $C_{\mathrm{pn}} = (17 \pm 3)\,\%$ [13], in reasonable agreement with the Elliott et al. experimental observation.

9.2.2 *Energy Selective Scanning Electron Microscopy*

Rodenburg et al. [24] experimentally demonstrated that the image contrast in *p-n* junctions, obtained considering only the low energy electrons, is significantly higher than the one obtained under standard conditions (where secondary electrons of all energies contribute to the formation of the image). As a consequence, selecting secondary electrons in a given (low) energy window, instead of permitting to all the secondary electrons to form the image, allows more accurate quantification of the contrast.

It is well known that the built-in potential is smaller close to the surface – with respect to the value that one can calculate using Eq. (9.2) – due to *surface band bending* [25]. Thus secondary electrons emitted from the surface region, where surface band bending reduces the built-in potential, will not see the full built-in voltage of the bulk. For a pure silicon specimen, our Monte Carlo simulated spectra are presented in Fig. 9.6. The maximum of the distribution of the secondary electrons that are generated at a depth of 1 Å is located at ≈10 eV. We can observe that the distribution of the secondary electrons generated within a depth of up to 20 Å presents a maximum located at an energy ≈2 eV. Thus, secondary electrons leaving the material with lower kinetic energy were generated deeper in the specimen than those with higher energy. Our Monte Carlo results, relative to Si, are similar to those published by other authors relative to Cu [26] and to SiO_2 [27]. According to the experimental observations, the larger the V_{bi}, the higher the contrast. Since the high energy electrons are generated close to the surface, where the built-in potential is smaller, selecting secondary electrons of low energy increases the dopant contrast: this is in perfect agreement with the experimental observations provided by Rodenburg et al. [24].

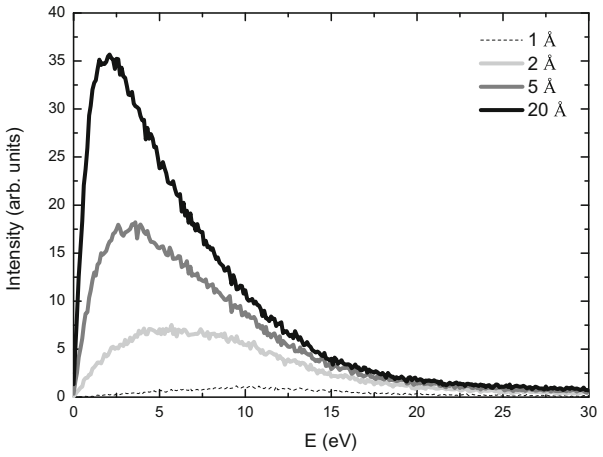

Fig. 9.6 Monte Carlo calculated contributions of secondary electron originating from different depths to secondary electron spectrum in Si [24]

9.3 Proton Cancer Therapy

The ionization yield of ion tracks in polymers and bio-molecular systems reaches a maximum, known as the Bragg peak, close to the end of the ion trajectory. Many electrons are generated along the path of MeV protons in the materials. They produce a cascade of further ionizations and, consequently, a shower of secondary electrons. These very low energy secondary electrons can produce damage in the biomolecules by dissociative electron attachment. By following in detail the motion of all the secondary electrons, we can find the radial distribution of the energy they deposit in the material along the proton track.

9.3.1 Proton Track Simulation and Bragg Peak

Interaction of energetic ions with matter is present in many aspects of our daily lifes. Cosmic radiation contains an enormous amount of projectiles [28]. 99 % of primary cosmic rays are atomic nuclei and about 1 % are electrons. 90 % of the atomic nuclei are hydrogen nuclei (protons), 9 % alpha particles, and 1 % nuclei of heavier elements. They produce showers of secondary particles that penetrate the atmosphere and can reach the surface of the Earth. Many of these particles can also reach delicate microelectronic devices present in spatial missions, as well as the crew of manned spatial missions. Besides these potential hazards, energetic projectiles properly used can be employed to characterize and modify the properties of materials. Also, swift ion beams represent a useful tool in radiotherapy [29–37]; in particular, ion-beam cancer therapy is based on the characteristic pattern of the energy deposited by ion beams in condensed targets. The depth-dose profile presents a sharp and narrow maximum, called Bragg's peak, at the end of the particle trajectory, close to the ions maximum range. This particular feature of the energy deposition pattern of ion beams is exploited to maximize the damage in the tumor regions minimizing the effects of the irradiation on the healthy tissues near the diseased cells [38].

9.3.2 Damage in the Biomolecules by Dissociative Electron Attachment

From the modeling point of view, the interaction of charged particles with condensed matter represents a very tricky and complicated multi-scale problem. In particular, hadron therapy concerns biological materials: the relevant bio-physical processes are very complex, as they involve reactions of nuclear fragmentation, secondary electron emission, damages to the cells, and repair mechanisms of macromolecules (e.g. DNA, proteins, etc.), among other things.

It is known that a relevant part of the biological damage is due to secondary electrons. In particular, very small energy secondary electrons play an important role in determining the damage. The secondary electrons of very small energy play an important role in causing the damage, which they infringe by the dissociative electron attachment in the nascent stages of DNA radiolysis within cells [39, 40].

9.3.3 Simulation of Electron Transport and Further Generation

The first step for the buildup of the radial energy deposition profile is the generation of secondary electrons by the primary energetic ion. The motion of the swift protons through the target is accounted for in detail by means of the SEICS code (Simulation of Energetic Ions and Clusters through Solids), which has been described elsewhere [41, 42]. By combining molecular dynamics and Monte Carlo techniques, the SEICS code incorporates the electronic energy loss of the projectile (including stochastic fluctuations), multiple Coulomb scattering and elastic energy loss, electron charge exchange processes, as well as the nuclear fragmentation reactions induced by the incoming projectile. The energy distribution of the electrons generated by each proton are obtained from the corresponding cross-sections evaluated according to a recently developed semi-empirical model [43].

Due to the interaction with the target atoms (electrons and nuclei), the projectile energy degrades as it moves along the target. Therefore the proton beam has an energy distribution that broadens as it reaches deeper regions in the target. As the ionization cross section is a function of the projectile energy, the energy spectra of the electrons generated along the proton track are obtained by convoluting the energy distribution of the primary proton beam at each depth (obtained with the SEICS code) with the differential ionization cross section with respect to the electron ejection energy.

As a consequence of the energy delivered by a swift proton along its path, electrons are emitted due to ionization of the target atoms. These electrons move away from the region where they originated experiencing elastic and inelastic scattering with the target constituents, generating secondary electrons. These, in turn, produce new ionizations, which result in an avalanche of electrons [44, 45].

9.3.4 Radial Distribution of the Energy Deposited in PMMA by Secondary Electrons Generated by Energetic Proton Beams

The energy distributions of the electrons generated by each proton were evaluated according to a semi-empirical model described in Ref. [43]. Their cumulative probabilities were used to calculate the initial energy of each electron. Then the secondary

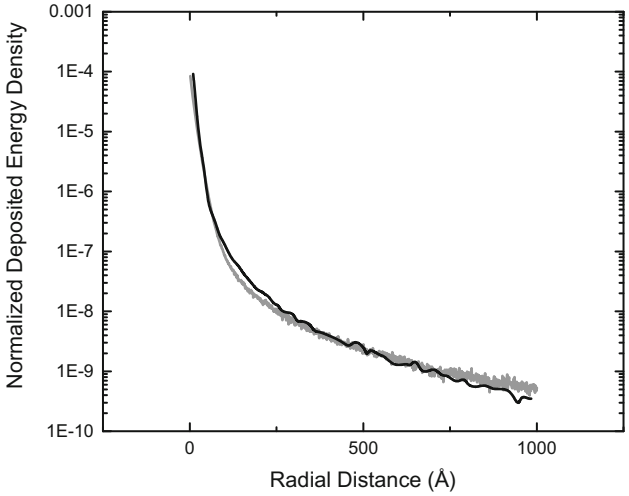

Fig. 9.7 Deposited energy density at a given radial distance away from a 3 MeV proton track in PMMA by the secondary electrons. *Gray line* Monte Carlo data. *Black line* Udalagama et al. data [46]. The initial energy distribution of the secondary electrons generated by the proton impact with the PMMA target atoms was calculated according to a semi-empirical model described in Ref. [43] and kindly provided by the authors

electron avalanche was followed in order to calculate the energy density radially deposited in the PMMA target along the proton track. The Monte Carlo simulated energy density radially deposited by the secondary electrons for a 3 MeV proton beam impinging on PMMA is presented in Fig. 9.7, where the Udalagama et al. results are also shown for a comparison.

9.4 Summary

In this chapter we described some applications of the Monte Carlo method in nanometrology, doping contrast and proton therapy.

In particular, some fundamental aspects related to a possible use of the Monte Carlo code for line width measurements by secondary electron imaging at very low primary beam energy were discussed. In order to extract information about critical dimensions for accurate nanometrology in CMOS processes, we described Monte Carlo investigation of the physics of image formation in scanning electron microscopy [6].

Furthermore, Monte Carlo simulation demonstrated that secondary electrons leaving the material with lower kinetic energy are generated deeper in the specimen compared to those with higher energy. As a consequence, as the built-in potential is smaller close to the surface, selecting low energy secondary electrons – instead

of permitting all the secondary electrons to form the image – enhances contrast, thus improving the quality of the measurement of two dimensional dopant atom distributions [24].

Starting from a realistic description of the energy and angular distribution of the electrons ejected by protons moving through PMMA [43], the simulation of the emission of secondary electrons was used to calculate electron-energy deposition (due to the entire cascade of the generated electrons) around the ion track, for different depths in the target.

References

1. A. Koschik, M. Ciappa, S. Holzer, M. Dapor, W. Fichtner, Proc. SPIE **7729**, 77290X-1 (2010)
2. C.G. Frase, D. Gnieser, H. Bosse, J. Phys. D: Appl. Phys. **42**, 183001 (2009)
3. J.S. Villarrubia, A.E. Vladár, B.D. Bunday et al., Proc. SPIE **5375**, 199 (2004)
4. J.S. Villarrubia, A.E. Vladár, M.T. Postek, Surf. Interface Anal. **37**, 951 (2005)
5. J.S. Villarrubia, N. Ritchie, J.R. Lowney, Proc. SPIE **6518**, 65180K (2007)
6. M. Ciappa, A. Koschik, M. Dapor, W. Fichtner, Microelectron. Reliab. **50**, 1407 (2010)
7. J.P. Ganachaud, A. Mokrani, Surf. Sci. **334**, 329 (1995)
8. M. Dapor, M. Ciappa, W. Fichtner, J. Micro/Nanolith, MEMS MOEMS **9**, 023001 (2010)
9. M. Dapor, Nucl. Instrum. Methods Phys. Res. B **269**, 1668 (2011)
10. F. Salvat, J.M. Fernández-Varea, E. Acosta, J. Sempau, *PENELOPE: A Code System for Monte Carlo Simulation of Electron and Photon Transport* (Nuclear Energy Agency - Organisation for Economic Cooperation and Development Publishing, 2001)
11. J. Baró, J. Sempau, J.M. Fernández-Varea, F. Salvat, Nucl. Instrum. Methods Phys. Res. B **84**, 465 (1994)
12. J.M. Fernández-Varea J. Baró, J. Sempau, F. Salvat, Nucl. Instrum. Methods Phys. Res. B **100**, 31 (1995)
13. M. Dapor, B.J. Inkson, C. Rodenburg, J.M. Rodenburg, Europhys. Lett. **82**, 30006 (2008)
14. A. Howie, Microsc. Microanal. **6**, 291 (2000)
15. A. Shih, J. Yater, P. Pehrrson, J. Buttler, C. Hor, R. Abrams, J. Appl. Phys. **82**, 1860 (1997)
16. F. Iwase, Y. Nakamura, S. Furuya, Appl. Phys. Lett. **64**, 1404 (1994)
17. F. Iwase, Y. Nakamura, Appl. Phys. Lett. **71**, 2142 (1997)
18. D.D. Perovic, M.R. Castell, A. Howie, C. Lavoie, T. Tiedje, J.S.W. Cole, Ultramicroscopy **58**, 104 (1995)
19. D. Venables, H. Jain, D.C. Collins, J. Vac. Sci. Technol. B **16**, 362 (1998)
20. S.L. Elliott, R.F. Broom, C.J. Humphreys, J. Appl. Phys. **91**, 9116 (2002)
21. T.H.P. Chang, W.C. Nixon, Solid-State Electron. **10**, 701 (1967)
22. N. Ashcroft, N.D. Mermin, *Solid State Physics*, (W.B Saunders, 1976)
23. P. Kazemian, *Progress towards Quantitive Dopant Profiling with the Scanning Electron Microscope* (Doctorate Dissertation, University of Cambridge, 2006)
24. C. Rodenburg, M.A.E. Jepson, E.G.T. Bosch, M. Dapor, Ultramicroscopy **110**, 1185 (2010)
25. A.K.W. Chee, C. Rodenburg, C.J. Humphreys, Mater. Res. Soc. Symp. Proc. **1026**, C04–02 (2008)
26. T. Koshikawa, R. Shimizu, J. Phys. D. Appl. Phys. **7**, 1303 (1974)
27. H.J. Fitting, E. Schreiber, JCh. Kuhr, A. von Czarnowski, J. Electron. Spectrosc. Relat. Phenom. **119**, 35 (2001)
28. L. Anchordoqui, T. Paul, S. Reucroft, J. Swain, Int. J. Modern Phys. A **18**, 2229 (2003)
29. T. Kanai, Y. Furusawa, K. Fukutsu, H. Itsukaichi, K. Eguchi-Kasai, H. Ohara, Radiat. Res. **147**, 78 (1997)

30. M. Krämer, O. Jäkel, T. Haberer, G. Kraft, D. Schardt, U. Weber, Phys. Med. Biol. **45**, 3299 (2000)
31. I. Turesson, K.-A. Johansson, S. Mattsson, Acta Oncologica **42**, 107 (2003)
32. A. Brahme, Int. J. Radiat. Oncol. Biol. Phys. **58**, 603 (2004)
33. D. Schulz-Ertner, H. Tsujii, J. Clin. Oncol. **25**, 953 (2007)
34. T. Elsässer, W.K. Weyrather, T. Friedrich, M. Durante, G. Iancu, M. Krämer, G. Kragl, S. Brons, M. Winter, K.-J. Weber, M. Scholz, Int. J. Radiat. Oncol. Biol. Phys. **78**, 1177 (2010)
35. M. Durante, J. Loeffler, Nat. Rev. Clin. Oncol. **7**, 37 (2010)
36. J.S. Loeffler, M. Durante, Nat. Rev. Clin. Oncol. **10**, 411 (2013)
37. E. Scifoni, Modern Phys. Lett. A **30**, 1540019 (2015)
38. R. Baskar, K.A. Lee, R. Yeo, K.-W. Yeoh, Int. J. Med. Sci. **9**, 193 (2012)
39. B. Boudaïffa, P. Cloutier, D. Hunting, M.A. Huels, L. Sanche, Science **287**, 1658 (2000)
40. X. Pan, P. Cloutier, D. Hunting, L. Sanche, Phys. Rev. Lett. **90**, 20812 (2003)
41. R. Garcia-Molina, I. Abril, S. Heredia-Avalos, I. Kyriakou, D. Emfietzoglou, Phys. Med. Biol. **56**, 6475 (2011)
42. R. Garcia-Molina, I. Abril, P. de Vera, I. Kyriakou, D. Emfietzoglou, Proton beam irradiation of liquid water: a combined molecular dynamics and Monte Carlo simulation study of the Bragg peak profile, in *Fast Ion-Atom and Ion-Molecule Collisions*, ed. by D. Belkic, Chap. 8, pp. 271–304 (World Scientific Publishing Company, Singapore, 2012)
43. P. de Vera, R. Garcia-Molina, I. Abril, A.V. Solov'yov, Phys. Rev. Lett. **110**, 148104 (2013)
44. M. Dapor, I. Abril, P. de Vera, R. Garcia-Molina, Eur. Phys. J. D **69**, 165 (2015)
45. M. Dapor, I. Abril, P. de Vera, R. Garcia-Molina, Int. J. Chem. Mol. Nucl. Mater. Metall. Eng. **10**, 965 (2016)
46. C. Udalagama, A.A. Bettiol, F. Watt, Phys. Rev. B **80**, 224107 (2009)

Chapter 10
Appendix A: The First Born Approximation and the Rutherford Cross-Section

The Rutherford formula describes the non-relativistic problem of electron–atom elastic scattering. It can be deduced by solving the Schrödinger equation in the first Born approximation [1].

10.1 The Elastic Scattering Cross-Section

The solid angle $d\Omega$ depends on the scattering angles $[\theta, \theta + d\theta]$ and the azimuthal angles $[\phi, \phi + d\phi]$. The differential elastic scattering cross-section $d\sigma/d\Omega$ is defined as the ratio between the flux of particles per unit of time emerging in the solid angle $d\Omega$ (divided by $d\Omega$) and the incident flux.

The flux of particles per unit time emerging after the collision in the solid angle $d\Omega$ depends on the component j_r of the current density in the outgoing direction from the centre of the atomic nucleus. The number of electrons emerging in the solid angle $d\Omega$ per unit time is given by $j_r r^2\, d\Omega$ (note that $r^2\, d\Omega$ is the cross-sectional area normal to the radius).

Let us consider a beam of incident electrons in the direction z normalised to one particle per unit of volume. Let $K = m\upsilon/\hbar$ be the electron momentum in the z direction, where υ is the electron velocity, m the electron mass and $\hbar$ the Planck constant divided by 2π. This beam can be represented by the plane wave $\exp(iKz)$.

Since the incident beam has been normalised to one particle per unit of volume, then the electron velocity υ is the incident flux. As a consequence,

$$I(\theta, \phi) \equiv \frac{d\sigma}{d\Omega} = \frac{j_r r^2\, d\Omega}{\upsilon\, d\Omega} = \frac{j_r r^2}{\upsilon}\,. \tag{10.1}$$

At a large distance from the atomic nucleus, the potential $V(r)$ is negligible and the scattered particles can be described by a spherical wave, i.e. a function which is proportional to $\exp(iKr)/r$. If $f(\theta, \phi)$ is the constant of proportionality (scattering

M. Dapor, *Transport of Energetic Electrons in Solids*,
Springer Tracts in Modern Physics 257, DOI 10.1007/978-3-319-47492-2_10

amplitude), then the wave function $\Psi(\boldsymbol{r})$ of the whole scattering process (i.e. of the incident and the scattered electrons) satisfies the boundary conditions

$$\Psi(r) \underset{r\to\infty}{\sim} \exp(iKz) + f(\theta,\phi)\frac{\exp(iKr)}{r} \,. \tag{10.2}$$

The electron position probability density P is given by $|\Psi|^2 = \Psi^*\Psi$, and the current density $\boldsymbol{j}(\boldsymbol{r},t)$ is

$$\boldsymbol{j}(\boldsymbol{r},t) = \frac{i\hbar}{2m}[(\nabla\Psi^*)\Psi - \Psi^*(\nabla\Psi)] \,. \tag{10.3}$$

Let us now calculate the radial component of the current density $\boldsymbol{j}$, j_r:

$$\begin{aligned} j_r = \; & \frac{i\hbar}{2m}\left\{ f(\theta,\phi)\frac{\exp(iKr)}{r}\frac{\partial}{\partial r}\left[f^*(\theta,\phi)\frac{\exp(-iKr)}{r}\right]\right. \\ - \; & \left. f^*(\theta,\phi)\frac{\exp(-iKr)}{r}\frac{\partial}{\partial r}\left[f(\theta,\phi)\frac{\exp(iKr)}{r}\right]\right\} \\ = \; & \frac{v|f(\theta,\phi)|^2}{r^2} \,. \end{aligned} \tag{10.4}$$

Comparing this equation with (10.1), we can see that the differential elastic scattering cross-section is the square of the modulus of $f(\theta,\phi)$:

$$I(\theta,\phi) = \frac{d\sigma}{d\Omega} = |f(\theta,\phi)|^2 \,. \tag{10.5}$$

10.2 The First Born Approximation

The first Born approximation is a high-energy approximation. If E is the incident electron energy, e the electron charge, a_0 the Bohr radius and Z the target atomic number, the first Born approximation is quite accurate if

$$E \gg \frac{e^2}{2a_0}Z^2 \,. \tag{10.6}$$

10.3 Integral-Equation Approach

Let us now introduce the Green function and the integral-equation approach. Starting from the Schrödinger equation,

$$(\nabla^2 + \boldsymbol{K}^2)\Psi(\boldsymbol{r}) = \frac{2m}{\hbar^2} V(r)\Psi(\boldsymbol{r}) \,, \tag{10.7}$$

with the boundary condition expressed by (10.2), it is possible to show that this is a problem equivalent to the following integral equation:

$$\Psi(\boldsymbol{r}) = \exp(iKz) + \frac{2m}{\hbar^2} \int d^3r' g(\boldsymbol{r}, \boldsymbol{r}') V(\boldsymbol{r}') \Psi(\boldsymbol{r}') \,, \tag{10.8}$$

in which

$$g(\boldsymbol{r}, \boldsymbol{r}') = -\frac{\exp(iK|\boldsymbol{r} - \boldsymbol{r}'|)}{4\pi|\boldsymbol{r} - \boldsymbol{r}'|} \tag{10.9}$$

is the Green function of the operator $\nabla^2 + \boldsymbol{K}^2$. As is known, this operator satisfies the equation

$$(\nabla^2 + \boldsymbol{K}^2) g(\boldsymbol{r}, \boldsymbol{r}') = \delta(\boldsymbol{r} - \boldsymbol{r}') \,, \tag{10.10}$$

where $\delta(\boldsymbol{r} - \boldsymbol{r}')$ is the Dirac delta function.

Let us apply the operator $\nabla^2 + \boldsymbol{K}^2$ to the function $\Psi(\boldsymbol{r})$ defined by the integral Eq. (10.8):

$$\begin{aligned} (\nabla^2 + \boldsymbol{K}^2)\Psi(\boldsymbol{r}) = \; & (\nabla^2 + \boldsymbol{K}^2) \exp(iKz) \\ & + \frac{2m}{\hbar^2} \int d^3r' (\nabla^2 + \boldsymbol{K}^2) g(\boldsymbol{r}, \boldsymbol{r}') V(\boldsymbol{r}') \Psi(\boldsymbol{r}') \,. \end{aligned} \tag{10.11}$$

The application of the operator ∇^2 to the plane wave $\exp(iKz)$ gives

$$\nabla^2 \exp(iKz) = \frac{\partial^2}{\partial z^2} \exp(iKz) = -K^2 \exp(iKz) \tag{10.12}$$

and, as a consequence, we can write

$$(\nabla^2 + \boldsymbol{K}^2) \exp(iKz) = 0 \,. \tag{10.13}$$

Therefore,

$$\begin{aligned} (\nabla^2 + \boldsymbol{K}^2)\Psi(\boldsymbol{r}) = \; & \frac{2m}{\hbar^2} \int d^3r' (\nabla^2 + \boldsymbol{K}^2) g(\boldsymbol{r}, \boldsymbol{r}') V(\boldsymbol{r}') \Psi(\boldsymbol{r}') \\ = \; & \frac{2m}{\hbar^2} \int d^3r' \delta(\boldsymbol{r} - \boldsymbol{r}') V(\boldsymbol{r}') \Psi(\boldsymbol{r}') \\ = \; & \frac{2m}{\hbar^2} V(\boldsymbol{r}) \Psi(\boldsymbol{r}) \,. \end{aligned} \tag{10.14}$$

For the boundary conditions, we have

$$\begin{aligned} |\boldsymbol{r}-\boldsymbol{r}'| &= \sqrt{\boldsymbol{r}^2-2\boldsymbol{r}\cdot\boldsymbol{r}'+\boldsymbol{r}'^2} \\ &= r\sqrt{1-\frac{2\hat{\boldsymbol{r}}\cdot\boldsymbol{r}'}{r}+\frac{\boldsymbol{r}'^2}{\boldsymbol{r}^2}} \\ &\sim r\left(1-\frac{\hat{\boldsymbol{r}}\cdot\boldsymbol{r}'}{r}+O\left(\frac{1}{\boldsymbol{r}^2}\right)\right) . \end{aligned} \tag{10.15}$$

Note that in the last equation,

$$\hat{\boldsymbol{r}}=\frac{\boldsymbol{r}}{r} . \tag{10.16}$$

Let us introduce $\mathcal{K}$, the wave number in the direction of the outgoing unit vector $\hat{\boldsymbol{r}}$,

$$\mathcal{K}\equiv K\hat{\boldsymbol{r}} . \tag{10.17}$$

So the Green function for the operator $\nabla^2+\boldsymbol{K}^2$, expressed by (10.9), has the following asymptotic behaviour:

$$g(\boldsymbol{r},\boldsymbol{r}') \underset{r\to\infty}{\sim} -\frac{\exp(iKr-i\mathcal{K}\cdot\boldsymbol{r}')}{4\pi r} . \tag{10.18}$$

Let us now introduce the asymptotic behaviour of the Green function (10.18) into the integral Eq. (10.8):

$$\Psi(\boldsymbol{r}) \underset{r\to\infty}{\sim} \exp(iKz)-\frac{2m}{\hbar^2}\int d^3r'\frac{\exp(iKr-i\mathcal{K}\cdot\boldsymbol{r}')}{4\pi r}V(\boldsymbol{r}')\Psi(\boldsymbol{r}') . \tag{10.19}$$

From the equation

$$\begin{aligned} &\int d^3r'\frac{\exp(iKr-i\mathcal{K}\cdot\boldsymbol{r}')}{4\pi r}V(\boldsymbol{r}')\Psi(\boldsymbol{r}') \\ &= \frac{\exp(iKr)}{r}\int d^3r'\frac{\exp(-i\mathcal{K}\cdot\boldsymbol{r}')}{4\pi}V(\boldsymbol{r}')\Psi(\boldsymbol{r}') , \end{aligned} \tag{10.20}$$

we can conclude that, if the scattering amplitude is given by

$$f(\theta,\phi)=-\frac{m}{2\pi\hbar^2}\int d^3r\exp(-i\mathcal{K}\cdot\boldsymbol{r})\,V(\boldsymbol{r})\Psi(\boldsymbol{r}) , \tag{10.21}$$

then the boundary conditions are satisfied. In (10.21), $\mathcal{K}$ is the wave number of the scattered particles, and $\Psi(\boldsymbol{r})$ is the scattering wave function.

Let us suppose that the ratio between the electron kinetic energy and the atomic potential energy is high enough to make the scattering weak and $\Psi(\boldsymbol{r})$ not very different from the incident plane wave $\exp(i\,K\,z)$. This is the assumption which is the basis of the first Born approximation, i.e.

$$\Psi(\boldsymbol{r}) = \exp(i\,K\,z) = \exp(i\,\boldsymbol{K}\cdot\boldsymbol{r})\ . \tag{10.22}$$

Utilising the first Born approximation, expressed by (10.22), the previous Eq. (10.21) becomes

$$f(\theta,\phi) = -\frac{m}{2\pi\hbar^2}\int d^3r\,\exp(-i\boldsymbol{\mathcal{K}}\cdot\boldsymbol{r})\,V(\boldsymbol{r})\,\exp(i\,\boldsymbol{K}\cdot\boldsymbol{r})\ . \tag{10.23}$$

If we use $\hbar\boldsymbol{q}$ to indicate the momentum lost by the incident electron,

$$\hbar\boldsymbol{q} = \hbar(\boldsymbol{K}-\boldsymbol{\mathcal{K}})\ , \tag{10.24}$$

for fast particles we can write that

$$f(\theta,\phi) = -\frac{m}{2\pi\hbar^2}\int d^3r\,\exp(i\boldsymbol{q}\cdot\boldsymbol{r})\,V(\boldsymbol{r})\ . \tag{10.25}$$

As we are interested in a central potential, then

$$V(\boldsymbol{r}) = V(r)\ , \tag{10.26}$$

and as a result,

$$\begin{aligned} f(\theta,\phi) &= f(\theta) \\ &= -\frac{m}{2\pi\hbar^2}\int_0^{2\pi} d\phi\int_0^{\pi}\sin\theta\,d\theta\int_0^{\infty} r^2\,dr\ \exp(iqr\cos\theta)\,V(r)\ . \end{aligned} \tag{10.27}$$

We carry out the integrations over ϕ and over θ and obtain

$$f(\theta) = -\frac{2m}{\hbar^2 q}\int_0^{\infty}\sin(qr)\,V(r)\,r\,dr\ . \tag{10.28}$$

10.4 The Rutherford Formula

Let us calculate the differential elastic scattering cross-sections in the first Born approximation for a screened Coulomb potential, such as a Wentzel-like potential [2],

$$V(r) = -\frac{Ze^2}{r}\exp\left(-\frac{r}{a}\right) . \tag{10.29}$$

The exponential factor here represents a rough approximation of the screening of the nucleus by the orbital electrons, while the a parameter is

$$a = \frac{a_0}{Z^{1/3}} , \tag{10.30}$$

where $a_0 = \hbar^2/me^2$ is the Bohr radius.

Let us calculate the scattering amplitude:

$$f(\theta) = \frac{2m}{\hbar^2}\frac{Ze^2}{q}\int_0^\infty \sin(qr)\,\exp\left(-\frac{r}{a}\right)\,dr . \tag{10.31}$$

As the equation

$$\int_0^\infty \sin(qr)\,\exp\left(-\frac{r}{a}\right)\,dr = \frac{q}{q^2 + (1/a)^2} \tag{10.32}$$

holds, we can conclude that

$$\frac{d\sigma}{d\Omega} = |f(\theta)|^2 = \frac{4m^2}{\hbar^4}\frac{Z^2e^4}{[q^2 + (1/a)^2]^2} . \tag{10.33}$$

On the other hand, $|\boldsymbol{K}| = |\boldsymbol{\mathcal{K}}|$ and $\boldsymbol{q} = \boldsymbol{K} - \boldsymbol{\mathcal{K}}$, and, as a consequence

$$\begin{aligned} \boldsymbol{q}^2 &= (\boldsymbol{K} - \boldsymbol{\mathcal{K}})\cdot(\boldsymbol{K} - \boldsymbol{\mathcal{K}}) \\ &= \boldsymbol{K}^2 + \boldsymbol{\mathcal{K}}^2 - 2K\mathcal{K}\cos\theta \\ &= 2\boldsymbol{K}^2(1 - \cos\theta) , \end{aligned} \tag{10.34}$$

where θ is the scattering angle.

The electron kinetic energy is given by

$$E = \frac{\hbar^2\boldsymbol{K}^2}{2m} , \tag{10.35}$$

so that the differential elastic scattering cross-section for the collision of an electron beam with a Wentzel-like atomic potential is given in the first Born approximation by

$$\frac{d\sigma}{d\Omega} = \frac{Z^2 e^4}{4E^2} \frac{1}{(1 - \cos\theta + \alpha)^2} \,. \tag{10.36}$$

In the last equation, α is the *screening parameter*, given by

$$\alpha = \frac{1}{2K^2 a^2} = \frac{m e^4 \pi^2}{h^2} \frac{Z^{2/3}}{E} \,. \tag{10.37}$$

The well-known classical Rutherford formula,

$$\frac{d\sigma}{d\Omega} = \frac{Z^2 e^4}{4E^2} \frac{1}{(1 - \cos\theta)^2} \,, \tag{10.38}$$

can be obtained by imposing $\alpha = 0$ in (10.36).

The total elastic scattering cross-section can be obtained from

$$\sigma_{el} = \int \frac{d\sigma}{d\Omega} d\Omega \,. \tag{10.39}$$

For a Wentzel-like potential, the total elastic scattering cross-section can be easily calculated as follows:

$$\begin{aligned} \sigma_{el} &= \frac{Z^2 e^4}{4E^2} \int_0^{2\pi} d\phi \int_0^{\pi} \sin\vartheta \, d\vartheta \frac{1}{(1 - \cos\vartheta + \alpha)^2} \\ &= \frac{\pi Z^2 e^4}{E^2} \frac{1}{\alpha(2 + \alpha)} \,. \end{aligned} \tag{10.40}$$

If $\alpha \to 0$ and, as a consequence, the differential elastic scattering cross-section is given by the classical Rutherford formula, the total elastic scattering cross-section diverges, reflecting the long-range nature of the pure Coulomb potential.

The elastic mean free path is the reciprocal of the total elastic scattering cross-section divided by the number N of atoms per unit of volume in the target:

$$\lambda_{el} = \frac{1}{N\sigma_{el}} = \frac{\alpha(2 + \alpha)E^2}{N\pi e^4 Z^2} \,. \tag{10.41}$$

10.5 Summary

In this chapter we have deduced the Rutherford formula by solving the Schrödinger equation in a central field in the first Born approximation.

References

1. J.E.G. Farina, *The International Encyclopedia of Physical Chemistry and Chemical Physics*, vol. 4 (Pergamon, Oxford, 1973)
2. G. Wentzel, Z. Phys. **40**, 590 (1927)

Chapter 11
Appendix B: The Mott Theory

The original version of the Mott theory (also known as the relativistic partial wave expansion method, RPWEM) can be found in Ref. [1]. Also see Refs. [2–4] for details and applications.

According to Mott, the elastic scattering process can be described by calculating the so-called phase shifts. If we indicate with r the radial coordinate, since the large-r asymptotic behavior of the radial wave function is known, the phase shifts can be computed by solving the Dirac equation for a central electrostatic field up to a large radius where the atomic potential can be neglected.

11.1 The Dirac Equation in a Central Potential

In order to appropriately treat the quantum-relativistic scattering theory, we need to know the form assumed by the Dirac equation for an electron in the presence of a central electrostatic field described by a central potential $e\varphi(r) = V(r)$. The natural units $\hbar = c = 1$ are used here and in the following section, as they are particularly convenient for the quantum-relativistic equations.

Let us first introduce the operator $\mathcal{K}$ defined by

$$\mathcal{K} \equiv \beta(1 + \boldsymbol{\sigma} \cdot \boldsymbol{L}) \,, \tag{11.1}$$

where $\boldsymbol{L}$ is the electron orbital angular momentum. For an electron in a central electrostatic field, it is possible to show that

$$2\frac{d\boldsymbol{L}}{dt} = -\frac{d\boldsymbol{\sigma}}{dt} \,. \tag{11.2}$$

M. Dapor, *Transport of Energetic Electrons in Solids*,
Springer Tracts in Modern Physics 257, DOI 10.1007/978-3-319-47492-2_11

As a consequence, the total angular momentum, defined as $\boldsymbol{J} = \boldsymbol{L} + (1/2)\boldsymbol{\sigma}$, is a constant of the motion. On the other hand,

$$\boldsymbol{J}^2 - \boldsymbol{L}^2 = \boldsymbol{\sigma} \cdot \boldsymbol{L} + \frac{3}{4} , \tag{11.3}$$

so we can conclude that

$$\mathcal{K} = \beta(\boldsymbol{J}^2 - \boldsymbol{L}^2 + 1/4) . \tag{11.4}$$

$\mathcal{K}$ commutes with H and is, as a consequence, a constant of the motion.

Let us now define the radial-momentum operator p_r, where

$$p_r \equiv -i\frac{1}{r}\frac{\partial}{\partial r}r = \frac{\boldsymbol{r} \cdot \boldsymbol{p} - i}{r} , \tag{11.5}$$

and introduce the radial component α_r of the α operator, where

$$\alpha_r = \frac{\boldsymbol{\alpha} \cdot \boldsymbol{r}}{r} ; \tag{11.6}$$

this obeys the relation

$$\alpha_r^2 = 1 . \tag{11.7}$$

For any pair of vectors $\boldsymbol{a}$ and $\boldsymbol{b}$, the following equations hold:

$$(\boldsymbol{\sigma} \cdot \boldsymbol{a})(\boldsymbol{\sigma} \cdot \boldsymbol{b}) = \boldsymbol{a} \cdot \boldsymbol{b} + i\boldsymbol{\sigma} \cdot \boldsymbol{a} \times \boldsymbol{b} \tag{11.8}$$

and

$$(\boldsymbol{\alpha} \cdot \boldsymbol{a})(\boldsymbol{\alpha} \cdot \boldsymbol{b}) = (\boldsymbol{\sigma} \cdot \boldsymbol{a})(\boldsymbol{\sigma} \cdot \boldsymbol{b}) . \tag{11.9}$$

As a consequence,

$$(\boldsymbol{\alpha} \cdot \boldsymbol{r})(\boldsymbol{\alpha} \cdot \boldsymbol{p}) = rp_r + i\beta\mathcal{K} . \tag{11.10}$$

This last equation is equivalent to

$$(\boldsymbol{\alpha} \cdot \boldsymbol{p}) = \alpha_r \left(p_r + \frac{i\beta\mathcal{K}}{r} \right) . \tag{11.11}$$

As a result, the Dirac equation with the Hamiltonian

$$H = \alpha_r \left(p_r + \frac{i\beta\mathcal{K}}{r} \right) + \beta m + V(r) \tag{11.12}$$

can be rewritten as the following:

$$\left[\alpha_r \left(p_r + \frac{i\beta\mathcal{K}}{r}\right) + \beta m + V(r)\right]\phi = E\phi \ . \tag{11.13}$$

The operators β, $\mathcal{K}$, L^2 and J_z are mutually commutative. In the following, $\mathcal{X}$ indicates an eigenvector common to those operators, so that

$$\beta\mathcal{X} = \mathcal{X} \ , \tag{11.14}$$

$$\mathcal{K}\mathcal{X} = -k\mathcal{X} \ , \tag{11.15}$$

$$\boldsymbol{L}^2\mathcal{X} = l(l+1)\mathcal{X} \ , \tag{11.16}$$

$$J_z\mathcal{X} = m_j\mathcal{X} \ . \tag{11.17}$$

Introducing the function $\mathcal{Y}$, where

$$\mathcal{Y} = -\alpha_r\mathcal{X} \ , \tag{11.18}$$

we can observe that it has the following properties:

$$\mathcal{X} = -\alpha_r\mathcal{Y} \ , \tag{11.19}$$

$$\mathcal{K}\mathcal{Y} = -k\mathcal{Y} \ , \tag{11.20}$$

$$\beta\mathcal{Y} = \alpha_r\beta\mathcal{X} = -\mathcal{Y} \ . \tag{11.21}$$

Let us now consider the following linear combination of $\mathcal{X}$ and $\mathcal{Y}$:

$$\phi = F(r)\mathcal{Y} + iG(r)\mathcal{X} \ , \tag{11.22}$$

which is an eigenvector common to H, $\mathcal{K}$ and J_z and thus the spinor we are looking for.

Our objective is to determine the functions $F(r)$ and $G(r)$. The eigenvalues of $\boldsymbol{L}^2$ are $(j \pm 1/2)(j \pm 1/2 + 1)$. As $\mathcal{K} = \beta(\boldsymbol{J}^2 - \boldsymbol{L}^2 + 1/4)$, the eigenvalues of $\mathcal{K}$ for the case $j = l + 1/2$ (spin up) are therefore given by

$$k = -\left(j + \frac{1}{2}\right) = -(l+1) \ . \tag{11.23}$$

In the other case, where $j = l - 1/2$ (spin down), the eigenvalues of $\mathcal{K}$ are

$$k = \left(j + \frac{1}{2}\right) = l \ . \tag{11.24}$$

We are now able to find the equations corresponding to the radial behaviour of the functions F and G. In order to do this, let us consider the Dirac equation (11.13) and observe the following:

$$\alpha_r p_r F(r)\mathcal{Y} = i\left[\frac{dF(r)}{dr} + \frac{F(r)}{r}\right]\mathcal{X}\,, \tag{11.25}$$

$$i\alpha_r p_r G(r)\mathcal{X} = -\left[\frac{dG(r)}{dr} + \frac{G(r)}{r}\right]\mathcal{Y}\,, \tag{11.26}$$

$$\frac{i\alpha_r\beta\mathcal{K}}{r}F(r)\mathcal{Y} = -\frac{i}{r}F(r)k\mathcal{X}\,, \tag{11.27}$$

$$\frac{i\alpha_r\beta\mathcal{K}}{r}iG(r)\mathcal{X} = -\frac{1}{r}G(r)k\mathcal{Y}\,, \tag{11.28}$$

$$\beta m F(r)\mathcal{Y} = -mF(r)\mathcal{Y}\,, \tag{11.29}$$

$$\beta m i G(r)\mathcal{X} = imG(r)\mathcal{X}\,. \tag{11.30}$$

Hence, since $\mathcal{X}$ and $\mathcal{Y}$ belong to different eigenvalues of β and are, consequently, linearly independent, the fundamental equations of the theory of the elastic scattering of electrons (and positrons) by atoms are

$$[E + m - V(r)]F(r) + \frac{dG(r)}{dr} + \frac{1+k}{r}G(r) = 0\,, \tag{11.31}$$

$$-[E - m - V(r)]G(r) + \frac{dF(r)}{dr} + \frac{1-k}{r}F(r) = 0\,. \tag{11.32}$$

11.2 Relativistic Partial Wave Expansion Method

The fundamental equation of relativistic quantum mechanics is the Dirac equation. The wave function, as is well known, is a four-component spinor, and the asymptotic forms of the four components of the scattered wave are

$$\Psi_i \underset{r\to\infty}{\sim} a_i \exp(iKz) + b_i(\theta,\phi)\frac{\exp(iKr)}{r}\,. \tag{11.33}$$

The differential elastic scattering cross-section is given by

$$\begin{aligned}\frac{d\sigma}{d\Omega} &= \frac{|b_1|^2+|b_2|^2+|b_3|^2+|b_4|^2}{|a_1|^2+|a_2|^2+|a_3|^2+|a_4|^2} \\ &= \frac{|b_1|^2+|b_2|^2+c|b_1|^2+c|b_2|^2}{|a_1|^2+|a_2|^2+c|a_1|^2+c|a_2|^2} \\ &= \frac{|b_1|^2+|b_2|^2}{|a_1|^2+|a_2|^2}, \end{aligned} \tag{11.34}$$

where c is a constant of proportionality which takes into account the fact that the a_i and the b_i coefficients are not all independent. Indeed, asymptotically the scattered wave is made up of plane waves proceeding, from the centre, in various directions; the coefficients of the solutions for a plane wave are not all independent.

If the spin is parallel to the direction of incidence (spin up), $a_1 = 1, a_2 = 0$, $b_1 = f^+(\theta,\phi), b_2 = g^+(\theta,\phi)$, where f^+ and g^+ are two scattering amplitudes.

The asymptotic behaviour is described by the following equations:

$$\Psi_1 \underset{r\to\infty}{\sim} \exp(iKz) + f^+(\theta,\phi)\frac{\exp(iKr)}{r}\,, \tag{11.35}$$

$$\Psi_2 \underset{r\to\infty}{\sim} g^+(\theta,\phi)\frac{\exp(iKr)}{r}\,. \tag{11.36}$$

The case of spin antiparallel to the direction of incidence (spin down) corresponds to $a_1 = 0, a_2 = 1, b_1 = g^-(\theta,\phi), b_2 = f^-(\theta,\phi)$. The asymptotic behaviour is now given by

$$\Psi_1 \underset{r\to\infty}{\sim} g^-(\theta,\phi)\frac{\exp(iKr)}{r}\,, \tag{11.37}$$

$$\Psi_2 \underset{r\to\infty}{\sim} \exp(iKz) + f^-(\theta,\phi)\frac{\exp(iKr)}{r}\,. \tag{11.38}$$

The Dirac equations for an electron in a central field are given by the following (see previous section):

$$[E+m-V(r)]F_l^{\pm}(r) + \frac{dG_l^{\pm}(r)}{dr} + \frac{1+k}{r}G_l^{\pm}(r) = 0\,, \tag{11.39}$$

$$-[E-m-V(r)]G_l^{\pm}(r) + \frac{dF_l^{\pm}(r)}{dr} + \frac{1-k}{r}F_l^{\pm}(r) = 0\,. \tag{11.40}$$

The superscript "+" refers to the electrons with spin up ($k = -(l+1)$) while "−" refers to electrons with spin down ($k = l$). Once the new variables

$$\mu(r) \equiv E + m - V(r) \,, \tag{11.41}$$

$$\nu(r) \equiv E - m - V(r) \,, \tag{11.42}$$

$$\mu' = \frac{d\mu}{dr} \tag{11.43}$$

have been introduced, the Dirac equations become

$$F_l^{\pm}(r) = -\frac{1}{\mu}\left(\frac{dG_l^{\pm}}{dr} + \frac{1+k}{r}G_l^{\pm}\right) \tag{11.44}$$

and

$$\begin{aligned}\frac{dF_l^{\pm}}{dr} = & \frac{\mu'}{\mu^2}\left(\frac{dG_l^{\pm}}{dr} + \frac{1+k}{r}G_l^{\pm}\right) \\ & - \frac{1}{\mu}\left(\frac{d^2G_l^{\pm}}{dr^2} + \frac{1+k}{r}\frac{dG_l^{\pm}}{dr} - \frac{1+k}{r^2}G_l^{\pm}\right) \,.\end{aligned} \tag{11.45}$$

Therefore, after simple algebraic manipulations, we obtain the following:

$$\frac{d^2G_l^{\pm}}{dr^2} + \left(\frac{2}{r} - \frac{\mu'}{\mu}\right)\frac{dG_l^{\pm}}{dr} + \left(\mu\nu - \frac{k(k+1)}{r^2} - \frac{1+k}{r}\frac{\mu'}{\mu}\right)G_l^{\pm} = 0 \,. \tag{11.46}$$

Let us now introduce the function $\mathcal{G}_l^{\pm}$, where

$$\mathcal{G}_l^{\pm} \equiv \frac{r}{\mu^{1/2}}G_l^{\pm} \,. \tag{11.47}$$

Upon observing that

$$K^2 = E^2 - m^2 \,, \tag{11.48}$$

it is possible to see that

$$\mu\nu = K^2 - 2EV + V^2 \,. \tag{11.49}$$

We conclude that, once the function $U_l^{\pm}(r)$ has been defined, i.e.

$$-U_l^{\pm}(r) = -2EV + V^2 - \frac{k}{r}\frac{\mu'}{\mu} + \frac{1}{2}\frac{\mu''}{\mu} - \frac{3}{4}\frac{\mu'^2}{\mu^2} \,, \tag{11.50}$$

the following equation holds:

$$\left[\frac{d^2}{dr^2} - \frac{k(k+1)}{r^2} + K^2 - U_l^{\pm}(r)\right]\mathcal{G}_l^{\pm} = 0 \,. \tag{11.51}$$

For large values of r, $\mathcal{G}_l^{\pm}$ is essentially sinusoidal. Indeed, when r is large enough, $V(r)$ is negligible, $U_l^{\pm}$ is almost constant and the solution of the equation is therefore a linear combination of the regular and irregular spherical Bessel functions multiplied by Kr. Taking account of the fact that $\mathcal{G}_l^{\pm} = (r/\mu^{1/2})\, G_l^{\pm}$, we can therefore conclude that

$$G_l^{\pm} \underset{r\to\infty}{\sim} j_l(Kr)\cos\eta_l^{\pm} - n_l(Kr)\sin\eta_l^{\pm} \,. \tag{11.52}$$

Here $\eta_l^{\pm}$ are constants to be determined. Taking into account the asymptotic behaviour of the Bessel functions,

$$j_l(Kr) \underset{r\to\infty}{\sim} \frac{1}{Kr}\sin\left(Kr - \frac{l\pi}{2}\right) \,, \tag{11.53}$$

$$n_l(Kr) \underset{r\to\infty}{\sim} -\frac{1}{Kr}\cos\left(Kr - \frac{l\pi}{2}\right) \,, \tag{11.54}$$

we can conclude that

$$G_l^{\pm} \underset{r\to\infty}{\sim} \frac{1}{Kr}\sin\left(Kr - \frac{l\pi}{2}\right)\cos\eta_l^{\pm} + \frac{1}{Kr}\cos\left(Kr - \frac{l\pi}{2}\right)\sin\eta_l^{\pm} \,. \tag{11.55}$$

Therefore,

$$G_l^{+} \underset{r\to\infty}{\sim} \frac{1}{Kr}\sin\left(Kr - \frac{l\pi}{2} + \eta_l^{+}\right) \,, \tag{11.56}$$

and

$$G_l^{-} \underset{r\to\infty}{\sim} \frac{1}{Kr}\sin\left(Kr - \frac{l\pi}{2} + \eta_l^{-}\right) \,. \tag{11.57}$$

The phase shifts $\eta_l^{\pm}$ represent the effect of the potential $V(r)$ on the phases of the scattered waves.

Before proceeding, we need to demonstrate the following equation:

$$\exp(iKr\cos\theta) = \sum_{l=0}^{\infty}(2l+1)i^l\, j_l(Kr)\, P_l(\cos\theta) \,, \tag{11.58}$$

where $P_l(\cos\theta)$ are the Legendre polynomials and $j_l(Kr)$ the spherical Bessel functions. In order to demonstrate this, let us first observe that a plane wave describing a free particle with the z axis in the direction of $\boldsymbol{K}$ may be expressed as an expansion in a series of Legendre polynomials $P_l(\cos\theta)$:

$$\exp(iKz) = \exp(iKr\cos\theta) = \sum_{l=0}^{\infty} c_l\, j_l(Kr) P_l(\cos\theta)\ . \tag{11.59}$$

Let us define the two new variables $s \equiv Kr$ and $t \equiv \cos\theta$, to have

$$\exp(ist) = \sum_l c_l\, j_l(s) P_l(t)\ . \tag{11.60}$$

Differentiating with respect to s,

$$it\exp(ist) = \sum_l itc_l\, j_l(s) P_l(t) = \sum_l c_l \frac{dj_l(s)}{ds} P_l(t)\ . \tag{11.61}$$

Recalling the properties of the Legendre polynomials, we have:

$$P_l(t) = \frac{(l+1)P_{l+1}(t) + lP_{l-1}(t)}{t(2l+1)}\ . \tag{11.62}$$

Therefore,

$$\begin{aligned} it\exp(ist) &= \sum_l itc_l\, j_l(s) \frac{(l+1)P_{l+1}(t) + lP_{l-1}(t)}{t(2l+1)} \\ &= \sum_l i P_l(t) \left[\frac{l}{2l-1} c_{l-1} j_{l-1}(s) + \frac{l+1}{2l+3} c_{l+1} j_{l+1}(s) \right]\ . \end{aligned} \tag{11.63}$$

On the other hand, it is well known that

$$\frac{dj_l(s)}{ds} = \frac{l}{2l+1} j_{l-1}(s) - \frac{l+1}{2l+1} j_{l+1}(s)\ , \tag{11.64}$$

and as a consequence,

$$it\exp(ist) = \sum_l c_l P_l(t) \left[\frac{l}{2l+1} j_{l-1}(s) - \frac{l+1}{2l+1} j_{l+1}(s) \right]\ . \tag{11.65}$$

Consequently, from (11.63) and (11.65), the following is obtained:

$$\begin{aligned} &\sum_l P_l(t) \left[j_{l-1}(s) l \left(\frac{c_l}{2l+1} - \frac{ic_{l-1}}{2l-1} \right) \right. \\ &\left. - j_{l+1}(s)(l+1) \left(\frac{c_l}{2l+1} + \frac{ic_{l+1}}{2l+3} \right) \right] = 0\ . \end{aligned} \tag{11.66}$$

The Legendre polynomials $P_l(t)$ are linearly independent (orthonormal), and therefore

$$j_{l-1}(s)\, l \left(\frac{c_l}{2l+1} - \frac{i c_{l-1}}{2l-1} \right) = j_{l+1}(s)\,(l+1) \left(\frac{c_l}{2l+1} + \frac{i c_{l+1}}{2l+3} \right) . \tag{11.67}$$

Every value of s satisfies the last equation if and only if

$$\frac{1}{2l+1} c_l = \frac{i}{2l-1} c_{l-1} . \tag{11.68}$$

In order to obtain an explicit expression for c_l we need to know the value of the first coefficient of the set, i.e. c_0. Imposing $r = 0$ in (11.59), we obtain

$$\exp(0) = 1 = \sum_l c_l j_l(0) P_l(\cos\theta) . \tag{11.69}$$

Since $j_l(0) = 0$ for any $l \neq 0$, while $j_0(0) = 1$ and $P_0(\cos\theta) = 1$, we may conclude that $c_0 = 1$. The recursive repetition of the relation (11.68) allows us to obtain the values of the coefficients,

$$c_l = (2l+1) i^l , \tag{11.70}$$

and the expansion of the plane wave in Legendre polynomials,

$$\exp(iKr\cos\theta) = \exp(iKz) = \sum_{l=0}^{\infty} (2l+1) i^l j_l(Kr) P_l(\cos\theta) . \tag{11.71}$$

Let us remind the reader that we are looking for functions Ψ_1 and Ψ_2 which satisfy the asymptotic conditions. So, we must begin by expanding them in spherical harmonics:

$$\Psi_1 = \sum_{l=0}^{\infty} [A_l G_l^+ + B_l G_l^-] P_l(\cos\theta) , \tag{11.72}$$

$$\Psi_2 = \sum_{l=1}^{\infty} [C_l G_l^+ + D_l G_l^-] P_l^1(\cos\theta) \exp(i\phi) . \tag{11.73}$$

The coefficients A_l, B_l, C_l and D_l can be determined by considering the asymptotic behaviours of the functions involved. Let us begin with the function Ψ_1 and observe that

$$\Psi_1 - \exp(iKz) = \sum_{l=0}^{\infty} [A_l G_l^+ + B_l G_l^- - (2l+1) i^l j_l(Kr)] P_l(\cos\theta) \ . \tag{11.74}$$

As

$$\Psi_1 - \exp(iKz) \underset{r\to\infty}{\sim} \frac{\exp(iKr)}{r} f^+(\theta, \phi) \ , \tag{11.75}$$

the following occurs:

$$\begin{aligned} &\frac{1}{Kr} \sum_{l=0}^{\infty} \left[A_l \sin\left(Kr - \frac{l\pi}{2} + \eta_l^+ \right) + B_l \sin\left(Kr - \frac{l\pi}{2} + \eta_l^- \right) \right. \\ &\left. -(2l+1) i^l \sin\left(Kr - \frac{l\pi}{2} \right) \right] P_l(\cos\theta) \\ &= \frac{\exp(iKr)}{r} f^+(\theta, \phi) \ . \end{aligned} \tag{11.76}$$

As a consequence,

$$\begin{aligned} &\frac{\exp(iKr)}{2iKr} \sum_{l=0}^{\infty} \exp\left(-i \frac{l\pi}{2} \right) \\ &\times [A_l \exp(i\eta_l^+) + B_l \exp(i\eta_l^-) - (2l+1) i^l] P_l(\cos\theta) \\ &- \frac{\exp(-iKr)}{2iKr} \sum_{l=0}^{\infty} \exp\left(i \frac{l\pi}{2} \right) \\ &\times [A_l \exp(-i\eta_l^+) + B_l \exp(-i\eta_l^-) - (2l+1) i^l] P_l(\cos\theta) \\ &= \frac{\exp(iKr)}{r} f^+(\theta, \phi) \ . \end{aligned} \tag{11.77}$$

The asymptotic conditions are satisfied if

$$A_l \exp(-i\eta_l^+) + B_l \exp(-i\eta_l^-) = (2l+1) i^l \ . \tag{11.78}$$

With the choices

$$A_l = l i^l \exp(i\eta_l^+) \ , \tag{11.79}$$

$$B_l = (l+1) i^l \exp(i\eta_l^-) \ , \tag{11.80}$$

(11.78) is satisfied.

Proceeding in a similar way for the Ψ_2 function, we can therefore choose

$$C_l = i^l \exp(i\eta_l^+) \ , \tag{11.81}$$

$$D_l = -i^l \exp(i\eta_l^-) \ . \tag{11.82}$$

In conclusion, for electrons with spins parallel to the direction of incidence, we have

$$\Psi_1 = \sum_{l=0}^{\infty}[(l+1)\exp(i\eta_l^-)G_l^- + l\exp(i\eta_l^+)G_l^+]i^l P_l(\cos\theta) \ , \tag{11.83}$$

$$\Psi_2 = \sum_{l=1}^{\infty}[\exp(i\eta_l^+)G_l^+ - \exp(i\eta_l^-)G_l^-]i^l P_l^1(\cos\theta)\exp(i\phi) \ , \tag{11.84}$$

and, by using (11.77),

$$\begin{aligned} f^+(\theta,\phi) &= f^+(\theta) \\ &= \frac{1}{2iK}\sum_{l=0}^{\infty}\{(l+1)[\exp(2i\eta_l^-)-1] \\ &\quad + l[\exp(2i\eta_l^+)-1]\}P_l(\cos\theta) \ , \end{aligned} \tag{11.85}$$

$$g^+(\theta,\phi) = \frac{1}{2iK}\sum_{l=1}^{\infty}[\exp(2i\eta_l^+) - \exp(2i\eta_l^-)]P_l^1(\cos\theta)\exp(i\phi) \ . \tag{11.86}$$

For electrons with spins antiparallel to the direction of incidence (spin down), where we indicate the scattering amplitudes by f^- and g^-, we can see that

$$f^-(\theta,\phi) = f^+(\theta,\phi) \tag{11.87}$$

and

$$g^-(\theta,\phi) = -g^+(\theta,\phi)\exp(-2i\phi) \ . \tag{11.88}$$

It is therefore convenient to define the functions

$$f(\theta) = \sum_{l=0}^{\infty}\mathcal{A}_l P_l(\cos\theta) \ , \tag{11.89}$$

$$g(\theta) = \sum_{l=0}^{\infty}\mathcal{B}_l P_l^1(\cos\theta) \ , \tag{11.90}$$

where

$$\mathcal{A}_l = \frac{1}{2iK}\{(l+1)[\exp(2i\eta_l^-)-1] + l[\exp(2i\eta_l^+)-1]\} \ , \tag{11.91}$$

$$\mathcal{B}_l = \frac{1}{2iK}\{\exp(2i\eta_l^+) - \exp(2i\eta_l^-)\} \ . \tag{11.92}$$

With this notation, we have

$$f^+ = f^- = f \ , \tag{11.93}$$

$$g^+ = g\exp(i\phi) \tag{11.94}$$

and

$$g^- = -g\exp(-i\phi) \ . \tag{11.95}$$

For an arbitrary spin direction, the electron incident plane wave will be given by $\Psi_1 = A\exp(iKz)$ and $\Psi_2 = B\exp(iKz)$, and as a consequence $a_1 = A$, $a_2 = B$. Furthermore,

$$b_1 = Af^+ + Bg^- = Af - Bg\exp(-i\phi) \ , \tag{11.96}$$

$$b_2 = Ag^+ + Bf^- = Bf + Ag\exp(i\phi) \ . \tag{11.97}$$

Consequently,

$$\frac{d\sigma}{d\Omega} = (|f|^2 + |g|^2)\left\{1 + iS(\theta)\left[\frac{AB^*\exp(i\phi) - A^*B\exp(-i\phi)}{|A|^2 + |B|^2}\right]\right\}, \tag{11.98}$$

where $S(\theta)$ is the Sherman function, defined by

$$S(\theta) = i\frac{fg^* - f^*g}{|f|^2 + |g|^2} \ . \tag{11.99}$$

Note that

$$i\frac{AB^*\exp(i\phi) - A^*B\exp(-i\phi)}{|A|^2 + |B|^2} = \xi^\dagger(\sigma_2\cos\phi - \sigma_1\sin\phi)\xi \ , \tag{11.100}$$

where σ_1, σ_2 and σ_3 are the Pauli matrices and ξ is the two-component spinor

$$\xi = \begin{pmatrix} A/\sqrt{|A|^2 + |B|^2} \\ B/\sqrt{|A|^2 + |B|^2} \end{pmatrix} \ , \tag{11.101}$$

$$\xi^\dagger = \begin{pmatrix} \dfrac{A^*}{\sqrt{|A|^2 + |B|^2}} & \dfrac{B^*}{\sqrt{|A|^2 + |B|^2}} \end{pmatrix} . \tag{11.102}$$

As the z axis has been chosen along the incidence direction, the unit vector perpendicular to the plane of scattering is given by

$$\hat{\boldsymbol{n}} = (-\sin\phi, \cos\phi, 0) \,, \tag{11.103}$$

so we can write

$$\xi^{\dagger}(\sigma_2 \cos\phi - \sigma_1 \sin\phi)\xi = \boldsymbol{P} \cdot \hat{\boldsymbol{n}} \,, \tag{11.104}$$

where $\boldsymbol{P}$ is the initial polarisation vector of the electron beam. The differential elastic scattering cross-section can then be recast as follows:

$$\frac{d\sigma}{d\Omega} = (|f|^2 + |g|^2)[1 + S(\theta)\boldsymbol{P} \cdot \hat{\boldsymbol{n}}] \,. \tag{11.105}$$

Note that, if the beam is completely unpolarised, then $P = 0$ and

$$\frac{d\sigma}{d\Omega} = |f|^2 + |g|^2 \,. \tag{11.106}$$

The total elastic scattering cross-section (σ_{el}) and the transport cross-section (σ_{tr}) are defined by

$$\sigma_{el} = 2\pi \int_0^{\pi} \frac{d\sigma}{d\Omega} \sin\theta \, d\theta \,, \tag{11.107}$$

$$\sigma_{tr} = 2\pi \int_0^{\pi} (1 - \cos\theta) \frac{d\sigma}{d\Omega} \sin\theta \, d\theta \,, \tag{11.108}$$

which can be easily calculated by numerical integration.

Note that by assigning

$$\eta_l^- = \eta_l^+ = \eta_l \tag{11.109}$$

in the previous equations, we can obtain the non-relativistic results. Indeed,

$$\begin{aligned} \mathcal{A}_l &= \frac{1}{2iK}\{(l+1)[\exp(2i\eta_l) - 1] + l[\exp(2i\eta_l) - 1]\} \\ &= \frac{1}{2iK}(2l+1)[\exp(2i\eta_l) - 1] \,, \end{aligned} \tag{11.110}$$

$$\mathcal{B}_l = 0 \,, \tag{11.111}$$

so that

$$\begin{aligned} f(\theta) &= \frac{1}{2iK} \sum_{l=0}^{\infty} (2l+1)[\exp(2i\eta_l) - 1] P_l(\cos\theta) \\ &= \frac{1}{K} \sum_{l=0}^{\infty} (2l+1) \exp(i\eta_l) \sin\eta_l P_l(\cos\theta) \,, \end{aligned} \tag{11.112}$$

$$g(\theta) = 0 \tag{11.113}$$

and

$$\frac{d\sigma}{d\Omega} = |f|^2 \,. \tag{11.114}$$

11.3 Phase Shift Calculations

In order to proceed, it is useful to perform the following transformation [5]:

$$F_l^{\pm}(r) = a_l^{\pm}(r)\frac{\sin\phi_l^{\pm}(r)}{r} \,, \tag{11.115}$$

$$G_l^{\pm}(r) = a_l^{\pm}(r)\frac{\cos\phi_l^{\pm}(r)}{r} \,. \tag{11.116}$$

After simple algebraic manipulations, (11.39) and (11.40) become

$$\begin{aligned}&[E+m-V(r)]\tan\phi_l^{\pm}(r) + \frac{1}{a_l^{\pm}(r)}\frac{da_l^{\pm}(r)}{dr}\\ &-\tan\phi_l^{\pm}(r)\frac{d\phi_l^{\pm}(r)}{dr} + \frac{k}{r} = 0 \,,\end{aligned} \tag{11.117}$$

$$\begin{aligned}&-[E-m-V(r)]\cot\phi_l^{\pm}(r) + \frac{1}{a_l^{\pm}(r)}\frac{da_l^{\pm}(r)}{dr}\\ &+\cot\phi_l^{\pm}(r)\frac{d\phi_l^{\pm}(r)}{dr} - \frac{k}{r} = 0 \,,\end{aligned} \tag{11.118}$$

and therefore

$$\frac{d\phi_l^{\pm}(r)}{dr} = \frac{k}{r}\sin 2\phi_l^{\pm}(r) - m\cos 2\phi_l^{\pm}(r) + E - V(r) \,, \tag{11.119}$$

$$\frac{1}{a_l^{\pm}(r)}\frac{da_l^{\pm}(r)}{dr} = -\frac{k}{r}\cos 2\phi_l^{\pm}(r) - m\sin 2\phi_l^{\pm}(r) \,. \tag{11.120}$$

For $0 < r < \hbar/mc$, the spherical symmetric electrostatic potential experienced by a point charge at distance r from the nucleus, $V(r)$, may be approximated by the following:

$$V(r) \underset{r\to 0}{\sim} -\frac{Z_0 + Z_1 r + Z_2 r^2 + Z_3 r^3}{r} \,. \tag{11.121}$$

Expressing the electrostatic potential as the product of the potential of a bare nucleus multiplied by a screening function $\xi(r)$ having the analytical form

$$\xi(r) = \sum_{i=1}^{p} A_i \exp(-\alpha_i r) \,, \tag{11.122}$$

$$\sum_{i=1}^{p} A_i = 1 \,, \tag{11.123}$$

we can easily evaluate Z_0, Z_1, Z_2 and Z_3:

$$Z_0 = Ze^2 \sum_i A_i = Ze^2 \,, \tag{11.124}$$

$$Z_1 = -Z_0 \sum_{i=1}^{p} \alpha_i A_i \,, \tag{11.125}$$

$$Z_2 = \frac{Z_0}{2} \sum_{i=1}^{p} \alpha_i^2 A_i \,, \tag{11.126}$$

$$Z_3 = -\frac{Z_0}{6} \sum_{i=1}^{p} \alpha_i^3 A_i \,. \tag{11.127}$$

Let us expand $\phi_l^{\pm}$ as a power series

$$\phi_l^{\pm}(r) = \phi_{l0}^{\pm} + \phi_{l1}^{\pm} r + \phi_{l2}^{\pm} r^2 + \phi_{l3}^{\pm} r^3 + \ldots \,. \tag{11.128}$$

As we can see see, after simple algebraic manipulations, the relationships between the coefficients of this expansion and Z_0, Z_1, Z_2 and Z_3 are the following [6]:

$$\sin 2\phi_{l0}^{\pm} = -\frac{Z_0}{k} \,, \tag{11.129}$$

$$\phi_{l1}^{\pm} = \frac{E + Z_1 - m \cos 2\phi_{l0}^{\pm}}{1 - -2k \cos 2\phi_{l0}^{\pm}} \,, \tag{11.130}$$

$$\phi_{l2}^{\pm} = \frac{2\phi_{l1}^{\pm} \sin 2\phi_{l0}^{\pm}(m - k\phi_{l1}^{\pm}) + Z_2}{2 - 2k \cos 2\phi_{l0}^{\pm}} \,, \tag{11.131}$$

$$\phi_{l3}^{\pm} = \frac{2\phi_{l2}^{\pm} \sin 2\phi_{l0}^{\pm}(m - 2k\phi_{l1}^{\pm}) + 2\phi_{l1}^{\pm 2} \cos 2\phi_{l0}^{\pm}[m - (2/3)k\phi_{l1}^{\pm}] + Z_3}{3 - 2k \cos 2\phi_{l0}^{\pm}} , \tag{11.132}$$

with the extra conditions

$$0 \leq 2\phi_{l0}^{\pm} \leq \frac{1}{2}\pi \tag{11.133}$$

if $k < 0$, and

$$\pi \leq 2\phi_{l0}^{\pm} \leq \frac{3}{2}\pi \tag{11.134}$$

if $k > 0$.

Let us now calculate the phase shifts, examining (11.116):

$$G_l'^{\pm} = \frac{a_l'^{\pm} \cos \phi_l^{\pm}(r)}{r} - \frac{a_l^{\pm}}{r} \sin \phi_l^{\pm}(r)\phi_l'^{\pm}(r) - \frac{a_l^{\pm} \cos \phi_l^{\pm}(r)}{r^2} , \tag{11.135}$$

so that

$$\frac{G_l'^{\pm}}{G_l^{\pm}} = \frac{a_l'^{\pm}}{a_l^{\pm}} - \phi_l'^{\pm}(r) \tan \phi_l^{\pm}(r) - \frac{1}{r} , \tag{11.136}$$

or

$$\frac{G_l'^{\pm}}{G_l^{\pm}} = -(E + m - V) \tan \phi_l^{\pm}(r) - \frac{1 + k}{r} . \tag{11.137}$$

Let us observe that the asymptotic form of the solution in the regions corresponding to large values of r for which $V(r) \approx 0$ is (see (11.52))

$$G_l^{\pm} = j_l(Kr) \cos \eta_l^{\pm} - n_l(Kr) \sin \eta_l^{\pm} , \tag{11.138}$$

where $K^2 = E^2 - m^2$, $\eta_l^{\pm}$ are the lth phase shifts, and j_l and n_l are respectively the regular and irregular spherical Bessel functions. Therefore,

$$\frac{G_l'^{\pm}}{G_l^{\pm}} = \frac{Kj_l'(Kr) \cos \eta_l^{\pm} - Kn_l'(Kr) \sin \eta_l^{\pm}}{j_l(Kr) \cos \eta_l^{\pm} - n_l(Kr) \sin \eta_l^{\pm}} . \tag{11.139}$$

Taking into account the properties of the Bessel functions

$$j_l'(x) = \frac{l}{x} j_l(x) - j_{l+1}(x) , \tag{11.140}$$

$$n_l'(x) = \frac{l}{x} n_l(x) - n_{l+1}(x) , \tag{11.141}$$

we can conclude that

$$\tan \eta_l^{\pm} = \frac{(l/r) j_l(Kr) - K j_{l+1}(Kr) - j_l(Kr)(G_l'^{\pm}/G_l^{\pm})}{(l/r) n_l(Kr) - K n_{l+1}(Kr) - n_l(Kr)(G_l'^{\pm}/G_l^{\pm})} \,. \tag{11.142}$$

Let us define

$$\tilde{\phi}_l^{\pm} = \lim_{r \to \infty} \phi_l^{\pm}(r) \,. \tag{11.143}$$

For large values of r, (11.137) becomes

$$\frac{G_l'^{\pm}}{G_l^{\pm}} = -(E+m) \tan \tilde{\phi}_l^{\pm} - \frac{1+k}{r} \,, \tag{11.144}$$

and therefore

$$\tan \eta_l^{\pm} = \frac{K j_{l+1}(Kr) - j_l(Kr)[(E+m) \tan \tilde{\phi}_l^{\pm} + (1+l+k)/r]}{K n_{l+1}(Kr) - n_l(Kr)[(E+m) \tan \tilde{\phi}_l^{\pm} + (1+l+k)/r]} \,. \tag{11.145}$$

Using this last equation, we can calculate the phase shifts of the scattered wave and, therefore, the functions $f(\theta), g(\theta)$ and the differential elastic scattering cross-section.

The Mott theory predicts that it is given by

$$\frac{d\sigma_{\text{el}}}{d\Omega} = \mid f(\vartheta) \mid^2 + \mid g(\vartheta) \mid^2 \,. \tag{11.146}$$

It should be noted that, in molecular solids, the differential elastic scattering cross-section can be approximated as the sum total of the atomic differential elastic scattering cross-sections of the atoms in the molecule.

11.4 Analytic Approximation of the Mott Cross-Section

Taking advantage of the simple closed form of the equations deduced starting by the Rutherford cross-section, it is sometimes possible to look for an approximation where similar equations are used for the Mott cross-section [8, 9]. For low atomic number elements and for some oxides, the Mott differential elastic scattering cross-section can be roughly approximated by the following equation:

$$\frac{d\sigma_{\text{el}}}{d\Omega} = \frac{\Phi}{(1 - \cos\theta + \Psi)^2} \,, \tag{11.147}$$

where the unknown parameters Φ and Ψ are calculated with the aim to get the best fit of the total and the first transport elastic scattering cross-section previously calculated using the RPWEM. With

$$\Phi = \frac{Z^2 e^2}{4E^2} \tag{11.148}$$

and

$$\Psi = \frac{m e^4 \pi^2 Z^{2/3}}{h^2 E} \tag{11.149}$$

Eq. (11.147) becomes the screened Rutherford formula.

Once we know the total elastic scattering cross-section and of the transport elastic scattering cross-section previously calculated using the Mott theory we can now calculate Φ and Ψ in order to approximate the Mott theory [8]. From Eq. (3.2), it follows that:

$$\sigma_{\text{el}} = \frac{4\pi\Phi}{\Psi(\Psi+2)}\,. \tag{11.150}$$

As a consequence the differential elastic scattering cross-section can be rewritten as:

$$\frac{d\sigma_{\text{el}}}{d\Omega} = \frac{\sigma_{\text{el}}}{4\,\pi}\frac{\Psi(\Psi+2)}{(1-\cos\theta+\Psi)^2} \tag{11.151}$$

Using Eqs. (3.3) and (11.151) it is possible to obtain the ratio Ξ between the transport and the total elastic scattering cross-sections:

$$\Xi \equiv \frac{\sigma_{\text{tr}}}{\sigma_{\text{el}}} = \Psi\left[\frac{\Psi+2}{2}\ln\left(\frac{\Psi+2}{\Psi}\right)-1\right]. \tag{11.152}$$

Once the values of the total and transport elastic scattering cross-sections have been numerically calculated using the RPWEM, the ratio Ξ is determined as a function of electron kinetic energy E. In such a way it is possible to get the screening parameter Ψ as a function of E (using a bisection algorithm).

11.5 The Atomic Potential

To calculate the atomic potential, the self-consistent Dirac-Hartree-Fock-Slater field should be used. In order to reduce the computer calculation time, the analytic approximation proposed by Salvat et al. [7] for the Dirac-Hartre-Fock-Slater field can be utilized instead. The Salvat et al. atomic potential is a superposition of Yukawa's potentials based on a number of parameters which have been determined by lookingfor the best fit of the numericallyi in the calculated self-consistent Dirac-Hartree-

Fock-Slater fields. The atomic potential is expressed by a pure Coulomb potential multiplied by a function $\psi(r)$ approximating the screening of the nucleus by the orbital electrons. The Salvat et al. screening function is given by:

$$\psi(r) = \sum_{i=1}^{3} A_i \exp(-\alpha_i r)\,, \tag{11.153}$$

where A_i and α_i are parameters whose values can be found in Ref. [7] for all the elements of the periodic table.

11.6 Electron Exchange

As electrons are identical particles, exchange effects have to be taken into account, since it can occur that the incident electron is captured by an atom and a new electron is emitted. Exchange effects are well described by adding, to the atomic potential described above, the Furness and McCarthy exchange potential [10]:

$$V_{ex} = \frac{1}{2}(E - V) - \frac{1}{2}[(E - V)^2 + 4\pi\rho e^2\hbar^2/m]^{1/2}\,. \tag{11.154}$$

In this equation, E is the electron energy, V the electrostatic potential, ρ the atomic electron density (obtained by Poisson's equation), and e the electron charge.

11.7 Solid-State Effects

For atoms bound in solids, the outer orbitals are modified, so that solid-state effects should be introduced. In the so-called *muffin-tin* model, the potential of every atom in the solid is changed by the nearest-neighbor atoms. If we assume that the nearest-neighbor atoms are located at distances equal to $2r_{ws}$, where r_{ws} is the radius of the Wigner-Seitz sphere [11], then the potential can be calculated, for $r \leq r_{ws}$, as follows

$$V_{solid}(r \leq r_{ws}) = V(r) + V(2r_{ws} - r) - 2V(r_{ws})\,. \tag{11.155}$$

It is equal to zero outside the Wigner-Seitz sphere, i.e.,

$$V_{solid}(r \geq r_{ws}) = 0\,. \tag{11.156}$$

The term $2V(r_{ws})$ was introduced in Eq. (11.155) to shift the energy scale so that $V_{solid}(r = r_{ws}) = 0$. According to Salvat and Mayol, it also has to be subtracted from the kinetic energy of the incident electrons [12].

11.8 Positron Differential Elastic Scattering Cross-Section

The electron differential elastic scattering cross-section shows diffraction-like structures. It is a typical quantum-mechanical phenomenon due to the interaction of the incident electron with the atomic electron cloud. On the contrary, the positron elastic scattering cross-section is a decreasing and monotonic Rutherford-like function [13, 14]. This is due to the different sign of the electric charges of electrons and positrons. Positrons are rejected by the atomic nucleus: as a consequence, they do not penetrate the atomic electron cloud as deeply as electrons do. Since electrons penetrate deeper into the core of atomic electrons, they draw closer to the nucleus than positron dos. Thus, electrons can loop around the nucleus once or more times and electron outgoing wave – a superposition of the incoming and of the scattered wave – exhibits interference effects also in the backward direction. This is just a semiclassical description that qualitatively explains the reason why the atomic electron cloud influences electrons more than positrons during elastic scattering.

11.9 Summary

The Mott theory [1] (also known as the relativistic partial wave expansion method, RPWEM) was described in this chapter. It allows to calculate the electron elastic scattering cross section. Electron exchange and solid state effects were also introduced. Differences among elastic scattering cross sections of electrons and positrons were discussed.

References

1. N.F. Mott, Proc. R. Soc. London Ser. **124**, 425 (1929)
2. A. Jablonski, F. Salvat, C.J. Powell, J. Phys. Chem. Data **33**, 409 (2004)
3. M. Dapor, J. Appl. Phys. **79**, 8406 (1996)
4. M. Dapor, *Electron-Beam Interactions with Solids: Application of the Monte Carlo Method to Electron Scattering Problems* (Springer, Berlin, 2003)
5. S.-R. Lin, N. Sherman, J.K. Percus, Nucl. Phys. **45**, 492 (1963)
6. P.J. Bunyan, J.L. Schonfelder, Proc. Phys. Soc. **85**, 455 (1965)
7. F. Salvat, J.D. Martínez, R. Mayol, J. Parellada, Phys. Rev. A **36**, 467 (1987)
8. J. Baró, J. Sempau, J.M. Fernández-Varea, F. Salvat, Nucl. Instrum. Methods Phys. Res. B **84**, 465 (1994)
9. M. Dapor, Phys. Lett. A **333**, 457 (2004)
10. J.B. Furness, I.E. McCarthy, J. Phys. B **6**, 2280 (1973)
11. N. Ashcroft, N.D. Mermin, *Solid State Physics* (W.B. Saunders, Philadelphia, 1976)
12. F. Salvat, R. Mayol, Comput. Phys. Commun. **74**, 358 (1993)
13. M. Dapor, A. Miotello, At. Data Nucl. Data Tables **69**, 1 (1998)
14. M. Dapor, J. Electron Spectrosc. Relat. Phenom. **151**, 182 (2006)

Chapter 12
Appendix C: The Fröhlich Theory

The original version of the Fröhlich theory can be found in Ref. [1]. Also see Ref. [2] for further details. In his theory of the electron-phonon interaction, Fröhlich [1] considered, in particular, the interaction of free electrons with the longitudinal optical mode lattice vibrations. The interaction was described considering both phonon creation and phonon annihilation, corresponding to electron energy loss and to electrons energy gain, respectively. As the phonon generation probability is much higher than the phonon absorption probability, the latter is often neglected in Monte Carlo simulations. Furthermore, since, according to Ganachaud and Mokrani [3], the dispersion relation of the longitudinal phonons can be neglected in the optical branch, one can use a single phonon frequency. As a matter of fact, the Fröhlich theory adopts a single value of the frequency for all momenta, corresponding to a flat longitudinal optical branch. This approximation is quite reasonable and experimentally confirmed (see, for example, Fujii et al. [4] for the ionic crystal AgBr). In semiconductors the longitudinal optical branch is flat as well, as demonstrated both experimentally (see, for example, Nilsson and Neil for Ge [5] and Si [6]) and theoretically (see, for example, Gianozzi et al. for Si, Ge, GaAs, AlAs, GaSb, and AlSb [7]).

12.1 Electrons in Lattice Fields. Interaction Hamiltonian

According to Fröhlich [1], an electron traveling in a dielectric material polarizes the medium and the polarization reacts on the charged particle. Let us indicate with $\boldsymbol{\mathcal{P}}(\boldsymbol{r})$ the electric polarization. The only source of the displacement vector, $\boldsymbol{\mathcal{D}}(\boldsymbol{r}) = \boldsymbol{\mathcal{E}}(\boldsymbol{r}) + 4\pi\,\boldsymbol{\mathcal{P}}(\boldsymbol{r})$, are the free charges. If $\boldsymbol{r}_{\mathrm{el}}$ represents the position of a single free electron, then

$$\nabla \cdot \boldsymbol{\mathcal{D}} = -4\pi\, e\, \delta(\boldsymbol{r} - \boldsymbol{r}_{\mathrm{el}}), \tag{12.1}$$

M. Dapor, *Transport of Energetic Electrons in Solids*,
Springer Tracts in Modern Physics 257, DOI 10.1007/978-3-319-47492-2_12

where e is the electron charge. The electric polarization can be written as

$$\mathcal{P}(\boldsymbol{r}) = \mathcal{P}_{\rm uv}(\boldsymbol{r}) + \mathcal{P}_{\rm ir}(\boldsymbol{r}), \tag{12.2}$$

where $\mathcal{P}_{\rm uv}(\boldsymbol{r})$ and $\mathcal{P}_{\rm ir}(\boldsymbol{r})$ are the polarizations corresponding, respectively, to the ultraviolet (atomic polarizability) and the infrared (displacement polarizability) optical absorptions [8]. They satisfy the harmonic oscillator equations

$$\frac{d^2\mathcal{P}_{\rm uv}(\boldsymbol{r})}{dt^2} + \omega_{\rm uv}^2\,\mathcal{P}_{\rm uv}(\boldsymbol{r}) = \frac{\mathcal{D}(\boldsymbol{r},\boldsymbol{r}_{\rm el})}{\delta}, \tag{12.3}$$

$$\frac{d^2\mathcal{P}_{\rm ir}(\boldsymbol{r})}{dt^2} + \omega^2\,\mathcal{P}_{\rm ir}(\boldsymbol{r}) = \frac{\mathcal{D}(\boldsymbol{r},\boldsymbol{r}_{\rm el})}{\gamma}. \tag{12.4}$$

In these equations, $\omega_{\rm uv}$ (atomic deformation) and ω (atomic displacement) are the angular frequencies for ultraviolet and infrared optical absorption, respectively, and δ and γ are constants that are related to the dielectric function.

To determine these constants, let us firstly consider the static case and indicate with ε_0 the static dielectric constant. Since

$$\mathcal{D}(\boldsymbol{r}) = \varepsilon_0\,\mathcal{E}(\boldsymbol{r}), \tag{12.5}$$

then

$$4\pi\mathcal{P}(\boldsymbol{r}) = \left[1 - \frac{1}{\varepsilon_0}\right]\mathcal{D}(\boldsymbol{r}). \tag{12.6}$$

Furthermore, let us assume that the high frequency dielectric constant ε_∞ is determined in the hypothesis that the angular frequency ω_∞ of the external field is low compared with the atomic excitation frequencies $\omega_{\rm uv}$ and high compared with the lattice vibrational frequencies ω [8]. Then $\mathcal{P}_{\rm ir} \approx 0$, $d^2\mathcal{P}_{\rm uv}/dt^2 \ll \omega_{\rm uv}^2\mathcal{P}_{\rm uv}(\boldsymbol{r})$, and $\mathcal{D}(\boldsymbol{r}) = \varepsilon_\infty\,\mathcal{E}(\boldsymbol{r})$, where ε_∞ is the high frequency dielectric constant ($\varepsilon_\infty^{1/2}$ is the refraction index). As a consequence, $\mathcal{P}_{\rm uv}(\boldsymbol{r})$ can be approximated assuming that it has the value corresponding to a static field of the same strength [1]

$$4\pi\mathcal{P}_{\rm uv}(\boldsymbol{r}) = \left[1 - \frac{1}{\varepsilon_\infty}\right]\mathcal{D}(\boldsymbol{r}) \tag{12.7}$$

so that

$$4\pi\mathcal{P}_{\rm ir}(\boldsymbol{r}) = \left[\frac{1}{\varepsilon_\infty} - \frac{1}{\varepsilon_0}\right]\mathcal{D}(\boldsymbol{r}) \tag{12.8}$$

Since, in the static case, $d^2\mathcal{P}_{\rm uv}/dt^2 = 0$ and $d^2\mathcal{P}_{\rm ir}/dt^2 = 0$,

$$\mathcal{P}_{\rm uv}(\boldsymbol{r}) = \frac{\mathcal{D}(\boldsymbol{r})}{\delta\,\omega_{\rm uv}^2}, \tag{12.9}$$

$$\mathcal{P}_{\rm ir}(\boldsymbol{r}) = \frac{\mathcal{D}(\boldsymbol{r})}{\gamma\,\omega^2}, \tag{12.10}$$

and hence we obtain

$$\frac{1}{\delta} = \frac{\omega_{\rm uv}^2}{4\,\pi}\left(1 - \frac{1}{\varepsilon_\infty}\right). \tag{12.11}$$

$$\frac{1}{\gamma} = \frac{\omega^2}{4\,\pi}\left(\frac{1}{\varepsilon_\infty} - \frac{1}{\varepsilon_0}\right). \tag{12.12}$$

In order to describe a slow electron interacting with an ionic lattice field, Fröhlich considered the infrared contribution to the polarization and introduced the complex field $\mathcal{B}(\boldsymbol{r})$ such that

$$\mathcal{B}(\boldsymbol{r}) = \sqrt{\frac{\gamma\,\omega}{2\,\hbar}}\left(\mathcal{P}_{\rm ir}(\boldsymbol{r}) + \frac{i}{\omega}\,\frac{d\mathcal{P}_{\rm ir}(\boldsymbol{r})}{dt}\right). \tag{12.13}$$

The phonon annihilation operators $a_{\boldsymbol{q}}$ are defined by the equation

$$\mathcal{B}(\boldsymbol{r}) = \sum_{\boldsymbol{q}} \frac{\boldsymbol{q}}{q}\,a_{\boldsymbol{q}}\,\frac{\exp(i\boldsymbol{q}\cdot\boldsymbol{r})}{\sqrt{V}}, \tag{12.14}$$

where $\mathcal{B}(\boldsymbol{r})$ is subject to a boundary condition over a cube of volume V. As a consequence

$$\left(\mathcal{P}_{\rm ir}(\boldsymbol{r}) + \frac{i}{\omega}\,\frac{d\mathcal{P}_{\rm ir}(\boldsymbol{r})}{dt}\right) = \sqrt{\frac{2\,\hbar}{\gamma\,\omega\,V}}\,\sum_{\boldsymbol{q}} \frac{\boldsymbol{q}}{q}\,a_{\boldsymbol{q}}\,\exp(i\boldsymbol{q}\cdot\boldsymbol{r}). \tag{12.15}$$

Taking the Hermitian adjoint we obtain

$$\left(\mathcal{P}_{\rm ir}(\boldsymbol{r}) - \frac{i}{\omega}\,\frac{d\mathcal{P}_{\rm ir}(\boldsymbol{r})}{dt}\right) = \sqrt{\frac{2\,\hbar}{\gamma\,\omega\,V}}\,\sum_{\boldsymbol{q}} \frac{\boldsymbol{q}}{q}\,a_{\boldsymbol{q}}^\dagger\,\exp(-i\boldsymbol{q}\cdot\boldsymbol{r}), \tag{12.16}$$

so that

$$\mathcal{P}_{\rm ir}(\boldsymbol{r}) = \sqrt{\frac{\hbar}{2\,\gamma\,\omega\,V}}\,\sum_{\boldsymbol{q}} \hat{\boldsymbol{q}}\,[a_{\boldsymbol{q}}\,\exp(i\boldsymbol{q}\cdot\boldsymbol{r}) + a_{\boldsymbol{q}}^\dagger\,\exp(-i\boldsymbol{q}\cdot\boldsymbol{r})], \tag{12.17}$$

where

$$\hat{\boldsymbol{q}} = \frac{\boldsymbol{q}}{q} \tag{12.18}$$

and

$$q_{\mathrm{i}} = \frac{2\,\pi}{L}\, n_{\mathrm{i}}, \tag{12.19}$$

with $n_{\mathrm{i}} = 0, \pm 1, \pm 2, \ldots$ and $L = V^{1/3}$. The quantities $a_{\boldsymbol{q}}^{\dagger}$ represent the phonon creation operators.

In order to write the interaction Hamiltonian, $\mathcal{H}_{\mathrm{inter}}$, let's observe that the displacement vector $\boldsymbol{\mathcal{D}}$ is the external field that determines the crystal polarization. Since $\boldsymbol{\mathcal{D}} = 0$ in the absence of free charges, the potential ϕ_{ir} is given by

$$-\,4\pi\,\boldsymbol{\mathcal{P}}_{\mathrm{ir}} = \boldsymbol{\mathcal{E}} = -\nabla\,\phi_{\mathrm{ir}}, \tag{12.20}$$

so that

$$\mathcal{H}_{\mathrm{inter}} = e\,\phi_{\mathrm{ir}} = \\ 4\,\pi\,i\,\sqrt{\frac{\hbar\,e^2}{2\,\gamma\,\omega\,V}} \sum_{\boldsymbol{q}} \frac{1}{q}\,[a_{\boldsymbol{q}}^{\dagger}\,\exp(-i\boldsymbol{q}\cdot\boldsymbol{r}) - a_{\boldsymbol{q}}\,\exp(i\boldsymbol{q}\cdot\boldsymbol{r})], \tag{12.21}$$

with $\boldsymbol{q} \neq 0$.

12.2 Electron-Phonon Scattering Cross-Section

If we indicate with ω the angular frequency of the longitudinal optical vibrations of the lattice, then the average number of phonons at temperature T is given by the occupation function

$$n(T) = \frac{1}{\exp\left(\hbar\,\omega/k_{\mathrm{B}}\,T\right) - 1}, \tag{12.22}$$

where k_{B} is the Boltzmann constant. Fröhlich theory [1] uses the perturbation approach, assuming that the electron-lattice coupling is weak. If the electron energy, measured with respect to the bottom of the conduction band, is given by

$$E_k = \frac{\hbar^2\,k^2}{2\,m^*}, \tag{12.23}$$

where m^* is the electron effective mass and $\boldsymbol{k}$ the electron wavenumber, then the unperturbed electron wavefunction can be written as

$$|\,\boldsymbol{k}\rangle = \frac{\exp\left(i\,\boldsymbol{k}\cdot\boldsymbol{r}\right)}{V^{1/2}}, \tag{12.24}$$

where, as above, we have indicated with V a cubic volume containing the electron. We know that, according to Fröhlich [1], the interaction Hamiltonian is given by Eq. (12.21)

$$\mathcal{H}_{\text{inter}} = 4\,\pi\,i\,\sqrt{\frac{e^2\,\hbar}{2\,\gamma\,\omega\,V}}\sum_{\boldsymbol{q}}\frac{1}{q}[a_{\boldsymbol{q}}^{\dagger}\,\exp\left(-i\,\boldsymbol{q}\cdot\boldsymbol{r}\right) - a_{\boldsymbol{q}}\,\exp\left(i\,\boldsymbol{q}\cdot\boldsymbol{r}\right)],$$

where $\boldsymbol{q}\neq 0$ is the phonon wavenumber, $a_{\boldsymbol{q}}^{\dagger}$ and $a_{\boldsymbol{q}}$ are, respectively, the operators of creation and annihilation of phonons, and γ is related to the static dielectric constant ε_0 and to the high frequency dielectric constant ε_∞ by the Eq. (12.12)

$$\frac{1}{\gamma} = \frac{\omega^2}{4\,\pi}\left(\frac{1}{\varepsilon_\infty} - \frac{1}{\varepsilon_0}\right).$$

In order to calculate the transition rate $W_{kk'}$ from the state $|\,\boldsymbol{k}\rangle$ to the state $|\,\boldsymbol{k}'\rangle$, Llacer and Garwin [2] used the standard result of the perturbation theory. In the case of phonon annihilation, corresponding to an electron energy gain, once should consider the frequency

$$\beta = \frac{E_{\mathrm{k}'} - E_{\mathrm{k}} - \hbar\,\omega}{2\,\hbar}, \tag{12.25}$$

while, for phonon creation (electron energy loss), the frequency to be considered is the following

$$\beta = \frac{E_{\mathrm{k}'} - E_{\mathrm{k}} + \hbar\,\omega}{2\,\hbar}. \tag{12.26}$$

The rate is given by

$$W_{\mathrm{kk}'} = \frac{|M_{\mathrm{kk}'}|^2}{\hbar^2}\frac{\partial}{\partial t}\left(\frac{\sin^2\beta t}{\beta^2}\right) \tag{12.27}$$

where M'_{kk} is the matrix element for the transition from the state $\boldsymbol{k}$ to the state $\boldsymbol{k}'$. They can be calculated by using the interaction Hamiltonian, Eq. (12.21), taking into account the properties of the creation and annihilation operators,

$$a_{\boldsymbol{q}}\,|n\rangle = \sqrt{n}\,|n-1\rangle, \tag{12.28}$$

$$a_{\boldsymbol{q}}^{\dagger}\,|n\rangle = \sqrt{n+1}\,|n+1\rangle, \tag{12.29}$$

and utilizing the condition of orthonormality satisfied by the set of vectors $|n(T)\rangle$,

$$\langle n|n\rangle = 1, \tag{12.30}$$

$$\langle n|n+m\rangle = 0. \tag{12.31}$$

where m is any integer $\neq 0$.

For the case of annihilation of a phonon of wavenumber $\boldsymbol{q}$ (electron energy gain), $\boldsymbol{k}' = \boldsymbol{k} + \boldsymbol{q}$ and

$$M_{\mathrm{kk}'} = 4\,\pi\,i\,\sqrt{\frac{e^2\,\hbar}{2\,\gamma\,\omega\,V}}\,\frac{\sqrt{n(T)}}{q}, \tag{12.32}$$

while, in the case of the creation of a phonon of wavenumber $\boldsymbol{q}$ (electron energy loss), $\boldsymbol{k}' = \boldsymbol{k} - \boldsymbol{q}$ and

$$M_{\mathrm{kk}'} = -\,4\,\pi\,i\,\sqrt{\frac{e^2\,\hbar}{2\,\gamma\,\omega\,V}}\,\frac{\sqrt{n(T)+1}}{q}. \tag{12.33}$$

The total scattering rate from a state $\boldsymbol{k}$ to all the available states $\boldsymbol{k}'$ can be obtained by integrating over $\boldsymbol{q}$. Let us first perform the integration for the case of phonon annihilation:

$$W_{\mathrm{k}}^{-} = \int_{q_{\min}}^{q_{\max}} dq \int_0^{2\,\pi} d\phi \int_0^{\pi} \frac{16\,\pi^2\,e^2}{2\,\hbar\,\gamma\,\omega\,V}\,\frac{n(T)}{q^2}\,\frac{\partial}{\partial\,t}\,\frac{\sin^2\,\beta\,t}{\beta^2}\,\frac{V}{8\,\pi^3}\,q^2\,\sin\alpha\,d\alpha. \tag{12.34}$$

Note that α represents in this context the angle between the direction of $\boldsymbol{k}$ and that of $\boldsymbol{q}$, while we shall use the symbol θ to indicate the angle between $\boldsymbol{k}$ and $\boldsymbol{k}'$. As

$$k'^2 = k^2 + q^2 - 2\,k\,q\,\cos\alpha, \tag{12.35}$$

some simple algebraic manipulations allow as to to see that

$$\beta = \frac{\hbar}{4\,m^*}\,q^2 - \frac{\hbar}{2\,m^*}\,k\,q\,\cos\alpha - \frac{\omega}{2}, \tag{12.36}$$

so that

$$\sin\alpha\,d\alpha = \frac{2\,m^*}{\hbar}\,\frac{1}{k\,q}\,d\beta. \tag{12.37}$$

As a consequence

$$W_{\mathrm{k}}^{-} = \int_{q_{\min}}^{q_{\max}} dq \int_{\beta_{\min}}^{\beta_{\max}} \frac{4\,m^*\,e^2\,n(T)}{\hbar^2\,\gamma\,\omega}\,\frac{1}{k\,q}\,\frac{\partial}{\partial\,t}\,\frac{\sin^2\beta\,t}{\beta^2}\,d\beta, \tag{12.38}$$

where

$$\beta_{\min} = \frac{\hbar}{4\,m^*}\,q^2 - \frac{\hbar}{2\,m^*}\,k\,q - \frac{\omega}{2}, \tag{12.39}$$

and

$$\beta_{\max} = \frac{\hbar}{4\,m^*}\,q^2 + \frac{\hbar}{2\,m^*}\,k\,q - \frac{\omega}{2}, \tag{12.40}$$

Now

$$\begin{aligned}
&\int_{\beta_{\min}}^{\beta_{\max}} \frac{\partial}{\partial\,t}\,\frac{\sin^2\beta\,t}{\beta^2}\,d\beta = \int_{\beta_{\min}}^{\beta_{\max}} \frac{\sin\,2\,\beta\,t}{\beta}\,d\beta\,= \\
&= \int_{\beta_{\min}}^{\beta_{\max}} \frac{\sin(2\,\beta\,t)}{(2\,\beta\,t)}\,2\,t\,d\beta\,= \int_{2\,\beta_{\min}\,t}^{2\,\beta_{\max}\,t} \frac{\sin x}{x}\,dx\,= \\
&= \int_{0}^{2\,\beta_{\max}\,t} \frac{\sin x}{x}\,dx - \int_{0}^{2\,\beta_{\min}\,t} \frac{\sin x}{x}\,dx.
\end{aligned}$$

In order to carry out the calculation, we need to know the limits of integration, $q_{\min}$ and $q_{\max}$. They can be obtained by using the law of conservation of energy, $E'_{\mathrm{k}} = E_{\mathrm{k}} + \hbar\,\omega$, which corresponds to $\beta = 0$.

Since $\cos\alpha$ can take all the values between -1 and $+1$, the limits of integration satisfy the following equations

$$q^2 + 2\,k\,q - \frac{k^2\,\hbar\,\omega}{E_{\mathrm{k}}} = 0, \tag{12.41}$$

$$q^2 - 2\,k\,q - \frac{k^2\,\hbar\,\omega}{E_{\mathrm{k}}} = 0, \tag{12.42}$$

so that, as q is positive,

$$q_{\min} = k\left(\sqrt{1 + \frac{\hbar\,\omega}{E_{\mathrm{k}}}} - 1\right), \tag{12.43}$$

$$q_{\max} = k\left(\sqrt{1 + \frac{\hbar\,\omega}{E_{\mathrm{k}}}} + 1\right). \tag{12.44}$$

Inserting these limits of integration in the definition of $\beta_{\min}$ and $\beta_{\max}$, we see that $\beta_{\min} \leq 0$ and $\beta_{\max} \geq 0$. Therefore,

$$\begin{aligned}
&\lim_{t\to\infty} \int_{\beta_{\min}}^{\beta_{\max}} \frac{\partial}{\partial t} \frac{\sin^2 \beta t}{\beta^2}\, d\beta = \\
&= \lim_{t\to\infty} \left(\int_0^{2\beta_{\max} t} \frac{\sin x}{x}\, dx - \int_0^{2\beta_{\min} t} \frac{\sin x}{x}\, dx \right) = \\
&= \int_0^{+\infty} \frac{\sin x}{x}\, dx - \int_0^{-\infty} \frac{\sin x}{x}\, dx = \\
&= \mathrm{si}(+\infty) - \mathrm{si}(-\infty) = \frac{\pi}{2} - \left(-\frac{\pi}{2}\right) = \pi,
\end{aligned}$$

so that

$$W_{\mathrm{k}}^{-} = \int_{q_{\min}}^{q_{\max}} \frac{4\,\pi\, m^*\, e^2\, n(T)}{\hbar^2\, \gamma\, \omega} \frac{1}{k\, q}\, dq. \tag{12.45}$$

As a consequence, we conclude that the total scattering rate for the phonon annihilation (electron energy gain) is given by

$$W_{\mathrm{k}}^{-} = \frac{4\,\pi\, e^2\, m^*\, n(T)}{\hbar^2\, \gamma\, \omega\, k} \ln\left(\frac{\sqrt{1 + \hbar\,\omega/E_{\mathrm{k}}} + 1}{\sqrt{1 + \hbar\,\omega/E_{\mathrm{k}}} - 1} \right). \tag{12.46}$$

The case of phonon creation (electron energy loss) is similar. Remember that, in this case, we have to use $\sqrt{n(T)+1}$ instead of $\sqrt{n(T)}$ in the matrix element of the transition of electron in state $\boldsymbol{k}$ to $\boldsymbol{k}'$. Furthermore, in this case,

$$\beta = \frac{1}{2\,\hbar} \left[E_{\mathrm{k}'} - (E_{\mathrm{k}} + \hbar\,\omega) \right] = \frac{\hbar}{4\, m^*}\, q^2 - \frac{\hbar}{2\, m^*}\, k\, q\, \cos\alpha + \frac{\omega}{2}, \tag{12.47}$$

so that

$$q_{\min} = k \left(1 - \sqrt{1 - \frac{\hbar\,\omega}{E_{\mathrm{k}}}} \right), \tag{12.48}$$

$$q_{\max} = k \left(1 + \sqrt{1 - \frac{\hbar\,\omega}{E_{\mathrm{k}}}} \right). \tag{12.49}$$

Therefore,

$$W_{\mathrm{k}}^{+} = \frac{4\,\pi\, e^2\, m^*\, [n(T)+1]}{\hbar^2\, \gamma\, \omega\, k} \ln\left(\frac{1 + \sqrt{1 - \hbar\,\omega/E_{\mathrm{k}}}}{1 - \sqrt{1 - \hbar\,\omega/E_{\mathrm{k}}}} \right). \tag{12.50}$$

Concerning the angular distribution of the scattering, let us consider the angle θ between $\boldsymbol{k}$ and $\boldsymbol{k}'$, so that

$$q^2 = k^2 + k'^2 - 2\,k\,k'\,\cos\theta \tag{12.51}$$

and, hence,

$$q\,dq = k\,k'\,\sin\theta\,d\theta. \tag{12.52}$$

The probability of scattering between θ and $\theta + d\theta$ can be calculated by considering the integrand of Eq. (12.45):

$$\begin{aligned} A\,\frac{dq}{k\,q} &= A\,\frac{q\,dq}{k\,q^2} = A\,\frac{k\,k'\,\sin\theta\,d\theta}{k\,(k^2 + k'^2 - 2\,k\,k'\,\cos\theta)} = \\ &= A\,\frac{k'\,\sin\theta\,d\theta}{k^2 + k'^2 - 2\,k\,k'\,\cos\theta}, \end{aligned}$$

where, for phonon annihilation,

$$A = \frac{4\,\pi\,e^2\,m^*\,n(T)}{\hbar^2\,\gamma\,\omega}. \tag{12.53}$$

Similar considerations hold for phonon creation, so that we conclude that the angular distribution is proportional, in both cases, to

$$d\eta = \frac{E_{\mathrm{k}'}^{1/2}\,\sin\theta\,d\theta}{E_{\mathrm{k}} + E_{\mathrm{k}'} - 2\,(E_{\mathrm{k}}\,E'_{\mathrm{k}})^{1/2}\,\cos\theta} \tag{12.54}$$

After an electron-phonon collision, the new angle θ' is obtained inverting this distribution. Indicating with μ the cumulative probability, we have

$$\begin{aligned} \mu &= \frac{\int_0^{\theta'} d\eta}{\int_0^{\pi} d\eta} = \\ &= \int_0^{\theta'} \frac{E_{\mathrm{k}'}^{1/2}\,\sin\theta\,d\theta}{E_{\mathrm{k}} + E_{\mathrm{k}'} - 2\,(E_{\mathrm{k}}\,E'_{\mathrm{k}})^{1/2}\,\cos\theta} \Big/ \\ &\Big/ \int_0^{\pi} \frac{E_{\mathrm{k}'}^{1/2}\,\sin\theta\,d\theta}{E_{\mathrm{k}} + E_{\mathrm{k}'} - 2\,(E_{\mathrm{k}}\,E'_{\mathrm{k}})^{1/2}\,\cos\theta}, \end{aligned} \tag{12.55}$$

and, as a consequence,

$$\cos\,\theta' = \frac{E_{\mathrm{k}} + E_{\mathrm{k}'}}{2\,\sqrt{E_{\mathrm{k}}\,E_{\mathrm{k}'}}}\,(1 - B^{\mu}) + B^{\mu}, \tag{12.56}$$

$$B = \frac{E_{\mathrm{k}} + E_{\mathrm{k}'} + 2\sqrt{E_{\mathrm{k}}\, E_{\mathrm{k}'}}}{E_{\mathrm{k}} + E_{\mathrm{k}'} - 2\sqrt{E_{\mathrm{k}}\, E_{\mathrm{k}'}}}. \tag{12.57}$$

The relationship between the mean free path $\lambda_{\mathrm{phonon}}$ and the total scattering rate from a state $\boldsymbol{k}$ to all the other available states $\boldsymbol{k}'$ is

$$\lambda_{\mathrm{phonon}} = \left(\frac{1}{v}\frac{dP}{dt}\right)^{-1}, \tag{12.58}$$

where v is the electron velocity before the electron-phonon collision

$$v = \frac{\hbar k}{m^*} \tag{12.59}$$

and

$$\frac{dP}{dt} = W_{\mathrm{k}}^{-} + W_{\mathrm{k}}^{+}. \tag{12.60}$$

The electron-phonon mean free path can then be written as

$$\lambda_{\mathrm{phonon}} = \frac{\hbar k/m^*}{W_{\mathrm{k}}^{-} + W_{\mathrm{k}}^{+}} = \frac{\sqrt{2\,E_k/m^*}}{W_{\mathrm{k}}^{-} + W_{\mathrm{k}}^{+}}, \tag{12.61}$$

and, as a consequence,

$$\begin{aligned}\lambda_{\mathrm{phonon}}^{-1} = {} & \frac{1}{a_0}\left[\frac{\varepsilon_0 - \varepsilon_\infty}{\varepsilon_0\ \varepsilon_\infty}\right]\frac{\hbar\omega}{E_{\mathrm{k}}}\frac{1}{2}\ \times \\ \times {} & \left\{[n(T)\ +1]\ \ln\left[\frac{1+\sqrt{1-\hbar\omega/E_{\mathrm{k}}}}{1-\sqrt{1-\hbar\omega/E_{\mathrm{k}}}}\right] + \right. \\ + {} & \left. n(T)\ \ln\left[\frac{\sqrt{1+\hbar\omega/E_{\mathrm{k}}}+1}{\sqrt{1+\hbar\omega/E_{\mathrm{k}}}-1}\right]\right\},\end{aligned} \tag{12.62}$$

where we have assumed that the electron effective mass m^* is equal to that of a free electron, $m^* = m$.

The probability of phonon creation is much higher than that of phonon annihilation [2, 3, 9], so that one can safely ignore the electron energy gain due to the phonon annihilation. As a consequence we can write

$$\lambda_{\mathrm{phonon}} = \frac{\hbar k/m^*}{W_{\mathrm{k}}^{+}}, \tag{12.63}$$

so that, indicating with $E = E_k$ the energy of the incident electron and with $W_{\text{ph}} = \hbar\omega$ the energy of the created phonon (and assuming that $m^* = m$) we conclude that the inverse inelastic mean free path for electron energy loss due to phonon creation can be written as [2]

$$\lambda_{\text{phonon}}^{-1} = \\ = \frac{1}{a_0} \frac{\varepsilon_0 - \varepsilon_\infty}{\varepsilon_0\ \varepsilon_\infty} \frac{W_{\text{ph}}}{E} \frac{n(T)+1}{2} \ln\left[\frac{1+\sqrt{1-W_{\text{ph}}/E}}{1-\sqrt{1-W_{\text{ph}}/E}}\right]. \tag{12.64}$$

This equation was used in the Monte Carlo simulations of secondary electron emission from insulating materials presented in this book [3, 9, 10].

12.3 Summary

The Fröhlich theory [1, 2] concerning the interaction of free electrons with the longitudinal optical mode lattice vibrations, was described in this chapter. Both phonon creation and phonon annihilation, corresponding to electron energy loss and to electrons energy gain respectively, are described by the theory.

References

1. H. Fröhlich, Adv. Phys. **3**, 325 (1954)
2. J. Llacer, E.L. Garwin, J. Appl. Phys. **40**, 2766 (1969)
3. J.P. Ganachaud, A. Mokrani, Surf. Sci. **334**, 329 (1995)
4. Y. Fujii, S. Hoshino, S. Sakuragi, H. Kanzaki, J.W. Lynn, G. Shirane, Phys. Rev. B **15**, 358 (1977)
5. G. Nilsson, G. Nelin, Phys. Rev. B **3**, 364 (1971)
6. G. Nilsson, G. Nelin, Phys. Rev. B **6**, 3777 (1972)
7. P. Giannozzi, S. De Gironcoli, P. Pavone, and S. Baroni Phys. Rev. B **43**, 7231 (1991)
8. N. Ashcroft, N.D. Mermin, *Solid State Physics* (W.B Saunders, 1976)
9. M. Dapor, M. Ciappa, W. Fichtner, J. Micro/Nanolith, MEMS MOEMS **9**, 023001 (2010)
10. M. Dapor, Nucl. Instrum. Methods Phys. Res. B **269**, 1668 (2011)

Chapter 13
Appendix D: The Ritchie Theory

The Ritchie theory describes the relationship between the dielectric function and the electron energy loss in a solid. It allows to calculate the differential inverse inelastic mean free path, the elastic mean free path, and the stopping power. The original version of the Ritchie theory can be found in Ref. [1]. Also see Refs. [2–6] for further details.

13.1 Energy Loss and Dielectric Function

The response of the ensemble of conduction electrons to the electromagnetic disturbance due to electrons passing through a solid and losing energy in it, is described by a complex dielectric function $\varepsilon(\boldsymbol{k}, \omega)$, where $\boldsymbol{k}$ is the wave vector and ω is the frequency of the electromagnetic field. If, at time t, the electron position is $\boldsymbol{r}$ and its speed is $\boldsymbol{v}$, then, indicating with e the electron charge, the electron that passes through the solid can be represented by a charge distribution given by

$$\rho(\boldsymbol{r}, t) \;=\; -e\,\delta(\boldsymbol{r} - \boldsymbol{v}t)\,. \tag{13.1}$$

The electric potential φ generated in the medium can be calculated as[1]

$$\varepsilon(\boldsymbol{k}, \omega)\,\nabla^2\varphi(\boldsymbol{r}, t) \;=\; -4\pi\,\rho(\boldsymbol{r}, t)\,. \tag{13.2}$$

In the Fourier space we have

$$\varphi(\boldsymbol{k}, \omega) \;=\; -\frac{8\pi^2 e}{\varepsilon(\boldsymbol{k}, \omega)}\,\frac{\delta(\boldsymbol{k}\cdot\boldsymbol{v} \,+\, \omega)}{k^2}\,. \tag{13.3}$$

[1] The vector potential is zero due to the chosen gauge.

M. Dapor, *Transport of Energetic Electrons in Solids*,
Springer Tracts in Modern Physics 257, DOI 10.1007/978-3-319-47492-2_13

In fact, on the one hand,

$$\varphi(\boldsymbol{r},t) \;=\; \frac{1}{(2\pi)^4}\int d^3k \int_{-\infty}^{+\infty} d\omega \exp[i(\boldsymbol{k}\cdot\boldsymbol{r}+\omega\, t)]\,\varphi(\boldsymbol{k},\omega)\,, \tag{13.4}$$

so that

$$\nabla^2\,\varphi(\boldsymbol{r},t) \;=\; -\frac{1}{(2\pi)^4}\int d^3k \int_{-\infty}^{+\infty} d\omega\, \exp[i(\boldsymbol{k}\cdot\boldsymbol{r}+\omega\, t)]\,k^2\,\varphi(\boldsymbol{k},\omega)\,, \tag{13.5}$$

and, on the other hand,

$$\begin{aligned}
&\rho(\boldsymbol{k},\omega) \;=\; \int d^3r \int_{-\infty}^{+\infty} dt\, \exp[-i(\boldsymbol{k}\cdot\boldsymbol{r}+\omega\, t)]\,\rho(\boldsymbol{r},t) \;=\\
&=\; \int d^3r \int_{-\infty}^{+\infty} dt\, \exp[-i(\boldsymbol{k}\cdot\boldsymbol{r}+\omega\, t)]\,[-e\,\delta(\boldsymbol{r}-\boldsymbol{v}t)] \;=\\
&=\; -2\pi e\frac{1}{2\pi}\int_{-\infty}^{+\infty} dt\, \exp[-i(\boldsymbol{k}\cdot\boldsymbol{v}+\omega)t] \;=\\
&=\; -2\pi e\,\delta(\boldsymbol{k}\cdot\boldsymbol{v}+\omega)\,,
\end{aligned} \tag{13.6}$$

so that

$$\rho(\boldsymbol{r},t) \;=\; \frac{1}{(2\pi)^4}\int d^3k \int_{-\infty}^{+\infty} d\omega \exp[i(\boldsymbol{k}\cdot\boldsymbol{r}+\omega\, t)]\,[-2\pi e\,\delta(\boldsymbol{k}\cdot\boldsymbol{v}+\omega)]\,. \tag{13.7}$$

Then, using Eqs. (13.2), (13.5), and (13.7), we obtain

$$\varepsilon(\boldsymbol{k},\omega)\,k^2\,\varphi(\boldsymbol{k},\omega) \;=\; -8\pi^2\,e\,\delta(\boldsymbol{k}\cdot\boldsymbol{v}+\omega))\,, \tag{13.8}$$

which is equivalent to Eq. (13.3).

We are interested in calculating the energy loss $-dE$ of an electron due to its interaction with the electric field $\boldsymbol{\mathcal{E}}$ generated by the electrons passing through the solid. Let us indicate with $\mathcal{F}_z$ the z component of the electric force, so that

$$-\,dE \;=\; \boldsymbol{\mathcal{F}}\cdot d\boldsymbol{r} \;=\; \mathcal{F}_z\,dz\,. \tag{13.9}$$

It should be noted that here and in the following equations, the electric force (and the electric field $\boldsymbol{\mathcal{E}} \;=\; \boldsymbol{\mathcal{F}}/e$) are considered at $\boldsymbol{r} \;=\; \boldsymbol{v}\,t$. Since

$$\mathcal{E}_z\,dz \;=\; \frac{dz}{dt}\,dt\,\mathcal{E}_z \;=\; \frac{d\boldsymbol{r}}{dt}\cdot\boldsymbol{\mathcal{E}}\,dt \;=\; \frac{\boldsymbol{v}\cdot\boldsymbol{\mathcal{E}}}{v}\,dz \tag{13.10}$$

the energy loss $-dE$ per unit path length dz, $-dE/dz$, is given by

$$-\frac{dE}{dz} = \frac{e}{v}\,\boldsymbol{v}\cdot\boldsymbol{\mathcal{E}}\,. \tag{13.11}$$

Since

$$\boldsymbol{\mathcal{E}} = -\nabla\,\varphi(\boldsymbol{r},t) \tag{13.12}$$

and $\varphi(\boldsymbol{k},\omega)$ is the Fourier transform of $\varphi(\boldsymbol{r},t)$ [see Eq. (13.4)], then

$$\begin{aligned}&\boldsymbol{\mathcal{E}} = \\ &= -\nabla\left\{\frac{1}{(2\,\pi)^4}\int d^3\,k\int_{-\infty}^{+\infty} d\omega\,\exp[i(\boldsymbol{k}\cdot\boldsymbol{r}+\omega\,t)]\,\varphi(\boldsymbol{k},\omega)\right\}\,.\end{aligned} \tag{13.13}$$

As a consequence

$$\begin{aligned}&-\frac{dE}{dz} = \\ &= \mathrm{Re}\left\{-\frac{8\pi^2e^2}{(2\pi)^4 v}\;\times\right. \\ &\left.\times\int d^3k\int_{-\infty}^{+\infty} d\omega(-\nabla)\exp[i(\boldsymbol{k}\cdot\boldsymbol{r}+\omega\,t)]\cdot\;\boldsymbol{v}\;\frac{\delta(\boldsymbol{k}\cdot\boldsymbol{v}+\omega)}{k^2\,\varepsilon(\boldsymbol{k},\omega)}\bigg|_{\boldsymbol{r}=\boldsymbol{v}\,t}\right\} = \\ &= \mathrm{Re}\left\{-\frac{8\pi^2e^2}{(2\pi)^4 v}\;\times\right. \\ &\left.\times\int d^3k\int_{-\infty}^{+\infty} d\omega(-i\boldsymbol{k})\cdot\boldsymbol{v}\exp[i(\boldsymbol{k}\cdot\boldsymbol{r}+\omega\,t)]\;\frac{\delta(\boldsymbol{k}\cdot\boldsymbol{v}+\omega)}{k^2\,\varepsilon(\boldsymbol{k},\omega)}\bigg|_{\boldsymbol{r}=\boldsymbol{v}\,t}\right\} = \\ &= \mathrm{Re}\left\{\frac{i8\pi^2e^2}{16\pi^4 v}\;\times\right. \\ &\left.\times\int d^3k\int_{-\infty}^{+\infty} d\omega(\boldsymbol{k}\cdot\boldsymbol{v})\exp[i(\boldsymbol{k}\cdot\boldsymbol{r}+\omega\,t)]\;\frac{\delta(\boldsymbol{k}\cdot\boldsymbol{v}+\omega)}{k^2\,\varepsilon(\boldsymbol{k},\omega)}\bigg|_{\boldsymbol{r}=\boldsymbol{v}\,t}\right\}\,.\end{aligned} \tag{13.14}$$

Taking into account (i) that the electric field has to be calculated at $\boldsymbol{r} = \boldsymbol{v}\,t$ and (ii) of the presence in the integrand of the $\delta(\boldsymbol{k}\cdot\boldsymbol{v}+\omega)$ distribution, we have

$$
\begin{aligned}
&-\frac{dE}{dz} = \\
&= \mathrm{Re}\left\{\frac{i\,e^2}{2\,\pi^2\,v}\ \times\right. \\
&\left.\times \int d^3k \int_{-\infty}^{+\infty} d\omega\, \boldsymbol{k}\cdot\boldsymbol{v}\, \exp[i(\boldsymbol{k}\cdot\boldsymbol{v}\,t\,+\,\omega\,t)]\,\frac{\delta(\boldsymbol{k}\cdot\boldsymbol{v}\,+\,\omega)}{k^2\,\varepsilon(\boldsymbol{k},\omega)}\right\} = \\
&= \mathrm{Re}\left\{\frac{i\,e^2}{2\,\pi^2\,v}\ \times\right. \\
&\left.\times \int d^3k \int_{-\infty}^{+\infty} d\omega\, \boldsymbol{k}\cdot\boldsymbol{v}\, \exp[i(-\omega\,t\,+\,\omega\,t)]\,\frac{\delta(\boldsymbol{k}\cdot\boldsymbol{v}\,+\,\omega)}{k^2\,\varepsilon(\boldsymbol{k},\omega)}\right\} = \\
&= \mathrm{Re}\left\{\frac{i\,e^2}{2\,\pi^2\,v}\ \times\right. \\
&\left.\times \int d^3k \int_{-\infty}^{+\infty} d\omega\,(-\omega)\, \exp[i(-\omega\,t\,+\,\omega\,t)]\,\frac{\delta(\boldsymbol{k}\cdot\boldsymbol{v}\,+\,\omega)}{k^2\,\varepsilon(\boldsymbol{k},\omega)}\right\} = \\
&= \mathrm{Re}\left\{\frac{-i\,e^2}{2\,\pi^2\,v}\int d^3k \int_{-\infty}^{+\infty} d\omega\,\omega\,\frac{\delta(\boldsymbol{k}\cdot\boldsymbol{v}\,+\,\omega)}{k^2\,\varepsilon(\boldsymbol{k},\omega)}\right\}. \qquad (13.15)
\end{aligned}
$$

Since

$$
\begin{aligned}
&\mathrm{Re}\left\{i\int_{-\infty}^{+\infty} d\omega\,\omega\,\frac{\delta(\boldsymbol{k}\cdot\boldsymbol{v}\,+\,\omega)}{\varepsilon(\boldsymbol{k},\omega)}\right\} = \\
&= 2\,\mathrm{Re}\left\{i\int_0^{+\infty} d\omega\,\omega\,\frac{\delta(\boldsymbol{k}\cdot\boldsymbol{v}\,+\,\omega)}{\varepsilon(\boldsymbol{k},\omega)}\right\},
\end{aligned}
$$

we conclude that[2]

$$
-\frac{dE}{dz} = \frac{e^2}{\pi^2\,v}\int d^3k \int_0^{\infty} d\omega\,\omega\,\mathrm{Im}\left[\frac{1}{\varepsilon(\boldsymbol{k},\omega)}\right]\frac{\delta(\boldsymbol{k}\cdot\boldsymbol{v}\,+\omega)}{k^2}, \qquad (13.16)
$$

or

$$
-\frac{dE}{dz} = \int_0^{\infty} d\omega\,\omega\,\tau(\boldsymbol{v},\omega), \qquad (13.17)
$$

where

$$
\tau(\boldsymbol{v},\omega) = \frac{e^2}{\pi^2\,v}\int d^3k\,\mathrm{Im}\left[\frac{1}{\varepsilon(\boldsymbol{k},\omega)}\right]\frac{\delta(\boldsymbol{k}\cdot\boldsymbol{v}\,+\,\omega)}{k^2} \qquad (13.18)
$$

[2]Note that, for any complex number z, $\mathrm{Re}(i\,z) = -\,\mathrm{Im}(z)$.

is the probability of an energy loss ω per unit distance traveled by a non-relativistic electron of velocity $\boldsymbol{v}$ [1].

13.2 Homogeneous and Isotropic Solids

Let us assume now that the solid is homogeneous and isotropic, and ε is a scalar depending only on the magnitude of $\boldsymbol{k}$ and not on its direction

$$\varepsilon(\boldsymbol{k}, \omega) = \varepsilon(k, \omega) \tag{13.19}$$

so that

$$\begin{aligned}
&\tau(v, \omega) = \\
&= \frac{e^2}{\pi^2 v} \int_0^{2\pi} d\phi \int_0^{\pi} d\theta \int_{k_-}^{k_+} dk\, k^2 \sin\theta \times \\
&\times \mathrm{Im}\left[\frac{1}{\varepsilon(k, \omega)}\right] \frac{\delta(k v \cos\theta + \omega)}{k^2} = \\
&= \frac{2 e^2}{\pi v} \int_0^{\pi} d\theta \int_{k_-}^{k_+} dk \sin\theta\, \mathrm{Im}\left[\frac{1}{\varepsilon(k, \omega)}\right] \delta(k v \cos\theta + \omega)
\end{aligned} \tag{13.20}$$

where

$$\hbar k_{\pm} = \sqrt{2 m E} \pm \sqrt{2 m (E - \hbar\omega)}\,. \tag{13.21}$$

and $E = m v^2 / 2$. These limits of integration come from conservation of momentum (see Sect. 5.2.3).

Let us introduce the new variable ω' defined as

$$\omega' = -k v \cos\theta\,, \tag{13.22}$$

so that

$$d\omega' = k v \sin\theta\, d\theta \tag{13.23}$$

and, hence,

$$\begin{aligned}
\tau(v, \omega) &= \frac{2 e^2}{\pi v} \int_{-k v}^{k v} d\omega' \int_{k_-}^{k_+} \frac{dk}{k v} \mathrm{Im}\left[\frac{1}{\varepsilon(k, \omega)}\right] \delta(-\omega' + \omega) \\
&= \frac{2 m e^2}{\pi m v^2} \int_{k_-}^{k_+} \frac{dk}{k} \mathrm{Im}\left[\frac{1}{\varepsilon(k, \omega)}\right].
\end{aligned} \tag{13.24}$$

We thus can write that

$$\tau(E,\omega) \;=\; \frac{m\,e^2}{\pi\,E}\int_{k_-}^{k_+}\frac{dk}{k}\,\mathrm{Im}\left[\frac{1}{\varepsilon(k,\omega)}\right], \tag{13.25}$$

Indicating with $W = \hbar\omega$ the energy loss and with $W_{\max}$ the maximum energy loss, the inverse electron inelastic mean free path, $\lambda_{\mathrm{inel}}^{-1}$, can be calculated as

$$\begin{aligned}
&\lambda_{\mathrm{inel}}^{-1} \;= \\
&= \frac{m\,e^2}{\pi\,\hbar^2\,E}\int_0^{W_{\max}} d\hbar\omega\int_{k_-}^{k_+}\frac{dk}{k}\,\mathrm{Im}\left[\frac{1}{\varepsilon(k,\omega)}\right] = \\
&= \frac{1}{\pi\,a_0\,E}\int_0^{W_{\max}} d\hbar\omega\int_{k_-}^{k_+}\frac{dk}{k}\,\mathrm{Im}\left[\frac{1}{\varepsilon(k,\omega)}\right].
\end{aligned} \tag{13.26}$$

13.3 Summary

The Ritchie theory [1] was described. It allows to establish the relationship between electron energy loss and dielectric function, and to calculate the differential inverse inelastic mean free path, the inelastic means free path, and the stopping power.

References

1. R.H. Ritchie, Phys. Rev. **106**, 874 (1957)
2. H. Raether, *Excitation of Plasmons and Interband Transitions by Electrons* (Springer, Berlin, 1982)
3. P. Sigmund, *Particle Penetration and Radiation Effects* (Springer, Berlin, 2006)
4. R.F. Egerton, *Electron Energy-Loss Spectroscopy in the Electron Microscope*, 3rd edn. (Springer, New York, 2011)
5. R.F. Egerton, Rep. Prog. Phys. **72**, 016502 (2009)
6. S. Taioli, S. Simonucci, L. Calliari, M. Dapor, Phys. Rep. **493**, 237 (2010)

Chapter 14
Appendix E: The Chen and Kwei and the Li et al. Theory

The original version of the Chen and Kwei theory can be found in Ref. [1] for outgoing projectiles. It was generalized by Li et al. [2] for incoming projectiles. Below, the Chen and Kwei and the Li et al. formulas are rewritten in terms of angular variables, according to Ref. [3].

14.1 Outgoing and Incoming Electrons

Let us consider the component q_x and q_y of the momentum transfer parallel to the surface. For outgoing electrons,

$$q_x = \frac{mv}{\hbar}(\theta \cos\phi \cos\alpha + \theta_E \sin\alpha), \tag{14.1}$$

while, for incoming electrons,

$$q_x = \frac{mv}{\hbar}(\theta \cos\phi \cos\alpha - \theta_E \sin\alpha). \tag{14.2}$$

For both outgoing and incoming electrons we have

$$q_y = \frac{mv}{\hbar}\theta \sin\phi. \tag{14.3}$$

In these equations, α is the angle of the electron trajectory with respect to the normal to the target surface, θ and ϕ indicate the polar and azimuth angles, and

$$\theta_E = \frac{\hbar\omega}{2E}, \tag{14.4}$$

where E is the electron energy and $\hbar\omega$ the energy loss.

M. Dapor, *Transport of Energetic Electrons in Solids*,
Springer Tracts in Modern Physics 257, DOI 10.1007/978-3-319-47492-2_14

14.2 Probability of Inelastic Scattering

If z is the coordinate along the normal to the surface target, the probability for inelastic scattering (the differential inverse inelastic mean free path, DIIMFP) is given by:

$$P_{\text{outside}}(z,\alpha) = \frac{1}{2\pi^2 a_0 E}\int_0^{\theta_{\text{cutoff}}}\frac{\theta\, d\theta}{\theta^2+\theta_{\text{E}}^2}\int_0^{2\pi} d\phi\, f(z,\theta,\phi,\alpha) \tag{14.5}$$

in the vacuum, and

$$P_{\text{inside}}(z,\alpha) = \frac{1}{2\pi^2 a_0 E}\int_0^{\theta_{\text{cutoff}}}\frac{\theta\, d\theta}{\theta^2+\theta_{\text{E}}^2}\int_0^{2\pi} d\phi\, g(z,\theta,\phi,\alpha) \tag{14.6}$$

inside the material. The cutoff angle is taken to be the Bethe ridge angle [4]

$$\theta_{\text{cutoff}} = \sqrt{\frac{\hbar\omega}{E}}\,. \tag{14.7}$$

It should be noted that in the Chen and Kwei approach, [1] there is no proper limit for the high-momentum cutoff, while there exists a maximum angle, known as the Bethe ridge angle, only up to which electron excitation is allowed [5].

For outgoing electrons, functions $f(z,\theta,\phi,\alpha)$ and $g(z,\theta,\phi,\alpha)$ can be written as:

$$f(z,\theta,\phi,\alpha) = \text{Im}\left(\frac{2}{\varepsilon+1}\right) h(z,\theta,\phi,\alpha)\,[p(z,\theta,\phi,\alpha)-h(z,\theta,\phi,\alpha)]\,, \tag{14.8}$$

$$g(z,\theta,\phi,\alpha) = \text{Im}\left(\frac{2}{\varepsilon+1}\right) h^2(z,\theta,\phi,\alpha) + \text{Im}\left(\frac{1}{\varepsilon}\right)[1-h^2(z,\theta,\phi,\alpha)]\,. \tag{14.9}$$

For incoming electrons, the same functions $f(z,\theta,\phi,\alpha)$ and $g(z,\theta,\phi,\alpha)$ are given by:

$$f(z,\theta,\phi,\alpha) = \text{Im}\left(\frac{2}{\varepsilon+1}\right) h^2(z,\theta,\phi,\alpha)\,, \tag{14.10}$$

$$g(z,\theta,\phi,\alpha) = \text{Im}\left(\frac{2}{\varepsilon+1}\right) h(z,\theta,\phi,\alpha)\,[p(z,\theta,\phi,\alpha)-h(z,\theta,\phi,\alpha)] + \\ + \text{Im}\left(\frac{1}{\varepsilon}\right)[1-h(z,\theta,\phi,\alpha)p(z,\theta,\phi,\alpha)+h^2(z,\theta,\phi,\alpha)]\,. \tag{14.11}$$

Functions $h(z, \theta, \phi, \alpha)$ and $p(z, \theta, \phi, \alpha)$ are, in turn, given by:

$$h(z, \theta, \phi, \alpha) = \exp\left[\left(-|z|\frac{mv}{\hbar}\right)\sqrt{(\theta\cos\phi\cos\alpha + \theta_E\sin\alpha)^2 + \theta^2\sin^2\phi}\right], \tag{14.12}$$

$$p(z, \theta, \phi, \alpha) = 2\cos\left[\left(|z|\frac{mv}{\hbar}\right)(\theta_E\cos\alpha - \theta\cos\phi\sin\alpha)\right], \tag{14.13}$$

for outgoing electrons and by:

$$h(z, \theta, \phi, \alpha) = \exp\left[\left(-|z|\frac{mv}{\hbar}\right)\sqrt{(\theta\cos\phi\cos\alpha - \theta_E\sin\alpha)^2 + \theta^2\sin^2\phi}\right], \tag{14.14}$$

$$p(z, \theta, \phi, \alpha) = 2\cos\left[\left(|z|\frac{mv}{\hbar}\right)(\theta_E\cos\alpha + \theta\cos\phi\sin\alpha)\right], \tag{14.15}$$

for incoming electrons.

Finally, $\varepsilon(\omega)$ is the dielectric function. For the case of silicon, it can be calculated as:

$$\varepsilon(\omega) = 1 - \frac{\omega_p^2}{\omega^2 - \omega_g^2 - i\Gamma\omega}, \tag{14.16}$$

where $\hbar\omega$ is the electron energy loss, $\hbar\omega_g$ is the average excitation energy for valence electrons, $\hbar\Gamma$ is the damping constant, and $\hbar\omega_p$ is the plasmon energy.

14.3 Summary

The Chen and Kwei theory for outgoing electrons [1], and its generalization proposed by Li et al. [2] for incoming projectiles, were described and rewritten in terms of angular variables, according to Ref. [3].

References

1. Y.F. Chen, C.M. Kwei, Surf. Sci. **364**, 131 (1996)
2. Y.C. Li, Y.H. Tu, C.M. Kwei, C.J. Tung, Surf. Sci. **589**, 67 (2005)
3. M. Dapor, L. Calliari, S. Fanchenko, Surf. Interface Anal. **44**, 1110 (2012)
4. R.F. Egerton, *Electron Energy-Loss Spectroscopy in the Electron Microscope*, 3rd edn. (Springer, New York, 2011)
5. L. Calliari, S. Fanchenko, Surf. Interface Anal. **44**, 1104 (2012)

Chapter 15
Appendix F: The Mermin Theory and the Generalized Oscillator Strength Method

Dielectric formalism is the most used method for investigating the interaction of swift electrons with solid targets. In this chapter the Mermin energy loss function-generalized oscillator strength method (MELF-GOS method) is briefly described within the framework of dielectric formalism [1–4].

15.1 The Mermin Theory

The Mermin dielectric function [1] is given by:

$$\varepsilon_M(\mathbf{q},\omega) = 1 + \frac{(1+i/\omega\tau)[\varepsilon^0(\mathbf{q},\omega+i/\tau)-1]}{1+(i/\omega\tau)[\varepsilon^0(\mathbf{q},\omega+i/\tau)-1]/[\varepsilon^0(\mathbf{q},0)-1]}\,, \tag{15.1}$$

where $\mathbf{q}$ is the momentum, ω the frequency, τ the relaxation time, and $\varepsilon^0(\mathbf{q},\omega)$ the Lindhard dielectric constant [5]

$$\varepsilon^0(\mathbf{q},\omega) = 1 + \frac{4\pi^2 q^2}{e^2} B(\mathbf{q},\omega)\,, \tag{15.2}$$

$$B(\mathbf{q},\omega) = \int \frac{d\mathbf{p}}{4\pi^3} \frac{f_{\mathbf{p}+\mathbf{q}/2} - f_{\mathbf{p}-\mathbf{q}/2}}{\omega - (\varepsilon_{\mathbf{p}+\mathbf{q}/2} - \varepsilon_{\mathbf{p}-\mathbf{q}/2})/\hbar}\,. \tag{15.3}$$

In these equations e is the electron charge, $f_{\mathbf{p}}$ is the Fermi-Dirac distribution, and $\varepsilon_{\mathbf{p}}$ the free electron energy.

Note that the Lindhard dielectric function [5] can be numerically calculated by using Eqs. (15.2) and (15.3). The integration can also be carried out in closed form. The result of the integration is the following [2, 3, 6]:

M. Dapor, *Transport of Energetic Electrons in Solids*,
Springer Tracts in Modern Physics 257, DOI 10.1007/978-3-319-47492-2_15

$$\varepsilon^0(q,\omega) \;=\; 1+\frac{\chi^2}{z^2}[f_1(u,z)\;+\;i\;f_2(u,z)]\,, \tag{15.4}$$

where $u=\omega/(qv_F)$, $z=q/(2q_F)$, and $\chi^2=e^2/(\pi\,\hbar\,v_F)$ is a measure of the electron density [6]. In this equation, v_F is the Fermi velocity of the valence electrons of the target and $q_F=mv_F/\hbar$. The functions $f_1(u,z)$ and $f_2(u,z)$ are given by

$$f_1(u,z) \;=\; \frac{1}{2}\;+\;\frac{1}{8z}\,[g(z-u)\;+\;g(z+u)]\,, \tag{15.5}$$

$$f_2(u,z)=\begin{cases}\frac{\pi}{2}u, & z+u<1\\ \frac{\pi}{8z}[1-(z-u)^2], & |z-u|<1<z+u\\ 0, & |z-u|>1\,,\end{cases} \tag{15.6}$$

where

$$g(x) \;=\; (1-x^2)\,\ln\left|\frac{1+x}{1-x}\right|\,. \tag{15.7}$$

15.2 The Mermin Energy Loss Function-Generalized Oscillator Strength Method (MELF-GOS)

Let us now consider a superposition of free and bound oscillators. For any oscillator, the energy loss function is given by the opposite of the imaginary part of the inverse of the Mermin dielectric function:

$$\mathrm{Im}\left[\frac{-1}{\varepsilon_M(\omega_i,\gamma_i\,;q,\omega)}\right] \;=\; \frac{\varepsilon_{M_2}}{\varepsilon_{M_1}^2+\varepsilon_{M_2}^2}\,, \tag{15.8}$$

where

$$\varepsilon_M \;=\; \varepsilon_{M_1}+i\varepsilon_{M_2} \tag{15.9}$$

and ω_i and γ_i are, respectively, the frequency and the damping constant associated to each specific oscillator. A linear combination of Mermin-type energy loss functions, one per oscillator, allows to calculate the energy loss function (ELF) for $q\;=\;0$, for any specific material [2–4]:

$$\mathrm{Im}\left[\frac{-1}{\varepsilon(q\,=\,0,\omega)}\right] \;=\; \sum_i A_i\,\mathrm{Im}\left[\frac{-1}{\varepsilon_M(\omega_i,\gamma_i\,;q\,=\,0,\omega)}\right]\,. \tag{15.10}$$

In this equation, A_i, ω_i, and γ_i are determined by looking for the best fit of the available experimental optical ELF. Actually, as both Mermin and Drude-Lorentz oscillators converge on the same values in the optical limit (i.e. for $q = 0$) [7]

$$\mathrm{Im}\left[\frac{-1}{\varepsilon(q=0,\omega)}\right] = \sum_i A_i \mathrm{Im}\left[\frac{-1}{\varepsilon_M(\omega_i,\gamma_i\,;q=0,\omega)}\right] = \sum_i A_i \mathrm{Im}\left[\frac{-1}{\varepsilon_D(\omega_i,\gamma_i\,;q=0,\omega)}\right], \tag{15.11}$$

where the Drude-Lorentz functions $\mathrm{Im}\left[\frac{-1}{\varepsilon_D(\omega_i,\gamma_i\,;\mathbf{q}=0,\omega)}\right]$ are given by [8]

$$\mathrm{Im}\left[\frac{-1}{\varepsilon_D(\omega_i,\gamma_i\,;\mathbf{q}=0,\omega)}\right] = \frac{\gamma_i\omega}{(\omega_i^2-\omega^2)^2+(\gamma_i\omega)^2}, \tag{15.12}$$

the best fit can also be obtained using a linear combination of Drude-Lorentz functions, instead of Mermin functions. Once the values of the best fit parameters have been established (see, for example, Refs. [4, 9, 10]), the extension beyond the optical domain ($\mathbf{q} \neq 0$) can be obtained by [2–4]

$$\mathrm{Im}\left[\frac{-1}{\varepsilon(\mathbf{q},\omega)}\right] = \sum_i A_i \mathrm{Im}\left[\frac{-1}{\varepsilon_M(\omega_i,\gamma_i\,;\mathbf{q},\omega)}\right]. \tag{15.13}$$

Planes et al. [2], Abril et al. [3], and de Vera et al. [4] construct the ELF in the optical limit including the contribution of the electrons from the outermost atomic inner shells as follows:

$$\mathrm{Im}\left[\frac{-1}{\varepsilon(q=0,\omega)}\right] = \begin{cases} \sum_i A_i \mathrm{Im}\left[\frac{-1}{\varepsilon_M(\omega_i,\gamma_i\,;q=0,\omega)}\right] & \omega < \omega_{i,edge} \\ \sum_{i,sh} A_{i,sh} \mathrm{Im}\left[\frac{-1}{\varepsilon_M(\omega_{i,sh},\gamma_{i,sh}\,;q=0,\omega)}\right] & \omega \geq \omega_{i,edge} \end{cases} \tag{15.14}$$

where the first term represents the contribution of the outer electrons while the second one includes the electrons of the outermost atomic inner shells.

15.3 Summary

In this chapter, after a brief discussion about the Mermin theory [1], the Mermin energy loss function-generalized oscillator strength method (MELF-GOS method), in the framework of the dielectric formalism, was shortly described [2–4].

References

1. N.D. Mermin, Phys. Rev. B **1**, 2362 (1970)
2. D.J. Planes, R. Garcia-Molina, I. Abril, N.R. Arista, J. Electron Spectrosc. Relat. Phenom. **82**, 23 (1996)
3. I. Abril, R. Garcia-Molina, C.D. Denton, F.J. Pérez-Pérez, N.R. Arista, Phys. Rev. A **58**, 357 (1998)
4. P. de Vera, I. Abril, R. Garcia-Molina. J. Appl. Phys. **109**, 094901 (2011)
5. J. Lindhard, Kgl. Danske Videnskab. Selskab Mat.-fys. Medd. **28**, 8 (1954)
6. P. Sigmund, *Particle Penetration and Radiation Effects* (Springer, Berlin, 2006)
7. W. de la Cruz, F. Yubero. Surf. Interface Anal. **39**, 460 (2007)
8. R.H. Ritchie, A. Howie, Philos. Mag. **36**, 463 (1977)
9. R. Garcia-Molina, I. Abril, C.D. Denton, S. Heredia-Avalos, Nucl. Instr. Meth. Phys. Res. B **249**, 6 (2006)
10. M. Dapor, Nucl. Instr. Meth. Phys. Res. B **352**, 190 (2015)

Chapter 16
Appendix G: The Kramers–Kronig Relations and the Sum Rules

In this chapter, the response of a material to applied electromagnetic radiations is discussed [1–3]. In particular, the complex dielectric function is the response function of the medium corresponding to the electric polarization induced by an applied electric field. Similarly, the complex conductivity describes the electric current induced in response to an applied electric field. In general, the system response to a given stimulus is ruled by the complex analysis and, in particular, by the so-called Kramers–Kronig relations. A consequence of the Kramers–Kronig analysis is constituted by the sum rules which must be satisfied by several optical parameters.

16.1 Linear Response to External Perturbations

Polarization $\mathbf{P}(t)$ of a material at time t depends on the electric field $\mathbf{E}(t)$ applied to the material from $t' = -\infty$ to $t' = t$, according to the following equation:

$$\mathbf{P}(t) = \int_{-\infty}^{t} G(t - t')\, \mathbf{E}(t')\, dt', \tag{16.1}$$

where $G(t)$ is a real Green function of real variable [1]. Assuming that

$$\mathbf{E}(t) = \mathbf{E}_0 \exp[-i\omega t], \tag{16.2}$$

it is thus easy to see that

$$\mathbf{P}(t) = \mathbf{E} \int_{0}^{\infty} G(\tau) \exp[i\omega\tau]\, d\tau. \tag{16.3}$$

M. Dapor, *Transport of Energetic Electrons in Solids*,
Springer Tracts in Modern Physics 257, DOI 10.1007/978-3-319-47492-2_16

As a consequence, the electric susceptibility $\chi(\omega)$ can be written as

$$\chi(\omega) = \int_0^\infty G(\tau) \exp[i\omega\tau] d\tau. \tag{16.4}$$

Since

$$\varepsilon \mathbf{E} = \mathbf{E} + 4\pi \mathbf{P} = \mathbf{E} + 4\pi\chi \mathbf{E} = (1 + 4\pi\chi)\, \mathbf{E}, \tag{16.5}$$

we conclude that the dielectric function $\varepsilon(\omega)$ is given by

$$\varepsilon(\omega) = 1 + 4\pi\chi(\omega) \; = 1 + 4\pi \int_0^\infty G(\tau) \exp[i\omega\tau] d\tau. \tag{16.6}$$

Thus,

$$\begin{aligned} \varepsilon^*(\omega) = 1 + 4\pi \int_0^\infty G(\tau) \exp[-i\omega\tau] d\tau \; = \\ = \; \varepsilon(-\omega) = \varepsilon_1(-\omega) + i\varepsilon_2(-\omega). \end{aligned} \tag{16.7}$$

Since

$$\varepsilon^*(\omega) = [\varepsilon_1(\omega) + i\varepsilon_2(\omega)]^* = \varepsilon_1(\omega) - i\varepsilon_2(\omega), \tag{16.8}$$

we have demonstrated that the real part of the dielectric function is even

$$\varepsilon_1(\omega) = \varepsilon_1(-\omega), \tag{16.9}$$

while its imaginary part is odd

$$\varepsilon_2(\omega) = -\varepsilon_2(-\omega). \tag{16.10}$$

16.2 The Kramers–Kronig Relations

Using the Cauchy's residue theorem we obtain

$$\mathcal{P} \int_{-\infty}^{\infty} \frac{\chi(\omega)}{\omega - \omega_T} = i\pi\chi(\omega_T), \tag{16.11}$$

and, as a consequence, keeping in mind that

$$\chi(\omega) = \frac{\varepsilon(\omega) - 1}{4\pi} \tag{16.12}$$

$$\varepsilon(\omega) = 1 + \frac{1}{i\pi}\,\mathcal{P}\int_{-\infty}^{\infty} \frac{\varepsilon(\omega') - 1}{\omega' - \omega}\,d\omega'. \tag{16.13}$$

Therefore, the real and the imaginary parts of the dielectric function can be expressed as follows

$$\varepsilon_1(\omega) = 1 + \frac{1}{\pi}\,\mathcal{P}\int_{-\infty}^{\infty} \frac{\varepsilon_2(\omega')}{\omega' - \omega}\,d\omega', \tag{16.14}$$

$$\varepsilon_2(\omega) = -\frac{1}{\pi}\,\mathcal{P}\int_{-\infty}^{\infty} \frac{\varepsilon_1(\omega') - 1}{\omega' - \omega}\,d\omega', \tag{16.15}$$

or, after straightforward algebraic manipulations,

$$\varepsilon_1(\omega) = 1 + \frac{2}{\pi}\,\mathcal{P}\int_{0}^{\infty} \frac{\omega'\,\varepsilon_2(\omega')}{\omega'^2 - \omega^2}\,d\omega', \tag{16.16}$$

$$\varepsilon_2(\omega) = -\frac{2\,\omega}{\pi}\,\mathcal{P}\int_{0}^{\infty} \frac{\varepsilon_1(\omega') - 1}{\omega'^2 - \omega^2}\,d\omega'. \tag{16.17}$$

These are the Kramers–Kronig relations relating the real and imaginary parts of the dielectric function.

16.3 Sum Rules

Physical arguments can be used to establish some sum rules that, taking into account the Kramers–Kronig relations, must be satisfied. Let us consider, for example, the simple case of high frequency electric field interacting with a metal.

On the one hand, indicating as usual with ω_p the plasma frequency, according to the Drude model about the optical properties of metals we can write

$$\varepsilon_1(\omega) = 1 - \frac{\omega_p^2}{\omega^2}. \tag{16.18}$$

On the other hand, according to the Kramers–Kronig theory and taking into account the high frequency hypothesis as well, we obtain

$$\varepsilon_1(\omega) = 1 - \frac{2}{\pi\omega^2}\,\mathcal{P}\int_{0}^{\infty} \omega'\varepsilon_2(\omega')\,d\omega'. \tag{16.19}$$

Combining these two equations, we obtain the following sum rule that the imaginary part of the dielectric function must satisfy:

$$\int_0^\infty \omega\, \varepsilon_2(\omega)\, d\omega = \frac{\pi}{2}\, \omega_p^2. \tag{16.20}$$

It is well known from the electromagnetic theory that the following relationship exists between the complex dielectric function ε and the conductivity σ of a metal:

$$\varepsilon = 1 + i\, \frac{4\pi}{\omega}\, \sigma. \tag{16.21}$$

Simple algebraic manipulation allows us to express the real and imaginary parts of the complex conductivity, σ_1 and σ_2, respectively, as follows

$$\sigma_1 = \frac{\omega}{4\pi}\, \epsilon_2, \tag{16.22}$$

$$\sigma_2 = \frac{\omega}{4\,\pi}\, (1 - \varepsilon_1). \tag{16.23}$$

Thus, the real part of the complex conductivity must satisfy the sum rule

$$\int_0^\infty \sigma_1\, d\omega = \frac{\omega_p^2}{8}. \tag{16.24}$$

16.4 Summary

In this chapter, we discussed the system response to a given stimulus. In particular we deduced the Kramers–Kronig relations. We also described the sum rules which must be satisfied by the imaginary part of the complex dielectric function and by the real part of the complex conductivity of a metal.

References

1. F. Bassani, U.M. Grassano, *Fisica dello Stato Solido* (Bollati Boringhieri, Torino, 2000)
2. M. Dressel, G. Grüner, *Electrodynamics of Solids. Optical Properties of Electrons in Matter* (Cambridge University Press, New York, 2002)
3. R.F. Egerton, *Electron Energy-Loss Spectroscopy in the Electron Microscope*, 3rd edn. (Springer, New York, 2011)

Chapter 17
Appendix H: From the Electron Energy Loss Spectrum to the Dielectric Function

The ELF in the optical limit can be obtained by means of a transformation of the experimental transmitted electron energy loss spectrum (EELS). Such a transformation can be applied to the EELS after erasing the elastic peak and multiple scattering in order to deal with the single-scattering spectrum $S(W)$.

17.1 From the Single-Scattering Spectrum to the Energy Loss Function

The relationship between the single-scattering spectrum $S(W)$ and the ELF, $\mathrm{Im}\left[\frac{-1}{\varepsilon(q=0,W)}\right]$, is given by [1–3]

$$S(W) = \frac{I_0 t}{\pi a_0 m v^2} \mathrm{Im}\left[\frac{-1}{\varepsilon(q=0,W)}\right] \ln\left[1+\left(\frac{\beta}{\theta_W}\right)^2\right] \tag{17.1}$$

where I_0 is the zero-loss density, t is the sample thickness, a_0 is the Bohr radius, m is the electron mass, v is the incident electron velocity, β is the collection semi-angle, $\theta_W = \frac{W^2}{\gamma m v^2}$ is a characteristic scattering angle for energy loss W, and γ is the relativistic factor.

After collecting the transmitted electron energy loss spectrum and applying to it the so called Fourier-Log transformation –for erasing the elastic peak and multiple scattering [1]–, the transformation described by Eq. (17.1) allows to obtain the ELF.

M. Dapor, *Transport of Energetic Electrons in Solids*,
Springer Tracts in Modern Physics 257, DOI 10.1007/978-3-319-47492-2_17

17.2 Summary

We described a method for calculating the ELF in the optical limit using the experimental transmitted electron energy loss spectrum.

References

1. R.F. Egerton, *Electron Energy-Loss Spectroscopy in the Electron Microscope*, 3rd edn. (Springer, New York, 2011)
2. M. Stöger-Pollach, A. Laister, P. Schattschneider, Ultramicroscopy **108**, 439 (2008)
3. D.T.L. Alexander, P.A. Crozier, J.R. Anderson, Science **321**, 833 (2008)

Index

M. Dapor, *Transport of Energetic Electrons in Solids*,
Springer Tracts in Modern Physics 257, DOI 10.1007/978-3-319-47492-2